Nondestructive Evaluation of Adhesive Bonds by a Novel Ultrasonic Phase Measurement Method

---

A Ph.D. dissertation

Presented to

the Faculty at the School of Engineering and Applied Science

University of Virginia

---

in partial fulfillment

of the requirements for the degree

Doctor of Philosophy (Electrical and Computer Engineering)

by

Harold A. Haldren, III

B.S., Electrical Engineering, Liberty University, 2014

B.S., Mathematics, Liberty University, 2014

May 2020

Approval Sheet

This Ph.D. dissertation is submitted in partial fulfillment of the requirements for the degree

of

Doctor of Philosophy (Electrical and Computer Engineering)

Harold Haldren

This Ph.D. dissertation has been read and approved by the Examining Committee:

Professor Mool Gupta, Advisor

Professor Art Lichtenberger, Committee Chair

Professor Zongli Lin

Professor Sean Agnew

Dr. William Yost, NASA Langley Research Center

Accepted for the School of Engineering and Applied Science:

Dr. Craig H. Benson, Dean, School of Engineering and Applied Science
December 2019

Acknowledgements

First, I want to thank my advisor, Dr. Mool Gupta for his support and guidance throughout my graduate career. His position as NASA Langley Professor at the National Institute of Aerospace (NIA) has also provided me the wonderful chance to meet and collaborate with researchers at both NIA and NASA Langley Research (LaRC), and I am very appreciative of this opportunity.

To my friends and colleagues at UVa, especially Matt, Raj, and George, I really appreciate all of the valuable conversations we have had over the years. You all have helped to make graduate school more tolerable.

I would like to thank many members of NASA LaRC's Nondestructive Evaluation Sciences Branch (NESB) for all the help and support they have provided me over the past several years. I have interacted and talked with essentially every member of the NESB over the years, and they each have been wonderful to deal with and excited to talk. They have been gracious with both their time and resources to help me with my project, both in and out of the lab. First, I must thank Daniel Perey for his support on a day-to-day basis for my work, especially for his help in designing and testing the ultrasonic phase measurement instrument. Dr. Tom Yost has also been an essential resource for advice and feedback on my research, as well as allowing me to take up space in his lab for my studies. Elliott Cramer, as well, has provided me with advice, support, and great ideas on many occasions. I would also like to thank Angela Selden and John Callahan for their help in building and testing parts of the phase measurement instrument. Buzz Wincheski and Jason Moore must also be recognized for allowing me to use their lab equipment on numerous occasions and for their help with mechanically testing bonded joints. Josh Brown has helped me on numerous occasions with developing experimental setups and 3D printing parts for different experiments

Outside of the NESB, but still at NASA LaRC, John Connell and Frank Palmieri have both provided several useful discussions on adhesive bonding and mechanical testing, and they have promoted my work on adhesive bond strength evaluation to others. I really appreciate them allowing me to use their lab equipment on occasion, as well. Dr. Bill Winfree in the Research Directorate at NASA LaRC has provided me with excellent feedback on my work, and in recent years, he has provided me with greater advice and support at my semi-regular update meetings.

Next, I would like to thank all of the professors and mentors I met as an undergraduate, who helped me reach this goal. Both professors in the Liberty University Mathematics and Engineering departments helped me find my love for both math and engineering. Especially, I want to thank Dr. Pettiford and Dr. Bae in the engineering school for their consistent advice and support for me continuing my education and research pursuits. In addition, I thank Dr. Cook for his confidence in me and for encouraging me to pursue a mathematics degree; he really helped me realize my potential. I want to also thank all of the friends I met as an undergraduate, who all helped make that time memorable and fun.

Outside of Liberty University, I must thank Dr. Leda Lunardi and Jaladhi Mehta, who I met as a part of the Research Experience for Undergraduates (REU) program at NC State University. Additionally, I appreciate Dr. Beth Stadler and her team at the University of Minnesota, who I met as part of another REU. My experience working under Dr. Stadler helped me develop a love for research and was instrumental in my decision to pursue graduate school. The people I met that summer in Minneapolis helped make the REU experience great.

Next, I want to thank my friends Erik, Shoshana, Matt, Mark, Breen, Michael, Devin, and any others who have been part of the group over the years. With my focuses on going to school forever, I know I have not always been around to hang out with you all, but I really appreciate how easy it is to fit right back in to chat and play video or board games.

I would also like to thank my family for their love and support throughout the years. Mom, Dad, Rachel, grandparents, aunts, uncles, and cousins too numerous to individually list here: you all have always shown the utmost confidence in me and have supported my endeavors, even when they mean I have not been around as much. You all have helped me see and reach my potential.

I also thank my wife, Hannah, for her constant love and support throughout my years of graduate school. I could write a document longer than this one on all the ways she has helped me, and there is no way I could have done this without her. To my cats, Duchess, Duke (RIP), Milo, and Otis, you all have always been there for scratches and pets at any time, and your incessant meowing helps encourage me to get out of bed in the morning (to feed you).

Finally, I would like to thank God for providing me with the talent, determination, motivation, and opportunities to reach where I am today. I promise to continue using the talents you have given me to the best of my ability.

This work was supported by a NASA Space Technology Research Fellowship and the NASA Langley Professor Program.

Abstract

As modern aerospace and automotive designs have endeavored for higher performance, reduced cost, and lower weight, the use of advanced composite structures has greatly advanced. Consequently, the need for adhesive bonding, a preferred method of joining composite materials, has also drastically increased. As such, ensuring the strength of an adhesively bonded joint upon fabrication and throughout its service-life is of utmost importance. Conventional nondestructive evaluation (NDE) methods have been used to detect gross bonding defects, such as delaminations and voids, but are unable to detect weak adhesion and "kissing" bonds, leaving only destructive testing for quantitative bond strength measurement. As destructive testing is impractical for in-service structures, careful control of the bonding procedure and surface preparation methods are the primary methods of ensuring adequate adhesion quality.

While several specialized NDE methods have been developed to inspect adhesive bonds, few have shown the sensitivity to quantify weak adhesive/adherent interfaces. The focus of most NDE research into bonded joints has used ultrasonic methods to mechanically interrogate the bonded joint on the atomic level. In this work, a high-resolution ultrasonic phase measurement system is investigated for quantifiably measuring adhesive bond strength. This method uses constant-frequency pulsed phase-locked-loop (CFPPLL) technology to obtain high-resolution ultrasonic phase measurements with unprecedented accuracy and precision, even when swept over a range of frequencies.

When the adhesive bond line thickness is equal to half of the ultrasonic wavelength, the adhesive layer acts as an ultrasonic resonance cavity. By proper choice of driving ultrasonic frequency, the ultrasonic anti-resonance effect is observed from bond line reflections. The effect of weak bonding on the ultrasonic anti-resonance is investigated by modeling the ultrasonic interactions with adhesive/adherent interfaces by a distributed spring system. The phase of ultrasonic reflection from the bond line is extremely sensitive to material properties within the adhesive layer and is able to detect small differences in interfacial bond quality.

The swept-frequency ultrasonic phase measurement method is used to examine interfacial bonding of ideal bonded joints cured with ultraviolet light. These results show ultrasonic phase around the resonance frequency of the bond line is sensitive to both cohesive and adhesive changes as a function of cure. By fitting the measured phase vs. frequency response of bond line reflections, the interfacial stiffness is extracted. Studies on real-world metal/epoxy joints also prove ultrasonic phase measurements can identify kissing bonds and are sensitive to interfaces contaminated with either silicone or Teflon. Ultrasonically measured interfacial stiffness constants correlate linearly with mechanically measured bond strengths, showing good agreement with theory and indicating ultrasonic phase measurements have the sensitivity to quantify interfacial adhesion quality.

By nondestructively and quantitatively measuring adhesion quality, this method has the potential to promote the use of more complex, lightweight, and safe aerospace and automotive designs utilizing advanced composite structures and adhesive bonding. The demonstrated ultrasonic phase method is applicable to a variety of bonding material systems, is compatible with standard commercial ultrasonic transducers and conventional ultrasonic NDE setups, and can be used in many other applications in which sound velocity or ultrasonic phase monitoring can detect material properties degradation and changes.

Table of Contents

List of Tables

List of Figures

List of Symbols and Abbreviations

α	Acoustic attenuation coefficient $[Nepers/m]$
λ	Ultrasonic wavelength $[m]$
π	Ratio of a circle's circumference to its diameter, 3.14159 ...
ϕ	Ultrasonic phase $[deg]$
ϕ_0	Constant term of linear fit for phase vs. frequency response $[deg]$
ϕ_R	Phase of the ultrasonic reflection coefficient $[deg]$
ρ	Mass density $[kg/m^3]$
σ	Stress plane wave $[Pa]$
ω	Acoustic angular frequency, $2\pi f$ $[rad/Hz]$
ABUS	Angle beam ultrasonic spectroscopy
ADC	Analog-to-digital converter
AM	Additive manufacturing
c	Longitudinal wave velocity (sound velocity) $[m/s]$
CCZ	ClearCeram-Z, a glass-ceramic material from Ohara
CFPPLL	Constant frequency pulsed phase-locked-loop
CFRP	Carbon fiber reinforced polymer
DC	Direct current
DDS	Direct digital synthesizer
DIC	Digital image correlation
$d\phi/df$	Slope of ultrasonic phase shift with respect to frequency, $[deg/Hz]$
$d\phi/dT$	Slope of ultrasonic phase shift with respect to temperature, $[deg/°C]$
$d\phi/dt$	Slope of ultrasonic phase shift with respect to time, $[deg/s]$
E	Longitudinal elastic modulus, ρc^2 $[MPa]$
EC	Extrusion Coefficient of filament during additive manufacturing
EMAT	Electromagnetic acoustic transducer
f	Acoustic frequency $[Hz]$
f_{ar}	Anti-resonance frequency of lap joint $[Hz]$
FEM	Finite element modeling
FFT	Fast Fourier Transform
FL901AO	Epoxy film adhesive from MasterBond
FM73	Epoxy film adhesive from Cytec
FPGA	Field programmable gate array
i	Imaginary unit, $\sqrt{-1}$
K	Interfacial stiffness constant flux $[N/m^3]$
K_0	Interfacial stiffness causing peak phase value in $Z_1 > Z_2$ case
k	Complex acoustic wavenumber, $\omega/c + i\alpha$ $[1/m]$
L_{BL}	Bond line thickness $[m]$
LASAT	LAser Shock Adhesion Test
LBI	Laser Bond Inspection
LIBS	Laser induced breakdown spectroscopy

LSB	Least significant bit
m	Interfacial mass loading flux $[kg/m^2]$
NDE	Nondestructive evaluation
NDI	Nondestructive inspection
NDT	Nondestructive testing
NMR	Nuclear magnetic resonance
NOA	Norland Optical Adhesive
OSEE	Optically stimulated electron emission
PDMS	Polydimethylsiloxane, used for interface contamination (silicone-based)
PPLL	Pulsed phase-locked-loop
PTFE	Polytetrafluoroethylene (a.k.a. Teflon), used for interface contamination
PVDF	Polyvinylidene fluoride
PZT	Lead zirconate titanate
R	Normal-incidence ultrasonic displacement reflection coefficient
R_{BL}	Normal-incidence ultrasonic displacement bond line reflection coefficient
$Rayl$	Rayleighs, units for acoustic impedance $[Pa * s * m^{-1}]$
RMS	Root mean square
SAM	Scanning acoustic microscopy
S/H	Sample and hold
SEM	Scanning electron microscope
SHM	Structural health monitoring
SLJ	Single lap joint
SNR	Signal-to-noise ratio
T	Normal-incidence ultrasonic displacement transmission coefficient
t	Propagation time of ultrasonic plane wave $[s]$
ToF	Time-of-flight
TX	Transmit
u	Particle displacement of ultrasonic plane wave $[m]$
UV	Ultraviolet
x	Distance traveled by ultrasonic plane wave $[m]$
Z	Acoustic impedance, ρc $[Rayl]$

Chapter 1: Introduction and Motivation

1.1 Introduction

Methods for nondestructive assessment of adhesive bonds have been an active research area for some time. This problem is particularly important to the future of advanced composite structures in the aerospace, automotive, and other industries. Advancements in adhesive bonding applications in aerospace and automotive design has increased the need for bond strength validation, as adhesive bonding is a preferred method of joining advanced composite structures and is increasingly used in aerospace design and structural repair.

Currently, cleaning and control of surface preparation is used prior to bonding to ensure the ultimate joint meets strength specifications. While precise control of environmental conditions and the bonding process support the goal of consistent adhesion quality, inadequate surface preparation and accidental contamination still seriously degrade adhesion without being noticeable even to the trained observer or by conventional inspections. Mechanical fatigue and environmental degradation reduce the strength of critical bonds, leading to their premature failure, which could lead to loss of equipment or even loss of life. Thus, for adhesive bonding to be reliably used in joining critical structures, it is of utmost importance to be able to evaluate bonded joints non-destructively after fabrication and during service life.

Many nondestructive evaluation (NDE) methods have been characterized on their ability to identify weak bonding and have generally proved able to detect many bonding defects such as porosity, delaminations, and complete disbonds [1], [2], [3], [4]. However, such techniques have been unable to detect “kissing” bonds, where adhesive and adherent are in intimate contact but unable to support the transmission of tensile and shear stresses. As such, this work focuses on the development of a novel ultrasonic NDE method for interface characterization in adhesive bonds.

1.2 Fundamentals of Ultrasonic NDE of Adhesive Bonding

1.2.1 Adhesive Bond Failure

Before examining the methods of evaluating adhesively bonded joints, the modes by which bonds fail must be fully understood. The most commonly used type of bonded joint is known as the single lap joint (SLJ), which consists of two adherents bonded together with a thin layer of adhesive in between. Figure 1.1 shows a diagram of a SLJ configuration, which is the primary focus of the investigation in this work.

Figure 1.1: Single lap joint configuration of adhesive bonding

Broadly, adhesively bonded joints fail either cohesively (within the adhesive layer), adhesively at the adhesive/adherent interface, or within the adherent, itself [5]. Figure 1.2 shows images of broken bonded joints after undergoing cohesive and adhesive failure modes. For cohesive failure, adhesive residue is seen on both adherents after failure; while for pure adhesive failure, one adherent displays the intact adhesive layer and the other adherent has no adhesive residue.

For composite joints, out-of-plane adherent failure can also occur due to delamination in the composite adherents. Major defects in adhesively bonded joints include delaminations, complete disbonds, porosity, voids (large volume porosity), improper cure, and cracks [4]. Adherent failure will generally only occur below manufacturer rated adhesive bond strengths when the adherent has a significant defect or has become damaged, for which numerous NDE methods exist for defect detection [6] [7] [8] [9] [10] [11].

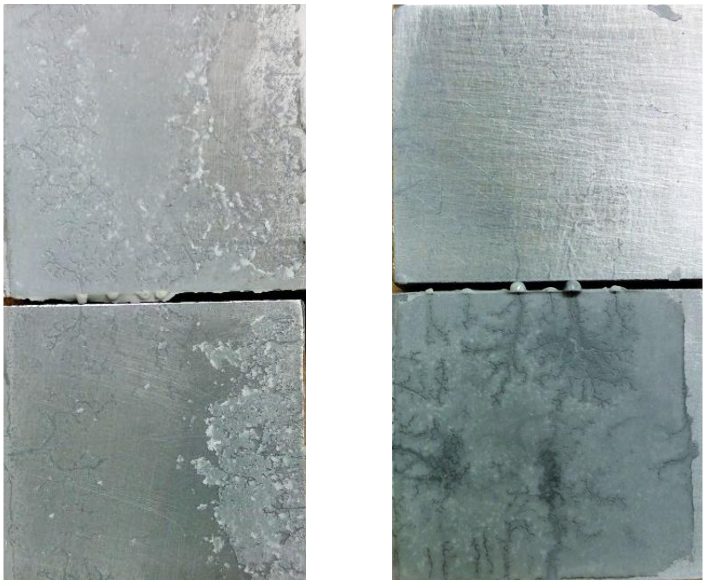

a) Cohesive Failure b) Adhesive/Interfacial Failure

Figure 1.2: Example images of broken aluminum/epoxy bonded joints showing a) cohesive failure and b) adhesive/interfacial failure

Assuming significant adherent defects can be detected through other NDE methods, this leaves cohesive and interfacial failure modes that must be characterized for bonded joint evaluation. For joints manufactured to specifications, weak bonding due to cohesive failure can generally be minimized. However, improper adhesive mixing or incorrect curing cycles can still occur, causing reduced cohesive strength. Even after pristine fabrication, both cohesion and adhesion can be affected over the service life of a joint through mechanical damage (e.g. physical impact), environmental damage (e.g. hot/wet aging), and fatigue (e.g. normal service stress/strain over time) [12]. Many NDE methods have been used to monitor cohesive properties during cure [13] [14] [15] [16], including an ultrasonic time-of-flight method described later in Chapter 6.

Even with a controlled bonding procedure, unwanted contaminants such as grease and oils can easily be exposed to adherents and greatly affect bond strength. As such, the major focus of recent research into NDE of bonded joints has focused on interfacial failure at the adhesive/adherent interface, which often occurs due to poor surface or material preparation [2]. These weak interfaces are often referred to as "kissing" bonds, where adhesive and adherent are in intimate contact but without the ability to transmit shear or tensile stress. However, no NDE method has shown satisfactory sensitivity to robustly detect kissing bonds and quantify interfacial bond strength in practical systems.

1.2.2 Quality Control of Adhesive Bonding

Numerous surface preparation methods exist to promote high adhesive bond strength and remove potential surface contaminants [17]. Simply cleaning the adherent with a solvent wipe prior to bonding can remove some surface contaminants. Additional solvent-based surface treatment methods include ultrasonic cleaning baths and vapor degreasing [18].

More complex surface preparation methods exist which modify the surface state of the adherent prior to bonding. Physically abrasive methods, such as surface sanding, sand blasting, and grit blasting each modify the adherent surface roughness to increase bonding surface area and mechanical interlocking with the adhesive. However, the relationship between bond strength and surface roughness is not well understood and can differ greatly depending upon material system and roughening method [19] [20] [21] [22] [23]. Laser ablation techniques improve on mechanical methods by also improving the adherent surface chemistry to promote adhesion [24] [25] [26]. Similarly, plasma surface treatments etch a thin layer from the adherent or modify surface contaminant molecules to clean and activate the surface [27] [28] [29] [30] [31]. Chemical methods to etch the surface prior to bonding are commonly used with metal adherents, as well [17].

After surface treatment and prior to bonding, several methods exist to characterize the surface state of the adherent surface. Classically, the most common method for determining whether an adherent is in an appropriate state for bonding is to measure the water contact angle of the surface [32] [33]. From the surface wettability, the free energy of the surface can be determined, which is an important parameter in determining adhesion strength after bonding. In general, the more wettable a surface, the more accepting the surface will be to the adhesive during the bonding process [1]. However, this technique does not work in all cases, as some surface contaminants can produce misleading results from contact angle tests.

Other surface characterization techniques include laser induced breakdown spectroscopy (LIBS) [34] and optically stimulated electron emission (OSEE) [35]. LIBS is an in-line laser ablation process monitoring method which detects the wavelengths of light emitted from a surface during laser ablation to determine when contamination has been removed. OSEE uses the photoelectric effect to shine an ultraviolet (UV) light source on a surface and measure very small currents caused by electrons emitted from the surface. When contamination is present, the current is reduced from its pristine surface value. Both of these methods have proved robust enough to be used for industrial processing and inspection.

1.2.3 Ultrasonic Testing

Ultrasound is defined as sound waves with a frequency higher than the upper limit of human hearing, greater than $\sim 20\ kHz$. Not simply used because they are inaudible to humans, higher frequency waves provide shorter wavelengths in test materials, allowing for higher resolution of detection of small material property changes. Ultrasound is used in a variety of applications, from medical sonograms to flaw detection in manufactured parts for the aerospace and automotive industries.

The basic idea behind any kind of ultrasonic testing involves transmitting sound waves into a test specimen and listening for echoes from the boundary between two media. The intensity of received echoes depends on the attenuation in the test medium and the difference in material properties at the boundary between two media with which the sound wave interacts. The time it takes for the echo to be received is used to determine how far away the boundary is from the sound source. In medical applications, ultrasound is used to provide images of structures inside the body in a cheap and efficient manner. In NDE of manufactured components, echoes from within a part typically indicate a flaw of some type. By careful analysis of the intensity and time-of-flight (ToF) of a received echo, valuable information about a flaw is determined. In general, ultrasonic testing can be done in pulse-echo mode, where the same transducer transmits and receives the waves, or in pitch-catch mode, where different transducers transmit and receive the waves.

1.2.3.1 Ultrasonic Echoes and Flaw Detection

Echoes occur because sound waves reflect at the boundary between two dissimilar media, due to differences in a parameter called the specific acoustic impedance. Specific acoustic impedance (Z) is the product of the mass density (ρ) and sound velocity (c), expressed $Z = \rho c$. The ultrasonic reflection coefficient at the boundary between two media is expressed in Equation 1.1.

$$R = \frac{Z_1 - Z_2}{Z_1 + Z_2} \tag{1.1}$$

In Equation 1.1, $Z_n = \rho_n c_n$ is the acoustic impedance in each medium and has the units of rayleighs (Rayl), where $1\ Rayl = 1\ Pa * s * m^{-1}$. In ultrasonic testing, a flaw in a part will induce an ultrasonic reflection, as the acoustic impedance of air is much lower than that of any solid. Figure 1.3 shows a cross-sectional diagram of a typical ultrasonic test for flaw detection. An ultrasonic transducer is scanned across the surface of a part while sending ultrasonic pulses into the material and listening for echoes. Thin flaws, like cracks, cause a small amplitude of reflection, while larger flaws, such a voids, cause a large amplitude of reflection. If no flaws are present or if the present flaws are small, ultrasound will be reflected from the back wall of the part and later received by the transducer. Ideally, a flaw’s shape, size, and location are determined with knowledge of the sound velocity and acoustic impedance in the material under test. Ultrasonic testing results are viewed in different time and spatial domain plots, which allow for visualization of echoes in 3D.

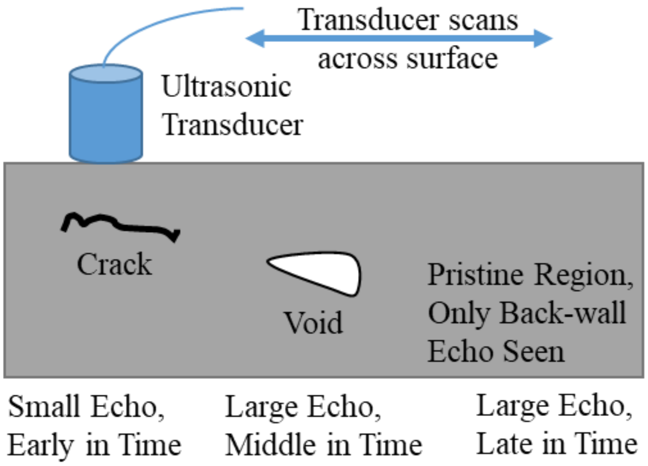

Figure 1.3: Typical ultrasonic pulse-echo flaw detection test

1.2.3.2 Ultrasonic Wave Modes

Ultrasonic waves can be generally categorized into a variety of different types: longitudinal or compressional, transverse or shear [36], surface or Rayleigh [37], and Lamb or guided waves [38]. Succinctly, longitudinal waves vibrate in the direction of propagation through a material; shear waves vibrate perpendicular to the direction of propagation through a material; Rayleigh and surface waves propagate across the surface of a material; and Lamb and guided waves propagate along a plate or bar guided by its boundaries. Each of these wave types has their own well-developed fields of research and primary uses, too vast to summarize here. In this work, however, longitudinal ultrasonic waves are the primary focus, and when ultrasonic waves are referenced throughout the remainder of this document, it can be safely assumed that longitudinal ultrasonic waves are being referenced.

Longitudinal waves are chosen for three primary reasons. First, they to propagate into the depth of a test material, unlike Rayleigh and surface waves. Second, they can be easily coupled into test materials with liquids, unlike shear waves, which do not propagate in non-viscous liquids.

Third and finally, conventional ultrasonic inspection processes, including large-area scanning systems, primarily use longitudinal ultrasound.

1.2.3.3 Ultrasonic Transducers and Couplant

In NDE applications, ultrasound is transmitted into a test article using a device called an ultrasonic transducer. These transducers convert an electrical signal to an acoustic signal when transmitting and convert an acoustic signal to an electrical signal when receiving. The active material in most ultrasonic transducers is a piezoelectric crystal, which operates based on the piezoelectric effect. Piezoelectric materials have the unique property of accumulating an electric charge when mechanical stress is applied. They also exhibit the reverse piezoelectric effect: they generate mechanical strain from an applied electric field. Piezoelectric materials most commonly found in ultrasonic transducers include lead zirconate titanate (PZT), lithium niobate, quartz, and polyvinylidene fluoride (PVDF).

Ultrasonic transducers are designed for operation around some center frequency. The center frequency of the transducer is based on the thickness of the piezoelectric element, which resonates when the thickness is one half of the acoustic wavelength. Transducers are typically defined by their center frequency and their bandwidth or Q-factor, which is a measure of the sharpness of the resonance response.

While piezoelectric crystals are the active material in many ultrasonic transducers, they have two design concerns that limit their use as-is. First, they generally have a very sharp frequency response, limiting the bandwidth of ultrasonic frequencies that can be transceived. When desiring short time-duration pulses, this presents a problem, as high bandwidths are needed. Second, bare piezoelectric crystals are usually not ideally matched to transmit ultrasound into a test material, due to acoustic impedance mismatch.

Commercial ultrasonic transducers overcome these limitations by placing a backing layer behind the piezoelectric material and a matching layer in front of the piezoelectric material [39]. The backing layer dampens the sharp ultrasonic response of the piezoelectric material in the time-domain, greatly broadening the bandwidth of the transducer. The matching layer has an acoustic impedance between that of the piezoelectric material and the test material, because a more gradual change in acoustic impedance allows a higher intensity of ultrasound to transmit into the test material. The thickness of the matching layer is usually chosen to be one quarter of the desired acoustic wavelength. Figure 1.4 shows the basic design of a damped piezoelectric transducer commonly used for ultrasonic NDE.

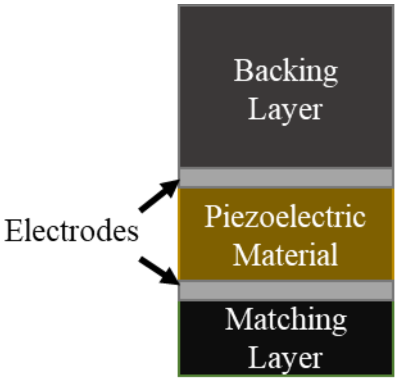

Figure 1.4: Typical damped piezoelectric ultrasonic transducer

While audible sound waves transmit through air well-enough that humans can communicate over great distances with just their voices, high frequency ultrasound attenuates extremely quickly in air. As such, piezoelectric ultrasonic transducers typically rely on an intermediate medium, known as couplant, to transfer ultrasonic waves to a test specimen. For longitudinal waves, water is very commonly used for its ease of use and simple cleanup. In fact, large water tanks are used to test large specimens by scanning a focused ultrasonic transducer across the surface of the part at a fixed distance. In direct-contact ultrasonic testing, couplant is usually applied to the surface, and the transducer is scanned by hand across the part. For automated part inspections without a water tank, methods using water sprayed on the surface while scanning the transducer or the transducer mounted in a trapped water column with rubber membrane on the end are sometimes employed. Direct-contact ultrasonic measurements are used throughout this work.

In many applications, non-contact ultrasonic testing is desirable. While there is research into air-coupled ultrasonic transducers for NDE [40] [41], they require much higher power to operate and are typically still limited in frequency to less than 1 MHz. Another type of non-contact ultrasonic transducer is called an electromagnetic acoustic transducer (EMAT), which use a magnet and a conducting coil that is driven by an electric signal to produce ultrasonic waves in a nearby test material [42] [43]. A final non-contact ultrasonic method, known as laser ultrasound, has generated much interest in recent years for its ability to generate higher frequencies and broader bandwidths that possible with piezoelectric transducers. By operating a short pulse duration laser in the thermoelastic regime of power density on the surface of a test specimen, ultrasonic pulses are generated in the test specimen due to very fast thermal expansion near the surface, which then propagates throughout the material [44] [45] [46]. Laser detection of ultrasound often utilizes the interferometric methods [47] [48] [49].

1.2.4 Ultrasonic Phase Assessment of Adhesive Bonds

Ultrasonic phase assessment of adhesive bond quality in this work involves the use of tone-bursts, or a short-duration of ultrasonic waves at a single frequency, to interrogate an adhesively bonded joint. Figure 1.5 shows a diagram of how adhesively bonded joints are interrogated with ultrasonic phase measurements.

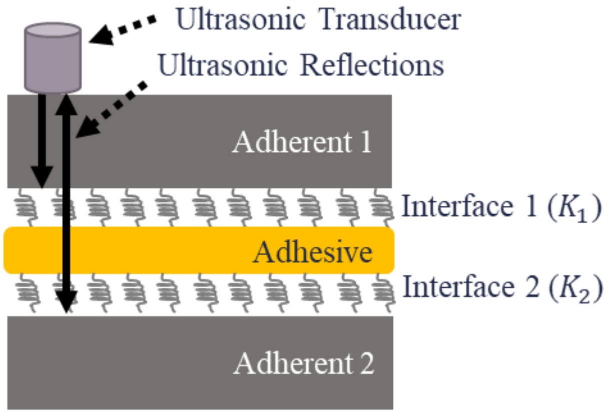

Figure 1.5: Ultrasonic assessment of reflections from an adhesively bonded joint

As shown in Figure 1.5, ultrasonic echoes from the bond line are measured with an ultrasonic transducer. The phase of the received echoes are measured with a custom-built instrument developed in this work, based on a pulsed phase locked loop design. The phase, or time-delay, of the received echoes are compared to a reference wave that stays within the circuit. The relative phase of the transceived wave is modified by the instrument to keep the phase difference with the reference wave constant at a known value. The change in phase offset needed to bring and keep the constant phase difference output is used to measure the ultrasonic phase of the reflection coefficient of the bonded joint.

The imperfectly bonded adhesive/adherent interfaces are modeled by a distributed spring system, where strong bonding is represented by high interfacial stiffness, and weak bonding is represented by low interfacial stiffness. The interfacial spring model modifies the reflection coefficient of the boundary between two media from Equation 1.1 to the modified reflection coefficient shown in Equation 1.2.

$$R_m = \frac{Z_1 - Z_2 + i\omega \frac{Z_1 Z_2}{K}}{Z_1 + Z_2 + i\omega \frac{Z_1 Z_2}{K}} \tag{1.2}$$

In Equation 1.2, $i = \sqrt{-1}$ is the imaginary unit, $\omega = 2\pi f$ is the ultrasonic angular frequency, and K is the interfacial stiffness constant. The modified reflection coefficient, R_m now contains a complex, frequency-dependent term in both the numerator and denominator. Whereas the standard reflection coefficient in Equation 1.1 only exhibits a phase shift of 0 deg or 180 deg, the modified reflection coefficient exhibits a wide range of phase shifts depending upon both frequency and interfacial stiffness, a measure of bond quality.

In SLJs, the adhesive layer acts as a resonance cavity due to phase-matching between reflected and transmitted waves within the layer when the bond line thickness is equal to half the ultrasonic wavelength in the layer (i.e. $L = \lambda/2$, where L is bond line thickness and λ is ultrasonic wavelength). While the transmission coefficient has its peak, the intensity of the reflection coefficient reaches a minimum value when $L = \lambda/2$. Meanwhile, the ultrasonic phase shifts very sharply from negative values to positive values on either side of the resonance frequency. Figure 1.6 shows how the amplitude and phase of the reflection coefficient vary as a function of frequency around the bond line resonance in a SLJ with perfect bonding conditions.

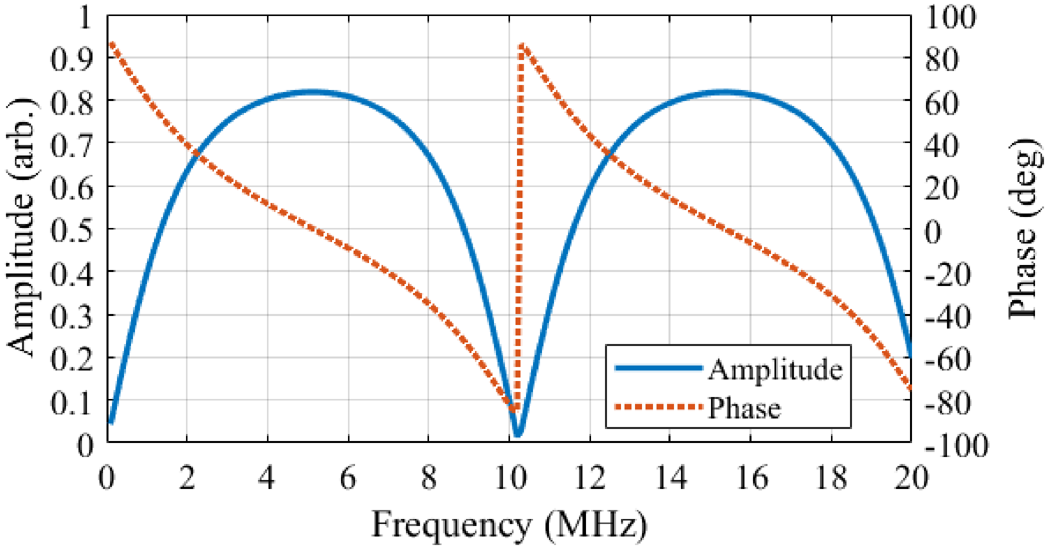

Figure 1.6: Amplitude and phase response of reflection coefficient around ultrasonic resonance frequency in a SLJ

By interrogating the bonded joint around the resonance frequency, the phase inversion from negative to positive values is measured. Changes in bond quality at the two interfaces in a SLJ, represented by changes in the interfacial stiffness constants, will modify the shape of the phase of the reflection coefficient from the ideal response shown in Figure 1.6. For instance, lower interfacial stiffness may reduce the bond line resonance frequency and change the slope of the phase inversion region. The heart of this work focuses on the modeling and measurement of the phase of ultrasonic reflections at imperfectly bonded interfaces, as well as the determination of bond quality from those measurements.

1.3 Problem Statement

As adhesive bonding is the preferred method of joining composite materials, assurance of bond quality is essential to the continued safe use of advanced composite structures in the aerospace, automotive, and other industries. No NDE method exists as an industry standard for measuring adhesive bond strength, which is needed for both manufactured joints and bonded repairs. Bond quality is currently only ensured via manufacturing process control and destructive testing. Accordingly, the use of composite materials and adhesive bonds throughout the aerospace, automotive, and other industries are hindered by the inability to measure adhesive bond strength quantitatively.

The primary objective of this research is to demonstrate a phase-based ultrasonic NDE method for measuring adhesive bond strength. By utilizing constant-frequency pulse phase-locked loop technology, this research aims to use high-resolution ultrasonic phase measurements to quantify adhesion quality of bonded joints. Based on a distributed spring model for imperfect adhesive/adherent interfaces, the phase vs. frequency response of a bonded joint should be sensitive to interfacial adhesion strength. Additionally, this method has the ability to monitor structural and mechanical property changes to monitor for early detection of adhesive bond failure. This ultrasonic phase measurement method can easily interface with conventional ultrasonic inspection setups and is compatible with commercially available ultrasonic transducers.

1.4 Overview of Dissertation

Chapter 2 describes a literature review of assessment methods for adhesive bond quality, focusing in most depth on ultrasonic NDE methods. Chapter 3 discusses how ultrasonic interactions with imperfect interfaces are modeled and demonstrates how ultrasonic phase is expected to change with the modification of material properties of the adhesive bond. Then, the high-resolution single-frequency ultrasonic phase measurement method developed as a part of this project is described and demonstrated in detail in Chapter 4. Chapter 5 demonstrates how the ultrasonic phase method is used to measure the interfacial stiffness between two media with different material setups. Next, the nondestructive evaluation of adhesive bond strength in single lap joints using ultrasonic phase measurements is demonstrated in Chapter 6, which was the primary goal from the outset of this project. Given the proof that the ultrasonic phase method is able to quantify adhesive bond quality, Chapter 7 discusses the limitations of the method as well as ideas for overcoming such challenges. Chapter 8 then investigates several additional applications of the ultrasonic phase method developed in this work with both theory and experimental results. Finally, Chapter 9 discusses general conclusions from this work as well as some interesting directions for future work using this method.

Chapter 2: Literature Review

Traditionally, adhesive bonding has been nondestructively inspected by visual and sonic methods. Visual inspections rely on an experienced technician to identify potential damage sites of adhesive bonds that can be seen on the surface of the adherent, which means that only egregious bonding defects are identified. Still, visual inspections are by far the most-common inspection method for damage detection, used to find damage on automobiles, building structures, and small aircraft.

A simple and still commonly used sonic method, known as the Coin Tap Test, makes use of an experienced technician to identify sound differences between good and bad bonds after tapping the adherent with a coin [3]. In a sufficiently damaged bond, the local structural stiffness is affected by the defect, and the characteristic amplitude and time response of the sound of the coin tap will be observable to the trained ear. These simple methods can only detect extremely damaged bonded joints and are highly susceptible to human error, so quantitative NDE methods have been developed to interrogate adhesively bonded joints in critical applications.

2.1 Destructive Methods

While destructive methods do not work for parts in service, destructive testing is still the most reliable method of adhesive bond strength validation for as-manufactured structures. Coupon-scale testing of new adhesives, surface preparation process, and bonded structures also make extensive use of destructive tests for bond strength assessment. For coupon-scale tests, there are a variety of destructive test methods, depending upon the desired information and mode of loading. For purposes of narrowing the scope of all destructive bond strength tests, only methods for SLJs are discussed. The American Society for Testing and Material (ASTM) defines standard test setups and methods for destructive adhesive bond strength tests, which are generally used or referenced throughout the literature. After destructive testing, visual inspection of the adherent surfaces is conducted to determine the failure mechanism. Figure 1.2 gives examples of adhesive and cohesive failure in metal/epoxy SLJs after destructive testing.

Destructive tests are generally classified by the mode of loading being applied. Figure 2.1 displays loading in each mode on a crack in a material. In Mode I, opening or tensile load is applied; in Mode II, shear or sliding load is applied; and in Mode III, out-of-plane shear or tearing load is applied. Modes I and II are most often used for loading in adhesive bonds strength evaluation. While there are numerous test methods for adhesively-bonded joints, only lap shear test for Mode II loads and the double cantilever beam (DCB) test for Mode I loads are highlighted here, as they are most often used for adhesive bond strength evaluation in the literature and for validation of NDE methods.

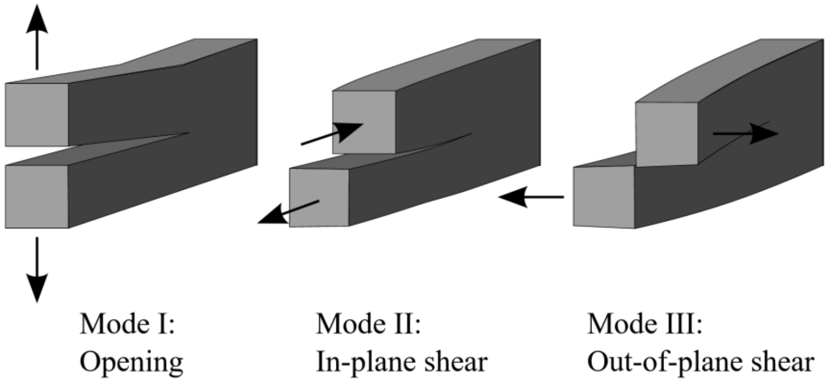

Figure 2.1: Three modes of loading in fracture mechanics

For testing SLJs under shear or Mode II load, the lap shear test is very commonly used, especially with metal adherents. As defined by the ASTM D1002 standard, long metal adherents are bonded together with a thin overlap region and placed within a load frame with wedge grips [50]. The joints are then slowly pulled with shear loading until failure, the maximum load is determined, and the maximum shear stress of the joint is calculated from the failure load divided by the bonded area. To make sure the loading is aligned through the bondline, shims are used on each side of the adherent where gripped. This promotes loading of the joint in only the shear mode and minimizes tensile or peeling forces. Figure 2.2 shows an image of a typical lap shear testing setup using a load frame. Typical load vs. displacement curves from lap shear tests are shown in Figure 8.3.

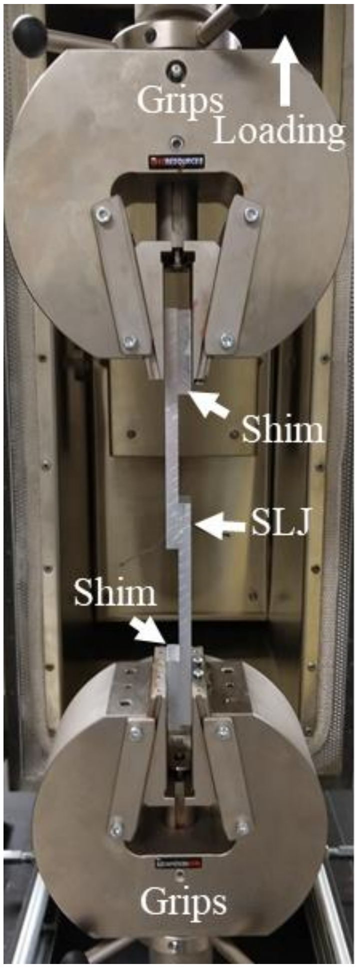

Figure 2.2: Image of lap shear testing setup

The lap shear destructive test produces only one bond strength value for the entire SLJ and gives no information about how bond strength might vary across the bonded region. While quite simple in setup, this method is often criticized for use in bonded joint design, because as the joint is loaded and deformed, the load path crosses the adhesive layer and causes out-of-plane loading [51]. This effect is magnified for thin adherents which bend more drastically when the SLJ is under high shear loads. Regardless, numerous theoretical and experimental studies have used lap shear testing to compare different bonded joint preparation methods [52] [53] [54] [19] [20] [28].

The double cantilever beam (DCB) test investigates tensile or Mode I bond strength, especially in composite specimens. As defined by ASTM D3433 standard [55], the SLJ specimen configuration is quite different for DCB testing than for lap shear testing, as shown in Figure 2.3. Rather than long adherents with a thin overlap region, the bonded joint has a short pre-cracked region followed by a long bonded overlap region. As tensile stress is applied to the pre-cracked end of the joint, the bonded region begins to break. Ideally, the bond breaks in discrete increments, and the crack length is tracked by optical methods from observing the side of the joint. A parameter called the fracture toughness of the adhesive bond is calculated using beam theory from the applied load, crack length, and joint geometry [56]. The parameter called G_{1c}, or the fracture toughness from load to start of crack, is often of primary interest. Unlike lap shear tests, however, DCB tests give information about the bond strength across the length of a SLJ specimen rather than just a single measurement for the entire joint.

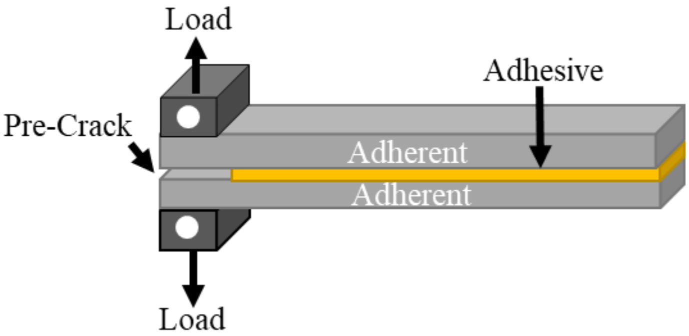

Figure 2.3: Double cantilever beam testing setup

Numerous studies have used DCB tests to understand crack formation and propagation in adhesive bonds from a fracture mechanics perspective [56] [57] [58]. Additionally, DCB tests are often employed to test surface preparation methods for adhesive bonding [26] [59], as well as manufacturing-induced and in-service defects [12] [60].

2.2 Ultrasonic NDE Methods

The focus of most research into bonded joints have used specialized ultrasonic methods to mechanically interrogate the bonded joint on the atomic level. Conventional pulse-echo ultrasonic testing can detect large bonding flaws, such as delaminations and missing adhesive, but are unable to detect kissing bonds. Several advanced ultrasonic methods have claimed sensitivity to the quality of the adhesive/adherent interface of bonded joint (i.e. the ability of the bond to transmit stresses). These methods often make use of a modelled mass-spring system.

A massless spring model for imperfect adhesion was originally proposed by Tattersall [61], while a more fully developed model of ultrasonic interactions with imperfect interfaces included a mass-spring system derived by Baik and Thompson [62]. For many commonly encountered adhesive interfaces, including a thin array of interfacial cracks, the interfacial mass contribution is negligible. As such, a massless spring interface model has been used in several studies of adhesive bond evaluation with ultrasound. Recent theoretical work investigated the interfacial spring model in single lap joints for the conditions under which a bonded joint can be modeled by a single interface, a single interlayer, and a double interface with an interlayer [63].

Analysis by Cantrell into adhesive bonding in alumina-epoxy [64] and carbon fiber-epoxy [65] bonded joints has related interfacial spring stiffness models to the number of intact bonds per unit area at the interface, which is directly related to mechanical bond strength. Further work by Cantrell links measured amplitude and phase data from ultrasonic tone-bursts to mechanical strength at the adhesive/adherent interface via a physico-chemical model [66].

Research into both linear [67] and modulated [68] angle beam ultrasonic spectroscopy (ABUS), supports Cantrell's analysis. In ABUS, the frequency-domain characteristics of a reflected ultrasonic pulse measures the bonded joint's interfacial properties. These methods relate the shift in frequency of the amplitude minimum of both the normal and oblique incidence ultrasonic reflection coefficients of a bonded joint to the normal and shear interfacial stiffness moduli. A method developed by Nagy estimates the normal and shear interfacial stiffness constants from the characteristic frequency of the ultrasonic reflection coefficient, which is identified by the transition between low and high frequency regions of the amplitude response [69]. Additional ultrasonic techniques making use of similar normal and transverse stiffness models have been demonstrated using lamb waves [70], shear-horizontally polarized guided waves [71], non-linear ultrasound [72], a combination of compression and shear waves during adhesive cure [73], and anisotropy observed in ultrasonic plane wave transmission coefficients [74].

While most work investigating adhesive bond strength with ultrasound has focused on lap joints with multiple adherent/adhesive interfaces, some research has been conducted into adhesion quality assessment at a single adherent/adhesive interface. In the single-interface case, diffusion bonds, where the same material is on both sides of the interface, have been invested with both amplitude and phase-based ultrasonic methods. By observing changes in the amplitude of the normal-incidence ultrasonic reflection coefficient, diffusion bond quality is assessed [75]. Further theoretical analysis can then infer information about the size of interfacial crack [76]. Recent work using the phase of ultrasonic pulses reflected from a diffusion bond have shown success in measuring bond quality by using double-sided [77] and single-sided [78] interrogation methods. These results also find that high signal-to-noise ratio is essential, and the standard deviation of phase measurements must be small enough to identify the diffusion bond as good or bad. Other studies have investigated coating/substrate adhesion quality using laser ultrasound [79], [80].

In addition to adhesive bonding, interfacial stiffness has been studied extensively by the tribology community to determine how two solid surfaces are interacting and to evaluate imperfect interfaces [81]. Similar to the adhesive/adherent interface, the solid/solid interface as distributed spring system, with the key measurement parameters being the normal and tangential interfacial stiffness. This approach to solid/solid interface quality assessment has been demonstrated with a variety of ultrasonic methods, including zero-group velocity lamb wave modes [82], normal and angular longitudinal ultrasound [83], and a combination of bulk and interface waves [84]. Other ultrasonic methods have used the phase response of a bonded joint to estimate adhesion quality. Królikowski and Szczepek used the pulse-echo overlap method to measure the phase of the reflection coefficient of an ultrasonic pulse in simulated kissing bonds. Kissing bonds are simulated by rough surface coupons in dry-contact held together by compressional stress. They found ultrasonic phase is sensitive to both interfacial stiffness and real surface area fractional contact [85].

2.3 Non-Ultrasonic NDE Methods

Numerous other NDE methods have been investigated for sensitivity to weak adhesion and kissing bonds, including shearography [86], thermography [87], digital image correlation (DIC) [88], radiography [3], and nuclear magnetic resonance (NMR) [89]. Broadly, these methods can detect large bonding defects such as complete disbonds and adhesive voids, but do not have the resolution to detect weak interfacial bonding or identify kissing bonds.

The most successful non-ultrasonic method of evaluating adhesive bonds is the Laser Shock Adhesion Test (LASAT) [90] [91]. LASAT is one of the few bond quality assessment methods to be developed into a commercial instrument, as Laser Bond Inspection (LBI) it is currently pursued by Boeing for use in the aerospace industry. By interrogating a bonded joint with a shock wave introduced by a pulsed laser, the strength of the bond can be evaluated. The shock wave will completely break weak bonds, causing a complete disbond that can be later viewed using conventional broadband pulse ultrasound. Bonds with strengths over the threshold of the shock wave are supposedly unaffected and considered sufficiently strong for service. The laser shock adhesion requires very expensive and bulky laser shock wave generation equipment, making it unfeasible to use in many practical applications. The method generally requires conventional ultrasonic inspection after the shock waves have interrogated the bond to inspect for broken bonds, requiring further time and testing equipment. Adhesion tests using laser shock waves have also been demonstrated on the bonding between coatings and substrates [92] [93].

2.4 Conclusions

Despite showing some sensitivity to adhesion quality, no ultrasonic method has yet become an industry-accepted method of quantifiably measuring adhesion strength. In fact, only a few studies have shown experimentally validated correlations between measured ultrasonic data and actual mechanical strength [94], [74], [95], [96], [97]. Conventional amplitude vs. time ultrasonic measurements are not sensitive enough to weak interfacial bonding and kissing bonds without gross bonding defects. Angle-beam spectroscopic ultrasonic methods show sensitivity to interface quality – especially using shear waves – yet utilize complex and time-consuming experimental setups, which makes it challenging to use in a manufacturing or repair-facility setting. Recent use of ultrasonic phase in single-interface diffusion bonds have shown excellent interfacial stiffness sensitivity; however, the high signal-to-noise ratio required for interface characterization are, in many cases, difficult to obtain with broadband pulse analysis.

In this work, an ultrasonic adhesion quality evaluation method is demonstrated, by combining the advantages of frequency-based with phase-based ultrasonic methods, while overcoming some of the challenges of previous techniques. Additionally, the interfacial stiffness model of weak adhesive bonding has been successfully used with ultrasonic amplitude measurements, but little validation and testing of this model has been conducted using ultrasonic phase. This method uses a tone-burst from a constant frequency pulsed phase-locked-loop (CFPPLL) instrument to measure the phase of a single-frequency – rather than broadband – ultrasonic pulse. By measuring ultrasonic phase at a single frequency and using narrowband filtering to suppress noise at unwanted frequencies, high signal-to-noise ratios and consequently, low phase measurement noise, is obtained with commercially-available damped transducers. By sweeping the frequency over a desired range and correcting for transducer phase response, a high-resolution ultrasonic phase vs. frequency spectrum – as opposed to the amplitude spectrum used in many previous studies – is obtained for characterization of adhesion quality. This method has advantages over amplitude-based techniques, by being insensitive to attenuation changes and other amplitude-based sources of uncertainty.

Chapter 3: Modeling of Ultrasonic Interactions with Imperfect Interfaces

Prior to discussing the method by which ultrasonic phase measurements are experimentally conducted in this work, a thorough understanding of the ultrasonic interactions with imperfect interfaces is developed. This work investigates the reflection of ultrasonic waves from imperfect interfaces and weak adhesive bonds by modeling theses interfaces by a linear distributed spring system. In contrast with the bulk of previous research, which has focused on how ultrasonic amplitude changes with interfacial stiffness, this work is entirely focused upon phase shifts.

In the linear distributed spring system model for imperfect interfaces, interface quality and adhesive bond quality are modeled by an interfacial spring stiffness, K, when interrogated by ultrasonic waves. For a perfect interface, K approaches infinity; while for a complete disbond, K approaches zero. In this chapter on modeling, K is referred to as a measure of bond quality, but the exact relationship between K and bond strength is not established until Chapter 6. For now, however, it can be safely assumed that bond quality has a monotonic, positive correlation with interfacial stiffness.

First, a model of ultrasonic interactions with a single imperfect interface is developed. Examples are provided to show how the ultrasonic phase of the reflection will change based on interfacial stiffness and the acoustic impedance of the interfacing media. Additionally, there is a section on modeling imperfect interfaces as a thin layer rather than a distributed spring boundary, and the conditions under which these two models are equivalent are determined.

Second, ultrasonic interactions with imperfect interfaces in tri-layer structures are modeled. As this work is targeted at characterizing adhesively bonded joints, it is prudent to understand how ultrasound interacts with one of the most simple and common bonded joint setups: the single lap joint (SLJ). SLJs consist of two adherents bonded together with an adhesive layer in between, creating a tri-layer structure. In practice, it is often difficult to time-resolve ultrasonic echoes from the two adhesive/adherent interfaces in a SLJ, so the total reflection coefficient after a number of internal echoes have been received (i.e. the steady-state response) is modeled. From modeling, it is shown how the phase vs. frequency response around the adhesive layer's acoustic resonance frequency changes depending upon interface quality. It is from this model of the reflection coefficient that a curve-fitting algorithm is later developed to determine interface stiffness from a measured phase vs. frequency response curve.

3.1 Ultrasonic Interactions with a Single Imperfect Interface

3.1.1 General Model

The reflection coefficient from a single adherent/adhesive interface is derived by assuming the imperfect interface is represented by a distributed spring system, as proposed by Baik and Thompson [98]. Assume an ultrasonic particle displacement plane wave, expressed in Equation 1, is excited into the adherent of a bonded joint at normal incidence. In Equation 3.1, T_i is the wave amplitude, $i = \sqrt{-1}$, ω is angular frequency, t is time, k_1 is the complex wavenumber in the incident medium, and x is the distance travelled by the wave. The complex wavenumber in a given medium is defined $k_n = \omega / c_n + i\alpha_n$, where α_n is the acoustic attenuation coefficient, and c_n is the longitudinal wave velocity – often referred to as the sound velocity.

$$u_i(x,t) = T_i e^{i(\omega t - k_1 x)} \tag{3.1}$$

Consider the configuration shown in Figure 3.1, which could be representative of an adherent/adhesive joint with imperfect bonding. In Figure 3.1, T_i is the input wave amplitude, R_1 is the reflection coefficient from the interface, T_2 is the transmission coefficient through the interface, E_n is the elastic modulus in each medium, and K is the interfacial stiffness per unit area – otherwise known as the stiffness constant flux. Assume the adherent and adhesive layers are half-spaces so that secondary echoes from the front-wall of the adherent and back wall of the adhesive are not observed. Also, the input amplitude is assumed unity for simplicity (i.e. $T_i = 1$).

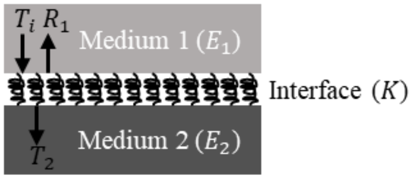

Figure 3.1: Joint configuration representing adherent/adhesive interface

From the incident ultrasonic displacement wave expressed in Equation 3.1, the reflection and transmission coefficients at the interface are found by applying the appropriate boundary conditions to the displacement and stress in each medium. Table 3.1 shows the ultrasonic displacement and stress wave equations in each medium as a function of position. The incident plane wave amplitude, T_i, is assumed unity in this derivation for simplicity, and the boundary between adhesive and adherent is taken to be at the position of $x = 0$. The ultrasonic stress was found from the displacement equations from the relation, $\sigma_n = E_n\, \partial u_n / \partial x$, where u_n is ultrasonic displacement, x is position, σ_n is stress, and E_n is the longitudinal elastic modulus. The longitudinal elastic modulus used here is approximated as $E_n \approx \rho_n c_n^2$, where ρ_n is the mass density and c_n is the sound velocity within the medium.

Table 3.1: Ultrasonic wave displacement and stress equations in single-interface bonded joint

Medium (Subscript)	**Displacement**	**Stress**
Adherent (1)	$u_1(x) = e^{-ik_1x} + R_1e^{ik_1x}$	$\sigma_1(x) = -iE_1k_1\left(e^{-ik_1x} - R_1e^{ik_1x}\right)$
Adhesive (2)	$u_2(x) = T_2e^{-ik_2x}$	$\sigma_2(x) = -iE_2k_2\left(T_2e^{-ik_2x}\right)$

With perfect bonding, the boundary conditions at the interface consist of continuity of displacement and stress. After applying such boundary conditions, solving for the reflection coefficient, and assuming acoustic attenuation is zero, the well-known acoustic reflection coefficient of $R_1 = (Z_1 - Z_2)/(Z_1 + Z_2)$, shown in Equation 1.1, is found. $Z_n = \rho_n c_n$ is the acoustic impedance of each medium. With imperfect bonding, however, the distributed spring boundary modifies the continuity of displacement boundary condition, while leaving the continuity of stress boundary condition intact [98]. The spring boundary condition is found by setting the interfacial spring constant equal to the average stress at the interface divided by the difference in displacement at the interface, and it is shown in Equation 3.2.

$$\big(\sigma_1(0) + \sigma_2(0)\big)/2 = K\big(u_2(0) - u_1(0)\big) \tag{3.2}$$

By combining the spring boundary condition with continuity of stress at the interface (i.e. $\sigma_1(0) = \sigma_2(0)$) the combined boundary condition at the interface is written in Equation 3.3.

$$\sigma_1(0) = \sigma_2(0) = K\big(u_2(0) - u_1(0)\big) \tag{3.3}$$

Using Equation 3.3, an equation is found for the stress and displacement in the adhesive and adherent at position $x = 0$, as shown in Table 3.2. Note, the only unknown parameters in the four displacement and stress equations at the interface are the reflection and transmission coefficients.

Table 3.2: Ultrasonic wave displacement and stress at the interface (i.e. $x = 0$)

Medium (Subscript)	Displacement	Stress
Adherent (1)	$u_1(0) = 1 + R_1$	$\sigma_1(0) = -iE_1k_1(1 - R_1)$
Adhesive (2)	$u_2(0) = T_2$	$\sigma_2(0) = -iE_2k_2(T_2)$

After applying the boundary conditions from Equation 3.3 to the interfacial stress and displacement equations in Table 3.2, a system of coupled equations is found in terms of unknowns R_1 and T_2. The system of coupled equation is expressed in matrix form in Equation 3.4.

$$Ax = b \tag{3.4}$$

$$A = \begin{bmatrix} K + iE_1k_1 & -K \\ -K & K + iE_2k_2 \end{bmatrix}, \qquad x = \begin{bmatrix} R_1 \\ T_2 \end{bmatrix}, \qquad b = \begin{bmatrix} -K + iE_1k_1 \\ K \end{bmatrix}$$

The reflection and transmission coefficients at the interface are found by the inverse matrix method. After simplification, the reflection coefficient R_1 is expressed in Equation 3.5, and the transmission coefficient T_2 is expressed in Equation 3.6.

$$R_1 = \frac{E_1 k_1 - E_2 k_2 + \frac{iE_1 k_1 E_2 k_2}{K}}{E_1 k_1 + E_2 k_2 + \frac{iE_1 k_1 E_2 k_2}{K}} \tag{3.5}$$

$$T_2 = \frac{2E_1 k_1}{E_1 k_1 + E_2 k_2 + \frac{iE_1 k_1 E_2 k_2}{K}} \tag{3.6}$$

In the case that the acoustic attenuation in each medium is negligible, $\alpha_n = 0$ and the reflection coefficient reduces to the form shown in Equation 3.7, and the transmission coefficient reduces to the form shown in Equation 3.8.

$$R_1 \approx \frac{Z_1 - Z_2 + i\omega \frac{Z_1 Z_2}{K}}{Z_1 + Z_2 + i\omega \frac{Z_1 Z_2}{K}} \tag{3.7}$$

$$T_2 \approx \frac{2Z_1}{Z_1 + Z_2 + i\omega \frac{Z_1 Z_2}{K}} \tag{3.8}$$

In both Equations 4.5 and 4.7, it can be seen that the reflection coefficient is modified by the distributed spring boundary with the addition of a complex, frequency-dependent term to both the numerator and denominator. This complex term induces measurable phase shifts of interest to this work. For large values of K, where bond quality is good, the complex term is small in comparison to the other terms, which depend on the acoustic impedance mismatch at the interface. As the bond quality decreases, however, K becomes small enough to have a large impact on the overall reflection coefficient, inducing changes in amplitude and phase that would not be observed with perfect bonding. At the limit where $K \rightarrow 0$, the bond line reflection coefficient approaches unity, depicting total acoustic reflection from the interface.

In the simplified case where attenuation is negligible, shown in Equation 3.7, the phase of the ultrasonic displacement wave reflection coefficient can be found by expressing R_1 as a complex number. In polar form, the reflection coefficient is written $R_1 = |R_1|e^{i\phi_{R_1}}$, where $|R_1|$ is the magnitude and ϕ_{R_1} is the phase. After simplification, the phase of the reflection coefficient is expressed in Equation 3.9, which is used to model the phase response from single adhesive/adherent interfaces.

$$\phi_{R_1} = \tan^{-1}\left(\frac{2\omega Z_1 Z_2^2 K}{K^2(Z_1^2 - Z_2^2) + (\omega Z_1 Z_2)^2}\right) \tag{3.9}$$

3.1.2 Examples of Ultrasonic Phase of Reflection Coefficient

The general shape of the phase of the reflection coefficient as a function of frequency and interfacial stiffness depends on the relationship between Z_1 and Z_2. Figure 3.2 shows examples of the phase response of the reflection coefficient with a driving frequency of 10 MHz for the three cases of acoustic impedance mismatch at the interface: $Z_1 > Z_2$, $Z_1 < Z_2$, and $Z_1 = Z_2$. For these three cases, material properties of aluminum 6061 (Al 6061) and epoxy adhesive are used such that an interface of Al/epoxy represents the $Z_1 > Z_2$ case, epoxy/Al represents the $Z_1 < Z_2$ case, and Al/Al represents the $Z_1 = Z_2$ case.

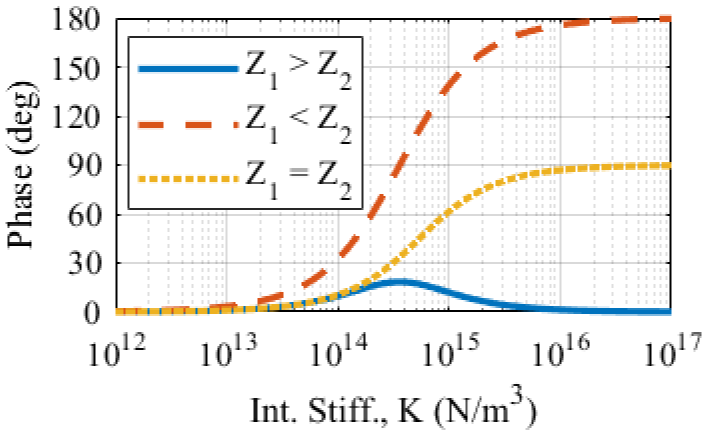

Figure 3.2: Ultrasonic phase at 10 MHz of reflection coefficient vs. interfacial stiffness flux with different acoustic impedance mismatch conditions

While Figure 3.2 is useful in understanding how different interface conditions change the phase of ultrasonic reflections, it only portrays part of the information about what is occurring, because it shows the phase at a constant frequency. To show how the phase spectrum varies for different interfacial stiffness values, the phase vs. frequency response of the reflection coefficient under different acoustic impedance mismatch conditions is plotted in Figure 3.3.

For the case where the acoustic impedances of each medium match and when the acoustic impedance of the first medium is smaller than that of the second medium, the phase varies from 0° with poor bonding to a much higher value for good bonding. In both of these cases, the phase is a monotonically increasing function of interfacial stiffness, and there is a high dynamic range of phase shift between good and bad bonding. Conversely in the case of $Z_1 > Z_2$, the phase shift is 0° for both good and bad bonding, with a small peak phase at some value of K. While having a much lower phase shift range in comparison to the other interface configurations, it is this $Z_1 > Z_2$ case that occurs in a wide variety of applications and is of interest to this work. The acoustic impedance in one medium is greater than that of the underlying medium in most adhesively bonded joints, such as those with metal adherents and epoxy adhesive; in coated or painted metal structures; and in thermal protection barriers.

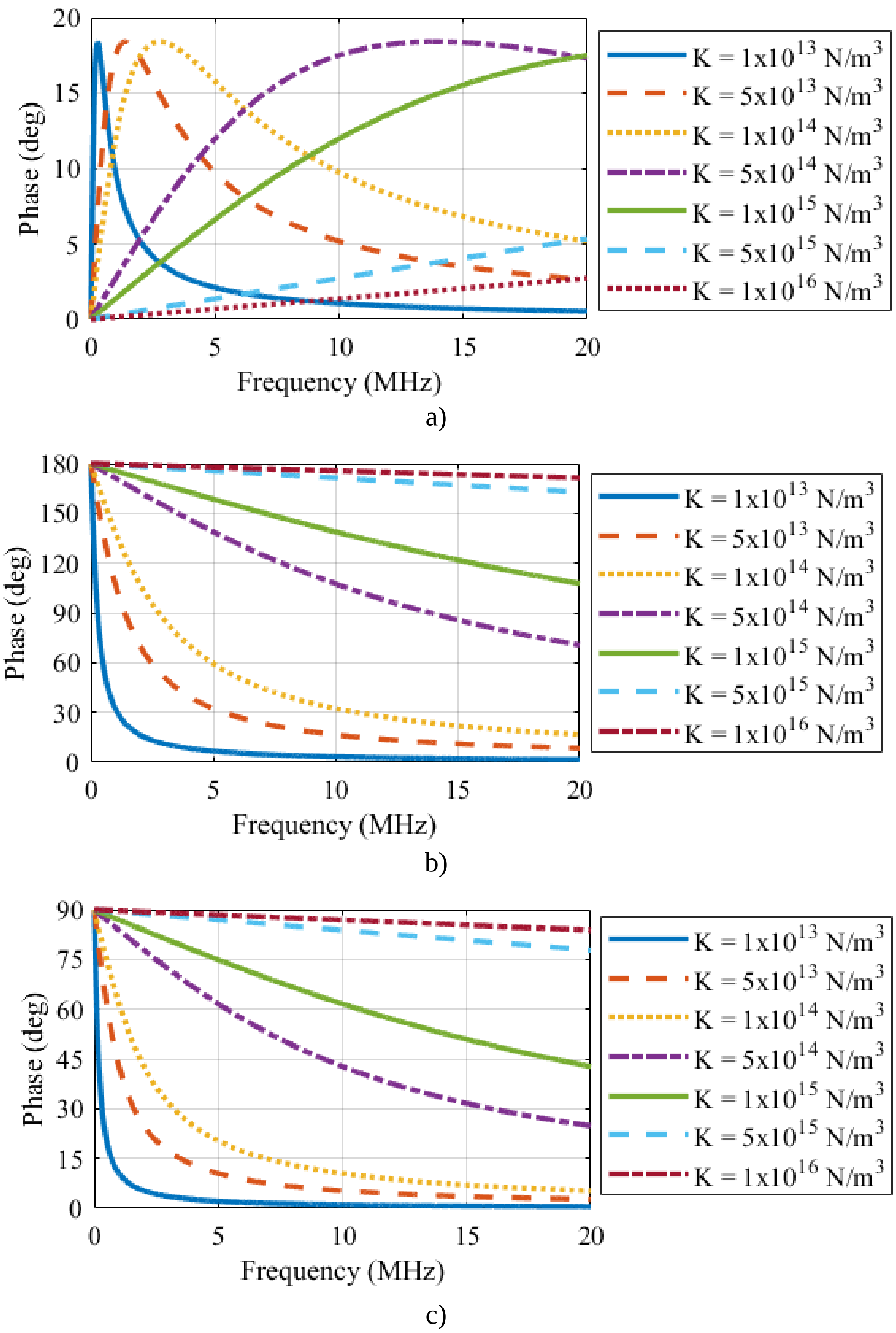

Figure 3.3: Phase vs. frequency response for different interfacial stiffness constants with different acoustic impedance mismatch conditions: a) $Z_1 > Z_2$, b) $Z_1 < Z_2$, and c) $Z_1 = Z_2$

To further analyze the phase response in the case $Z_1 > Z_2$, the position of the peak phase shift is determined by taking a partial derivative of the phase with respect to interfacial stiffness flux. After simplification, the partial derivative of ϕ_{R_1} with respect to K is shown in Equation 3.10.

$$\frac{\partial \phi_{R_1}}{\partial K} = \frac{(2\omega Z_1 Z_2^2)[(\omega Z_1 Z_2)^2 - (Z_1^2 - Z_2^2)K^2]}{2\omega Z_1 Z_2^2 K + [(\omega Z_1 Z_2)^2 + K^2(Z_1^2 - Z_2^2)]^2} \tag{3.10}$$

The interfacial stiffness constant that produces the peak phase of the reflection coefficient is found by setting $\partial \phi_{R_1}/\partial K = 0$ and solving for K. From this procedure, the interfacial stiffness of maximum phase is found and denoted K_0, as expressed in Equation 3.11. It is further noted from Equation 3.11 that a local maximum only occurs when Z_1 is greater than Z_2, as other cases result in infinite or complex values of K_0, which are physically unrealizable. Additionally, it is noted that the interfacial stiffness producing maximum phase depends on acoustic frequency. Consequently, by choosing appropriate driving frequency, ultrasonic phase monitoring can be used to find when the interface quality passes some threshold value, K_0.

$$K_0 = \frac{\omega Z_1 Z_2}{\sqrt{Z_1^2 - Z_2^2}} \tag{3.11}$$

The maximum phase of the reflection coefficient for a given bonded joint configuration is found by setting $K = K_0$ in Equation 3.9. The resulting maximum phase is denoted $\max(\phi_{R_1})$ and expressed in Equation 3.12.

$$\max(\phi_{R_1}) = \tan^{-1}\left(\frac{Z_2}{\sqrt{Z_1^2 - Z_2^2}}\right) \tag{3.12}$$

Of note in Equation 3.12 is that the maximum phase shift is not a function of frequency or interfacial stiffness flux. Only the relationship between the acoustic impedances of the two media affect the value of maximum phase. This relationship is advantageous in cases where the acoustic impedance of one medium may change at the same time interfacial stiffness changes, such as in the case of bonded joints undergoing degradation in the adhesive due to environmental aging. For example, when the peak phase shift is observed at a particular frequency, the acoustic impedance of the adhesive is determined from the maximum phase value and the acoustic impedance of the adherent. Then the acoustic frequency and both acoustic impedance values at maximum phase of the reflection coefficient are used to find the interfacial stiffness flux at that time.

3.1.3 Modeling Thin Layer as Distributed Spring Interface

In many applications of interest, such as adhesively bonded single lap joints, there exists a thin layer embedded between two much thicker surrounding media. Additionally, instead of using the distributed spring model of weak interfacial bonding, some researchers have modeled the interface region in bonded joints as an interphase layer. With this approach, the region where adhesive and adherent meet is treated as its own separate layer with ultrasonic properties such as acoustic impedance modeled as a combination of the properties of the surrounding media.

Consequently, before continuing with using the distributed spring model in practice, it is important to consider under what conditions a thin layer between two solids acts as an interfacial spring boundary. First, consider an incident ultrasonic particle displacement wave in the same form as Equation 3.1 is incident on the tri-layer structure shown in Figure 3.4. Unlike in Section 3.1.1 and later in Section 3.2, assume there is perfect bonding at both interfaces in the tri-layer structure. Again, assume the amplitude of the incident plane wave is unity for simplicity (i.e. $|T_i| = 1$).

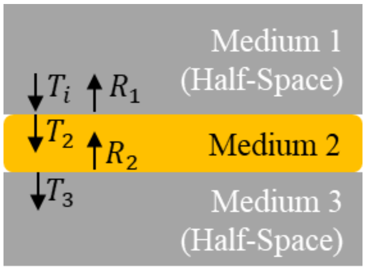

Figure 3.4: Configuration of ultrasonic interactions within thin layer between two solids

In Figure 3.4, T_i is the input wave amplitude, R_1 is the reflection coefficient of the entire thin layer, T_2 and R_2 are the total transmission and reflection coefficients within Medium 2, and T_3 is the transmission coefficient through the entire thin layer. The thickness of the thin layer, Medium 2, is denoted L_2. As this layer is assumed thin with respect to the surrounding layers, it is assumed that the reflected ultrasonic waves within the layer cannot be separated individually in the time-domain. As a result, the net effect of multiple internal reflections in Medium 2 is considered, which could also be referred to as the steady-state response of the reflection coefficient from the thin layer between two half-spaces.

To find the reflection and transmission coefficients at the two interfaces, apply the continuity of displacement and stress boundary conditions at each interface. Table 3.3 shows the displacement and stress waves in each medium as a function of position. It is assumed that the boundary between Medium 1 and Medium 2 is at position $x = 0$. As previously defined in Section 3.1.1, the ultrasonic stress is found from the displacement equations by using the relation, $\sigma_n = E_n\, \partial u_n / \partial x$, where u_n is ultrasonic displacement, x is position, σ_n is stress, and E_n is the longitudinal elastic modulus. The longitudinal elastic modulus used here is approximated as $E_n \approx \rho_n c_n^2$, where ρ_n is the mass density and c_n is the sound velocity within the medium.

Table 3.3: Displacement and stress equations in each medium of a tri-layer structure with a thin-layer between two half-spaces

Medium	Displacement	Stress
Medium 1	$u_1(x) = e^{-ik_1x} + R_1e^{ik_1x}$	$\sigma_1(x) = -iE_1k_1\left(e^{-ik_1x} - R_1e^{ik_1x}\right)$
Medium 2	$u_2(x) = T_2e^{-ik_2x} + R_2e^{ik_2x}$	$\sigma_2(x) = -iE_2k_2\left(T_2e^{-ik_2x} - R_2e^{ik_2x}\right)$
Medium 3	$u_3(x) = T_3e^{-ik_3(x-L_2)}$	$\sigma_3(x) = -iE_3k_3T_3e^{-ik_3(x-L_2)}$

With perfect bonding assumed at each interface, the boundary conditions are simply continuity of displacement and stress, as written in Table 3.4.

Table 3.4: Boundary conditions in tri-layer structure with a thin layer between two half-spaces

Interface	**Continuity of Displacement**	**Continuity of Stress**
Medium 1/Medium 2	$u_1(0) = u_2(0)$	$\sigma_1(0) = \sigma_2(0)$
Medium 2/Medium 3	$u_2(L_2) = u_3(L_2)$	$\sigma_1(L_2) = \sigma_2(L_2)$

After applying the boundary conditions from Table 3.4 to the displacement and stress equations in Table 3.3, a system of equations is found with unknown reflection and transmission coefficients. The system of equations is displayed in matrix form in Equation 3.13.

$$Ay = b \tag{3.13}$$

$$A = [A_1 \quad A_2 \quad A_3 \quad A_4]$$

$$A_1 = \begin{bmatrix} 1 \\ E_1 k_1 \\ 0 \\ 0 \end{bmatrix}, \qquad A_2 = \begin{bmatrix} -1 \\ -E_2 k_2 \\ e^{ik_2 L_2} \\ E_2 k_2 e^{ik_2 L_2} \end{bmatrix}$$

$$A_3 = \begin{bmatrix} -1 \\ E_2 k_2 \\ e^{-ik_2 L_2} \\ -E_2 k_2 e^{-ik_2 L_2} \end{bmatrix}, \qquad A_4 = \begin{bmatrix} 0 \\ 0 \\ -1 \\ E_3 k_3 \end{bmatrix}$$

$$y = \begin{bmatrix} R_1 \\ R_2 \\ T_2 \\ T_3 \end{bmatrix}, \qquad b = \begin{bmatrix} -1 \\ E_1 k_1 \\ 0 \\ 0 \end{bmatrix}$$

The system of equations in Equation 3.13 is solved by the inverse matrix method to find a closed-form solution for the reflection coefficient from the thin layer. The reflection coefficient is shown in Equation 3.14.

$$R_1 = \frac{(E_2 k_2)(E_1 k_1 - E_3 k_3)\cos(k_2 L_2) + i(E_1 k_1 E_3 k_3 - E_2^2 k_2^2)\sin(k_2 L_2)}{(E_2 k_2)(E_1 k_1 + E_3 k_3)\cos(k_2 L_2) + i(E_1 k_1 E_3 k_3 + E_2^2 k_2^2)\sin(k_2 L_2)} \tag{3.14}$$

To find when a thin layer between two half spaces behaves as an interfacial spring boundary, several assumptions made about the thin layer. First, let the middle layer be thin with respect to the wavelength of ultrasound or more generally, let $|k_2 L_2| \ll 1$. This assumption means

$\sin(k_2L_2) \approx k_2L_2$, $\cos(k_2L_2) \approx 1$, and $e^{-ik_2L_2} \approx 1$ based on their complex Taylor's series approximations. The resulting reflection coefficient approximation is shown Equation 3.15.

$$R_1 \approx \frac{(E_2k_2)(E_1k_1 - E_3k_3) + i(E_1k_1E_3k_3 - E_2^2k_2^2)k_2L_2}{(E_2k_2)(E_1k_1 + E_3k_3) + i(E_1k_1E_3k_3 + E_2^2k_2^2)k_2L_2} \tag{3.15}$$

Next, assume the thin middle layer is much less stiff than the surrounding media, or more specifically, assume $|E_1k_1E_3k_3| \gg |E_2k_2|$. Without attenuation considered, this assumption is the same as assuming the acoustic impedances in the surrounding media are much greater than the acoustic impedance of the intermediate layer (i.e. $Z_1Z_3 \gg Z_2^2$). Under this assumption, $E_1k_1E_3k_3 \pm E_2^2k_2^2 \approx E_1k_1E_3k_3$, and the resulting approximations for R_1 is written in Equation 3.16.

$$R_1 \approx \frac{(E_2k_2)(E_1k_1 - E_3k_3) + i(E_1k_1E_3k_3)k_2L_2}{(E_2k_2)(E_1k_1 + E_3k_3) + i(E_1k_1E_3k_3)k_2L_2} \tag{3.16}$$

By dividing the numerator and denominator of Equation 16 by E_2k_2 and making the substitution $K = E_2/L_2$, the reflection coefficient is re-written in the form shown in Equation 3.17.

$$R_1 \approx \frac{E_1k_1 - E_3k_3 + i\,\dfrac{E_1k_1E_3k_3}{K}}{E_1k_1 + E_3k_3 + i\,\dfrac{E_1k_1E_3k_3}{K}} \tag{3.17}$$

The approximation of R_1 in Equation 3.17 matches the reflection coefficient from a spring boundary derived in Section 3.1.1 and shown in Equation 3.7. As such, the acoustic reflection coefficient from an embedded thin layer behaves like a simple spring boundary when $|k_2L_2| \ll 1$ and $|E_1k_1E_3k_3| \gg |E_2k_2|$. Without attenuation considered, these assumptions simplify to $L_2 \ll \lambda_2$ and $Z_1Z_3 \gg Z_2^2$. The interfacial stiffness of the thin layer is directly proportional to the elastic modulus in the layer and inversely proportional to the thickness of the layer.

Consider several practical adhesively bonded single lap joint material setups used throughout the rest of this work. A single lap joint contains a relatively thin adhesive layer embedded between two adherents. For these examples, attenuation will be assumed negligible for simplicity, as this exercise is just to provide an idea of whether or not a spring boundary assumption for the adhesive layer joint is even close to valid.

First, consider an aluminum/epoxy single lap joint setup, where the acoustic impedance in the adherents are $Z_1 = Z_3 = 17.1\ MRayl$ and the acoustic impedance of the adhesive is $Z_2 = 5.44\ MRayl$. For the acoustic impedance condition, these values give $Z_2^2 \approx 0.101 * Z_1 Z_3$, which is very close to the common convention that a fraction of $1/10$th satisfies the "much less than" requirement. Next, consider the wavelength of epoxy, which is about $215\ \mu m$ for the ultrasonic driving frequency of 10 MHz commonly used in this work. From this wavelength, the adhesive layer would need to be at least thinner than about $21.5\ \mu m$ to satisfy the $L_2 \ll \lambda_2$ requirement. In practice, bond line thicknesses in aerospace applications are usually in the hundreds of microns, so this condition is not likely to be met in practice and is not met in the Al/epoxy single lap joints throughout this work. Consequently, an epoxy adhesive layer between Al adherents can only be reasonably approximated as a spring interface when the bond line is very thin or if a much lower frequency is used, and even then, it is not a good approximation as acoustic impedance condition is only barely satisfied.

Next, consider a single lap joint made with borosilicate glass adherents and adhesive curable via ultraviolet light, such as Norland Optical Adhesive 63. The acoustic impedance of the adherents is $Z_1 = Z_3 = 12.3\ MRayl$, and the acoustic impedance of the adhesive is $2.86\ MRayl$. Thus, $Z_2^2 \approx 0.054 * Z_1 Z_3$ in this case, and the $Z_2^2 \ll Z_1 Z_3$ condition is satisfied. Now consider the acoustic wavelength of the UV-curable adhesive, which is $\lambda_2 = 229\ \mu m$. Similar to the epoxy adhesive in the previous example, the adhesive layer would need to be at least thinner than about

$22.9\,\mu m$ to satisfy the $L_2 \ll \lambda_2$ condition. In this work, the bond line thickness is a little over $100\,\mu m$, so it is not reasonable to treat the UV-curable adhesive as a single spring interface.

3.2 Ultrasonic Interactions with Single Lap Joints

3.2.1 General Model

Starting again with quasi-static model for ultrasonic interactions with imperfect interfaces developed by Baik and Thompson [98], the normal-incidence particle displacement wave reflection coefficient from imperfect bonding within a tri-layer adhesive joint is found. A particle displacement plane wave is excited into the bond line at a normal incidence, represented by Equation 3.17, where T_i is the wave amplitude, $i = \sqrt{-1}$, ω is angular frequency, t is time, k_1 is the complex wavenumber in the incident medium, and x is the distance travelled by the wave.

$$u_i(x,t) = T_i e^{i(\omega t - k_1 x)} \tag{3.17}$$

Using the SLJ configuration in Figure 3.5, the incident ultrasonic plane wave amplitude transmitted into the bond line, T_i, is assumed to be unity for simplicity. For the purposes of this derivation, the Adherent 1 and Adherent 2 media are assumed semi-infinite half-spaces and only the area around the adhesive bond line is considered. Interfacial adhesive bond quality is represented by the distributed mass-spring system defined by Baik and Thompson, with stiffness per unit area constant K_n – also referred to as the spring constant flux -- and mass per unit area m_n at each adhesive/adherent interface [98].

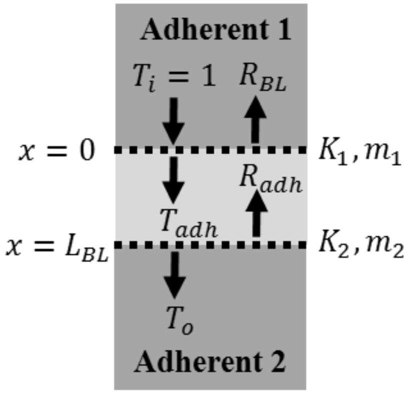

Figure 3.5: Normal-incidence ultrasonic reflections within thin-adhesive tri-layer structure

In Figure 3.5, x is the distance from the first adherent interface, L_{BL} is the bond line thickness, R_{adh} and T_{adh} are respectively the reflection and transmission coefficients within the adhesive, T_o is the ultrasonic transmission coefficient through the bond line, and R_{BL} is the bond line reflection coefficient. The reflected particle displacement waves within the bond line are separated by a time-of-flight (ToF) of $2L_{BL}/c_{adh}$, where c_{adh} is the sound velocity within the adhesive. Assuming the adhesive ToF is small with respect to the incident tone-burst duration, the net effect of multiple decaying reflections within the bond line is considered.

The ultrasonic reflection coefficient of the tri-layer structure with two imperfect interfaces is found by applying the appropriate boundary conditions at each interface and simultaneously solving coupled equations for the bond line particle displacement wave reflection coefficient, R_{BL}. Table 3.5 shows the assumed ultrasonic displacement and stress equations in each medium as a function of position. The time dependence portion of the equations is omitted throughout this derivation. The ultrasonic stress was found from the displacement equations from the relation, $\sigma = E\,\partial u/\partial x$, where u is ultrasonic displacement, x is position, σ is stress, and E is the longitudinal elastic modulus. The longitudinal elastic modulus used here is defined as $E = \lambda + 2G = \rho c^2$, where λ is Lamé's first parameter, G is the shear modulus, ρ is the mass density, and c is the sound velocity within the medium.

Table 3.5: Ultrasonic wave displacement and stress equations in each medium

Medium (Subscript)	Displacement	Stress
Adherent (1)	$u_1(x) = e^{-ik_1x} + R_{BL}e^{ik_1x}$	$\sigma_1(x) = -iE_1k_1\left(e^{-ik_1x} - R_1e^{ik_1x}\right)$
Adhesive (adh)	$u_{adh}(x) =$ $T_{adh}e^{-ik_{adh}x} + R_{adh}e^{ik_{adh}x}$	$\sigma_{adh}(x) =$ $-iE_{adh}k_{adh}\left(T_{adh}e^{-ik_{adh}x} - R_{adh}e^{ik_{adh}x}\right)$
Adherent (2)	$u_2(x) = T_oe^{-ik_2(x-L_{BL})}$	$\sigma_2(x) = -iE_2k_2T_oe^{-ik_2(x-L_{BL})}$

In Table 3.5, $k_n = \omega/c_n + i\alpha_n$ is the complex ultrasonic wavenumber in each medium given input angular frequency ω, sound velocity c_n, and as attenuation coefficient α_n; and $E_n = \rho_n c_n^2$ is the longitudinal elastic modulus in each medium given mass density ρ_n and sound velocity. While the attenuation coefficient is nominally frequency dependent, it is assumed constant in this study, as small frequency ranges are used. The imperfect interface boundary conditions from Baik and Thompson [98] are applied to each interface, as given in Table 3.6.

Table 3.6: Imperfect interface boundary conditions in tri-layer model

Interface	Interfacial Stiffness Boundary Condition	Interfacial Mass Boundary Condition
Upper Adherent – Adhesive ($\boldsymbol{x = 0}$)	$\sigma_1(0) + \sigma_{adh}(0) =$ $2K_1\left(u_{adh}(0) - u_1(0)\right)$	$-m_1\omega^2\left(u_{adh}(0) + u_1(0)\right)$ $= 2\left(\sigma_{adh}(0) - \sigma_1(0)\right)$
Lower Adhesive – Adherent ($\boldsymbol{x = L_{BL}}$)	$\sigma_{adh}(L_{BL}) + \sigma_2(L_{BL}) =$ $2K_2\left(u_2(L_{BL}) - u_{adh}(L_{BL})\right)$	$-m_2\omega^2\left(u_2(L_{BL}) + u_{adh}(L_{BL})\right)$ $= 2\left(\sigma_2(L_{BL}) - \sigma_{adh}(L_{BL})\right)$

After applying each of the four boundary conditions in Table 3.6 to the displacement and stress equations from Table 3.5, the resulting system of equations is written in terms of the four unknown reflection and transmission coefficients, displayed in matrix form in Equation 3.18.

$$Ay = b \tag{3.18}$$

$$A = [A_1 \quad A_2 \quad A_3 \quad A_4]$$

$$A_1 = \begin{bmatrix} 2K_1 + iE_1k_1 \\ -m_1\omega^2 + 2iE_1k_1 \\ 0 \\ 0 \end{bmatrix}, \qquad A_2 = \begin{bmatrix} -2K_1 + iE_{adh}k_{adh} \\ -m_1\omega^2 - 2iE_{adh}k_{adh} \\ (2K_2 + iE_{adh}k_{adh})e^{iL_{BL}k_{adh}} \\ (-m_2\omega^2 + 2iE_{adh}k_{adh})e^{iL_{BL}k_{adh}} \end{bmatrix}$$

$$A_3 = \begin{bmatrix} -2K_1 - iE_{adh}k_{adh} \\ -m_1\omega^2 + 2iE_{adh}k_{adh} \\ (2K_2 - iE_{adh}k_{adh})e^{-iL_{BL}k_{adh}} \\ (-m_2\omega^2 - 2iE_{adh}k_{adh})e^{-iL_{BL}k_{adh}} \end{bmatrix}, \qquad A_4 = \begin{bmatrix} 0 \\ 0 \\ -2K_2 - iE_2k_2 \\ -m_2\omega^2 + 2iE_2k_2 \end{bmatrix}$$

$$y = \begin{bmatrix} R_{BL} \\ R_{adh} \\ T_{adh} \\ T_o \end{bmatrix}, \qquad b = \begin{bmatrix} -2K_1 + iE_1k_1 \\ m_1\omega^2 + 2iE_1k_1 \\ 0 \\ 0 \end{bmatrix}$$

The coupled system in Equation 3.18 is solved by the inverse matrix method to find a closed-form solution for R_{BL}. After simplification, omitted here for brevity, the bond line reflection coefficient is displayed in Equation 3.19. The ultrasonic transmission coefficient of the bond line, T_o, can also be found from this coupled system of equations if through-transmission measurements of an adhesive bond line are desired. In this work, pulse-echo measurements are the focus so only the reflection coefficient is developed in detail.

$$R_{BL} = \frac{C_N\cos(k_{adh}L_{BL}) + iS_N\sin(k_{adh}L_{BL})}{C_D\cos(k_{adh}L_{BL}) + iS_D\sin(k_{adh}L_{BL})} \tag{3.19}$$

$$C_N = G_{adh}\left[(G_1 - G_2)F + \frac{4}{K_e}\left(\frac{4G_1G_2}{m_1m_2} - \omega^4\right) - \frac{4\omega^2}{m_e}\left(\frac{G_1G_2}{K_1K_2} - 4\right) - 16\omega^2\left(\frac{G_1}{K_1m_1} - \frac{G_2}{K_2m_2}\right)\right]$$

$$C_D = G_{adh}\left[(G_1 + G_2)F + \frac{4}{K_e}\left(\frac{4G_1G_2}{m_1m_2} + \omega^4\right) - \frac{4\omega^2}{m_e}\left(\frac{G_1G_2}{K_1K_2} + 4\right) - 16\omega^2\left(\frac{G_1}{K_1m_1} + \frac{G_1}{K_2m_2}\right)\right]$$

$$S_N = (G_1G_2 - G_{adh}^2)F + 4\left(\frac{G_1}{K_1} - \frac{G_2}{K_2}\right)\left(\frac{4G_{adh}^2}{m_1m_2} + \omega^4\right) - 4\omega^2\left(\frac{G_1}{m_1} - \frac{G_2}{m_2}\right)\left(\frac{G_{adh}^2}{K_1K_2} + 4\right)$$
$$+ 16\left(\frac{G_{adh}^2G_1G_2}{K_1K_2m_1m_2} - \omega^4\right)$$

$$S_D = (G_1G_2 + G_{adh}^2)F + 4\left(\frac{G_1}{K_1} + \frac{G_2}{K_2}\right)\left(\frac{4G_{adh}^2}{m_1m_2} + \omega^4\right) - 4\omega^2\left(\frac{G_1}{m_1} + \frac{G_2}{m_2}\right)\left(\frac{G_{adh}^2}{K_1K_2} + 4\right)$$
$$+ 16\left(\frac{G_{adh}^2G_1G_2}{K_1K_2m_1m_2} + \omega^4\right)$$

$$F = \frac{16}{m_1 m_2} + \frac{\omega^4}{K_1 K_2} - 4\omega^2 \left(\frac{1}{K_2 m_1} + \frac{1}{K_1 m_2} \right)$$

$$G_1 = iE_1 k_1, \qquad G_2 = iE_2 k_2$$

$$G_{adh} = iE_{adh} k_{adh}$$

$$K_e = (K_1^{-1} + K_2^{-1})^{-1}, \qquad m_e = (m_1^{-1} + m_2^{-1})^{-1}$$

While Equation 3.19 is useful in modeling the theoretical ultrasonic amplitude or phase response of nearly any given tri-layer material system, the complexity of the reflection coefficient can be simplified in many common situations. In most SLJ configurations and in each bonded joint in this work, the same material is used for both upper and lower adherent. Additionally, Baik and Thompson found that interfacial mass loading can be neglected in adhesive bonds without large interfacial inclusions or cracks, which is assumed true for thin-interface bonded joints. Under this condition, the interfacial mass at each interface is zero. Given the previous assumptions, $E_1 = E_2, k_1 = k_2$, and $m_1 = m_2 = 0\ kg/m^2$. The resulting R_{BL} approximation, shown in Equation 3.20, keeps the same form as Equation 3.19, but the coefficients in front of the sine and cosine terms are simplified.

$$R_{BL} = \frac{C_N \cos(k_{adh} L_{BL}) + S_N \sin(k_{adh} L_{BL})}{C_D \cos(k_{adh} L_{BL}) + S_D \sin(k_{adh} L_{BL})} \tag{3.20}$$

$$C_N = \frac{E_1^2 k_1^2 E_{adh} k_{adh}}{(K_1^{-1} + K_2^{-1})^{-1}}$$

$$C_D = E_1 k_1 E_{adh} k_{adh} \left(2 + \frac{E_{adh} k_{adh}}{(K_1^{-1} + K_2^{-1})^{-1}} \right)$$

$$S_N = (E_1^2 k_1^2 - E_{adh}^2 k_{adh}^2) + E_1 k_1 E_{adh}^2 k_{adh}^2 \left(\frac{1}{(K_1^{-1} - K_2^{-1})^{-1}} + \frac{E_1 k_1}{K_1 K_2} \right)$$

$$S_D = (E_1^2 k_1^2 + E_{adh}^2 k_{adh}^2) + E_1 k_2 E_{adh}^2 k_{adh}^2 \left(\frac{1}{(K_1^{-1} + K_2^{-1})^{-1}} + \frac{E_1 k_1}{K_1 K_2} \right)$$

3.2.2 Examples of Ultrasonic Phase vs. Frequency Response around Bond line Resonance

Of particular interest in this work is the frequency range surrounding the ultrasonic anti-resonance frequency (f_{ar}) of bond line reflections. Assuming perfect interfacial bonding – where $K_1, K_2 \rightarrow \infty$ -- the ultrasonic anti-resonance of the reflection coefficient occurs when the bond line thickness is one-half wavelength thick, corresponding to $f_{ar} = c_{adh}/2L_{BL}$. At the anti-resonance frequency, the amplitude of R_{BL} attains a local minimum and the phase of R_{BL} undergoes an inversion from negative to positive values.

However, weak bonding at the adhesive/adherent interface causes a shift of the anti-resonance frequency, as well. This effect can be thought of as the stiffness of the interfaces slightly changing the effective stiffness of the entire adhesive layer, including its interfaces. For very poor bonds, a dampening of the reflection coefficient is produced. The complex reflection coefficient in Equation 3.20 is used to model the phase vs. frequency response of bond line reflection coefficient to extract unknown adhesive bonding parameters. The amplitude and phase spectra are computed for a given set of material properties by expressing R_{BL} in complex polar form as a function of input acoustic frequency (i.e.$R_{BL}(f) = |R_{BL}(f)|e^{i\phi(f)}$).

Figure 3.6 shows the modeled phase spectra of the reflection coefficient of a $100\ \mu m$ thick bond line aluminum/epoxy SLJ where both interfacial stiffness constants are assumed equal. In this scenario, low interface quality drops the anti-resonance and zero-crossing frequency, but it has little effect on the slope of the phase shift during phase inversion.

While the exact relationship between interfacial stiffness and bond strength depends on the material properties and surface chemistry of the particular adhesive and adherent in use, it can be safely assumed that interfacial stiffness is generally a monotonically increasing function of bond strength. To put the stiffness values shown into perspective, Cantrell found that interfacial stiffness in aluminum/epoxy joints is linearly related to interfacial bond strength, with extreme values of $K \approx 3.8 \times 10^{17}\ N/m^3$ for a perfect bond and $K \approx 3.8 \times 10^{14}\ N/m^3$ for a disbond [64].

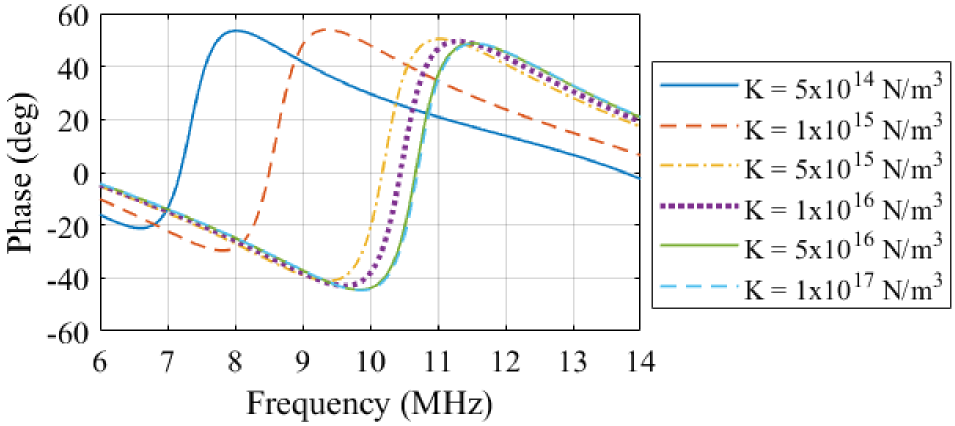

Figure 3.6: Example phase vs. frequency response around ultrasonic resonance of bond line with both interfaces of same stiffness and changing quality

In contrast, Figure 3.7 shows the phase response of the reflection coefficient of the same Al/epoxy bonded joint setup but with different interfacial stiffness constants on either side of the bond line. In particular, the upper interfacial stiffness constant flux, K_1, is allowed to change while the lower interface stiffness is assumed perfect and held fixed at $K_2 = 3.8 \times 10^{17}\ N/m^3$. In this scenario, reducing the interfacial stiffness causes a measureable effect on the “sharpness” of the phase inversion in addition to reducing the anti-resonance frequency.

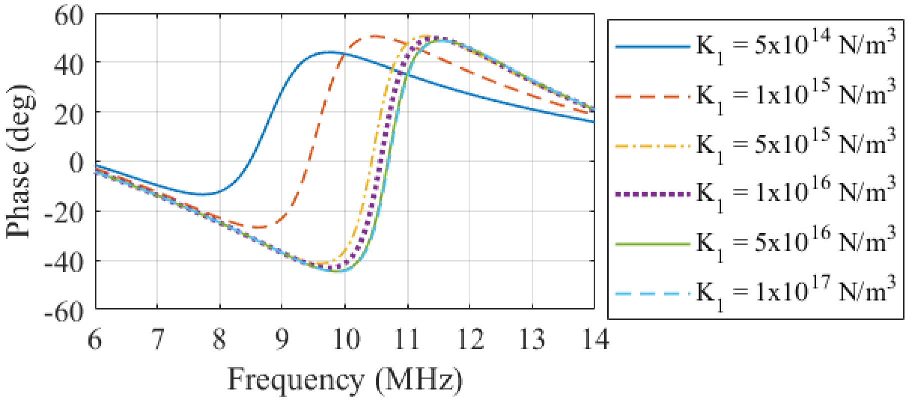

Figure 3.7: Example phase vs. frequency response around ultrasonic resonance of bond line with upper interface changing quality and perfect lower interface

The modeled phase response of bonded joints in Figure 3.6 and Figure 3.7 show how the ultrasonic resonance properties of phase spectra are effected by interfacial stiffness. In particular, it is noted that the anti-resonance frequency is generally reduced from its nominal value by poor bonding. Furthermore, a difference in interfacial stiffness on either side of the bond line produces a dampening of the phase inversion. These conclusions indicate the maximum slope of phase shift and the frequency at which maximum phase slope occurs (i.e. the anti-resonance frequency) may be used to determine the two unknown interfacial stiffness constants in a SLJ.

To further show how interface stiffness and bond strength affect the resonance properties, an Al/epoxy SLJ is again modeled under different interfacial stiffness conditions with a bond line thickness of $110\ \mu m$. First, the resonance frequency shift is calculated for the case of the upper interface quality changing while the lower interface remains pristine. Second, the resonance frequency shift is calculated for the case that both interfaces are of equal stiffness but are varying in value. Third and finally, the phase slope maximum occurring at the resonance frequency is determined in the case that the upper interface quality varies while the lower interface remains pristine. The results of this modeling study are shown in Figure 3.8.

The approximate interfacial bond strength at each given interfacial stiffness are also denoted on the x-axis of Figure 3.8 based on the theoretical relationship between interfacial stiffness and bond strength in alumina/epoxy joint by Cantrell [64]. It is noted that this is only showing the approximate bond strength, not the actual predicted bond strength by Cantrell. For instance, $K = 10^{15}\ N/m^3$ is not predicted to occur at a bond strength of exactly $10^{-1}\ MPa$, but each bond strength on the x-axis is the same order of magnitude as the predicted bond strength. This extra x-axis is meant only to provide a general idea of how ultrasonic phase resonance properties may be affected by interfacial bond strength.

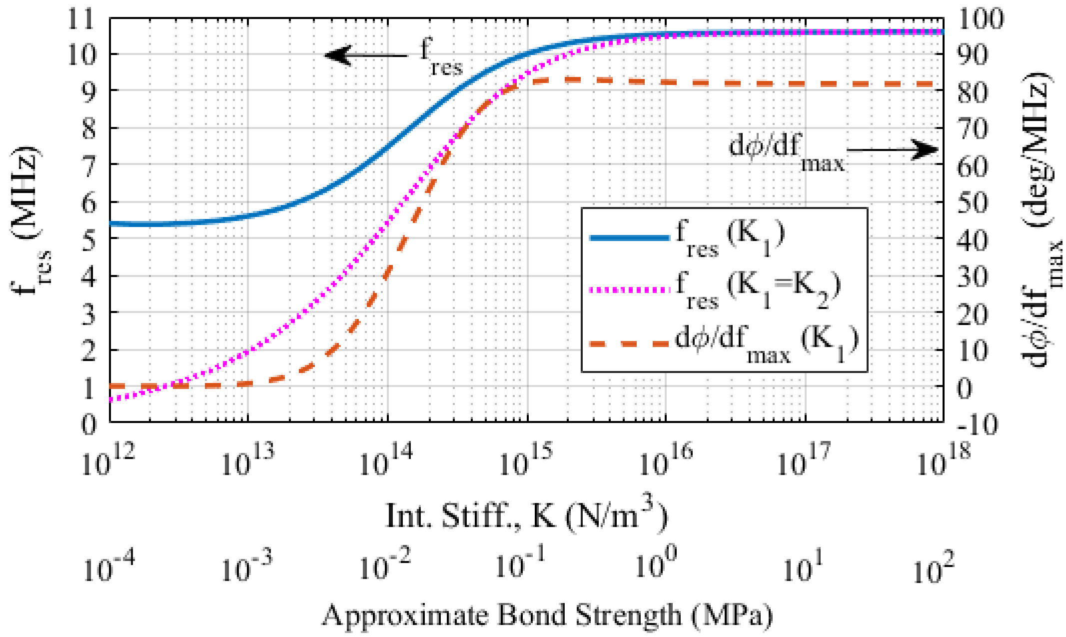

Figure 3.8: Theoretical changes in resonance frequency and maximum phase slope of reflection coefficient from a SLJ due to interface stiffness changes

For the both resonance frequency curves, there is an observable drop in resonance frequency below stiffness values of about $10^{16}\ N/m^3$. In real bonding between Al and epoxy, the interfacial bond strength is in the range of $30 - 40\ MPa$. As such, an order of magnitude loss of bond strength will be difficult to detect without very accurate knowledge of material properties of the adhesive layer, which also affect the resonance frequency. Of additional note in the resonance frequency curves is the sharper drop and overall greater dynamic range of resonance frequency change in the case of $K_1 = K_2$ as opposed to only the upper interfacial stiffness changing. This makes sense, as a drop in stiffness at two interfaces should have a larger effect on the overall resonance of the adhesive layer than a drop in stiffness at only one interface. This result implies that an ultrasonic phase measurement method will have greater sensitivity to bond strength changes in cases where both interfaces are affected. Additionally from Figure 3.8, there is not an apparent drop in maximum phase slope until about $K = 10^{15}\ N/m^3$. It therefore concluded that assessment of $d\phi/df_{max}$ may only be sensitive to kissing bonds and not intermediate bond strengths.

3.3 Conclusions

A mathematical model for ultrasonic interactions with imperfect adherent/adhesive interfaces has been developed. Weak bonding is modeled as a distributed spring system at the interface, and changes in the interfacial stiffness flux have an impact on the phase of ultrasonic reflections. At a single interface, it is shown how the phase response of interfacial reflections is dependent upon the acoustic impedance values on either side of the interface. For $Z_1 < Z_2$ and $Z_1 = Z_2$ the phase of the ultrasonic reflection coefficient varies from $0\ deg$ for low interface stiffness to a much higher value for high interface stiffness. Meanwhile for $Z_1 > Z_2$, both low and high interface stiffness constants display a phase of ultrasonic reflection of $0\ deg$, and the phase response rises to some maximum value at some interfacial stiffness value in between. Additionally, it is discussed that a thin layer behaves like an interfacial spring boundary when the layer thickness is small with respect to the wavelength and the acoustic impedance in the layer is much smaller than the surrounding media.

For double-interface joints, or SLJs where a thin adhesive layer is sandwiched between two adherents, the phase response of ultrasonic reflections is much more complicated. As it is difficult to time-resolve individual echoes within the adhesive layer, the sum of all internal reflections are modelled, and the adhesive layer acts as a resonance cavity when the bond line thickness is equal to half the acoustic wavelength. It is shown that changes in the interfacial stiffness affect the shape and location of the phase inversion around the resonance frequency in a predictable way. Therefore, by assessing the phase spectra around acoustic resonance of the bond line, interfacial stiffness constants are measurable.

Chapter 4: The Constant-Frequency Ultrasonic Phase Measurement Method

In this chapter, the novel method to obtain high-resolution ultrasonic phase measurements is presented, discussed in detail, and demonstrated. The design, building, and testing of this instrument was one the first major parts of this project. Using a digitally controlled constant frequency pulsed phase-locked-loop (CFPPLL) design, this method is capable of obtaining high-resolution, low-uncertainty ultrasonic phase measurements at a single frequency. Additional development on this instrument made it possible to change the driving frequency while maintaining phase information, enabling the use of swept-frequency ultrasonic phase measurements for the characterization of adhesive bond quality.

In the first section, a background on ultrasonic phase measurement methods from the literature is presented. Next, the basic operation of the CFPPLL ultrasonic phase measurement instrument and its capabilities are explained in detail, followed by a section discussing considerations affecting the time it takes to obtain these phase measurements. Then, the swept-frequency ultrasonic phase measurement method is demonstrated in an application of thickness gaging and compared to conventional broadband ultrasonic time-of-flight thickness gaging methods. Finally, the effect of pressure on the ultrasonic transducer during contact measurements is analyzed before concluding remarks.

4.1 Background

The phase or time-delay of an ultrasonic wave has been used for many years to measure absolute and relative material properties. The phase, rather than amplitude, of ultrasonic waves is ideally suited for these measurements due to its sensitivity to the wavelength and thickness of a material specimen. Methods of accurately determining the time delay between received ultrasonic echoes date back as far as the 1960s with the pulse-superposition method by McSkimin [99] and the pulse-echo-overlap method by Papadakis [100]. Several improvements to broadband time-domain ultrasonic velocity-change measurements with damped transducers have been made throughout the years [101], [102], [103], [104]. Other pulse-echo methods involve finding the resonance frequency of the material [105], [67] or utilize continuous-wave sources to introduce standing waves rather than broadband sources [106]. A comprehensive overview of high-resolution ultrasonic velocity measurement methods in liquids was compiled by Kaatze, Eggers, and Lautscham [107].

Another method of measuring ultrasonic time delays focuses on the cross-correlation between transmitted and received ultrasonic pulses, where the peak of the cross-correlation function indicates the time-of-flight (ToF) of the ultrasonic signal within the specimen [108]. Cross-correlation ToF measurements can be setup entirely digitally to monitor ultrasonic propagation changes within a system, and it is well-suited for cases where signal amplitude may vary significantly due to attenuation and scattering. The cross-correlation method has been applied to cases of ultrasonic velocity measurements [109] [110] [111] [112], flow monitoring [113], distance measurements [114], and material crack and flaw identification [115]. Liang, *et. al.* investigated the fundamental limits of cross-correlation-based phase measurements, describing phase errors introduced by quantization as well as non-integral sampling [116]. While improving ToF accuracy and precision over conventional methods, cross-correlation suffers from the time and computational expense needed for post-processing of the transmitted and received signals to find the ToF, limiting its ability to provide inexpensive real-time ToF monitoring for certain applications.

For high-accuracy measurements, single frequency gated continuous wave (i.e. tone-burst) ultrasonic techniques increase the signal-to-noise ratio of their broadband counterparts. By comparing a received ultrasonic wave signal with a reference signal and adjusting the driving frequency until the waves are in quadrature (π/2 phase difference), a highly-sensitive measurement of changes in sound velocity or material thickness is obtained [117]. The phase comparison technique has since spawned several variations of pulsed phase-locked loop (PPLL) ultrasonic phase measurement methods.

The initial variable-frequency PPLL systems were used in applications of bolt tension monitoring [118] , as well as detecting changes in sound velocity [119]. A major drawback of variable-frequency phase measurement methods is their sensitivity to frequency-dependent sources of phase error in the instrumentation electronics, transducers, and material. Furthermore, variable-frequency methods can only measure relative phase changes within a solid specimen, as they rely on changing frequency to make a single-phase measurement. Consequently, the constant-frequency PPLL (CFPPLL) provides a major improvement for conducting ultrasonic phase measurements [119].

The original CFPPLL design utilized a single driving frequency, a voltage-controlled phase shifter, and a phase detector to lock the transmitted and reference waves in quadrature [120]. This instrument measured absolute phase velocities in liquids by tracking the phase shift induced when changing the ultrasonic path length; however, only changes in ultrasonic velocity due to external stimuli, such as pressure or temperature, were measurable in solids. Nonetheless, in comparison to the variable frequency PPLL counterpart, the CFPPLL provided very high accuracy and sensitivity.

A digitally controlled CFPPLL instrument capable of real-time ultrasonic tracking of phase and swept-frequency phase measurements on both solids and liquids is explored. This instrument offers significant improvements in ease-of-use due to digital control and data collection capabilities. Whereas previous PPLL-based instruments required the changing of path-length to conduct absolute sound velocity measurements in liquids, both constant-frequency phase tracking and phase vs. frequency measurements of this CFPPLL instrument permit other experimental approaches.

To illustrate its flexibility, experimental measurements of small differences in path-length in borosilicate glass via the CFPPLL instrument are shown and compared with conventional pulse-echo time-of-flight (ToF) measurements for thickness measurement accuracy and precision.
To obtain high accuracy phase measurements, the internal and external sources of uncertainty with this method were examined in detail.

While simple pulse-echo ToF measurements are often sufficient for ultrasonic velocity measurements for flaw detection in large industrial parts, high accuracy phase measurements are extremely important in the measurement of ultrasonic velocity for other disciplines, including the aerospace, automotive, material science, and medical industries. In particular, high-resolution ultrasonic velocity measurements have been used to measure clamping force in bolts under high tension [121], gas and liquid flow metering [113], phase diagrams of superconductors [122], grain size estimation in steel [123], human bone quality [124], and molecular relaxation processes [125]. Additionally, high-resolution ultrasonic phase measurements have proved able to noninvasively measure intracranial pressure, which has classically only been measurable invasively [126]. Without corrections for commonly encountered external factors, such as transducer coupling and temperature variations, the accuracy of these highly sensitive techniques are greatly affected.

4.2 The Digitally-Controlled Constant-Frequency Pulsed Phase-Locked Loop

4.2.1 Basic Operation of the Ultrasonic Phase Measurement Instrument

All PPLL devices consist of two signal paths along which the first, an ultrasonically transceived tone-burst, is phase-compared to a reference wave. On Path 1, the transducer generates an ultrasonic tone-burst that traverses a material specimen. In a pulse-echo arrangement, the same transducer receives and converts the tone-burst back into an electrical signal. However, in a pitch-catch arrangement, a second transducer is used to receive the tone-burst. On Path 2, the reference wave is phase-compared to the transceived tone-burst from the first path. In a variable-frequency PPLL, the frequency of the transceived tone-burst is varied until the signals are in quadrature. However, in a CFPPLL, the relative phase of the transceived signal is changed until quadrature. The system is then considered to be in a locked state, and quadrature is maintained through continual updates to frequency or relative phase of the transceived signal.

In the digitally controlled CFPPLL instrument, a pair of direct digital synthesizers (DDSs) generate sine waves with a repeatable constant phase offset, permitting absolute ultrasonic phase measurements. While the system is in a locked state, the voltage output of a phase-detector is sampled by a microcontroller, which commands the DDS to adjust the transceived tone-burst's phase to maintain quadrature with the reference wave. A field-programmable gate array (FPGA) controls timing parameters and gating within the system.

A block diagram of the developed CFPPLL-based ultrasonic phase measurement instrument is shown in Figure 4.1. Using a computer terminal, the user adjusts waveform and system parameters such as sample-and-hold (S/H) position, number of tone-burst cycles, repetition rate of the tone-burst, and number of sampled data points to average when taking phase measurements. After initial setup, the user locks the system, which outputs the phase adjustments to the computer.

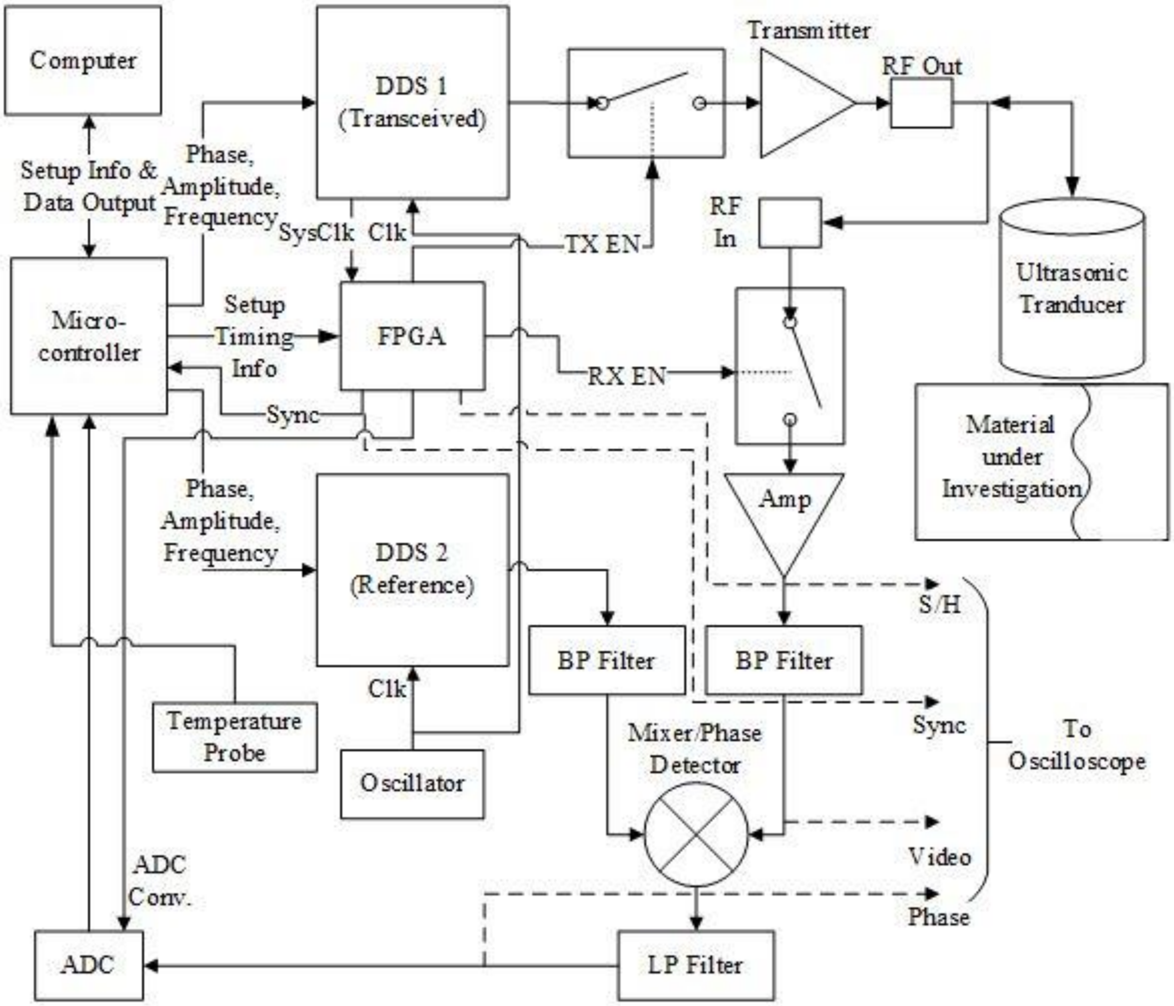

Figure 4.1: Block diagram of digitally-controlled CFPPLL instrument

The twin DDSs generate sine waves at the frequency, amplitude, and phase set by the microcontroller. The same 1 GHz input timing clock is used for both DDSs, and upon system startup, the microcontroller synchronizes their output via a simultaneous reset command. The DDSs use lookup tables to generate the frequency and phase of the ultrasonic waves, which provide absolute frequency and phase adjustment resolution limits. The DDSs have 14 bits of phase resolution and 48 bits of frequency resolution, resulting in a minimum phase shift of $2\pi/2^{14} \approx 0.00038\ [rad] \approx 0.022°$ and a minimum frequency shift of ~3.55 μHz. Based on the timing information set by the microcontroller, the FPGA uses a transmit enable (TX EN) signal to gate the transceived wave in Path 1, forming a tone-burst of a set number of cycles.

The tone-burst in Path 1 is amplified and sent to a transducer, which ultrasonically interrogates a material specimen through a coupling medium. After being reflected off the back wall of the test specimen, the acoustic tone-burst is received by the same transducer in the pulse-echo setup, as shown in Figure 4.1. Material property variations due to external stimuli such as pressure, temperature, elasticity, or path length are then detectable via ultrasonic phase shifts. After receiving the ultrasonic reflection, the transducer converts the tone-burst into an electrical signal. The FPGA timing ensures signals are continuously received using a receive enable (RX EN) signal, except for the short duration during tone-burst transmission.

The received tone-burst is amplified and band-pass filtered to reduce signal noise, and the reference wave passes through an identically designed band-pass filter. Currently, the instrument operates with center frequency around 10 MHz, and the band-pass filtering circuits were both measured to have a -6 dB pass-band of 8.8-11.0 MHz. In practice, commercial damped transducers have displayed wider bandwidths than the band-pass filtering circuits, providing a minimal change to system bandwidth but providing a measurable phase response, which must be characterized for high accuracy phase measurements.

After filtering, the received and reference signals pass into the phase detector. The phase detector outputs a voltage dependent on the phase difference between the two signals, using $\pi/2$ offset at the 0 V reference. The output voltage is low-pass filtered to minimize non-DC noise and is subsequently sampled and held using an analog-to-digital converter (ADC), whose output passes into the microcontroller. The S/H position on the received phase detector output signal is set by the FPGA and is user-specified.

Table 4.1: Major components used in CFPPLL instrument

Component	Model
Microcontroller	ATMEL ATmega644
FPGA	FreeForm/104 board with Xilinx Spartan 3E FPGA
DDS	Analog Devices AD9912
Transducer	¼” Diameter 10 MHz, Olympus V112-RM

Each time the phase output is received by the microcontroller, the voltage output of a temperature probe -- typically adhered to the material test specimen -- is also sampled. With oversampling and decimation, the temperature measurement resolution of the system reaches $0.008°C$.

4.2.2 Example of Ultrasonic Phase Measurement System in Operation

To monitor the system, the S/H pulse from the FPGA, the amplitude of the transceived tone-burst after band-pass filtering, and the phase detector output voltage are all viewed on an oscilloscope. Figure 4.2 shows an example of the oscilloscope CFPPLL signal display. The SYNC signal output from the FPGA, mentioned in Figure 4.1, represents the beginning of each tone-burst transmission and is the trigger for the oscilloscope (not shown in Figure 4.2). The filtered amplitude signal, or video signal in Figure 4.1, is used to observe ultrasonic reflections and helps the user determine waveform parameters. Often, the number of transmitted cycles is chosen to minimize the gap between successive reflections without overlapping. The phase and S/H signals are used to set the S/H position, typically in the portion of the received tone-burst where the phase appears flat. It should be noted there is a slight time delay between the video amplitude signal and the output of the phase detector; thus, the S/H position occurs slightly earlier than it appears on the amplitude signal.

The “bleed-thru” portion of the waveform is never actually transceived ultrasonically, but instead stays within the circuit. While the RX EN signal is off during the transmission period, some small amplitude leaks through and is amplified like the received ultrasonic reflections. It was first thought that this “bleed-thru” signal was undesirable; however, it has since proved useful in measuring the phase response of the filtering circuits.

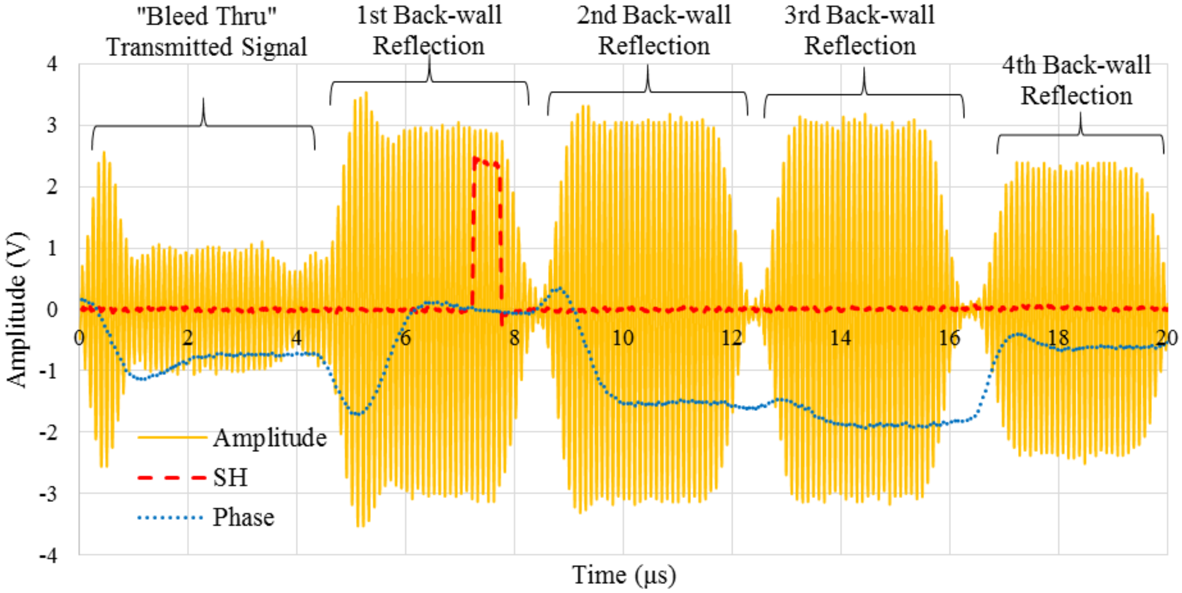

Figure 4.2: Typical waveforms seen on oscilloscope when using ultrasonic phase measurement instrument

4.2.3 Additional System Capabilities

Figure 4.3 shows a typical setup of the CFPPLL ultrasonic phase measurement system in the laboratory. The laboratory used for most experiments in this work is environmentally controlled to keep relative humidity near 50% and temperature near $20°C$. Additionally, a custom-built environmental chamber is used for some experiments. The environmental chamber has both heating and cooling capabilities controlled by an Omega CN7823 proportional-integral-derivative (PID) controller. Near room temperature, it can hold temperature to a standard deviation of $\pm 0.01°C$ over one hour.

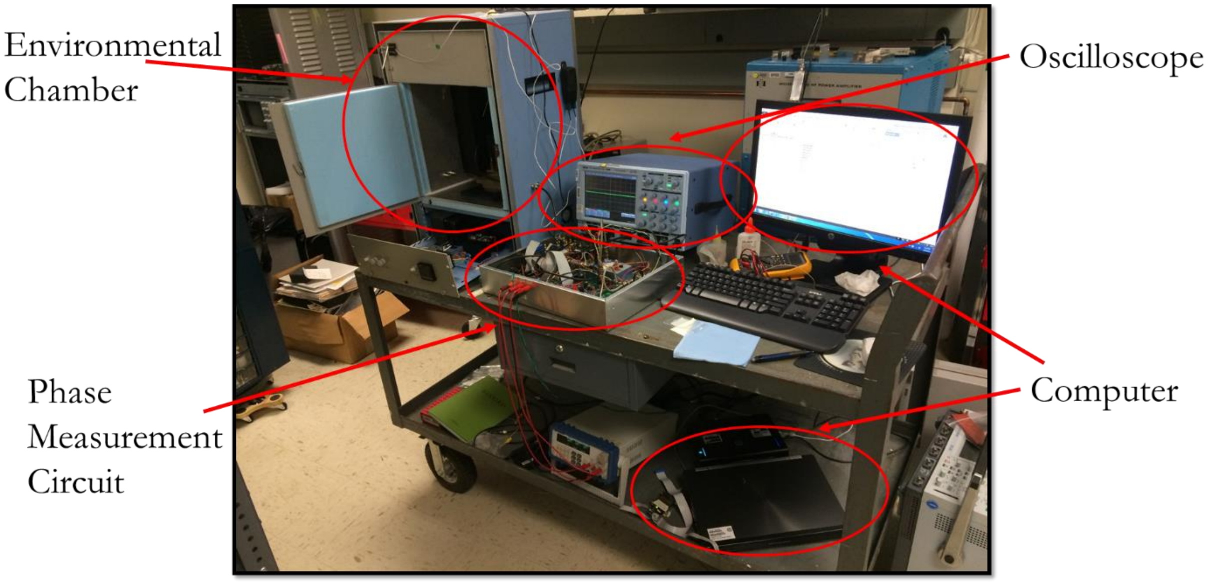

Figure 4.3: Ultrasonic phase measurement laboratory setup

The CFPPLL system is capable of using both undamped, bare piezoelectric element crystal transducers and commercially available damped transducers. Figure 4.4 shows ultrasonic transducer mounting optioned developed for this system. For use with bare-element piezoelectric crystals, the setup in Figure 4.4a contains of two spring-loaded contacts which can be lowered onto the transducer on a surface using an adjustable-height stage. The setup in Figure 4.4b has an adjustable-height stage, as well, operated by a screw clamp. The use of a load cell in line with the ultrasonic transducer allows the load on the transducer to be controlled, as well.

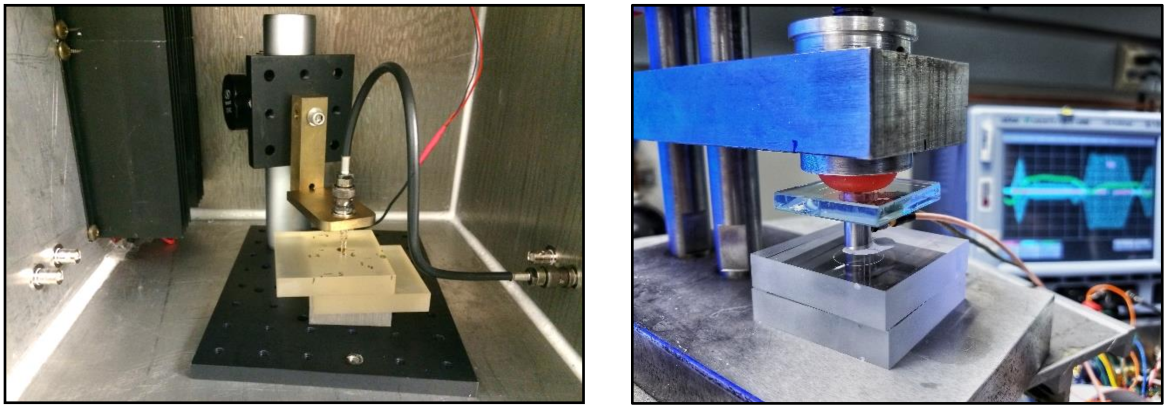
a) b)

Figure 4.4: Images of ultrasonic transducer mounting capabilities with a) un-damped, bare-element PZT transducer and b) commercially-available damped transducer

4.3 Detection Limits of Ultrasonic Phase Measurements

4.3.1 Theoretical Limits

Unlike other time-delay measurement methods, the phase resolution and phase quantization error of the CFPPLL method is not frequency dependent. Set by the constant phase shift resolution by the DDSs regardless of frequency of the generated tone-burst, the relative phase between the generated sine waves can only be changed in multiples of 0.022°. In contrast to conventional time-delay methods, a consequence of constant phase resolution with this method is that time resolution will be worse for lower frequencies and better for higher frequencies, based on the relationship between time delay and phase: $\Delta t = \Delta\phi/360f$.

In the absence of changing external variables, such as temperature or couplant layer thickness, the phase measurement error of the system will have a lower limit of the quantization error of the DDSs. One least significant bit (LSB) of phase shift within the DDSs is $360/2^{14} \approx 0.0220°$. Thus, the standard deviation of phase due to quantization error within the DDS is $LSB/\sqrt{12} = 0.0063°$.

4.3.2 Measured Limits

A set of experiments was performed to examine the error of the constant-frequency ultrasonic phase measurements in the absence of external variables. A 5.08 cm x 5.08 cm, 11 mm thick specimen made of Schott Borofloat® 33 was monitored for phase shifts from its first back wall echo. A nominally 10 MHz, Olympus V112 ultrasonic transducer was coupled to the glass specimen with Sono 600 commercial couplant. To maintain consistent couplant layer thickness between measurements, a screw clamp was used to hold constant pressure and a load cell was placed in the path between the clamp and ultrasonic transducer. The transducer clamping setup was placed within a custom-built environmental chamber with temperature stability of $\pm 0.01°C$ over one hour.

While holding pressure steady at ~2.8 MPa, the temperature was held constant at 21°C, and the ultrasonic phase response of the first back wall echo was monitored at a driving frequency of 10 MHz. While transducer pressure and temperature were held constant, the standard deviation of phase was measured over a 30 minute period. To view the effect of averaging, the number of phase measurements averaged when making phase adjustments within the microcontroller was varied in powers of four from $4^0 = 1$ to $4^4 = 256$, with a single phase measurement obtained every 6 ms.

Figure 4.5 displays one standard deviation of phase measurements over a 30 minute period with the temperature and transducer pressure held constant. The signal-to-noise ratio (SNR) for the first back wall echo after narrowband filtering was measured to be 26.1 dB in this experiment.

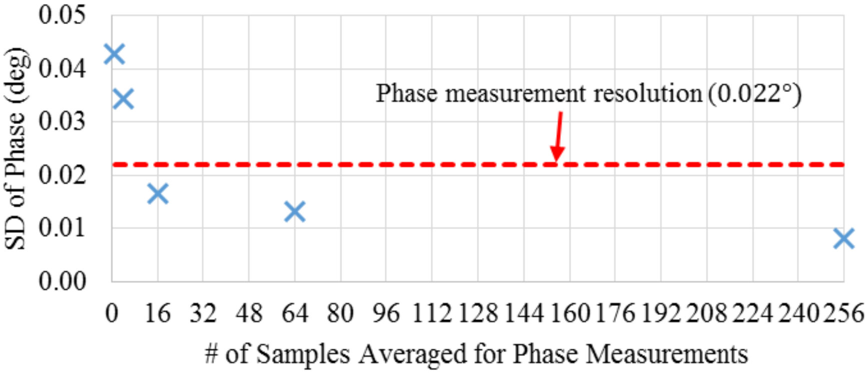

Figure 4.5: Phase error over 30 minute period vs. number of samples averaged

The standard deviation of phase error due to quantization within the DDS, calculated to be $0.0063°$, is much lower than the measured phase errors seen in Figure 4.5. As such, white noise seems to contribute much more to the phase error than ADC quantization noise. It is thought that better suppression of the transmitted wave during the receiving period of the circuit and more narrowband filtering may help improve SNR. Also shown in Figure 4.5, averaging over as few as 16 samples has a large effect on the phase measurement error, bringing the uncertainty below the phase adjustment resolution of the DDS of $0.0220°$. Averaging over more samples continues to drop the phase measurement uncertainty to below $0.01°$ at 256 samples.

The CFPPLL-based method outperforms high-resolution cross-correlation ToF methods in terms of phase error due to white noise and quantization error. As the effects of changing environmental factors were removed in this experiment, the phase measurement uncertainty over a long period of time should only be due to ADC quantization error and random noise. Thus, it should be comparable to the phase error in cross-correlation methods due to quantization error and white noise. By comparing Figure 4.5 in this work with FIG. 2 of [116] by Liang, *et al*, the improvement in phase error for smaller SNRs can be seen. In this work, the measured SNR of 26.1 dB and 14 bit ADC produced a standard deviation of phase error of under 0.02° with 16 samples, while the cross-correlation method in [116] requires much higher SNRs or samples averaged to obtain similar phase errors. Using the same SNR of 26.1 and assuming phase error due to white noise and quantization error are approximately equal, the standard deviation of phase error with 256 samples for cross-correlation is 0.251° according to Equation 22 in [116], compared to 0.008° measured with the CFPPLL-based method.

4.4 Demonstration of High-Resolution Thickness Measurements via Swept-frequency Ultrasonic Phase

4.4.1 Method Description

Assume an ultrasonic displacement plane wave is propagating within a non-dispersive medium of finite thickness, Medium 1. After reflection off the boundary with some half-space, Medium 2, and being received, as shown in Figure 4.6, the phase of the ultrasonic wave is expressed in Equation 4.1, where $k_1 = \omega/c_1$ is the wavenumber in Medium 1 with sound velocity c_1, $\omega =$

$2\pi f\ [rad] = 360f\ [deg]$ is the driving angular frequency with driving frequency f, and L_1 is the thickness of Medium 1.

$$\phi_{u_R} = -2k_1L_1 = -\frac{720fL_1}{c_1}[deg] \tag{4.1}$$

The factor of two occurs due to the propagation through the thickness of Medium 1 twice. It is assumed in Equation 4.1 that the acoustic impedance of Medium 1 is greater than in Medium 2 or else the reflected wave would be π out of phase with the incident wave, as the normal-incidence ultrasonic particle displacement wave reflection coefficient is $R = (Z_1 - Z_2)/(Z_1 + Z_2)$ where Z_j is the acoustic impedance of each medium.

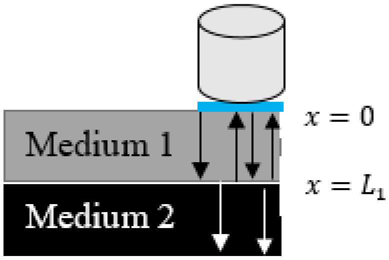

Figure 4.6: Representation of ultrasonic wave reflections at boundary between Medium 1 and Medium 2 as well as couplant layer

4.4.1.1 Swept-Frequency Phase Measurements

The phase of the reflected wave is used to measure either sound velocity or thickness of a material, given the other parameter. In non-dispersive media, the group velocity, $c_g = d\omega/dk$, is equal to the phase velocity, $c_p = dx/dt$ [119]. Thus, single-frequency phase measurements can find group velocity as well as phase velocity in non-dispersive media.

As constant-frequency phase measures relative fractions of a wavelength, expressed between $-\pi$ and π, it is difficult to obtain absolute thickness or sound velocity measurements since the total number of propagating wavelengths is unknown. Previous PPLL-based methods could measure absolute sound velocity in fluid media, where the acoustic path length was varied and

$\partial\phi_{u_R}/\partial L_1$ measured [119], [120]. In solid media, only changes in sound velocity are measured as path length cannot be changed.

With the digitally controlled CFPPLL instrument, the ultrasonic driving frequency can be altered while maintaining the phase relationship between the transceived and reference signals, allowing for a measurement of $\phi_{u_R}(f)$. By sweeping the driving frequency and measuring the phase response, the sound velocity or path length is extracted by the relation in Equation 4.2.

$$\frac{\partial\phi_{u_R}}{\partial f} = -\frac{720L_1}{c_1}\ [deg/Hz] \tag{4.2}$$

4.4.1.2 Pulse-Echo Time-of-Flight Measurements

Traditional pulse-echo ultrasound can measure sound velocity or material thickness given knowledge of one of the parameters. After sending a broadband ultrasonic pulse through a material, the time-of-flight (ToF) of the received pulse is measured. Given the material setup in Figure 4.6, the ToF for reflected waves is found by substituting the relation between time delay and phase, $\Delta t = \phi/\omega$, into Equation 4.1 to find the equation for ToF shown in Equation 4.3. As the ToF does not suffer from a limited range of possible values like a constant-frequency phase measurement, a single ToF value can be used to measure sound velocity or specimen thickness.

$$ToF = -\frac{2L_1}{c_1}\ [s] \tag{4.3}$$

4.4.1.3 Characterizing External Sources of Phase Shifts/Time Delays

In a practical direct-contact ultrasonic measurement system, the electronic circuitry, ultrasonic transducer, and ultrasonic couplant layer each provide time delays or phase shifts to ultrasonic waves. To minimize these errors, different methods are used to reduce or negate their effect. In conventional pulse-echo ToF measurements, a primary method for negating external time delays is to measure the ToF difference between successive back wall echoes from a material. Delays due to the instrumentation, transducer, and double-transmission through the couplant layer affect successive echoes in the same way, so subtracting successive echoes will remove the circuit-based time-delays.

This technique can also be applied to constant-frequency phase measurements. Considering external phase shift sources for ultrasonic echoes from the material system, the measured phase for the n^{th} echo can be described by Equation 4.4.

$$\phi_n = \phi_{instr.} + \phi_{trans.} + 2\phi_{coup.T} + \phi_D^{(n)} + \phi_{U_R} + (n-1)\left(\phi_{U_R} + \phi_{coup.R}\right) \tag{4.4}$$

In Equation 4.4, $\phi_{instr.}$ is the phase shift from the instrumentation, $\phi_{trans.}$ is the phase shift from the ultrasonic transducer, $\phi_{coup.T}$ is the phase shift from transmission through couplant layer, $\phi_{coup.R}$ is the phase shift from reflection off the couplant layer occurring for secondary echoes, $\phi_D^{(n)}$ is the phase shift due to ultrasonic wave diffraction, and ϕ_{U_R} is the phase shift from the material under investigation as defined in Equation 4.1. Note, the superscript on the ϕ_D term corresponds to the diffraction phase shift from the n^{th} echo and is not ϕ_D to the n^{th} power. The phase difference between consecutive reflections from Equation 4.4 is written in Equation 4.5, where several of the external phase shift sources have been eliminated. Remaining in Equation 4.5 is the phase shift of the reflection from the test material-couplant-transducer interface as well as the phase shift due to ultrasonic diffraction.

$$\Delta\phi = \phi_{n+1} - \phi_n = \phi_D^{(n+1)} - \phi_D^{(n)} + \phi_{U_R} + \phi_{coup.R} \tag{4.5}$$

4.4.1.4 Effect of Ultrasonic Couplant Layer

There have been several treatments of the effect of the couplant layer on both the amplitude [127] [128] [129] [130] and time-delay [131] [132] on an ultrasonic wave. If using a bare-element piezoelectric transducer, the effect of the couplant layer on the reflected phase can be derived given the couplant thickness as well as the material properties of the active element, couplant, and material under test [132]. Commercially available broadband ultrasonic transducers, however, contain additional layers that complicate analysis [131]. Furthermore, the internal setup of commercial transducers is often proprietary, which makes analysis of the ultrasonic reflection coefficient difficult without many assumptions.

Despite difficulties with calculating the actual reflection coefficient from the couplant interface, it can be shown that as the couplant becomes thinner, its effect on ultrasonic amplitude and phase lessens. By assuming a thin fluid layer between two half-spaces, the effect of a thin couplant layer can be approximated [133]. Assuming a PZT5A transducer, water couplant, and borosilicate glass specimen, the phase of the ultrasonic reflection coefficient as a function of frequency for different couplant thicknesses is shown in Figure 4.7. The difference from the 180° phase shift for an infinitely thin couplant layer becomes more pronounced as the couplant layer thickness becomes larger with respect to wavelength. As the phase shift can vary dramatically for small differences in thickness, care must be taken to ensure a consistent couplant thickness to obtain high repeatability.

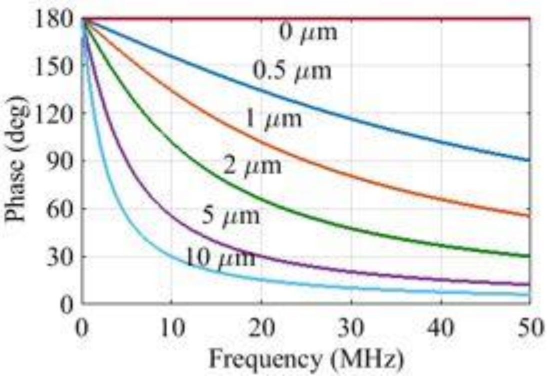

Figure 4.7: Phase vs. frequency of ultrasonic reflection from couplant interface for different couplant thicknesses

4.4.1.5 Effect of Ultrasonic Diffraction

The phase of diffraction terms in Equation 4.5 are computed by modeling ultrasonic diffraction within the test specimen for the $(n+1)^{th}$ and n^{th} echoes. Due to the use of a finite-radius piston source and receiver, ultrasonic signals do not, in practice, behave as a true plane wave within a specimen. Much research throughout the years has been completed into modeling the effect of diffraction on ultrasonic waves [134] [135] [136] [137].

Depending on the unit-less parameter sometimes referred to as the Seki parameter, amplitude and phase shifts due to diffraction can be calculated. The Seki parameter is defined $S = z\lambda/a^2$, where z is the distance traveled, $\lambda = c/f$ is the ultrasonic wavelength, and a is the transducer radius. Numerous works have used corrections for diffraction to obtain more accurate ultrasonic velocity, time-delay, and attenuation measurements [100] [132] [138] [139] [140]. In this work, the exact phase shift due to diffraction due to different back wall echoes within the test specimen is determined by solving the exact Lommel diffraction correction integral found by Williams [136] and written in a different form by Rogers and Van Buren [141].

4.4.2 Experimental Setup

To demonstrate the capabilities of the CFPPLL-based ultrasonic phase measurement method, measurements of micrometer-scale thickness variations in ~11 mm thick smooth glass specimens were performed. Six 5.08 cm x 5.08 cm square specimens were cut from a plate of Schott Borofloat® 33, a float-glass version of borosilicate glass purchased from the S. I. Howard Glass Company. The specimens were cleaned in an ultrasonic bath of ethanol for 30 minutes prior to testing. Next, a 3 x 3 grid was marked off on each specimen using thin strips of tape to be used for thickness measurements.

At each of the nine locations on the six test specimens, the thickness was measured using a calibrated Starrett micrometer. The micrometer was calibrated by using Starrett-Webber gage blocks in the thickness range of interest, 10.9-11.0 mm, in 1 μm increments. After correction, the micrometer measurements in the given range had a standard deviation of error of 1.05 μm.

To maintain consistent couplant layer thickness between measurements, a screw clamp is used to hold constant pressure and a load cell is placed in the path between the clamp and ultrasonic transducer, as shown in Figure 4.8. A similar measurement setup is shown in Figure 4.4b.

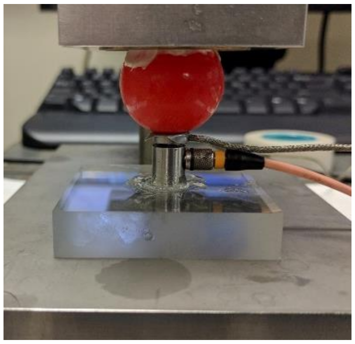

Figure 4.8: Image of load cell in path between screw clamp and ultrasonic transducer

Ultrasonic measurements for thickness estimation were taken at each of the nine locations on six test specimens. To maintain a consistent couplant thickness, the transducer was loaded with a pressure of ~2.8 MPa for each test. Water was used as a couplant for all measurements shown in this work due to its well-known material properties; however, other commercially available couplants produced similar results. A 6.35 mm diameter, highly damped, broadband Olympus V112 ultrasonic transducer nominally designed to operate at 10 MHz was used for most measurements, with the exception of some ToF measurements using a 50 MHz transducer.

Using the CFPPLL-based ultrasonic phase measurement instrument, the phase of the received wave was tracked as the frequency of the input tone-burst varied from 9 MHz to 10 MHz with a 10 kHz resolution. At each frequency, the phase was averaged over 32 repeated tone-bursts to reduce the effect of noise. The phase vs. frequency response of both the first and second back wall reflections from the Borofloat specimens were measured.

While still under pressure, the ultrasonic transducer was disconnected from the CFPPLL instrument and connected to a GE Panametrics Model 5900PR Pulser-Receiver to generate and receive broadband pulses for comparative ToF measurements. The generated pulse contained 1 μJ of energy, and the received wave was amplified by 29 dB. The bandwidth of the generated pulse was chosen to be 1 kHz-200 MHz to make the ultrasonic transducer the bandwidth-limiting element of the system. After amplification, the received echoes from the specimens were displayed on a LeCroy WaveRunner 6200 oscilloscope with 0.1 ns timing resolution. ToF measurements were taken by measuring the difference in time of the peak amplitudes of the first two back wall reflections and averaging over 500 transmitted pulses.

After the phase and ToF measurements, the 10 MHz ultrasonic transducer was replaced with a 6.35 mm diameter, highly damped, broadband Olympus V214 ultrasonic transducer designed to operate at 50 MHz. Conventional pulse-echo ToF measurements were obtained with the transducer, similar to the measurements taken with the 10 MHz transducer.

4.4.3 Results and Discussion

4.4.3.1 Correction for Time-Delay and Phase Offsets

Prior to analysis, the phase shift due to diffraction was found and subtracted out of the phase vs. frequency measurements. As borosilicate glass should have no long-range crystal structure, it is assumed isotropic. Table 4.2 shows the parameters used to solve the diffraction correction integral at each frequency and for each echo. The nominal specimen thickness of $L = 11\ mm$ was used for each diffraction correction.

Table 4.2: Parameters used in diffraction phase correction calculation

Parameter	Value
Sound Velocity, c	$5.640\ [mm/\mu s]$
Distance Traveled, $2Ln$ (n is echo #)	$22n\ [mm]$
Transducer Radius, a	$3.175\ [mm]$
Frequency, f	$9.00 - 10.00\ [MHz]$

Figure 4.9 shows the computed diffraction phase correction curves for the first and second back wall echoes as well as the phase difference between the same echoes. These curves were used to correct the measured phase vs. frequency response of the first and second back wall echoes from

each specimen in the 9-10 MHz. The diffraction phase correction provided an effect of $-0.854\,deg/MHz$ on the slope of the first echoes and an effect of $-1.567\,deg/MHz$ on the difference between back wall echoes in the 9-10 MHz range.

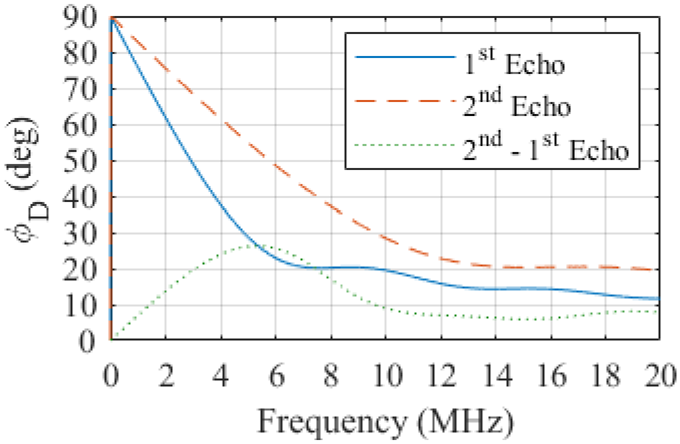

Figure 4.9: Diffraction phase correction and correction difference for multiple echoes

After diffraction correction, the effect of couplant reflection was removed by applying a linear fit to the ToF or phase vs. the measured thickness curve. The y-intercept of the line-of-best-fit at zero thickness corresponds to the extrapolated phase or time-delay offset. In total, four parameters were extracted from the ToF and phase measurements to predict Borofloat glass thickness: ToF difference between echoes with 10 MHz transducer, ToF difference between echoes with 50 MHz transducer, slope of phase vs. frequency in 9-10 MHz range from first back wall echo, and slope of phase difference between back wall echoes vs. frequency in 9-10 MHz range.

Figure 4.10 shows plots of two of the time-delay parameters as a function of the specimen thickness. Included in each plot is the line-of-best-fit for the data, which is used to interpolate the time-delay or phase offset at zero specimen thickness. Assuming the couplant thickness and quality is the same for each measurement, the offset measures the phase impact from all sources except for the test specimen. Comparing the phase difference between two consecutive echoes to the phase from the first echo, the phase offset dropped in magnitude, which is consistent with the theory that the phase difference would subtract out some external phase shift sources present in each echo.

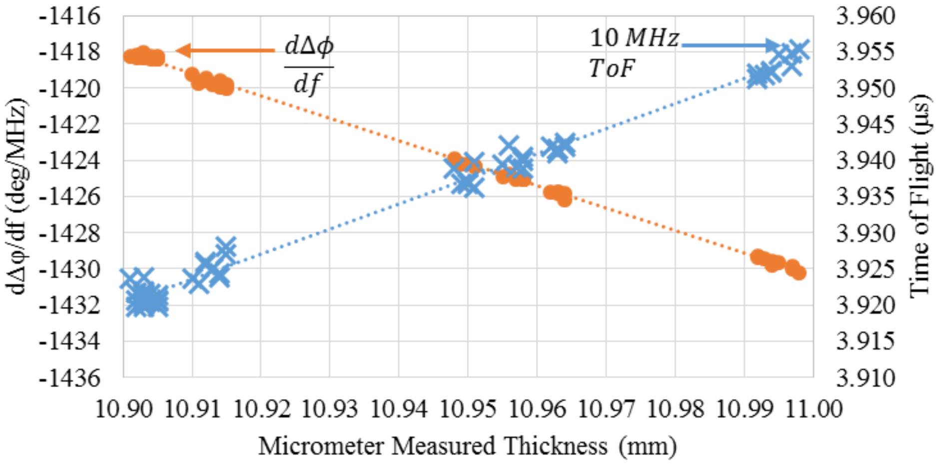

Figure 4.10: Time delay parameter vs. thickness, including linear fit, for ToF with 10 MHz transducer and $d\Delta\phi/df$

As there is only a weak dependence of diffraction for the small ~100 μm thickness difference range, the diffraction corrections only provided a constant offset to the $d\phi/df$ vs. thickness measurement curves. As such, diffraction corrections did not provide a measureable effect on the thickness predictions in this study. It should be noted, however, that the interpolation of the phase offset at zero thickness is only valid after diffraction correction have been applied, according to Equations 4.4 and 4.5. If gaging thickness over a greater range, the diffraction correction to $d\phi/df$ will become more pronounced.

4.4.3.2 Thickness Predictions from Ultrasonic Measurements

After finding the phase or time-delay offset for each parameter, a thickness for each measurement was calculated from Equations 4.2 and 4.3. Figure 4.11 shows the difference between the ultrasonically measured thickness and micrometer-measured thickness at each location, for two of the time-delay parameters.

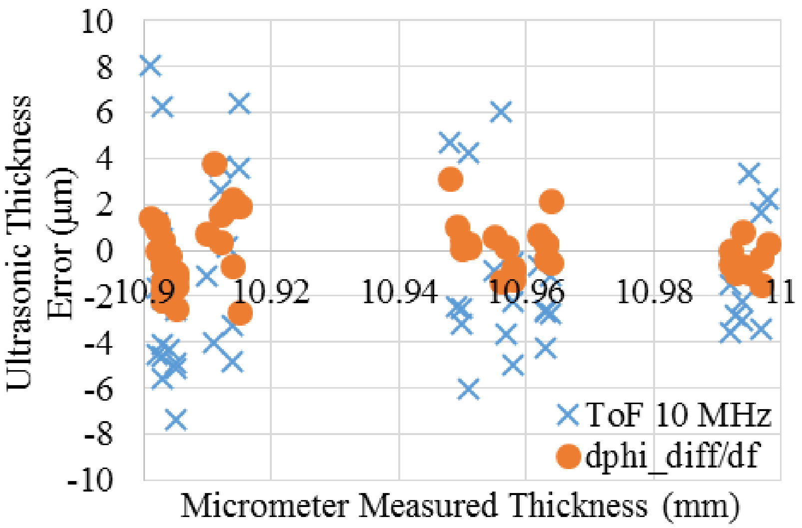

Figure 4.11: Difference between ultrasonically and micrometer measured thicknesses for ToF with 10 MHz transducer and $d\Delta\phi/df$

Additionally, Figure 4.12 shows a box plot of the predicted thickness error from all of the parameters, displaying the median as well as the first and third quartiles of the data. Small plus signs in the box plot represent potential outlier data that fall outside of the quartiles by greater than 1.5 times the interquartile range. Note, phi_diff is the $\Delta\phi$ phase difference between the first and second back wall echoes.

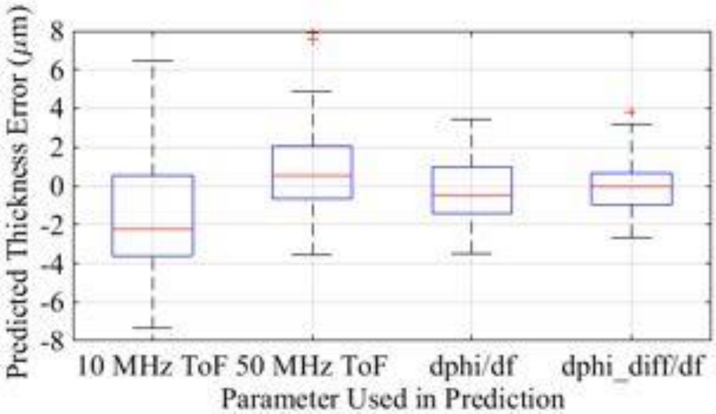

Figure 4.12: Box plot of predicted thickness error for each time-delay or phase parameter

From comparing predicted thicknesses with measurements with a calibrated micrometer, several conclusions can be drawn. The worst performing parameter tested was ToF measurements with the 10 MHz transducer, with the most significant mean and standard deviation of error. Using the same ultrasonic transducer, the CFPPLL-based ultrasonic measurement parameters performed more accurately and displayed less uncertainty. As predicted, the 50 MHz transducer performed more accurately and precisely than its 10 MHz counterpart. It is thought that the longer pulse duration from the 10 MHz transducer in comparison to the 50 MHz transducer results in higher uncertainty.

It is important to note that each of the CFPPLL-based phase parameters performed about the same or better in both accuracy and precision than the ToF measurements from the much higher frequency transducer. If the CFPPLL-based instrument was modified to have a pass-band around 50 MHz rather than 10 MHz, its thickness measurement resolution would be dropped by a factor of five, since the phase resolution is constant with respect to frequency. Thus, the CFPPLL-based method should outperform conventional ToF if operated at 50 MHz. In many media, higher frequencies will attenuate very quickly, making a 50 MHz driving frequency more difficult to use. Additionally, 50 MHz transducers are often very thin and easy to break, often requiring protective coverings or delay lines. As such, it is significant that the CFPPLL-based phase measurement method obtains similar thickness gaging performance at 10 MHz that conventional ToF measurements obtain at 50 MHz.

Additionally, the phase difference between consecutive echoes resulted in a decrease in the average error and uncertainty for the $d\phi/df$ parameter. This provided the lowest mean error and uncertainty in thickness of all parameters. The $d\Delta\phi/df$ between the first and second back wall echoes provided a mean predicted thickness error of -0.04 μm and standard deviation of predicted thickness error of 1.35 μm.

4.4.4 Sources of Phase Measurement Uncertainty

In addition to the internal sources of uncertainty inherent to the ultrasonic phase technique itself, as described in Section 4.3, the external sources of uncertainty have also been analyzed. Measurements of pressure applied to the transducer and ambient temperature during testing allowed for the impact of these sources of uncertainty to be examined. From an experiment tracking the phase shift due to pressure on the ultrasonic transducer, the phase was found to level off around ~2 MPa, above which $\partial\phi/\partial f$ varied linearly by 0.439 (deg/MHz)/MPa and the phase at 10 MHz varied 3.915 deg/MPa. During thickness gaging experiments, the mean pressure on the transducer was measured to be 2.754 MPa with a standard deviation of 0.031 MPa. Therefore, the phase measurement uncertainty due to applied pressure differences is 0.014 deg/MHz for $d\phi/df$ and 0.112 deg for the phase at 10 MHz.

To examine the effect of small temperature shifts, another experiment was performed on one a glass specimen to measure the phase response to temperature change near room temperature. The transducer clamping setup was placed within a custom-built environmental chamber with temperature stability of ± 0.01°C over one hour. While holding pressure steady at ~2.8 MPa, the temperature was cycled from 20°C to 25°C and the ultrasonic phase response of the first back wall reflection was monitored at a driving frequency of 10 MHz. The phase shift at 10 MHz in the glass specimens due small temperature variations was found to vary linearly 0.715 deg/°C in the 20°C-25°C range, based on testing in an environmental chamber.

The mean temperature during ultrasonic thickness gaging tests was measured to be 20.51°C with a standard deviation of 0.18°C. Using the relationship between phase and temperature found in an environmental chamber experiment, the phase measurement uncertainty at 10 MHz due to temperature uncertainty is 0.129 deg.

The standard deviation in phase measurements at 10 MHz due to external sources sums to 0.171 deg. The internal phase measurement uncertainty at 10 MHz were found in Section 4.3 to be 0.017 deg while averaging over 16 samples as in this study. Combining external and internal sources of uncertainty yield a total phase uncertainty at 10 MHz of 0.172 deg. Conversion to thickness measurement uncertainty in Borofloat glass via Equation 4.2 gives a standard deviation of thickness measurement uncertainty of 0.14 μm due to transducer pressure and temperature variations. Combined with the measurement uncertainty of the calibrated micrometer in the 10.9-11.0 mm thickness range, the thickness measurement uncertainty due to the micrometer uncertainty, temperature variations, and transducer pressure variations is 1.06 μm. Thus, most of the 1.35 μm uncertainty using the $d\Delta\phi/df$ phase measurement method is attributed to known sources, the bulk of which is attributed to micrometer thickness measurements. Comparing the CFPPLL-based ultrasonic phase measurements with a more accurate method or using test specimens with thicknesses known to sub-micron tolerances should improve the predicted thickness uncertainty.

Another potential source of uncertainty is the slight non-linearity of the phase response in the 9-10 MHz range introduced by the reflection off the couplant layer. Using the slope of the phase vs. frequency response of back wall reflections is dependent on the linear relationship between phase and frequency of the test specimen, as described by Equation 4.2. However, the reflection from the thin couplant layer has an upward concavity and can only be approximated as linear over a sufficiently small frequency range. Consequently, measurement accuracy and uncertainty could be further improved by sweeping over a smaller frequency range.

A final source of uncertainty is inconsistent flatness and parallelism of the test specimens. As seen in the thickness values from Figure 4.10, the specimens varied in thickness across their surfaces as much as 14 μm. Thus, the glass specimens do have some inherent lack of flatness or parallelism, which contributes to the uncertainties observed. No attempt to correct the phase measurements for flatness and parallelism issues was conducted in this work.

4.5 Effect of Pressure on Transducer and Couplant Layer Thickness on Ultrasonic Phase

As initially described in Section 4.4.1.4, it is extremely important to maintain a consistent couplant layer thickness between experiments to minimize differences in phase shifts due to the couplant interface. To maintain a consistent couplant layer thickness for each measurement a screw clamp was used to hold constant pressure during testing, and a load cell was placed in the path between the clamp and commercially available ultrasonic transducer so that a consistent pressure could be applied each time, as shown in Figure 4.8. An experiment was performed where the pressure on a 1/4” diameter ultrasonic transducer was changed while measuring the resulting phase shift of reflection from the back wall of a ~11 mm thick glass specimen. Distilled water was used as ultrasonic couplant in this experiment. Figure 4.13 shows how the slope of the phase shift in the 9-10 MHz range changes as the pressure on the transducer increases.

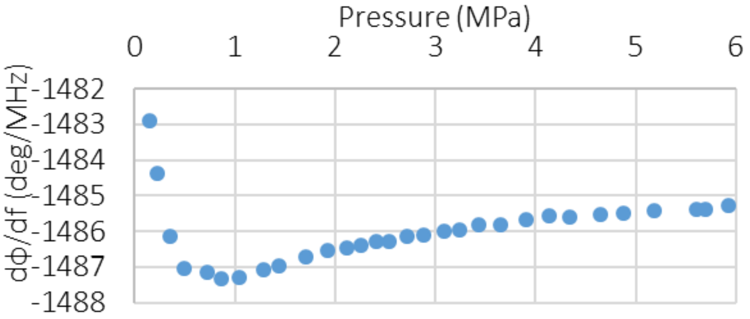

Figure 4.13: Slope of phase shift of first back wall reflection on glass specimen vs. pressure on ultrasonic transducer

As the phase slope varies only slightly for higher pressures, it was chosen to use a pressure above 2 MPa in future contact-measurement experiments with the ultrasonic phase method. In the region above 2 MPa, a linear fit of the curve implies a $0.439\ (deg/MHz)/MPa$ change due to small variations in applied pressure. From the same measurements at 10 MHz, the constant-frequency phase shift varied $3.915\ deg/MPa$ above a pressure of 2 MPa. Based on this study, it is determined to use a consistent transducer pressure of ~2.7 MPa for most of the ultrasonic measurements throughout this work.

The fact that there exists a measured minimum in the phase slope near a pressure of 1 MPa can also be further investigated for information about the couplant layer thickness. By modeling the couplant interface by a PZT5A crystal/distilled water/Borosilicate glass layer stack as was done to produce Figure 4.7, a minimum in the phase slope is predicted at the couplant thickness described by Equation 4.6.

$$L_{coupl} = \frac{c_{coupl} Z_{coupl} (Z_{PZT} - Z_{Glass})}{Z_{PZT} Z_{Glass} \omega_0} \tag{4.6}$$

In Equation 4.6, c_{coupl} is the sound velocity in the couplant, Z_n is the acoustic impedance in each layer, and ω_0 is the center angular frequency of the phase slope frequency range. At a center frequency of $9.5\ MHz$, the predicted phase slope minimum occurs at $L_{coupl} = 3.7\ \mu m$. Thus, it is concluded that at an applied pressure of ~1 MPa on the ultrasonic transducer, a couplant layer thickness of $\sim 3.7\ \mu m$ is produced.

It should be noted that it is difficult to model effect of the couplant layer on ultrasonic phase is only because contact ultrasonic measurements are used in this work. In many ultrasonic scanning applications, a water bath is used where the ultrasonic transducer is held at a fixed distance, multiple ultrasonic wavelengths away from the part under inspection. If this coupling layer is thick enough that echoes within the layer can be time-resolved from echoes within the part under inspection, then the analysis of phase shifts in the couplant layer is greatly simplified. Instead of the complicated layer stack modeled in Section 4.4.1.4, the phase shift through the coupling medium can be simply modeled by Equation 4.1 using the sound velocity and thickness of the couplant.

4.6 Conclusions

A novel single-frequency ultrasonic phase measurement instrument has been built and tested to show its efficacy against conventional ultrasonic time-delay measurement methods. The instrument is digitally controlled and based on a CFPPLL design, which allows unprecedented frequency independent ultrasonic phase measurement resolution of to 0.00038 radians (0.022°) or one part in 6.1×10^{-5} of an ultrasonic wavelength. Ultrasonic phase can be tracked in real-time for measurement of material property changes due to external stimuli. Unlike previous PPLL-based ultrasonic phase measurement instruments, the system can change driving frequency while also maintaining the previous phase relationship, so swept-frequency phase measurements can be conducted with resolution as low as 3.55 μHz. This new feature allows absolute sound velocity or thickness measurements to be obtained in solid media, opening up this instrument to many new applications beyond simple phase or sound velocity monitoring, like previous PPLL instruments.

Using glass specimens, swept-frequency ultrasonic phase measurements from the CFPPLL instrument were compared with conventional, broadband ToF measurements from a pulser-receiver. After correcting for diffraction effects and factoring out the time-delay offset due to external sources, the CFPPLL phase measurements outperformed conventional ToF measurements in both accuracy and precision. Furthermore, CFPPLL phase measurements near 10 MHz outperformed much higher frequency 50 MHz ToF measurements. The slope of the phase vs. frequency line taken with the CFPPLL instrument was able to predict thickness with an average error of $-0.04\ \mu m$ and standard deviation of error of $1.35\ \mu m$, which was close to the calibrated micrometer's 1.06 μm uncertainty. Given a mean thickness of about about 10.95 mm, the mean thickness measurement error was -0.00037% of the total thickness and standard deviation of thickness measurement uncertainty was 0.012%. Additional studies showed the CFPPLL method produces a standard deviation of phase error of only 0.008° due to quantization error and system noise, in comparison to a phase error of 0.251° for high-resolution cross-correlation phase measurements using the same SNR as 26.1 dB and number of samples as 256.

The CFPPLL-based phase measurement instrument provides high-resolution, low-uncertainty ultrasonic time-delay measurements. Its digital control and waveform generation provide major improvements in both resolution and ease-of-use to previous PPLL-based ultrasonic phase measurement instruments. In addition to improving on conventional ToF methods of sound velocity or thickness measurements in solids or liquids, high-resolution swept-frequency phase measurements may have applicability in areas such as adhesive bond quality assessment, thin film characterization, and analysis of complex structures. Characterizing this method's ability to assess adhesive bond quality is the basis for the remainder of this work.

Chapter 5: Interface Quality Assessment by Ultrasonic Phase Measurements

In this chapter, the constant-frequency ultrasonic phase method is demonstrated for quality assessment of a single imperfect interface. First, the interface between a glass adherent and adhesive curable using UV light is monitored with ultrasonic phase throughout its cure process. From this assessment, two methods are developed for monitoring the change in interface quality at the interface between an adherent with high acoustic impedance and adhesive with lower acoustic impedance. Next, the dry-contact interface between metals are investigated with constant-frequency ultrasonic phase measurements, and interface stiffness changes are determined. It is demonstrated that regardless of the acoustic impedance values of the materials at an interface, the interfacial stiffness can still be assessed with this method. The experimental results in this chapter are all matched with theory developed in Chapter 3.

5.1 Single-Interface Adhesive Bond Strength Assessment

5.1.1 Experimental Setup

5.1.1.1 Bonded Joint Fabrication

Several bonded joints are fabricated and ultrasonically interrogated to investigate single-interface characterization with the ultrasonic phase measurement method. Smooth glass adherents are chosen to minimize experimental uncertainty arising from surface roughness and internal scattering in this study. For high control over adhesion quality, adhesive curable with ultraviolet (UV) light is chosen. So that echoes from the adherent/adhesive interface are easily time-resolved from echoes from the back-wall of the adhesive, a thick adhesive layer is used.

Schott Borofloat® 33 glass cut into 5.08 cm wide x 5.08 cm long x 1.10 cm thick coupons were purchased from the S. I. Howard Glass Company to be used as adherents. Norland Optical Adhesive (NOA) 63, a UV-curable adhesive, was obtained from Norland Products Inc. to be used for bonding. NOA 63 cures optimally via UV light with wavelengths 350-380 nm and requires about $4.5\ J/cm^2$ of energy for full cure. NOA 63 is chosen because of its high transmission of UV light in the 350-380 nm range, meaning that thick layers of adhesive may be used without a strong gradient in degree-of cure throughout the thickness of the layer.

The UV light source is a 5.08 cm x 15.24 cm Model 22-UV manufactured by Optical Engineering, Inc (now manufactured by Macken Instruments, Inc.) and uses a low-pressure mercury fluorescent bulb with UV phosphor and blue-tinted glass to suppress visible emission. The source emits light with a maximum intensity of $5\ mW/cm^2$ and wavelengths primarily between 340 nm and 390 nm, with peak emission at 360 nm, according to the manufacturer. Assuming the full intensity of light reaches the adhesive layer, it is estimated that an exposure time of 15 minutes is required to fully-cure the NOA 63 adhesive at $4.5\ J/cm^2$.

Prior to the application of adhesive, each glass coupon was cleaned with an ethanol wipe, a 60 minute ultrasonic cleaning bath in reagent grade ethanol, and vapor degreasing with ethanol. After drying, the adherent was placed into a special apparatus designed for this study so that the ultrasonic phase of the reflection coefficient could be monitored during UV light exposure.

5.1.1.2 Ultrasonic Phase Measurement Setup

The apparatus shown in Figure 5.1 is designed so the ultrasonic phase of the reflection coefficient at the adherent/adhesive interface could be monitored during the UV light curing process. The lower part of the apparatus, depicted in Figure 5.1a, holds the glass adherent in place with an ultrasonic transducer mounted underneath with Sono 600 ultrasonic couplant. A 6.35 mm diameter, broadband Olympus V112 ultrasonic transducer is used throughout this study. While not clearly shown in the image, the height of the lower part is slightly less than the height of the ultrasonic transducer. When load is applied to the apparatus, the load is transferred from the glass to the transducer to the underlying metal substrate.

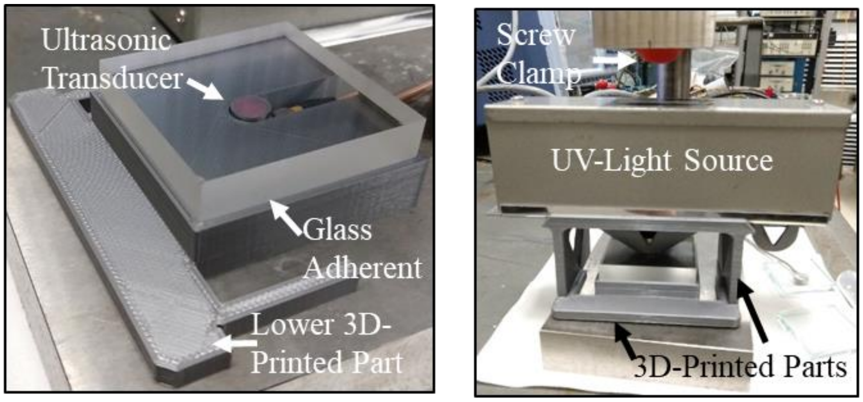

a) b)

Figure 5.1: Images of apparatus for monitoring phase shift during adhesive cure: a) lower part with ultrasonic transducer mounted underneath glass adherent, and b) UV-light source mounted on top of upper part resting on adherent

On top of the glass adherent is the second part of the apparatus, shown in Figure 5.1b, which has two functions. First, it acts as a reservoir for the liquid adhesive until it begins to cure. The upper part provides a circular opening 1.27 cm in diameter on top of the adherent with a vertical lip 3 mm in height. After the upper part is placed on the glass adherent surface, a reference ultrasonic measurement is obtained on the bare glass adherent. Next, drops of NOA 63 adhesive are applied to the glass surface until the height of the adhesive layer reaches the 3 mm lip of the upper part.

Next, the UV light source is placed on top of the upper part. A load cell is placed in-line between the UV source and a screw clamp above, so that the load on the ultrasonic transducer is measured. A constant load of ~133 N is applied to the ultrasonic transducer throughout this study to minimize phase uncertainty due to ultrasonic couplant layer thickness variations between experiments. A shutter is used to block light from reaching the adhesive layer when desired, seen protruding from under the UV source on the right side of Figure 5.1b.

Ultrasonic phase measurements are obtained using the constant-frequency pulsed phase-locked-loop (CFPPLL)-based method described in Chapter 4. After averaging over 64 phase samples, constant-frequency ultrasonic phase measurements are obtained every 0.384 s. The ultrasonic phase is sampled on the first echo from the adherent/adhesive interface. For each experiment, the ultrasonic phase is first measured on the bare glass adherent as a reference and then measured after the adhesive has been applied.

Two sets of experiments are performed to demonstrate the constant-frequency ultrasonic phase measurement method's ability to assess interfacial stiffness in the $Z_1 > Z_2$ case. First, broadband ultrasonic pulses are used to assess the acoustic time-of-flight (ToF) in the adhesive layer as a function of UV-light exposure time. At different time intervals during the cure process, the UV light source is blocked and the joint is evaluated with a broadband ultrasonic pulse from a GE Panametrics Model 5900PR pulser-receiver. A LeCroy WaveRunner 6200 oscilloscope captures echoes from the bonded joint. The broadband pulse has a pass-band of $1\ kHz - 200\ MHz$, a pulse energy of $4\ \mu J$, and is amplified by $42\ dB$ prior to being received.

From the ToF, bulk sound velocity in the adhesive is computed to be later used to separate sound velocity and acoustic impedance induced phase shifts from interfacial stiffness induced phase shifts. To verify that the sound velocity in the adhesive during cure does not appreciably change for different bondline thicknesses due to UV-light passing through the adhesive layer, the experiment is conducted for three different bondline thicknesses. An additional experiment is performed with a block of acrylic in line between the UV-light source and adhesive layer to reduce the intensity of UV-light reaching the adhesive and slow the cure process.

A study is also conducted to demonstrate the phase maximum's dependence on K_0. At 10 MHz, the ultrasonic phase is tracked as a function of UV-exposure time. For comparison, a second phase-tracking experiment is performed where a block of acrylic is used to reduce the UV light intensity reaching the adhesive layer during the curing process. It is predicted that this will result in an increase of the peak phase time, as the time it takes for the interfacial stiffness to reach K_0 will be increased.

5.1.2 Results and Discussion

5.1.2.1 Sound Velocity Measurement as Function of UV Exposure

Figure 5.2 shows the measured amplitude vs. time data from broadband ultrasonic pulse echoes within one of the standard UV-light intensity bonded joints. Note, the back wall echoes from the adhesive layer both decrease in ToF and increase in amplitude as UV-light exposure time increases. The ToF decreases during cure because of an increase in the elastic modulus of the adhesive. Adhesive stiffening results in an increase of the sound velocity in the adhesive due to the relationship between sound velocity and elastic modulus, $c = \sqrt{E/\rho}$, where c is sound velocity, E is longitudinal elastic modulus, and ρ is mass density.

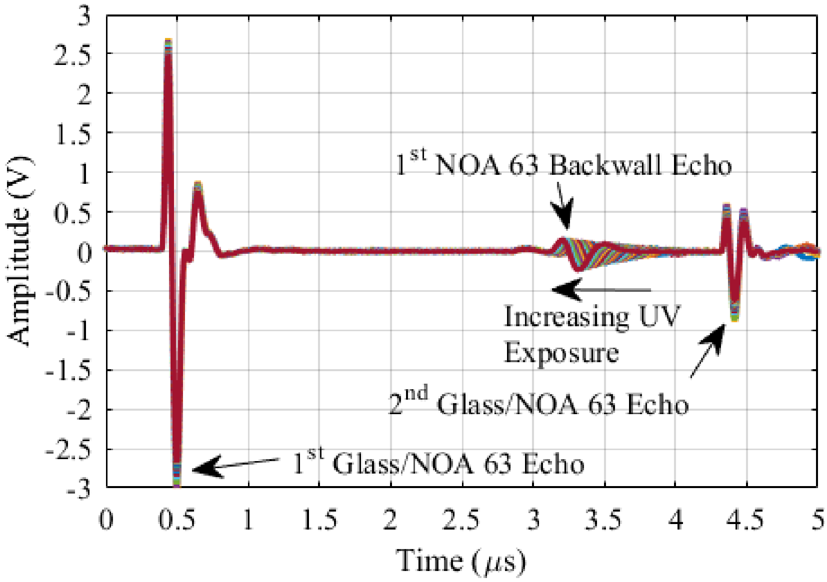

Figure 5.2: Amplitude vs. time of bonded joint reflections for varying UV-light exposure times with standard UV-intensity with 3.227 mm thick bond line

After the four bonded joints were cured, the bond line thickness of each joint was measured with a micrometer 8 times each and averaged. Table 5.1 shows the mean bond line thickness plus or minus one standard deviation for each bonded joint in this ToF measurement study.

Table 5.1: Measured bond line thickness of each bonded joint used for time-of-flight assessment after 60 minutes of UV-light exposure

Specimen	Measured Bond line Thickness: $\boldsymbol{Mean \pm Std.Dev.(mm)}$
Std. Intensity, #1	0.781 ± 0.010
Std. Intensity, #2	1.383 ± 0.011
Std. Intensity, #3	3.227 ± 0.021
Lower Intensity	1.802 ± 0.006

The ToF within the adhesive layer was determined from the time of the minimum amplitude of the first reflection from the NOA 63 back-wall minus the time of minimum amplitude from the first reflection from the glass/NOA 63 interface. For the thickest bond line, denoted “Std. Intensity, #3” in Table 5.1, it was difficult to obtain good ToF measurements for low UV-light exposure times, as the amplitude of reflection of from the back-wall of the adhesive is initially very low for the first minute or two of cure. Consequently, the measured peak position of the echo from the back-wall of the adhesive layer is more uncertain for these low UV-light exposure times but not for the remainder of the curing process.

Combined with the measured bond line thicknesses, the relation $c = 2L/ToF$ is used to compute the sound velocity in the adhesive as a function of UV exposure time, where L is the bond line thickness and c is the sound velocity. Figure 5.3 displays the computed sound velocity as a function of UV-light exposure time for each bonded joint.

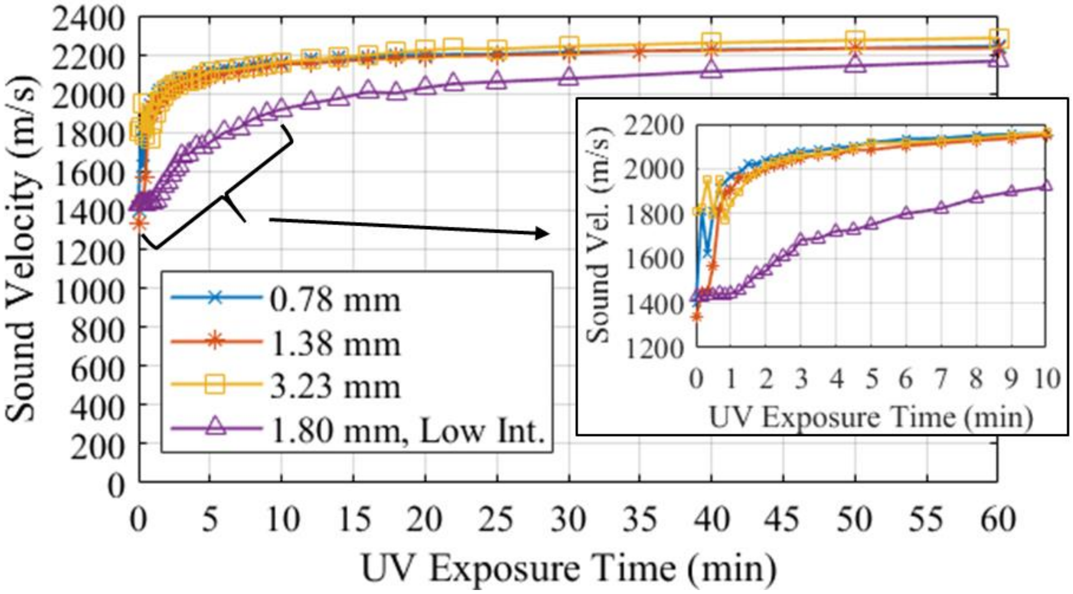

Figure 5.3: Sound velocity vs. UV-light exposure time for different UV-light intensities: standard intensity with 0.78 mm bond line thickness (blue crosses), standard intensity with 1.38 mm bond line thickness (red asterisks), standard intensity with 3.23 mm bond line thickness (yellow squares), and lower intensity with 1.80 mm bond line thickness (purple triangles)

From Figure 5.3, it is first noted that there is no noticeable difference in sound velocity depending on bond line thickness, as the standard intensity sound velocities are very similar throughout UV-light exposure time. Also, it is noted that for both standard and lower UV-light intensities, the sound velocities begin around $1400\ m/s$ in the un-cured state, with the exception of the $3.23\ mm$ thick bond line specimen, which is more easily seen in the inset of Figure 5.3.

As previously mentioned, there is much uncertainty in ToF for the first minute or so of UV-exposure for the thickest bond line specimen, which results in uncertainty in the computed sound velocity. A higher bond line thickness allows for more attenuation of the ultrasonic waves passing through the adhesive layer, resulting in a lower magnitude of the reflection coefficient. It is thus theorized that the low amplitude of reflection from the back wall of the adhesive in the $3.23\ mm$ thick bonded joint prevents the accurate measurement of sound velocity in the first minute or so of UV-light exposure. This results in the measured difference in sound velocity at 0 minutes of UV-light exposure, where there should otherwise be no difference.

Throughout the curing process, the sound velocity in the lower intensity joint lags behind the sound velocity in the standard intensity joints. Within the first 10 minutes of UV-light exposure, the sound velocity under standard UV-light exposure increases much more quickly than in the bonded joint with acrylic blocking the light source. This is consistent with the acrylic block lowering the intensity of light reaching the adhesive and thus slowing the curing process.

After 60 minutes of UV-light exposure, the $3.23\ mm$ thick standard intensity joint had an adhesive sound velocity of $2{,}285\ m/s$, and the lower intensity joint had an adhesive sound velocity of $2{,}167\ m/s$. As the lower intensity joint still had not reached the sound velocity of the standard intensity joints after 60 minutes, it was allowed to continue to cure. After 180 minutes of UV light exposure, the lower intensity joint finally displayed an adhesive sound velocity of $2{,}259\ m/s$, meaning it had approximately reached the same degree-of-cure as the standard intensity bonded joint.

5.1.2.2 Ultrasonic Phase Measurement Results

Figure 5.4 shows the measured ultrasonic phase at 10 MHz of the first echo from the glass/adhesive interface throughout curing of the adhesive for the standard UV-light intensity joint as well as the lower UV-light intensity joint, where an acrylic block reduces the light intensity reaching the adhesive. The phase shown here is the phase measurement of the first echo from the adherent/adhesive interface minus the reference phase measurement on the un-bonded glass adherent to factor out the phase shift due to propagation through the adherent. Again, these measurements were obtained at every $0.384\ s$ after averaging phase measurements over 64 samples, which is why the measurements are plotted continuously. The inset of Figure 5.4 shows the peaks of the phase curves, showing how phase varies in the first 10 minutes of cure.

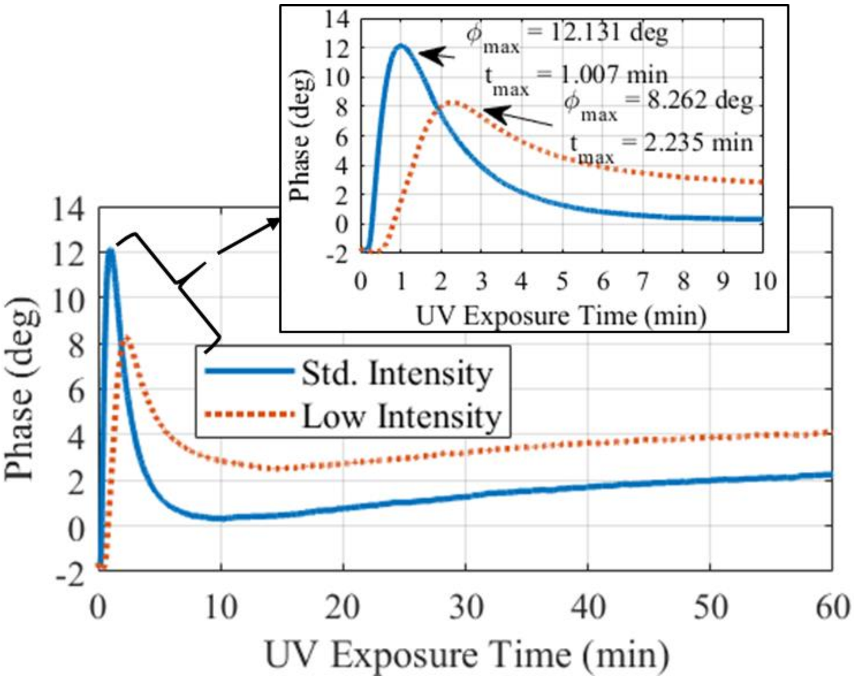

Figure 5.4: Measured phase at 10 MHz vs. UV exposure time for standard light intensity (blue, solid) and lower light intensity on adhesive (red, dotted)

Notably, the phase at 0 minutes of UV-light exposure begins near $-2\ deg$. The phase being below zero is likely caused by the presence of acoustic attenuation in one or both materials at the interface, as $\phi_{R_1} \geq 0\ deg$ in Equation 3.9 when $Z_1 > Z_2$ for all values of K without attenuation present. Additionally, the continued increase of ultrasonic phase after about 10 minutes of UV-light exposure is not predicted by a steady increase of interfacial stiffness. It is thought that this increase is related to changing acoustic attenuation caused by additional molecular cross-linking in the adhesive as a function of UV-light exposure. Other processes taking place in the adhesive during cure, such as shrinkage, are not assessed with this measurement, because the received tone-burst does not propagate through the adhesive layer.

5.1.2.2.1 Interfacial Stiffness Threshold Assessment

As predicted by theory in Section 3.1.2, there exists a peak phase at some point in the curing process at a particular interfacial stiffness value. Theory suggests the interfacial stiffness constant at which this peak occurs is a function of ultrasonic frequency and the acoustic impedances of the materials in contact at the interface. Without using the measured acoustic sound velocity as a function of UV-exposure time, the acoustic impedance of the adhesive and the interfacial stiffness constant at the peak phase time is computed using Equations 3.11 and 3.12. First, Equation 3.12 is solved for the unknown Z_2, given by Equation 5.1.

$$Z_2 = Z_1 \sin\big(max\big(\phi_{R_1}\big)\big) \tag{5.1}$$

From Equation 5.1, the acoustic impedance in the adhesive at the peak phase time is computed to be $Z_2 = 2.46\ MRayl$ for the standard intensity joint and $Z_2 = 2.04\ MRayl$ for the lower intensity joint. Next, Equation 3.11 is used to find unknown interfacial stiffness at the peak phase time: $K_0 = 1.58 \times 10^{14}\ N/m^3$ for the standard intensity bonded joint, and $K_0 = 1.30 \times 10^{14}\ N/m^3$ for the lower intensity bonded joint. Using this method, ultrasonic phase tracking can be used to find when the interfacial stiffness – an analog for bond quality – has crossed some threshold value. This method also works in situations where the bulk properties of the adhesive layer are changing, as the acoustic impedance at the phase peak position can be computed given knowledge of the acoustic impedance of the adherent. Furthermore, the threshold interfacial stiffness can be chosen by the driving ultrasonic frequency. If a higher threshold is desired, a higher frequency tone-burst may be used; however, such higher frequencies may attenuate quickly in certain adherent media.

5.1.2.2.2 Determination of Interface Stiffness from Phase Shifts

To further study the ultrasonic phase measurement results, the measured adhesive sound velocity as a function of UV-exposure time is used to model how changing interfacial stiffness affects the ultrasonic phase. The acoustic impedance in the adhesive over time is computed, and the theoretical maximum phase of the reflection coefficient from Equation 3.11 is plotted in Figure 5.5 as a function of UV-light exposure. Additionally, the measured maximum phase values from the two bonded joints in this study are plotted in Figure 5.5. Figure 5.5 shows that the measured phase maximum values match closely with the calculated value.

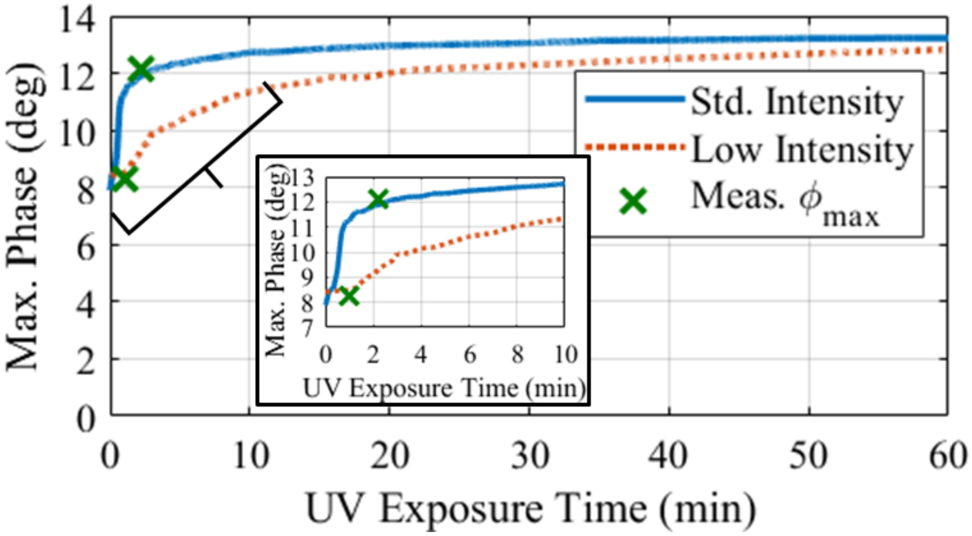

Figure 5.5: Calculated phase maximum vs. UV exposure time based on adhesive sound velocity measurements for standard light intensity (blue, solid) and lower light intensity (red, dotted), including measured phase maximum values (green crosses)

Given knowledge of the acoustic impedance in the adhesive, the interfacial stiffness throughout the curing process can be estimated from the constant-frequency ultrasonic phase measurements. The phase response to different interfacial stiffness constants using the phase of Equation 3.5 is plotted as a function of UV-light exposure time in Figure 5.6 for both light intensity setups. Both surface plots appear similar, with the largest differences occurring for low UV-light exposure times.

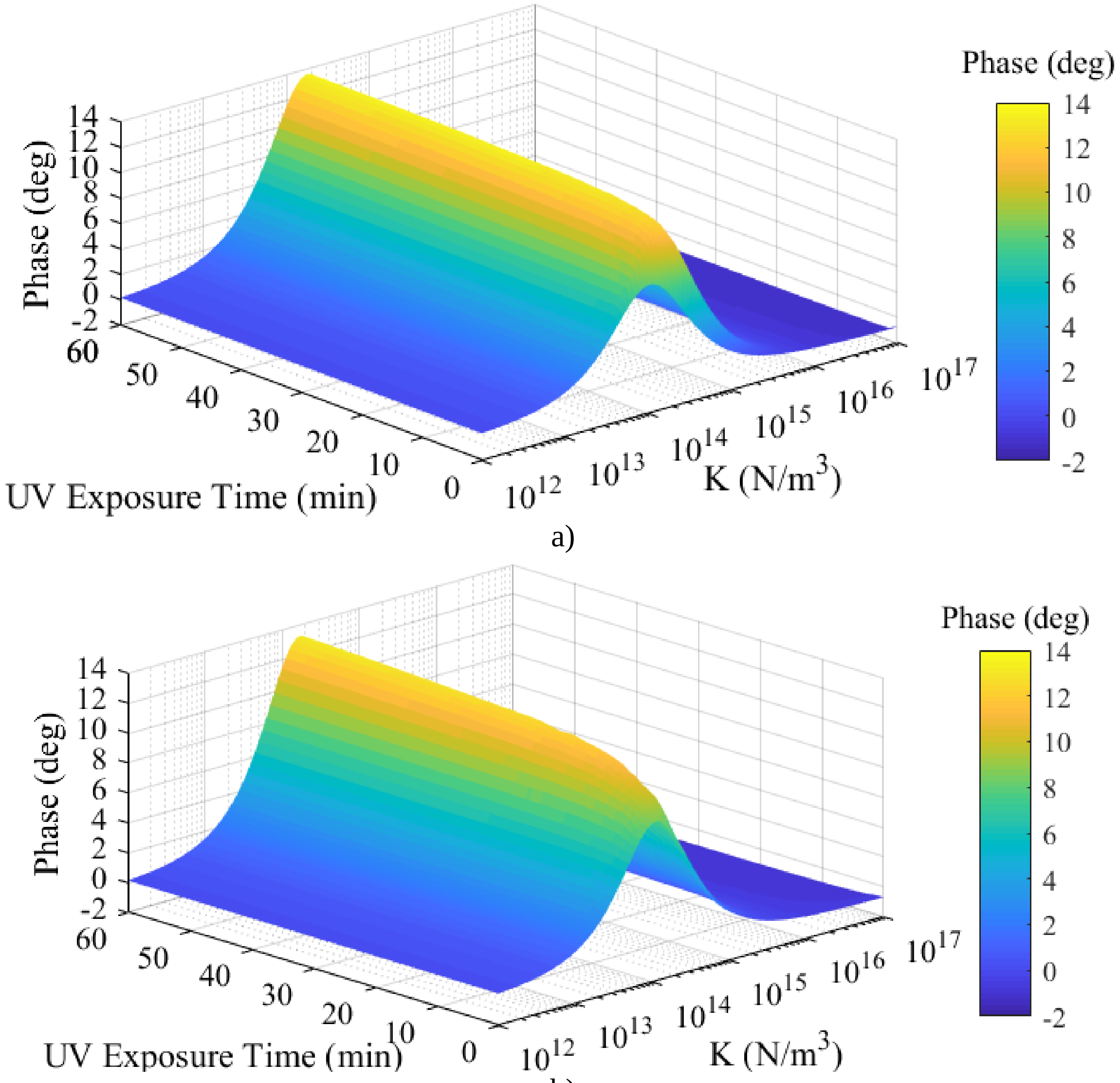

a)

b)

Figure 5.6: Surface plot of theoretical phase vs. interfacial stiffness constant throughout adhesive cure process for a) standard light intensity bonded joint and b) lower light intensity bonded joint

An inverse algorithm is used to find the interfacial stiffness from the phase curves in Figure 5.4, combined with the modeled phase responses in Figure 5.6. For each UV-light exposure time, the closest modeled phase to each measured phase value is found, and the corresponding interfacial stiffness producing that phase value is obtained. It is assumed that the interfacial stiffness constant below K_0 from Equation 3.11 are possible values in the time before the measured phase reaches its peak and K values above K_0 are possible values in the time after the measured phase peak. This assumption allows the algorithm to pick the more reasonable interfacial stiffness from the two possible K values seen in Figure 6.6. The extracted interfacial stiffness values from the measured phase responses as a function of UV-light exposure are plotted in Figure 5.7.

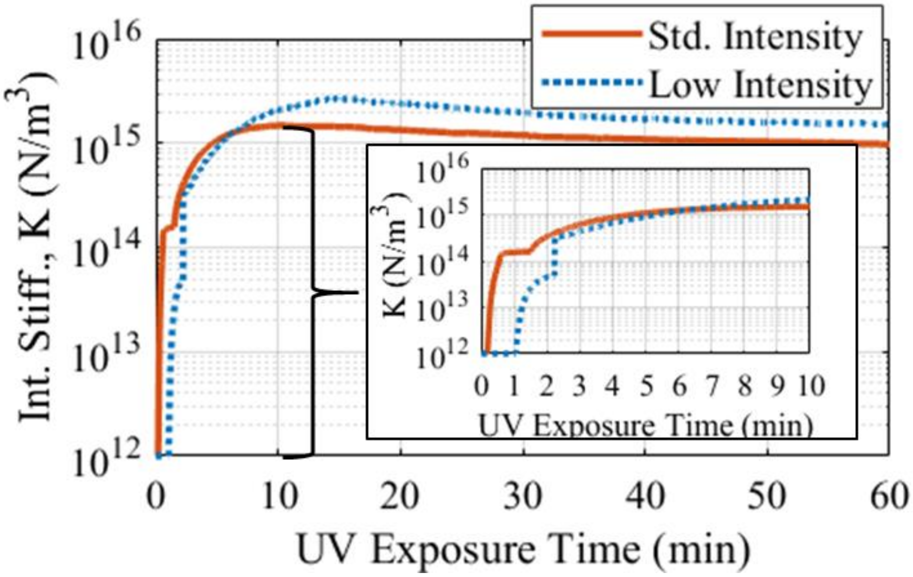

Figure 5.7: Predicted interfacial stiffness constants from measured phase at 10 MHz on glass/UV-curable adhesive joints with standard light intensity and lower light intensity

As shown in Figure 5.7, the interface stiffness of the bonded joint with lower incident UV-light intensity lags behind the standard intensity bonded joint over the first few minutes of curing. It is also notable that the extracted interfacial stiffness of the lower-intensity bonded joint increases above the interfacial stiffness of the standard intensity bonded joint after about 6 minutes. This effect occurs due to the increase in phase shift after about 10 minutes of cure, as shown in Figure 5.4. With only interface stiffness increasing, the phase continues to decrease down to 0 deg as the adhesive continues to cure. However in both bonded joints, the phase has some minimum value, after which it begins to increase slowly. As previously postulated, this effect is thought to be caused by a change in acoustic attenuation in the adhesive during cure. It is not expected that the interfacial stiffness of the lower-intensity bonded joint passes that of the standard intensity joint, but it is instead thought to be caused by un-modeled changes in acoustic attenuation.

There are notable jump discontinuities seen in both interfacial stiffness curves: a horizontal period appears in the standard intensity joint and a vertical period appears in the lower intensity joint. These discontinuities are caused by the measured peak phase shifts being slightly above or below the modeled values, as shown in Figure 5.5. It is thought that the modeled peak phase values could be slightly off due to slight errors in sound velocity measurements at a given UV-exposure time. As the sound velocity changes very quickly in the initial few minutes of cure, very small differences in time cause a large shift in sound velocity.

The sound velocity measurements in Figure 5.3 and interface stiffness measurements in Figure 5.7 both confirm the original predicted UV-exposure time of 15 minutes to reach full cure with the standard UV-light intensity. In both measurements, the values begin leveling off around 10 minutes of cure and vary only slightly between 15 minutes and 60 minutes of UV-light exposure. This further confirms that the ultrasonic measurement results agree well with the adhesive manufacturer’s specifications on curing.

Ultimately, the inverse method for determining interfacial stiffness from constant-frequency ultrasonic phase monitoring could be improved by using a higher UV-exposure time resolution to improve the accuracy of sound velocity measurements at a given time. Additionally, a thorough treatment of acoustic attenuation in the adherent and adhesive would provide more accurate interfacial stiffness measurements.

5.2 Single-Interface Dry-Contact Quality Assessment

5.2.1 Background

A study was devised to demonstrate the ability of the constant-frequency ultrasonic phase measurement method to assess interfacial stiffness in a variety of different material setups. In Section 5.1, adherent/adhesive interface stiffness was characterized from the adherent side of the interface, making the acoustic impedance mismatch at the interface to be of the form $Z_1 > Z_2$. While practically applicable in a wide variety of scenarios, including bond quality of thick adhesive layers as well as coatings on a substrate, this is the most difficult material setup for interfacial stiffness characterization with ultrasonic phase, since good and bad bonds give the same phase shift of the reflection coefficient.

The other two acoustic impedance mismatch scenarios -- $Z_1 < Z_2$ and $Z_1 = Z_2$ – are encountered in practice, as well. First, the $Z_1 < Z_2$ scenario is applicable in bond quality assessment of coatings on a substrate when measuring from the coating side. Most often, the coating will be made from some polymer with a lower acoustic impedance than the usually metal underlying substrate. In this case, there is an expected 180° phase difference between good bonding and a complete disbond, as shown in Figure 3.2. This setup has been studied for coating adhesion quality by laser-ultrasonic methods [79], [80].

Second, the $Z_1 = Z_2$ setup is found in diffusion bonds and in metal welds. Diffusion bonds, where two materials (commonly metals, especially titanium) are joined by applying heat and pressure to diffuse atoms from both materials together without melting, have been previously studied with broadband pulse-based ultrasonic measurement techniques [75], [76], [77], [78]. Similarly, inertia and friction welds have been studied with ultrasonic reflection measurements from both sides of the interface [69]. In another application with $Z_1 = Z_2$, a broadband pulse ultrasonic phase method was used to determine the thickness of an oil film layer between two glass plates by modeling the oil layer as a interfacial spring boundary [133].

In this study, metal coupons are placed in contact and compressively loaded while the constant-frequency ultrasonic phase response of the interface between the two solids is monitored. As compressive load is increased, the interface between the two solids becomes more able to transmit ultrasound, and the interfacial stiffness is varied from very low to very high values. This setup is sometimes called "simulated kissing bonds" in the literature. Here, aluminum and steel coupons are chosen for their different acoustic impedance values, and the ultrasonic phase method of interface characterization is demonstrated for all acoustic impedance mismatch conditions: $Z_1 > Z_2$, $Z_1 < Z_2$, and $Z_1 = Z_2$. Both rough and smooth coupons are used in this study, as smooth surfaces should more-easily transmit ultrasound when the coupons are under compressive load. In this simulated kissing bond study, the measurement of interfacial stiffness is simplified in comparison to the previous study involving bonding with a UV-curable adhesive, as the acoustic impedance of both media at the interface should stay constant throughout the experiment.

5.2.2 Experimental Setup

To examine interface stiffness with ultrasonic phase, two sets of 3.81 cm wide x 3.81 cm long Al 6061-T651 and A36 steel coupons were fabricated. The first set is 3.81 cm in height and was left with the as-manufactured surface roughness, while the second set is 0.79 cm in height and was hand-sanded and polished to a near-mirror finish. It was hypothesized that the smooth coupons would transmit ultrasound more easily when placed in contact, and thus the measured interfacial stiffness would increase much more quickly as a function of compressive load.

The as-manufactured surfaces in this study were measured with an optical profilometer to have an RMS surface roughness of $2.45\ \mu m$ for the Al 6061 coupons and $3.70\ \mu m$ for the A36 steel coupons. For the coupons that were hand-sanded and polished, the RMS surface roughness was $247\ nm$ for the Al 6061 coupons and $112\ nm$ for the A36 steel coupons. Figure 5.8 shows contour plots on the as-manufactured and polished coupons made from Al 6061 and A36 steel used in this study.

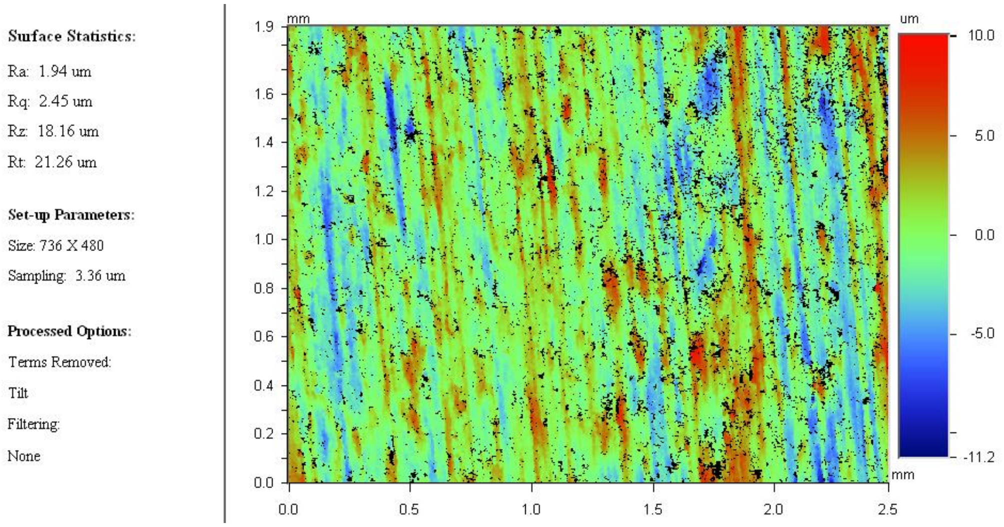

Surface Statistics:

Ra: 1.94 um

Rq: 2.45 um

Rz: 18.16 um

Rt: 21.26 um

Set-up Parameters:

Size: 736 X 480

Sampling: 3.36 um

Processed Options:

Terms Removed:

Tilt

Filtering:

None

a)

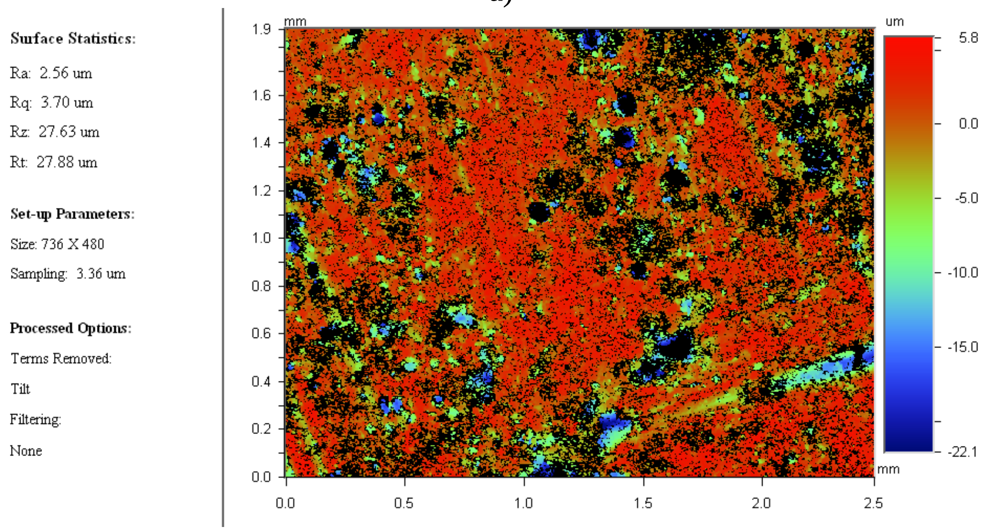

Surface Statistics:

Ra: 2.56 um

Rq: 3.70 um

Rz: 27.63 um

Rt: 27.88 um

Set-up Parameters:

Size: 736 X 480

Sampling: 3.36 um

Processed Options:

Terms Removed:

Tilt

Filtering:

None

b)

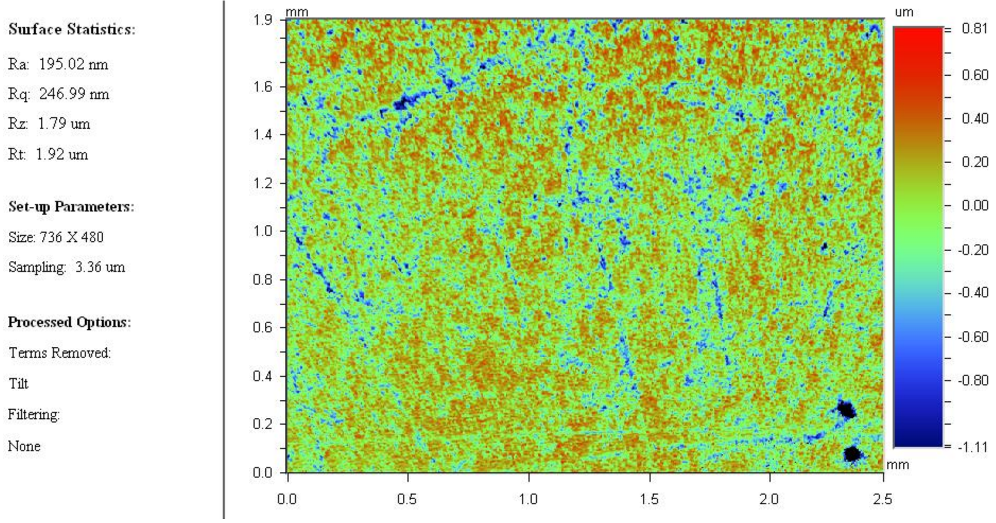

Surface Statistics:

Ra: 195.02 nm

Rq: 246.99 nm

Rz: 1.79 um

Rt: 1.92 um

Set-up Parameters:

Size: 736 X 480

Sampling: 3.36 um

Processed Options:

Terms Removed:

Tilt

Filtering:

None

c)

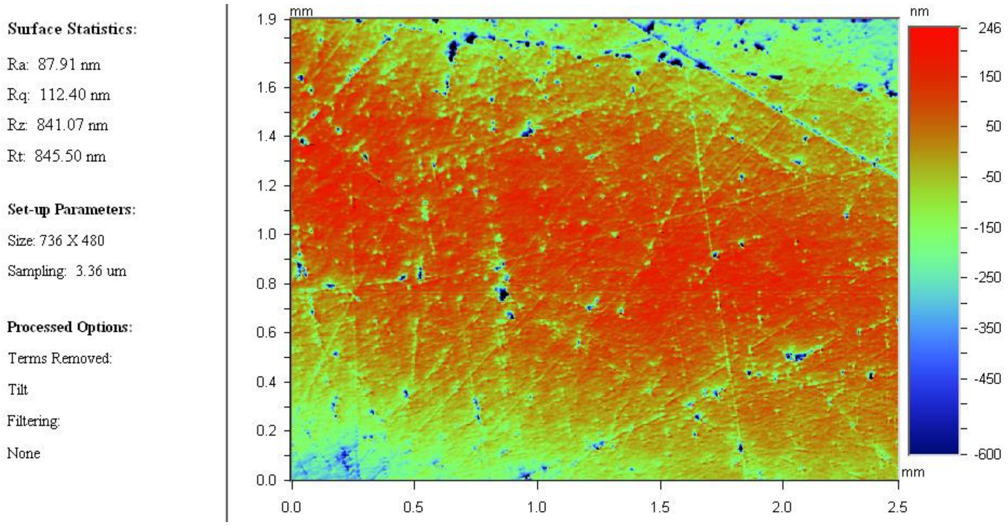
Surface Statistics:

Ra: 87.91 nm

Rq: 112.40 nm

Rz: 841.07 nm

Rt: 845.50 nm

Set-up Parameters:

Size: 736 X 480

Sampling: 3.36 um

Processed Options:

Terms Removed:

Tilt

Filtering:

None

d)

Figure 5.8: Optical profilometry contour plots for a) as-manufactured Al 6061 coupon, b) as-manufactured A36 steel coupon, c) polished Al 6061 coupon, and d) polished A36 steel coupon

Compression loading of the Al 6061 and A36 steel surfaces were conducted in an MTS Alliance RT/100 electromechanical load frame. Each set of coupons were compressed at a displacement rate of 5 $\mu m/s$ until a load of 90 kN was reached, which is near the upper limit for the load frame. At 90 kN, the pressure at the interface is about 60 MPa based on the cross-sectional area of the coupons in this study.

The ultrasonic phase of the reflection coefficient at the interface between the contacting solids is measured using the CFPPLL method described in Chapter 4. The phase of the reflection coefficient is monitored in real-time at a driving frequency of 9.0 MHz and with a phase sampling rate of 10.4 Hz after averaging. At the beginning of each experiment, the phase is locked to zero on the first echo from the interface. Then, any changes from zero are tracked as a function of interfacial loading.

So that ultrasonic measurements could be obtained in-situ during compressional loading, a 1.27 cm wide notch was milled into metal block with the same cross-sectional area of the metal coupons in this study. A rubber half-sphere was adhered within the notch to provide a highly compressible resting point for the ultrasonic transducer. The height of the notch and rubber half-sphere were chosen so that the ultrasonic transducer barely extends past the end of the notch with no load. After about 440 N of compressive load is applied, the rubber half-sphere has compressed enough that the path of the load is no longer passing through the transducer, and the load on the transducer no longer increases with higher compressive loads. As such, each experiment in this study begins with a 440 N pre-load to provide a consistent starting point for the ultrasonic phase measurements. Figure 5.9 shows a diagram and an image of the experimental setup, where the ultrasonic transducer is placed in-line with the compressive load so that the ultrasonic phase of the reflection coefficient from the interface can be monitored.

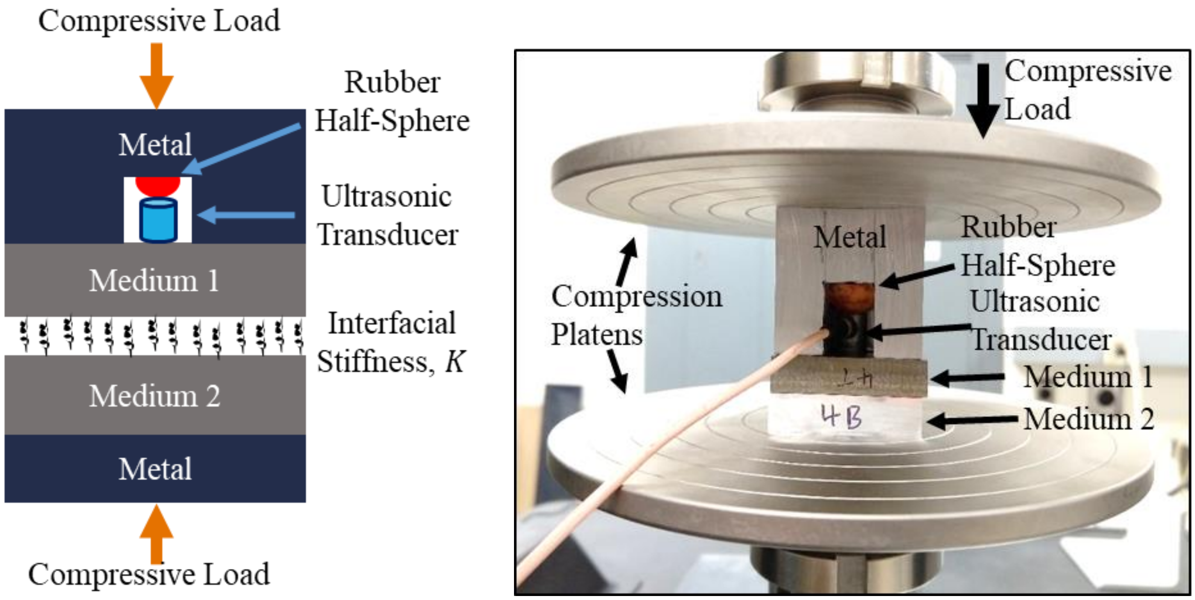

a) b)

Figure 5.9: a) Diagram of ultrasonic phase monitoring of metal coupons in dry contact during compressive loading, and b) Image of experimental setup with ultrasonic transducer monitoring phase of interface reflections during compression loading

5.2.3 Results and Discussion

5.2.3.1 Mechanical Testing

Figure 5.10 shows the measured compressive load vs. displacement curves for each acoustic impedance mismatch setup, as well as for both rough and smooth contacting surfaces. Most notable here is the fact that all load curves appear very similar for the same constant displacement rate of $5\ \mu m/s$. In each dry-contact joint, there is an initial region of slow load increase followed by a long linear region of load increase. There is no significant difference in the dry-contact joints detectable from the mechanical load vs. displacement curves.

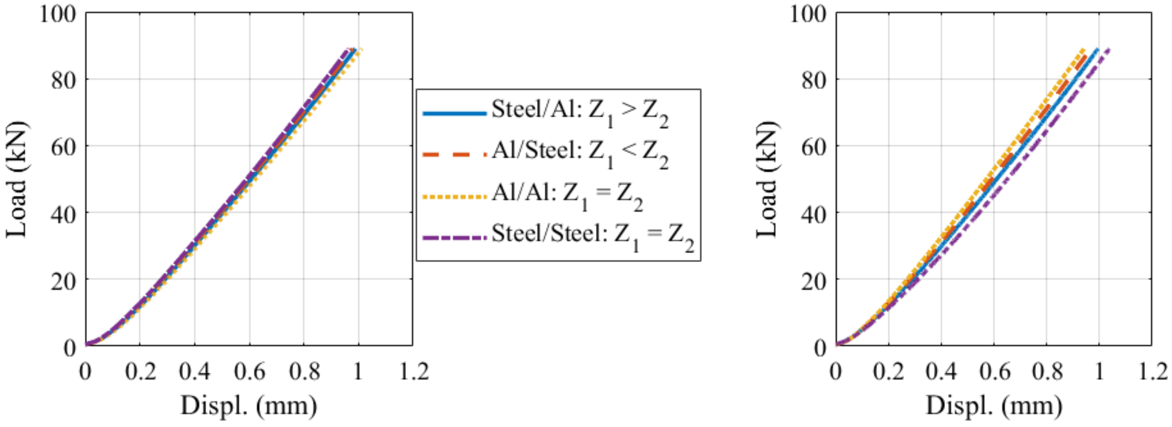

a) b)

Figure 5.10: Load vs. displacement curves for a) coupons with rough surfaces and b) coupons with smooth surfaces

5.2.3.2 Ultrasonic Phase Monitoring

Figure 5.11 shows the measured phase as a function of load for both the rough and smooth coupons. For the rough specimens, the measured phase response is mostly linear after about 10 kN. When steel is directly probed with either steel or Al underneath, the linear phase response is essentially the same. Likewise, when Al is directly probed with either steel or Al underneath, the linear phase response is essentially the same. From this, it is concluded that the phase shifts on highly roughened specimens is almost entirely assessing the compressive strain in the coupons with no phase response due to the interface. An increase in phase of the reflection coefficient corresponds with a shortening of the path length traveled by the ultrasonic waves. With this conclusion in mind, it also makes sense that the phase slope when probing steel is less than the phase slope when probing Al, since the elastic modulus of steel is much greater than the elastic modulus of Al.

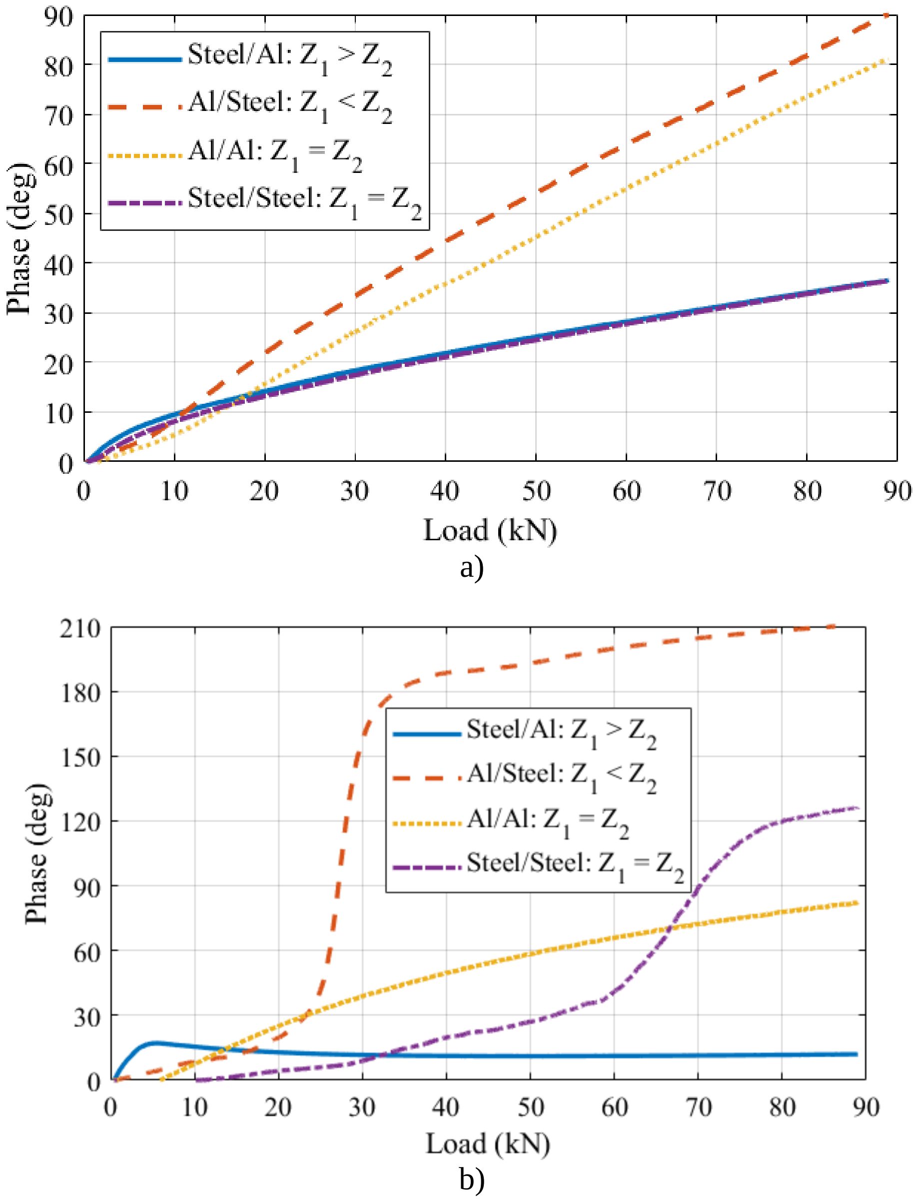

Figure 5.11: Measured phase at 9 MHz vs. load for each acoustic impedance mismatch scenario for coupons with a) rough surfaces and b) smooth surfaces

In contrast to the rough surface coupons, in the phase responses from the smooth coupons vary in a non-linear way with respect to compressive load, as shown in Figure 5.11b. Note, the thickness of the smooth surface coupons is about 1/5 of the thickness of the rough surface coupons, so the effect of strain on the phase measurement is suppressed in this data. It should be noted that for the Al/Al and steel/steel joints, there was very little amplitude of reflection as the load passed above 50-60 kN. This makes sense, because as K increases in the $Z_1 = Z_2$ case there is a higher intensity of ultrasound transmitted through the interface and a lesser amount reflected. As such, the phase data above about 60 kN is more uncertain than the rest of the plotted data for the smooth coupons.

Of immediate interest is the fact that the phase response to load is shown to depend on the acoustic impedance mismatch of the material at the interface. To better factor out the measured phase shifts due to compressive strain from the phase shifts due to interfacial stiffness changes, the phase response from the rough coupons -- which exhibited phase shift almost entirely due to strain – were subtracted out of the phase response from the smooth coupons after scaling the phase responses for coupon thickness. The resulting phase responses, primarily due to interfacial stiffness changes during compression loading, are shown in Figure 5.12.

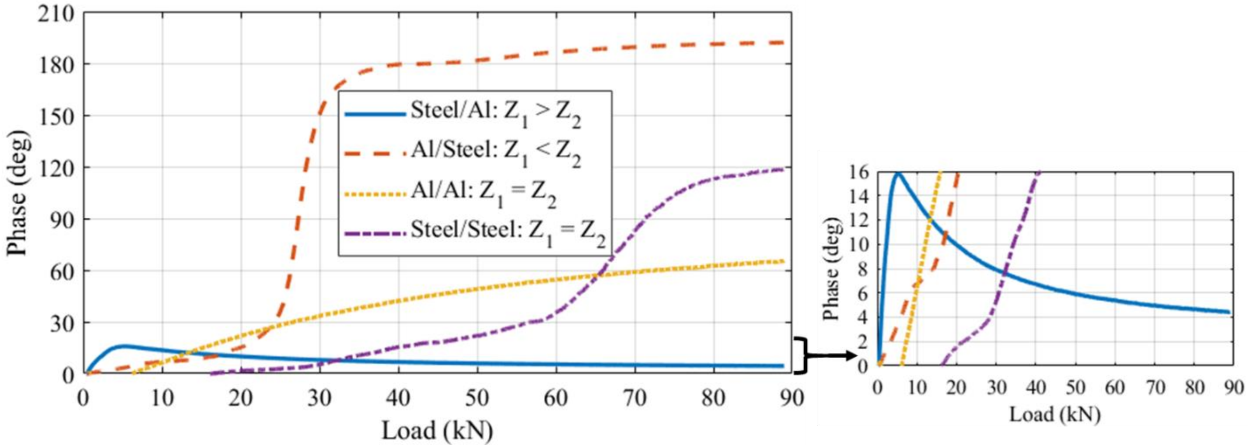

Figure 5.12: Phase at 9 MHz of reflection coefficient vs. load for smooth surface coupons with phase response due to strain subtracted out

5.2.3.3 Measurement of Interfacial Stiffness

The measured results in Figure 5.12 are compared to the theoretical results in Figure 5.13 for constant frequency phase measurements of the reflection coefficient as a function interfacial stiffness in the three different acoustic impedance mismatch scenarios. Note, the location of peak phase for the $Z_1 > Z_2$ case, seen in Figure 5.13, is higher than that of the $Z_1 > Z_2$ case for an Al/epoxy joint as shown in Figure 3.2 due to closer acoustic impedance matching between steel and Al.

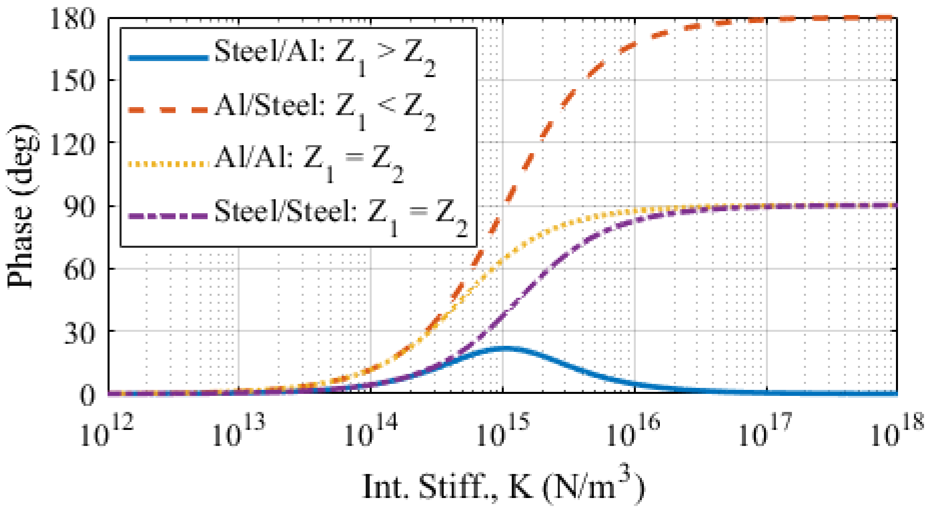

Figure 5.13: Theoretical phase of reflection coefficient vs. interfacial stiffness for interfaces between Al and steel

First, the Al/steel joint undergoes about 180 deg of phase shift over the course of compression loading as was predicted for the $Z_1 < Z_2$ case. At loads above about 50 kN, the phase increases above 180 deg, indicating there still may be a small amount of phase change due to strain remaining in the plotted data.

Second, the Al/Al and steel/steel joints change from 0 deg at no load to about 60 deg for the Al/Al joint and about 120 deg for the steel/steel joint. It was predicted that when $Z_1 = Z_2$, interfacial stiffness will increase from 0 deg for no bonding to 90 deg for good bonding. While on average the Al/Al and steel/steel joints ending phase was about 90 deg, there is much uncertainty in that number. As previously mentioned, there is very little amplitude of reflection for high loads in these two joints, which added phase measurement uncertainty. For the steel/steel joint that had its phase increase above the predicted value of 90 deg, it is thought that there is some leftover phase shift due to strain causing this phase shift. Meanwhile, it is thought that the phase response of the Al/Al joint would continue to increase if the load frame were capable of higher compression loads in this study. To better study the $Z_1 = Z_2$ case, reflection phase measurements may be combined with amplitude measurements or through-transmission pitch-catch phase measurements. Alternatively, reflection phase measurements from the back wall of the lower coupon may be used, which allows ultrasound to transmit through the interface twice before being received.

Finally, in the steel/Al joint, a bad interface and a good interface both look very similar with a peak phase value, as predicted. The inset in Figure 5.12 shows a zoomed in version of the plot, highlighting the peak phase shift observed in the steel/Al joint where $Z_1 > Z_2$. After the peak phase, the phase slowly decreases toward 0 deg as is predicted. This result supports the conclusion in Section 0 from the measured phase response during adhesive cure. In Figure 5.4, it was observed that the phase increased slowly after dropping after the initial phase peak, which was not predicted by the model assuming interfacial stiffness continues to increase with increased cure time. It was hypothesized that the phase increased in the adhesive joint, rather than dropping asymptotically toward 0 deg, due to un-modeled acoustic attenuation changes in the adhesive during cure. In this study where acoustic attenuation is not changing during compression loading, the phase is found to drop asymptotically toward 0 deg, as predicted.

Rather than conducting a curve-fitting method of the measured phase curves in Figure 5.12 to the theoretical phase curves in Figure 5.13, the interfacial stiffness for a given ϕ_R is found analytically so that the measured phase values can be substituted directly to find K. More specifically, Equation 3.9 is solved for K in terms of ϕ_R, which is then written in Equation 5.2 in the general form and in Equation 5.3 in the special case that $Z_1 = Z_2$. As K used in this work must be logically positive and real-valued due to physics, the appropriate choice of plus or minus in

Equation 5.2 must be made to make sure $K \geq 0\ N/m^3$ and is not complex. Figure 5.14 shows the interfacial stiffness constant for a given measured phase of the reflection coefficient, as predicted by Equation 5.2 and Equation 5.3.

$$K = \frac{\omega Z_1 Z_2 (Z_2 \pm \tan(\phi_R)\sqrt{Z_2^2 \csc(\phi_R) - Z_1^2}}{(Z_1^2 - Z_2^2)\tan(\phi_R)} \tag{5.2}$$

$$K = \frac{\omega Z_1 \tan(\phi_R)}{2} \tag{5.3}$$

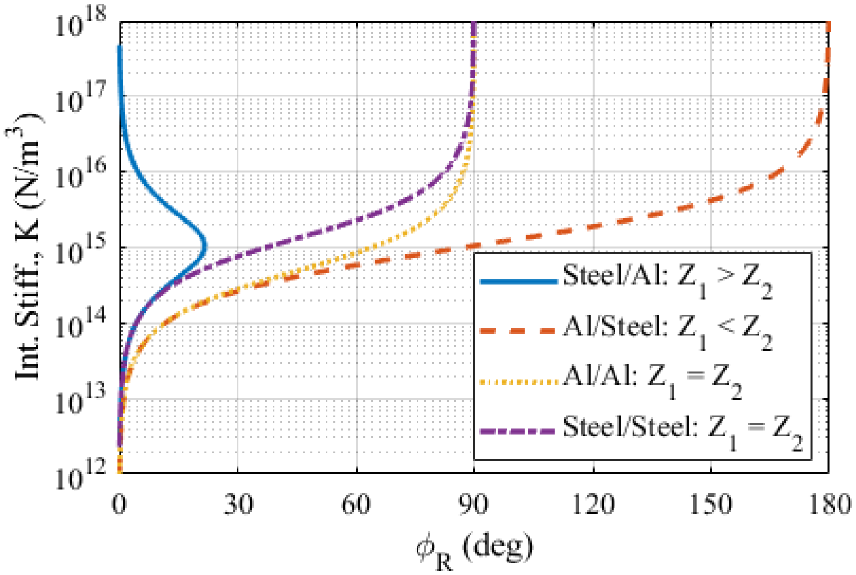

Figure 5.14: Theoretical interfacial stiffness vs. phase at 9 MHz of reflection coefficient for different Al and steel interfaces

In the case of $Z_1 > Z_2$, there is a maximum predicted phase shift with respect to K followed by a dropping phase shift for increasing K at the value given by Equation 3.11. Consequently, there are two possible K values for a given ϕ_R and the appropriate one must be chosen based on the context and knowledge of joint properties. To model the predicted interfacial stiffness as a function of ϕ_R then, the phase range from 0 deg to the peak phase value in Equation 3.11 is plotted with Equation 5.2 with both the plus and the minus options. This gives the entire range of interfacial stiffness values for a given measured phase. Using Equation 5.2 and Equation 5.3, the interfacial stiffness is calculated from the measured phase curves in Figure 5.12 and then plotted in Figure 5.15.

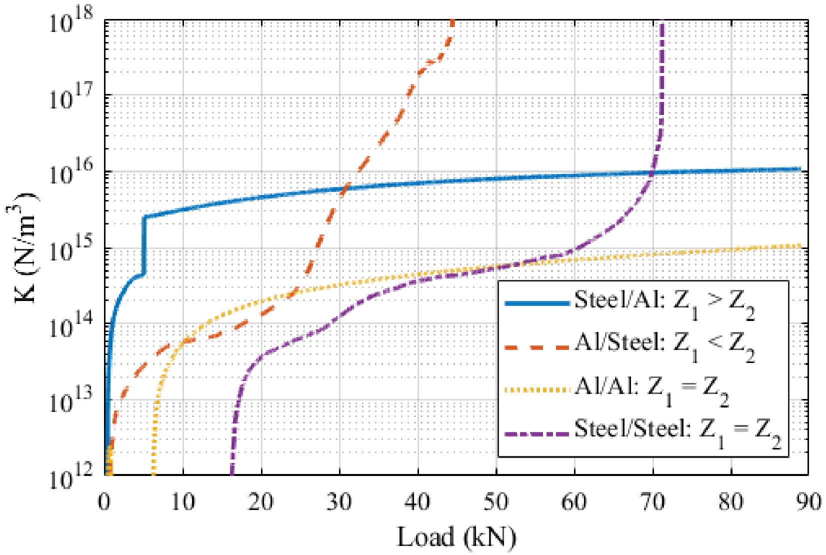

Figure 5.15: Interfacial stiffness vs. load obtained from measured ultrasonic phase at 9 MHz of reflection coefficient at interface between two solids

In Figure 5.15, both the Al/steel and steel/steel curves diverge toward infinite interfacial stiffness because the measured phase response passes above the theoretical phase maximum value of 180 deg for the Al/steel case and 90 deg for the steel/steel case. Also of note is the discontinuity of K in the steel/Al case, which is caused by the maximum phase value not reaching the theoretical maximum. Thus, it appears that the interface stiffness suddenly jumps from a point below the peak phase to one above the peak phase. More accurate interfacial stiffness assessment results could be obtained by better characterization of the phase shifts due to compressional strain in the probed medium and by using a load frame capable of much higher compressional loads to drive measured interfacial stiffness constants even higher than in this study.

As these are not actually bonded joints and this was only a proof-of-concept demonstration, it is unknown what the final interfacial stiffness constants should be with the applied load of 90 kN. Research with a different ultrasonic phase method has proved able to determine more information about the interface, such as real surface area of contact, by modeling the morphology of the interfacing surfaces and their effect on the interfacial stiffness [85]. It is likely that with further development this CFPPLL-based ultrasonic phase method could provide similar or better results, due to increased phase measurement resolution and accuracy. However, this study demonstrates a method by which the interfacial stiffness of two surfaces in contact can be evaluated for different the acoustic impedances of the interfacing media.

5.3 Conclusions

In this work, a constant-frequency ultrasonic phase measurement method is demonstrated for the assessment and monitoring of imperfect interfaces. The method is first demonstrated on an adherent/adhesive interface during the curing process. A glass adherent is bonded to an adhesive curable using UV light. During cure, an ultrasonic transducer is mounted directly under the bond line to monitor the ultrasonic phase of the reflection coefficient of the glass/adhesive interface. In the material setup in this study, the ultrasonic phase response of the interface is very close to zero for both good and bad bonding, rising to a peak value for some interfacial stiffness value in between. The peak phase was measured experimentally for a bonded joint with the standard UV-light source as well as a second bonded joint that experienced lower UV-light intensity.

From the ultrasonic phase response as a function of UV-light exposure, two key methods are demonstrated for assessing the quality of the adherent/adhesive interface. First, without a-priori knowledge of the adhesive sound velocity, the peak value of ultrasonic phase is used to determine the adhesive sound velocity and interfacial stiffness at the time of peak phase. The peak phase shift occurs at some value dependent upon acoustic impedances, ultrasonic driving frequency, and interface stiffness. This phenomenon is used here as a threshold to determine when the interfacial stiffness has crossed some value. This result is further validated by the lower UV-light intensity bonded joint, where ultrasonic phase measurements indicate a slower curing process and lower peak phase value. In practice, this method may be used to monitor an adhesive joint and determine whether the interface quality has crossed some threshold value selectable by the driving ultrasonic frequency. Second, with separate measurement of adhesive sound velocity, an inverse algorithm is used to determine interfacial stiffness throughout the entire cure process. This method further demonstrated that the bonded joint cured with lower UV-light intensity indeed lagged behind the standard-intensity joint in degree-of-cure.

In a second study, interface quality measurement is demonstrated in dry-contact joints under compressive load, sometimes referred to as “simulated kissing bonds”. The phase of the ultrasonic reflection coefficient from the imperfect interface is tracked as compressive loading is increased, which causes an increase in the interfacial stiffness flux. For different acoustic impedance values on either side of the interface, the ultrasonic phase method is able determine interface stiffness as a function of applied load.

This work is the first demonstration of interfacial stiffness assessment on an adherent/adhesive single interface with ultrasonic phase and the first time the peak phase predicted by the interfacial spring model has been verified experimentally. This method has many practical NDE and SHM applications, including the assessment of thick-adhesive single lap joints and coating adhesion quality on a substrate. It may be used as a bond quality threshold assessment when the acoustic impedance of the adhesive is unknown or may be changing, may be developed into an adhesive cure monitoring method, and may be used to track small changes in interface quality when the acoustic impedance of the adhesive is well known. The ultrasonic phase method is also applicable when the same material is used on both sides of the interface, such as in the study of contact interfaces and diffusion bonds. Finally, the demonstrated phase method may be used to characterize interface quality of coatings on substrates where the acoustic impedance of the probed medium is lower than that of the underlying medium.

Chapter 6: Single Lap Joint Adhesive Bond Strength Evaluation with Ultrasonic Phase Measurements

This chapter focuses on using the ultrasonic phase response of the reflection coefficient from the adhesive layer of a single lap joint (SLJ) to determine interfacial bond quality. In Section 6.1, an initial study is discussed, where constant frequency phase measurements from a SLJ are tracked as a function of small temperature changes. From these results, it was determined that obtaining steady-state phase vs. temperature measurements was very time-consuming and a more efficient bond quality assessment method should be explored.

Next in Section 6.2, the swept-frequency ultrasonic phase measurement method is studied with Al/epoxy SLJs where one set of joints is pristine and another is interfacially contaminated with silicone. This study compares the ultrasonic phase method with conventional broadband ultrasound, and it is shown how the phase method is able to distinguish between pristine and contaminated joints where the amplitude method does not. This study also indicated that the frequency range around the acoustic resonance of the adhesive layer provides even better results.

Interfacial bond quality determination from swept-frequency ultrasonic phase measurements around the resonance frequency of the bond line are demonstrated on ideal SLJ specimens in Section 6.3. Two major sets of experiments are performed on SLJs with smooth glass adherents and UV-curable adhesive. First, throughout the cure process, the phase response of the bond line is monitored. A curve-fitting algorithm is developed to solve inverse problem of determining interfacial stiffness from the measured phase spectra. Second, glass/UV-curable adhesive SLJs are cured to different degrees by varying UV-light exposure time. After curing, the SLJs are investigated with ultrasonic phase method and interface stiffness is determined using the curve-fitting method. This study demonstrates how the ultrasonic phase method quantifies interface stiffness and correlates interface stiffness with mechanically measured bond strengths.

Finally, the method of interfacial bond strength determination in ideal SLJ specimens is extended to Al/epoxy SLJs in Section 6.4. Rather than varying degree of cure, interfacial bond strength is modified by spray-coating Teflon-based contamination in different relative surface areas on one adherent surface prior to bonding. The SLJs are then interrogated with swept-frequency ultrasonic phase measurements around the bond line resonance frequency, and a curve-fitting method is used to determine interface stiffness from the measured phase spectra.

6.1 Phase vs. Temperature Evaluation of Adhesive Bonding

At the beginning of this project, one of the first ideas for investigating adhesive bonding with the ultrasonic phase was to track phase changes from ultrasonic echoes due to small temperature changes. By applying small temperature change to a bonded joint, thermal expansion will change the path length of sound through both the adherent and adhesive. This change in path length with temperature can be seen in the phase shift of an ultrasonic wave. Depending on the quality of the adhesive interfaces, different ultrasonic intensities will be reflected or transmitted at the interfaces, resulting in a change in the amount of phase shift coming from the adhesive layer.

The potential effect of temperature on the interfacial stiffness constant must also be considered. From Cantrell's theory on the physico-chemical relationship between interfacial stiffness and absolute interfacial bond strength, it is established that adhesive strength for alumina-epoxy bonds can be expressed $\sigma_{true} = P_{bond}\sigma_{max}$, where $P_{bond} = (1 - P_{n \geq m})$ is the probability a given bond is intact at a particular temperature [64]. The definition of $P_{n \geq m}$ from Cantrell is given in Equation 6.1.

$$P_{n \geq m} = e^{-\frac{h\nu(1+m)}{k_B T}} \left(1 - e^{-\frac{h\nu}{k_B T}}\right)^{-2} \tag{6.1}$$

The true bond strength is also related to interfacial stiffness by $\sigma_{true} = \left(\frac{F_{max}}{k}\right) K_N$. Using Equation 5.5 results in only a -0.00035% drop in σ_{true} and K_N as temperature increases from $20°C$ to $25°C$. As such, it is concluded that for the small applied temperature change in this study, the interfacial stiffness constants can be considered approximately constant.

The phase shift of the reflection coefficient from a SLJ with respect to temperature will be influenced by changes in the top adherent, the transducer itself, and the two imperfect interfaces mixed with the adhesive layer, leading to the relationship in Equation 6.2.

$$\Delta\phi_R|_{f=f_0} = \Delta T(\Delta\phi_{adherent} + \Delta\phi_{transducer} + \Delta\phi_{adhesive}) \tag{6.2}$$

6.1.1 Example of Phase vs. Temperature of Ultrasonic Reflections

To model how phase versus temperature measurements are used to quantitatively determine adhesion quality, consider Al 6061 bonded to an epoxy adhesive film of thickness 76 µm. The parameters in Table 6.1 are used in Equation 3.20 to model the phase response of the SLJ with a temperature change from $20°C$ to $25°C$.

Table 6.1: Parameters used to model Al/epoxy SLJ phase vs. temperature response

Parameter	Adherents	Adhesive
Density, ρ	$2681\ kg/m^3$	$2530\ kg/m^3$
Sound Velocity, c	$6.428\ mm/\mu s$	$2.149\ mm/\mu s$
Frequency, f	$10\ MHz$	$10\ MHz$
Thickness, L	$6.549\ mm$	$76.2\ \mu m$

A plot of the expected phase shift derivative with respect to temperature for different interfacial stiffness values of each interface can be seen in Figure 6.1. As previously mentioned, good adhesive interfaces have high interfacial stiffness constants, while poor interfaces have low interfacial stiffness constants. Note the phase shift between high and low interface stiffness is affected more by K_1 than by K_2. This implies phase versus temperature measurements are more sensitive to the quality of the first interface in a SLJ structure. From Figure 6.1, there is $\sim 0.45\ °/°C$ difference between good and bad interfaces. The total temperature change can be raised to increase sensitivity to $d\phi/dT$. Thus, a $5°C$ change will result in a $\sim 2.25°$ phase difference between both interfaces being good and being bad, while a $10°C$ change will induce a $\sim 4.5°$ phase difference between both good and bad interfaces assuming a continued linear response. With $0.022°$ phase resolution, this phase versus temperature technique should be able to quantitatively measure adhesion quality of imperfect interfaces.

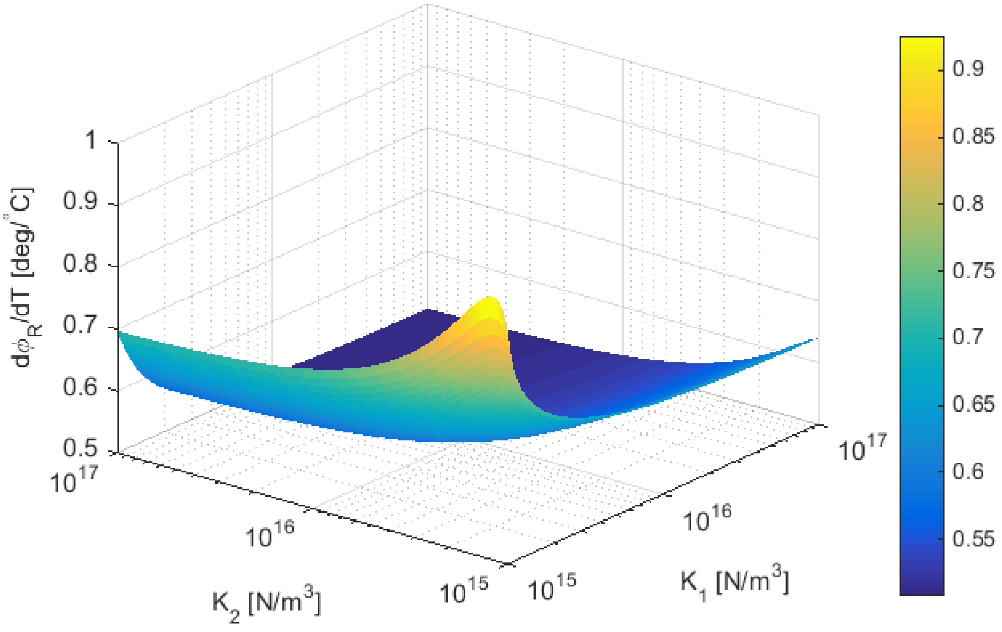

Figure 6.1: Modeled $d\phi_{R_{BL}}/dT$ of Al/epoxy SLJ for $20°C$ to $25°C$ temperature change

6.1.2 Experimental Setup

As an initial test of the CFPPLL ultrasonic phase measurement method, a bonded joint was created using adherents made from a glass-ceramic known as CLEARCERAM-Z (CCZ) from Ohara. This material was chosen for its low thermal expansion properties, which could minimize the effect of adherent thermal expansion on phase shift with respect to temperature measurements. The adhesive used for this specimen was the chemical, phenyl salicylate, also known as “salol”. Salol was chosen for ease of creation of bonded specimens due to its low melting point ($\sim 40°C$) and for reusability of adherents after bond destruction with simple cleaning. A cross-section depiction of the fabricated bonded joint is shown in Figure 6.2.

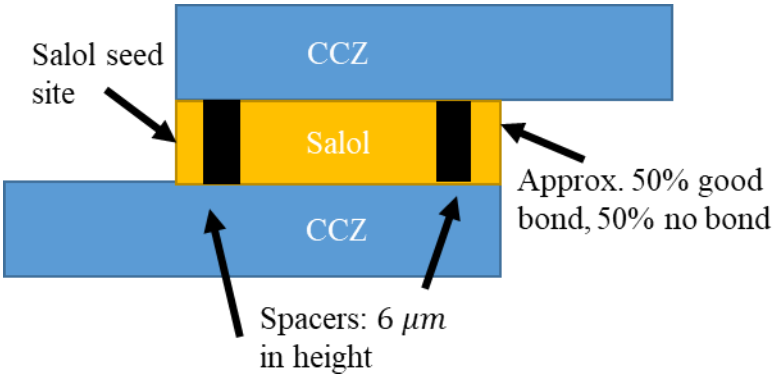

Figure 6.2: CCZ-salol bonded joint setup

The CCZ-salol bonded joint was formed by melting salol, applying some to a CCZ substrate, and applying the top adherent in place. Next, a small amount of crystallized (i.e. solid) salol was placed along the edges of the sample to seed salol crystallization during cooling. Bond line thickness was controlled with four $\sim 6\mu m$ metal film pieces used as spacers in the corners of the specimen. Pressure was applied to the joint during salol cooling to maintain uniform thickness. Liquid salol was purposefully placed on only one half of the joint in an attempt to create voided and porous regions as the salol spread across the region with pressure applied.

After salol cooling, the bonded joint was examined visually for defects. As planned, approximately half of the joint appeared visually to be well-bonded without noticeable pores or voids. However, the other half of the joint had obvious regions of voids and pores. Ultrasonic phase measurements were carried out on different regions of the specimen while in a custom-built environmental chamber, described in Section 4.2.2 and shown in Figure 4.3. The chamber was programmed to start at $\sim 20°C$ and ramp up in $0.5°C$, 20 minute long steps until $25°C$ was reached.

At each intermediate step, temperature was held constant for 85 minutes to ensure the specimen reached thermal equilibrium, as seen by both the temperature and phase signals flattening off near the end of each "soak" step.

A thermistor adhered to the side of the specimen was connected to the CFPPLL circuit to measure temperature every time the phase signal was sampled. Figure 6.3 shows an example of how the phase shift in the bonded specimen varies over time while the bonded joint is heated.

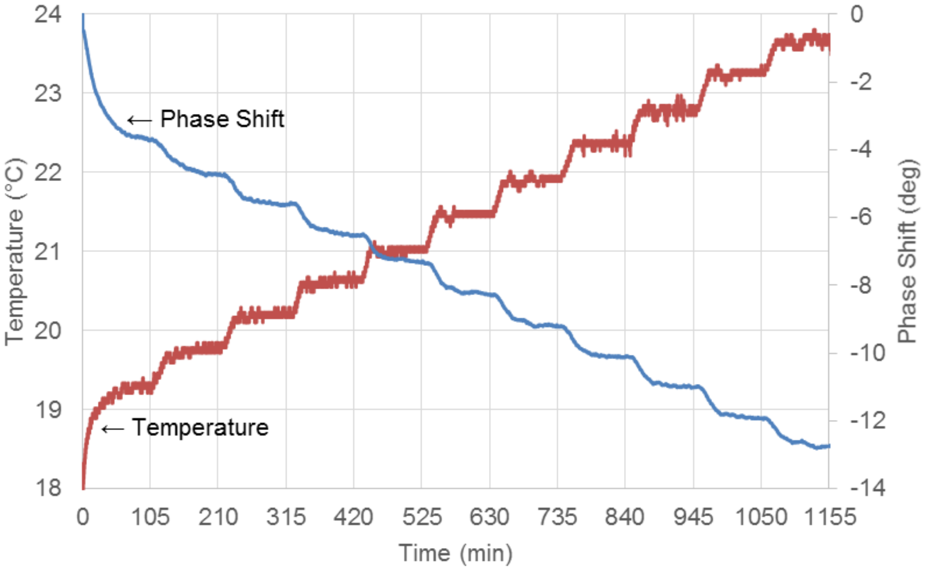

Figure 6.3: Phase shift and temperature vs. time CCZ-salol bonded joint while heating

Figure 6.4 shows the phase vs. temperature during bonded joint heating, extracted from the data in Figure 6.3. As can be seen, the phase shift tracks very well with the temperature change, as should be expected since they should have a linear relationship. As CCZ has very low thermal expansion $(0.0 \pm 1.0 \times 10^{-7}/°C)$, the phase shift in the CCZ is negative for increasing temperature due to the sound velocity increasing for increasing temperature, an effect seen in some glasses but not usually in other materials such as metals.

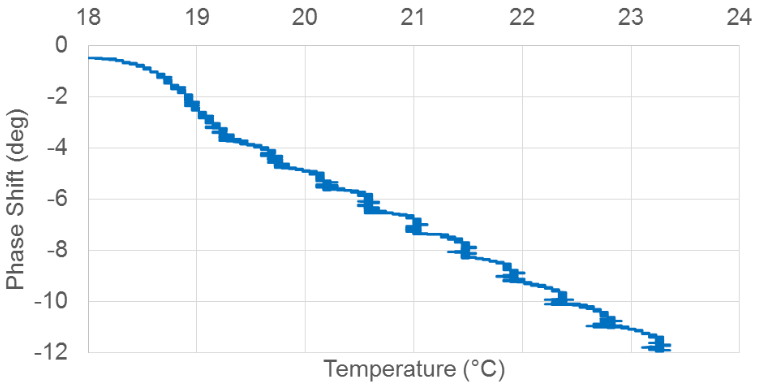

Figure 6.4: Phase shift vs. temperature for CCZ-Salol bonded joint during heating

6.1.3 Results and Discussion

For measurement of the slope of the phase vs. temperature response, one phase and temperature data point was taken at the end of a “soak” cycle after the structure had reached thermal equilibrium. Then, linear fits were applied to the temperature versus phase shift curves to obtain $d\phi/dT$ values.

Figure 6.5 shows the results from phase vs. temperature measurements at six locations on the CCZ-salol structure. These locations were picked out visually, as the glass was transparent enough to view macroscopic bonding issues such as large voids or porosity. Two tests were carried out at each location and the resulting $d\phi/dT$ value is obtained from the linear fit of the phase versus temperature curve.

First, $d\phi/dT$ was measured on a bare, unbonded region of the CCZ to have a reference representative of a complete disbond. Next, tests were conducted on the edge of the bonded area of the joint so that approximately half the tested region was well-bonded and half was completely disbonded. Tests were also performed on a region that appeared to have a large void in the salol, as well as two different locations appearing to have porosity. Finally, tests were performed on a bonded region that visually appeared well-bonded.

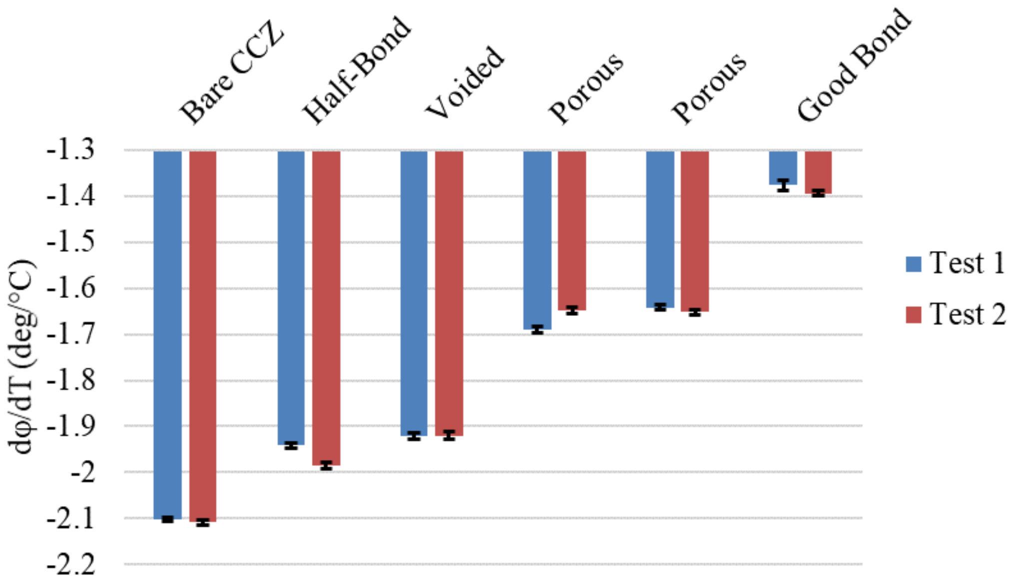

Figure 6.5: $d\phi/dT$ measurements from different locations on CCZ-salol-CCZ bonded joint

It should be noted that the bonding defects in this experiment are not the exact same as the modeled situation in Section 6.1.1, where only the interfacial stiffness constants change. In this experimental setup, parts of the entire bond line are defective via porosity and voids, not just the adhesive/adherent interfaces. However, the measured phase responses still show the general trend of poor bonding increasing the magnitude of $d\phi/dT$. Even though the qualitative bonding defects probed in this study do not directly reflect the modeled reflection coefficient response in Section 6.1.1, it does demonstrate that the ultrasonic phase measurement method was indeed sensitive to adhesive bond quality and bonding defects.

In practice, it is noted that this method has limited applicability due to the use of an environmental chamber and the length of testing. Each phase data point took 85 minutes to obtain, as the SLJ takes a long time to reach thermal equilibrium. Without a different heating mechanism and investigating thermal gradients or transient thermal responses, this approach is too slow for most practical applications. Adding further difficulty, reliably obtaining temperature-dependent material properties is found to be difficult in practice for many commonly encountered aerospace adherents and adhesives. While it has merit and could be developed further, an investigation of the phase vs. temperature response of bonded joints is not continued in this work. Other bond strength assessment studies involve a faster and more practical phase vs. frequency approach.

6.2 Swept-Frequency Ultrasonic Phase Evaluation of Adhesive Bonding below Bond line Resonance

After developing the capability of maintaining the phase relationship between transceived and reference waves in the CFPPLL-based ultrasonic phase measurement method, a study was conceived to investigate how phase vs. frequency measurements could interrogate adhesive bond quality. Based on the massless spring model of adhesive bonding described by the reflection coefficient in Equation 3.20, this work assesses the phase vs. frequency response of metal/epoxy SLJs with contamination at one of the adhesive/adherent interfaces. Rather than observing the phase response around the resonance frequency of the bond line, this initial study focuses on a frequency range of 8.5-10.75 MHz, below the bond line resonance frequency of $\sim 22\ MHz$. Below the adhesive bond line acoustic resonance frequency, the phase vs. frequency response is linear. Consequently, a linear fit of the measured phase vs. frequency of the bond line reflection coefficient is used to detect reduced interfacial adhesion in this study.

To predict the phase slope responses expected in this study, the Al/epoxy SLJ is modeled using Equation 3.20. It is assumed that the lower interface is perfectly bonded, so $K_2 \rightarrow \infty$. In this configuration, the slope of the phase vs. frequency response curve from the bond line reflection coefficient is shown in Figure 6.6. For good bonding, $d\phi/df$ is between $-5\ deg/MHz$ and $-6\ deg/MHz$, while for poor bonding, $d\phi/df$ approaches $0\ deg/MHz$. This trend can be understood by lower interface quality preventing ultrasound from passing into the bond line, reducing the influence of the adhesive layer on the measured phase shift.

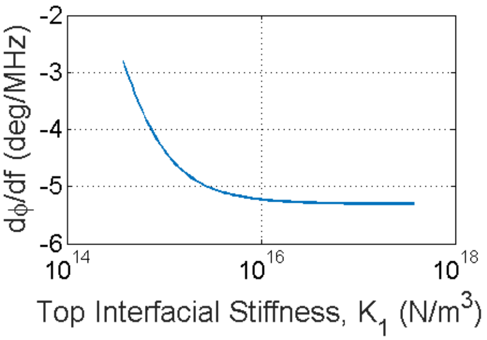

Figure 6.6: Modeled slope of phase shift in 9-11 MHz range for bond line reflection coefficient vs. upper interfacial stiffness constant

In this study, a comparison is made between ultrasonic phase results and broadband amplitude-based ultrasonic testing results for the ability to detect interfacial contamination. Additionally, the bonded joints were mechanically tested until failure to find their shear strengths for comparison with the ultrasonic results. It was from this study that it was determined that the resonance properties of the adhesive layer may be more sensitive to reduced adhesion quality.

6.2.1 Experimental Setup

Metal adherents were chosen to provide a more simple material system than composites for these initial experiments. Two sets of six SLJs comprised of Al 6061-T651 adherents bonded together with unsupported, 76 µm thick FL901AO epoxy film adhesive from Master Bond were fabricated. First, the Al adherents were cut to size with a water jet and then hand wet-sanded with up to 400 grit sandpaper. Next, each specimen was cleaned with a procedure consisting of a detergent wipe and rinse, ethanol wipe and rinse, 60 minute ultrasonic bath in ethanol, distilled water rinse, and vapor degreasing in ethanol.

After cleaning, the specimens in Set A were left pristine, while the specimens in Set B spray coated with polydimethylsiloxane (PDMS), a silicone-based contaminant, on one of the adherents prior to bonding. The coupons to be contaminated were spray-coated with one pass of 0.5% PDMS dissolved in hexanes and placed in an oven to evaporate away the solvent. A previous experiment with this process produced a 14.8 ± 4.8 nm layer of PDMS, as measured by ellipsometry. Next, the adherents were bonded with the film adhesive and held together with spring-based tension clips during cure for 2 hours at 125°C. The size specifications for these lap joints can be seen in Figure 6.7. Note, the adherents were 1” wide and were bonded together with 1” overlap, making the bonded region a 1”x1” square. While the nominal adhesive film thickness is 0.003”, it is believed the actual bond line thickness is closer to 0.002” due to adhesive squeezing out of the sides of SLJ.

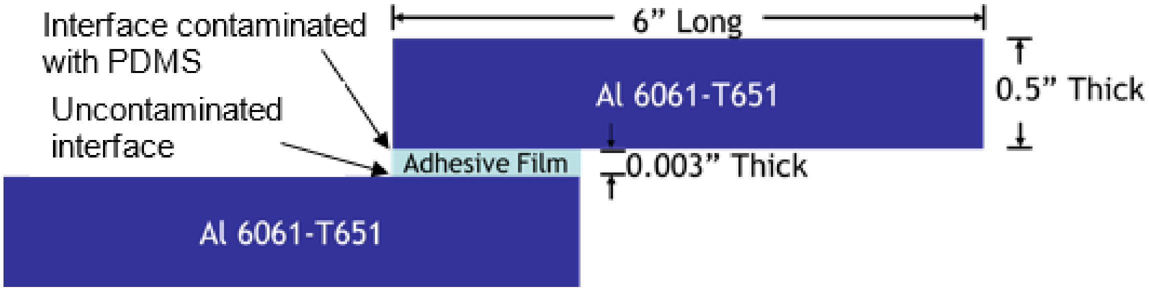

Figure 6.7. SLJ coupon specifications for sub-resonance ultrasonic phase evaluation study

After curing, both sets of bonded joints were ultrasonically evaluated with conventional broadband ultrasonic pulses as well as with the CFPPLL instrument. A comparison was then carried out between the two techniques for their abilities to detect the silicone contamination layer causing reduced adhesion strength.

The pulse-echo experiments were conducted with an ultrasonic transducer with a nominal center frequency of 50 MHz. The transducer was excited with a broadband pulse from a GE Panametrics Model 5900PR Pulser-Receiver, and the received reflection from the adhesive bond line was amplified to be viewed on an oscilloscope. In addition to each side of the lap joint, experiments were conducted on the un-bonded bare Al adherents as reference measurements for each SLJ coupon. Frequency domain analysis was conducted on the reflected pulses by taking a Fast Fourier Transform (FFT) of the time-domain data.

An analysis of the phase vs. frequency response of the bonded joints in Sets A and B was conducted. The CFPPLL instrument was used to sweep the frequency of an input ultrasonic tone-burst from 8.5 MHz to 10.75 MHz and measure the phase of the first echo from bond line. Additionally, the phase response over the same frequency range was extracted from the FFT data from the pulser-receiver experiments for comparison. After ultrasonic testing, the SLJs were mechanically tested under shear loading to failure by an MTS 810 Test System. The bonded joints were quasi-statically loaded at a rate of 200 lbs/min until bond failure.

A pristine witness specimen was also fabricated to determine the approximate bond line thickness of these SLJs. After bonding, the SLJ was cut in half through the middle of the adhesive layer with a band saw, and then the resulting face was sanded to view the cross section of the bond line. Figure 6.8 shows an optical micrograph of the bond line cross section, along with measurements showing the bond line thickness is approximately 55 μm.

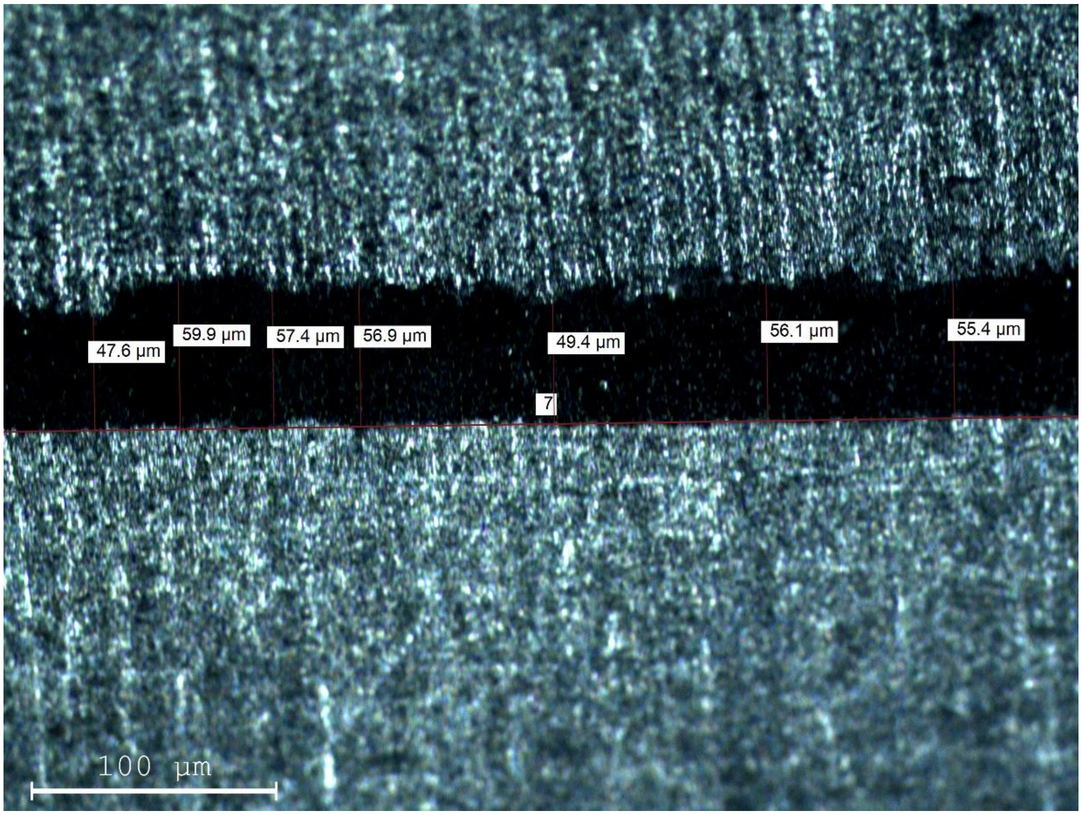

Figure 6.8: Optical micrograph at 20x magnification of bond line cross section in Al/epoxy SLJ

X-ray computed tomography (CT) was also conducted on a pristine witness bonded joint. Four CT images are shown in Figure 6.9 at different thicknesses within the plane of the adhesive layer, showing there is some unintentional porosity throughout the adhesive. The porosity seems to sweep across the layer due to a slight misalignment in the CT images normal to the plane of the adhesive layer, so in reality, the porosity exists across the layer and not as a function of thickness as these images make it seem. Later mechanical testing results find that the shear strength is close to the manufacturer's stated value, so this porosity does not significantly affect bond strength.

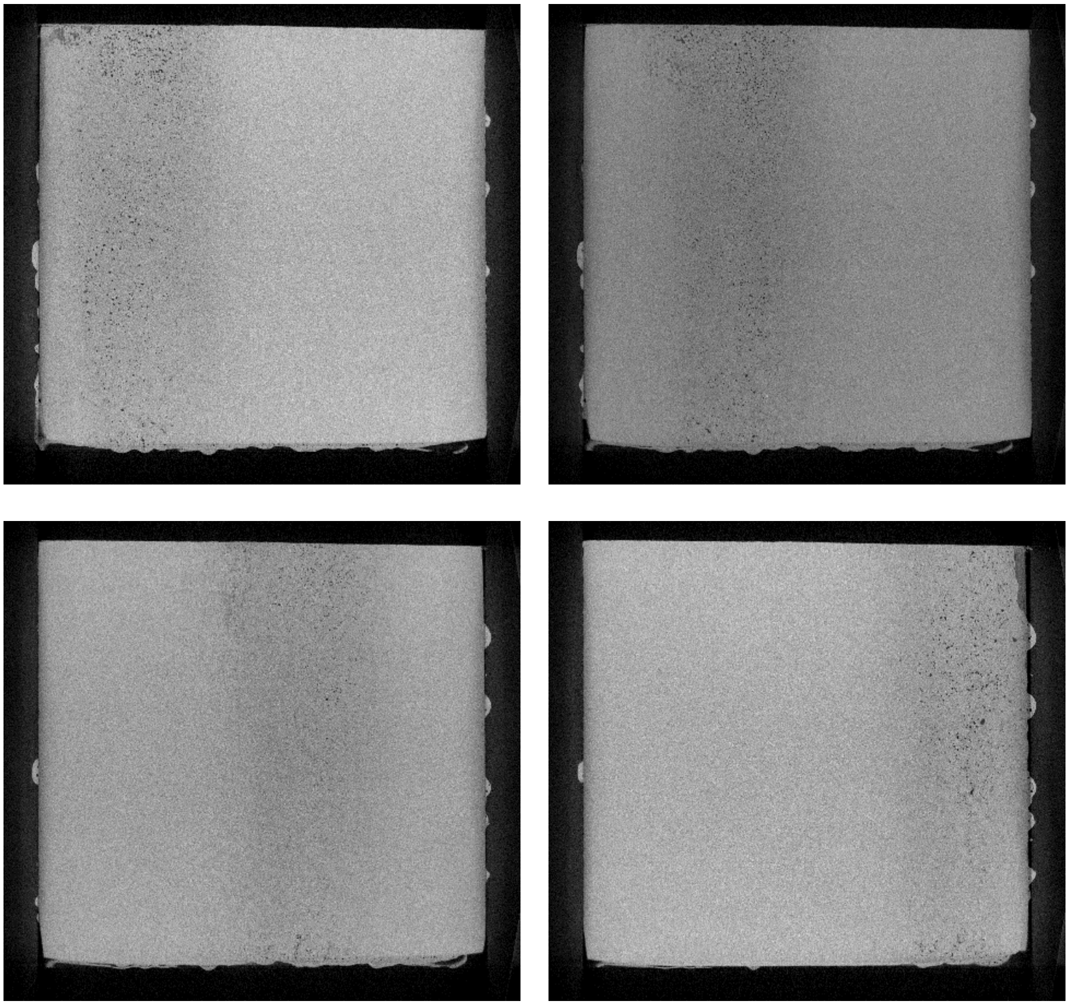

Figure 6.9: X-ray CT images showing porosity within adhesive layer

6.2.2 Results and Discussion

First the amplitude-based broadband pulse echoes from the bond line are analyzed. As an example of the shape of the signals received from joints, the time-domain results from the pulse-echo experiments on the top side of Set A can be seen in Figure 6.10. The colors in each figure correspond to measurements taken on each of the six SLJs in Set A. The reduction in amplitude of the lap joint reflections is caused by some of the incident energy being lost to transmission into the joint and bottom adherent rather than being completely reflected.

When the top side of a bonded joint is referenced in this study, it is referring to measurements from the adherent closest to the contaminated adhesive/adherent interface in Set B, as referenced in Figure 6.7, while in Set A (Pristine) the designation of the top side is arbitrary.

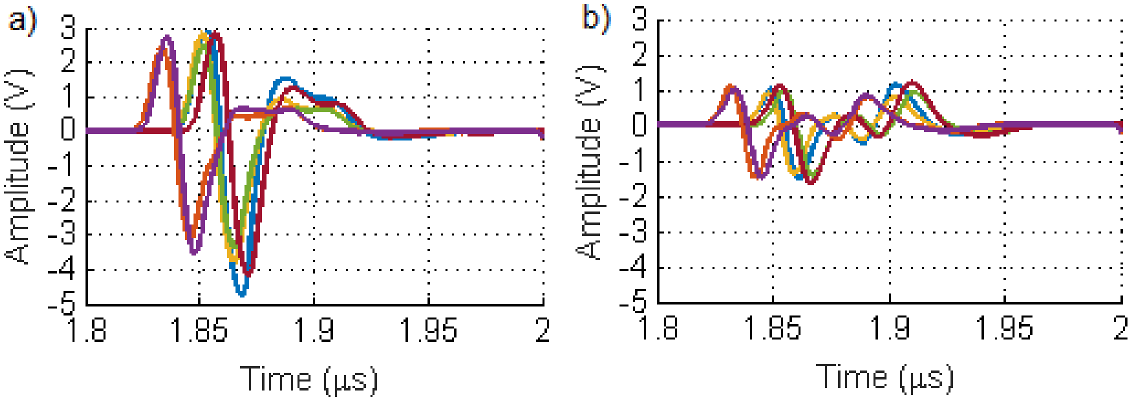

Figure 6.10: Amplitude vs. time of broadband ultrasonic pulse reflections for top side of Set A (Pristine); a) Reference measurements on bare Al, b) SLJ measurements

The peak power reflected from the bond line relative to the peak power reflected from the bare Al reference of each lap joint is shown in Figure 6.11. Analysis of variance showed there was not a significant difference between the relative maximum power of bond line reflections from Set A and Set B, meaning conventional time-domain amplitude analysis was unable to distinguish the pristine joints from the contaminated joints, no matter which side of the bond line was assessed.

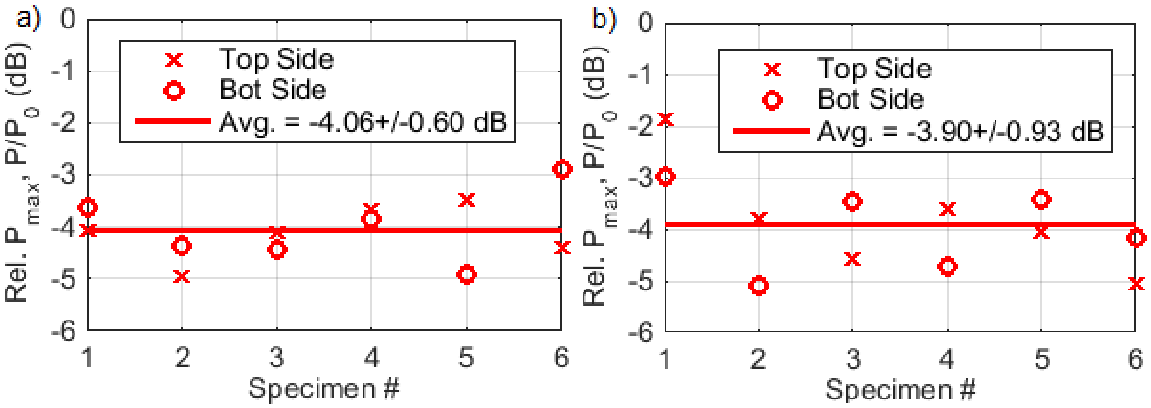

Figure 6.11. Relative peak power for each SLJ in a) Set A (Pristine) and b) Set B (PDMS Contaminated)

The amplitude vs. frequency spectra of reflections from the top side of each SLJ can be seen in Figure 6.12. As in Figure 6.10, the colors in each figure correspond to measurements taken on each of the six SLJs in each set.

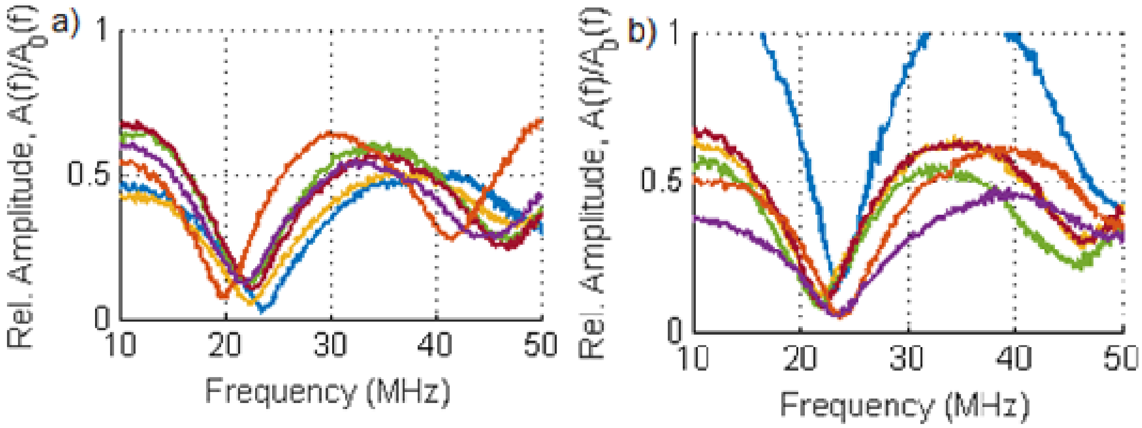

Figure 6.12. Relative amplitude vs. frequency of top side bond line reflections for a) Set A (pristine) and b) Set B (PDMS contaminated)

As previously mentioned in Section 3.2, the adhesive layer creates a resonant cavity which transmits ultrasound very well and reflects very little ultrasound when the incident wavelength is equal to twice the adhesive thickness. Theoretically, a layer of contamination or a weak adhesive interface will appear to decrease the effective stiffness of the entire adhesive layer, resulting in a decrease in frequency at which the minimum amplitude occurs. Analysis of the frequency minimum, however, does not reveal a statistically significant difference between Set A and Set B.

It is hypothesized that changes in frequency minimum due to the contamination layer are masked by variations in bond line thickness.

From the CFPPLL and pulse-echo measurements, the phase response of the reference bare Al measurements were subtracted out of the phase response on the lap joints in an attempt to observe the response of the bond line only. Below the resonance frequency of the bond line, such as here, the phase vs. frequency response from bond line echoes are linear with respect to frequency. As such, a linear fit on the phase vs. frequency response of each bonded joint was conducted, and the resulting slope was obtained, as it should be related to adhesion quality. The slope of linear fit of $\Delta\phi(f) = \phi_{SLJ}(f) - \phi_{Ref}(f)$ from lap joint reflections is plotted in Figure 6.13 for each specimen, for both the CFPPLL and broadband pulse-echo method, and for measurements on each side of the bond line.

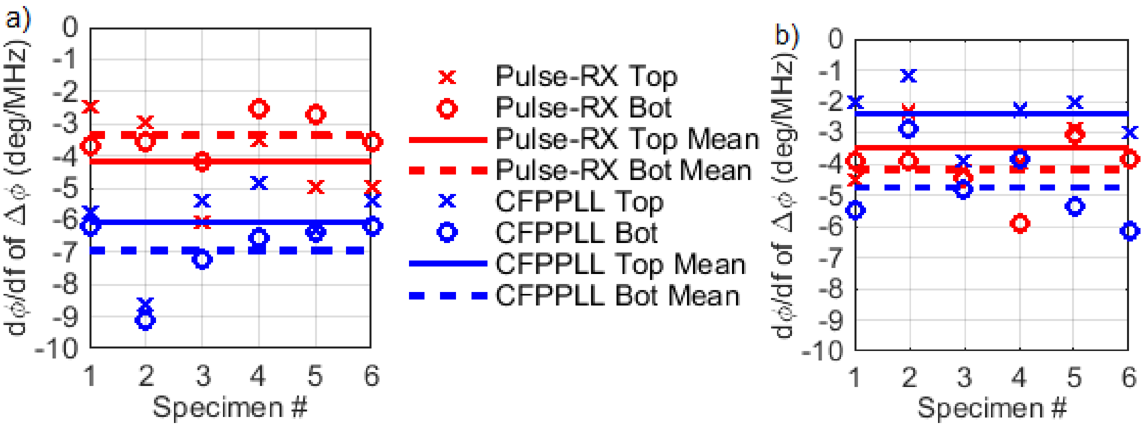

Figure 6.13. Slope of linear fit of bond line reflections for a) Set A (Pristine) and b) Set B (PDMS Contaminated)

From this data, it should be noted that no significant difference in slope between Sets A and B is seen in the pulser-receiver data. Conversely, the CFPPLL measurements show a clear difference in $d\phi/df$ between Set A and Set B. Notably, the $d\phi/df$ measurements on the top side of Set B are much closer to 0 deg/MHz than the other measurements, which is consistent with the contamination layer causing a lower adhesion quality at the interface between the adherent and adhesive. At the limit where contamination causes a complete disbond, there will be no contribution to phase by the adhesive bond line.

To verify the PDMS contamination truly affected interfacial bonding and for comparison to the ultrasonic data, the quasi-static load vs. displacement curves for each SLJ can be seen in Figure 6.14a, and the ultimate failure load of each SLJ can be seen in Figure 6.14b.

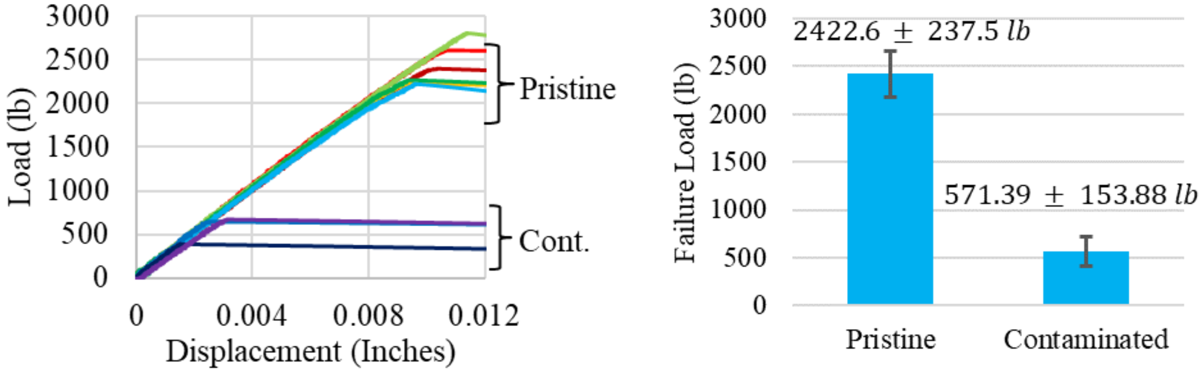

a) b)

Figure 6.14. a) Quasi-static loading results for pristine and contaminated SLJs; b) Max Load for Each Set (error bars denote 1 standard deviation)

For Al-Al bonding, the adhesive is rated for >1,500 psi, so the pristine specimens had strength well above that rating. In addition, from the final failure loads, it is clear that the PDMS contamination layer caused a significant decrease in adhesion strength, retaining ~24% of the pristine strength. Figure 6.15 shows an image of both adherents from one specimen from each set of SLJs after failure. Consistent with these images, it is worth noting that each of the pristine SLJs failed cohesively, with significant adhesive residue left on each adherent after failure. Conversely, each of the coupons from Set B failed completely adhesively at the contaminated interface.

.

a) b)

Figure 6.15: Images of bonded joints after failure; a) Specimen 1 from Set A (Pristine), and b) Specimen 1 from Set B (PDMS Contaminated)

From the time-domain, frequency-domain, and phase analysis of conventional normal incidence longitudinal ultrasonic pulses, no significant difference between the uncontaminated and contaminated bonded joints in this experiment can be observed. Conversely, the CFPPLL phase measurement method proved to be able to detect a ~20 nm silicone contamination layer at one of the interfaces. It is theorized that the high phase measurement resolution and high signal-to-noise ratio of the CFPPLL phase measurement method promote the phase sensitivity to distinguish the contamination layer where the conventional wideband ultrasonic pulse could not.

These initial results demonstrated the possibility of combining the ultrasonic phase and frequency response of bond line reflections to measure adhesion quality. While phase measurements below the ultrasonic resonance frequency of the joint are somewhat sensitive to reduced interfacial bond strength, it was hypothesized that phase measurements around the resonance frequency are much more sensitive to interfacial bond strength.

6.2.3 Repetition of Study with Different Adherent Surface Roughness

Extending the study of sub-resonance ultrasonic phase analysis of adhesive bonding in Al/epoxy SLJs, the effect of adherent surface roughness was studied. The surfaces of the adherents in the initial study were sanded with 400 grit sandpaper prior to bonding. It was thought that some of the measurement uncertainty in the original study could have been caused by the hand sanding process, inducing surface irregularities or a lack of parallelism that was not present in the as-manufactured coupons. It was thought that the adherent material thickness uncertainty could contribute to adhesive bond line thickness uncertainty, ultimately resulting in ultrasonic phase measurement uncertainty.

To test the theory that hand sanding introduced experimental uncertainty into the ultrasonic phase measurements, two sets of un-sanded Al/epoxy lap joints were fabricated for comparison with their sanded counterparts from the initial study. The SLJs were fabricated using the same process as in the initial study, described in Section 6.2.1, with the exception of the hand-sanding process that was excluded for these new SLJs. Figure 6.16 displays contour plots from optical profilometry of the sanded and un-sanded Al surfaces. The measured RMS surface roughness average was $0.57\ \mu m$ for the sanded surface and $2.40\ \mu m$ for the un-sanded surface. Again, a set of six pristine SLJs and a set of PDMS contaminated SLJs were fabricated.

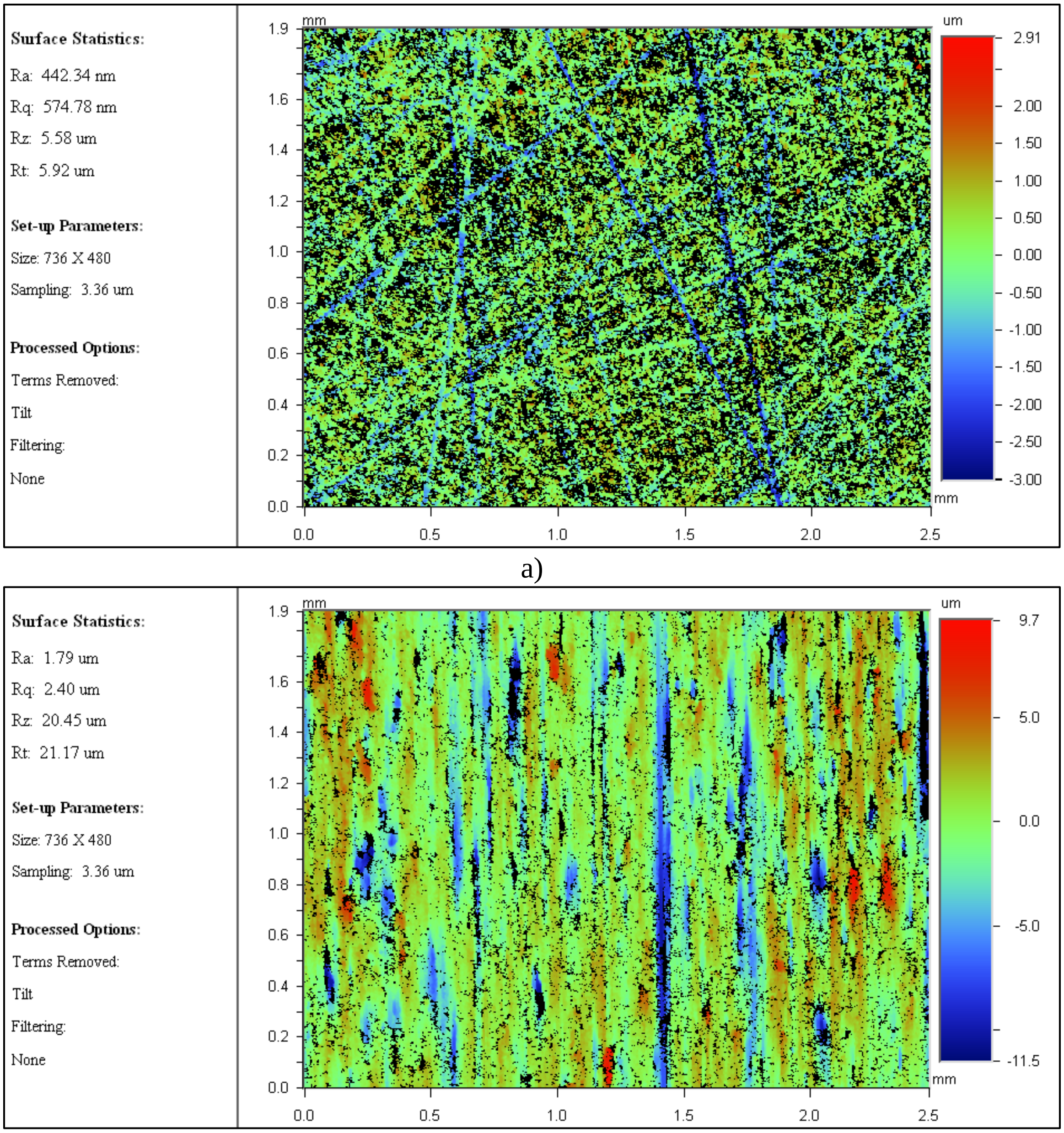

a)

Surface Statistics:
Ra: 442.34 nm
Rq: 574.78 nm
Rz: 5.58 um
Rt: 5.92 um

Set-up Parameters:
Size: 736 X 480
Sampling: 3.36 um

Processed Options:
Terms Removed:
Tilt
Filtering:
None

b)

Surface Statistics:
Ra: 1.79 um
Rq: 2.40 um
Rz: 20.45 um
Rt: 21.17 um

Set-up Parameters:
Size: 736 X 480
Sampling: 3.36 um

Processed Options:
Terms Removed:
Tilt
Filtering:
None

Figure 6.16: Optical profilometry contour plots for Al adherent coupons a) sanded with 400 grit sandpaper and b) un-sanded (i.e. as manufactured)

After bonding, the SLJs were ultrasonically evaluated with both conventional broadband pulse-echo ultrasound and the swept-frequency ultrasonic phase measurement method. Just as in the sanded SLJs, time-domain ultrasonic amplitude analysis was unable to distinguish pristine bonds from contaminated bonds.

Frequency domain analysis of the received ultrasonic pulses was carried out to find the frequency at the minimum amplitude or the acoustic resonance frequency of the bond line. Figure 6.17 shows the measured resonant frequency from each pristine specimen for both sanded and un-sanded SLJs. The spread in frequency minimums between specimens was less in the un-sanded specimens, implying less variation in bond line thickness in the un-sanded specimens. Additionally, the un-sanded specimens show generally lower frequency minimums, implying the un-sanded joints are slightly thicker than the sanded joints on average. Micrometer measurements of bond line and adherent thicknesses across each lap joint corroborated these results by showing less thickness variation in un-sanded specimens.

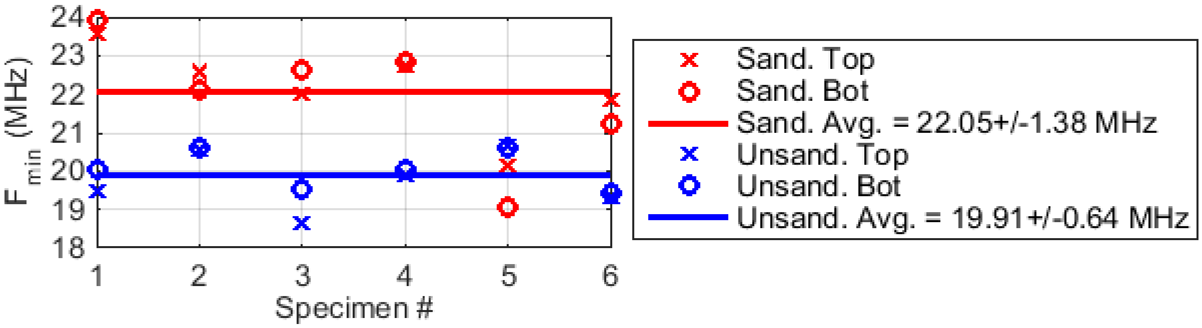

Figure 6.17: Frequency at amplitude minimum (i.e. resonant frequency) of ultrasonic reflections for pristine bonded joints with sanded and un-sanded adherents

Just as in sanded lap joints, the phase vs. frequency response of ultrasonic reflections from the un-sanded lap joints was able to detect reduced bond strength caused by PDMS contamination at one adhesive/adherent interface. Figure 6.18 shows the mean and standard deviation of $d\phi/df$ for each set of SLJs tested in this study. Seen in Figure 6.18, the top and bottom side measurements for the pristine lap joints show no noticeable difference in $d\phi/df$. Conversely, in the contaminated specimens, the top side measurements – nearest to the contaminated interface – are much closer to $0\ deg/MHz$ than the bottom side measurements. This implies the upper interface is acting more like a disbond than a well-bonded interface. Note, this effect is seen in both the sanded and un-sanded lap joints.

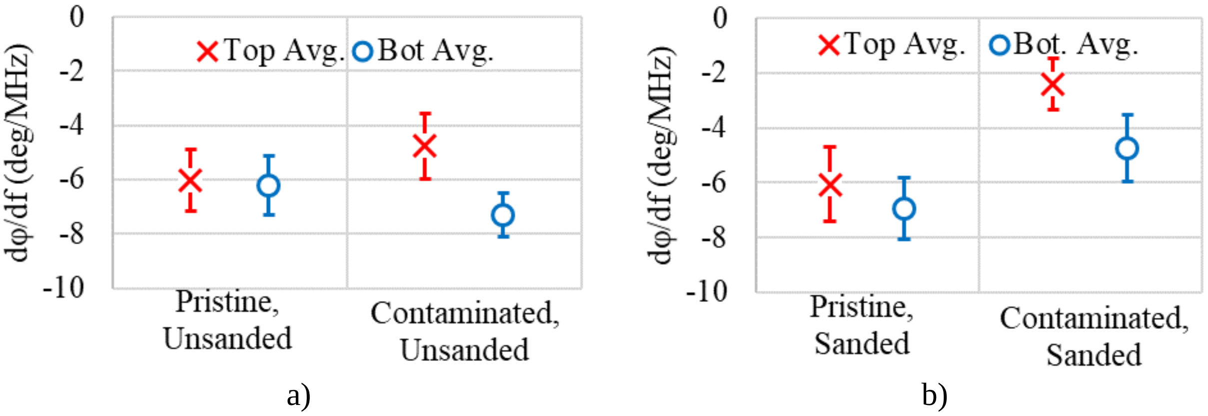

Figure 6.18: Average of $d\phi/df$ in 8.5-10.75 MHz range over 6 specimens in each set of pristine and contaminated SLJs which were a) left un-sanded and b) hand-sanded

After ultrasonic evaluation, all un-sanded Al/epoxy lap joints were pull tested with shearing loads until failure in the same manner as in the initial study. The lack of sanding in the bonded joints was found to reduce the mean pristine shear strength by ~23% of the pristine shear strength of the sanded joints. Unfortunately, each of the un-sanded, contaminated joints failed at the contaminated interface when installing into the load frame, preventing quasi-static shear loading but implying very low interfacial bond strengths.

Ultimately, the hand-sanding process did seem to increase the variability in the bond line thickness of each SLJ, resulting in increased ultrasonic measurement uncertainty. For both sanded and as-manufactured adherents, the slope of phase shift was able to distinguish pristine bonding from poor bonding when probing on the side of the bond closest to the contaminated interface. However, the pristine and contaminated joints were more-easily distinguished with ultrasonic phase when the adherents had been sanded prior to bonding. It is theorized that a lower surface roughness from sanding as well as a more consistent bonding surface result in a more consistent and reliable interfacial stiffness. It was also found that sanding the adherents resulted in an increase in the ultimate bond strength for pristine joints. This result is consistent with other studies in the literature, which show that mechanical surface modification of adherents prior to bonding can increase bond strength [19] [20] [21] [22] [23].

6.3 Evaluation of Ideal Bonded Joints during Adhesive Cure

In this study, a swept-frequency ultrasonic phase measurement method for the assessment of adhesive bond strength is demonstrated. This method combines the advantages of frequency-based and phase-based ultrasonic inspection methods, while overcoming some of the limitations of previous techniques. The swept-frequency ultrasonic phase measurement method is used to examine adhesive bonding properties of tri-layered bonded joints around the acoustic resonant frequency of the bond line.

Single lap joints are fabricated with smooth glass adherents and adhesive curable with ultraviolet (UV) light. To distinguish between adhesive and cohesive properties in the bonded joint, changes in elastic modulus of the adhesive layer during cure are measured using a broadband pulse-echo time-of-flight technique. The sound velocity at a UV-light exposure time is then used in an inverse algorithm for determining interfacial stiffness from the measured phase spectrum of the bond line reflection. Finally, ultrasonically measured interfacial stiffness values are correlated to destructive mechanical testing results.

6.3.1 Theory

The reflection coefficient from a glass/UV-curable adhesive SLJ is found using the same model for ultrasonic interactions within SLJs established in Section 3.2. While the bond line ultrasonic reflection coefficient in Equation 3.20 is applicable in this case, where the both adherents are the same material, R_{BL} can be further simplified. In this study, no modification or contamination is added to either adhesive/adherent interface to cause different bond strengths, so it is assumed both interfaces have the same properties. Under this additional assumption, $K = K_1 = K_2$, and R_{BL} keeps the same form as Equation 3.20, but the coefficients in front of the cosine and sine terms are simplified. The simplified reflection ultrasonic reflection coefficient for this study is shown in Equation 6.3. Again, the frequency range surrounding the ultrasonic reflection coefficient anti-resonance frequency (f_{ar}) is of particular interest to this study.

$$R_{BL} \approx \frac{C_N \cos(k_{adh}L_{BL}) + iS_N \sin(k_{adh}L_{BL})}{C_D \cos(k_{adh}L_{BL}) + i\,S_D \sin(k_{adh}L_{BL})} \tag{6.3}$$

$$C_N \approx \frac{2G_1^2 G_{adh}}{K}$$

$$C_D \approx 2G_1 G_{adh}\left(1 + \frac{G_1}{K}\right)$$

$$S_N \approx G_1^2 - G_{adh}^2 + \frac{G_1^2 G_{adh}^2}{K^2}$$

$$S_D \approx G_1^2 + G_{adh}^2 + \frac{G_1 G_{adh}^2}{K}\left(2 + \frac{G_1}{K}\right)$$

$$G_1 = iE_1 k_1, \quad G_{adh} = iE_{adh} k_{adh}$$

6.3.2 Experimental Setup

To investigate the ability of swept-frequency ultrasonic phase measurements to interrogate adhesive properties, several sets of experiments were performed. Idealized lap joints made with smooth glass adherents were chosen to minimize experimental uncertainty arising from surface roughness and internal ultrasonic scattering in this proof of concept study. Transparent adherents also permit visual inspection of bonding defects and allow for the use of adhesives curable with UV light. By varying the exposure time to UV light, the adhesive and cohesive properties of the lap joint are precisely controlled without the need for high temperatures, allowing for in-situ adhesive bond evaluation with commercial ultrasonic transducers.

Schott Borofloat® 33 glass cut into 5.08 cm wide x 5.08 cm long x 1.10 cm thick coupons were purchased from the S. I. Howard Glass Company to be used as adherents. The glass coupons were bonded together with Norland Optical Adhesive (NOA) 60, a UV-curable adhesive, obtained from Norland Products Inc. NOA 60 does not continue to cure at room temperature when not exposed to UV light, allowing for correlation between ultrasonically and mechanically evaluated bond strengths without a change in degree-of-cure.

Prior to bonding, each glass coupon was cleaned with an ethanol wipe, a 60 minute ultrasonic cleaning bath in reagent grade ethanol, and vapor degreasing with ethanol. After drying, a single drop of room temperature NOA 60 was applied to one of the adherents. Three small pieces of stainless steel shim stock were then placed on the adherent to hold a uniform bond line thickness between joints. The shim stock thickness was 204 µm for an experiment measuring the sound velocity measurement in the adhesive and 102 µm for the adhesive bond quality evaluation experiments. Next, a second glass adherent was placed on top of the other to form a single lap joint. Two 2.54 cm thick clamps on opposite sides of the joint held the thickness during cure. In each specimen, a dial micrometer was used to measure the adherent thicknesses before cure and lap joint thickness after cure to determine the bond line thickness. An example image of a fully cured lap joint is shown in Figure 6.19a.

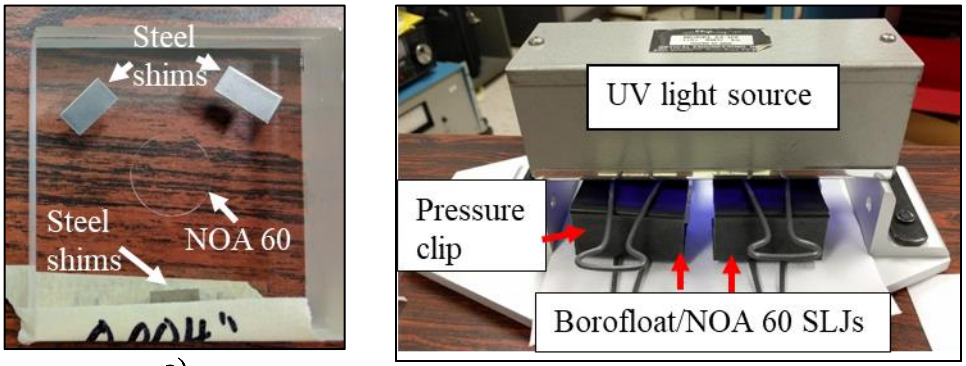

a)

b)

Figure 6.19: a) Post-cure image of Borofloat/NOA 60 single lap joint; b) UV light curing setup for bonded joints

The joints were placed under a UV light source to cure, as shown in Figure 6.19b. NOA 60 cures optimally via UV light with wavelengths of 350-380 nm and requires about 3 J/cm^2 of energy for full cure [142]. The UV light source is a 5.08 cm x 15.24 cm Model 22-UV manufactured by Optical Engineering, Inc (now manufactured by Macken Instruments, Inc.) and uses a low-pressure mercury florescent bulb with UV phosphor and blue tinted glass to suppress visible emission [143]. The source emits light with a maximum intensity of 5 mW/cm^2 and wavelengths primarily between 340 nm and 390 nm, with peak emission at 360 nm. The transmission spectrum of Schott Borofloat® 33 is only given by the manufacturer for thicknesses up to 5 mm but is assumed ~ 80% in the 350-380 nm range [144]. Assuming an intensity of 2.5 mW/cm^2 in the 350-380 nm range reaches the top of the adherent and 80% of that light transmits through the adherent, it is conservatively estimated that a cure time of 25 minutes is required to fully-cure the adhesive with 3 J/cm^2 of energy.

6.3.2.1 Sound Velocity Measurements via Ultrasonic Time-of-Flight

As both sound velocity and interfacial stiffness flux shift the frequency of anti-resonance of ultrasonic bond line reflections, it is necessary to independently determine the adhesive sound velocity as a function of cure. A 12.7 mm diameter, nominally 50 MHz damped ultrasonic transducer (model V214BA from Olympus) was adhered under a Borofloat glass/NOA 60 lap joint with Sono 600 ultrasonic couplant (obtained from Magnaflux) during cure. The shim thickness was made to easily separate ultrasonic reflections coming from each interface within the bond line.

At 27 different time intervals within cure process, the UV light source was blocked and the bonded joint was evaluated with a broadband ultrasonic pulse from a GE Panametrics Model 5900PR pulser-receiver. The time-of-flight between consecutive reflections within the bond line was measured with a LeCroy WaveRunner 6200 oscilloscope. The broadband pulse had a passband of 1 kHz – 200 MHz and a pulse energy of 1 μJ. The received echo was amplified by 38 dB prior to viewing on the oscilloscope.

6.3.2.2 In-Situ Ultrasonic Bond Evaluation During Cure

A glass/UV-curable adhesive lap joint was fabricated and ultrasonically evaluated in-situ throughout its cure process. A 6.35 mm diameter, broadband Olympus V112 ultrasonic transducer was mounted underneath the bonded joint during cure and was coupled into the bottom adherent with Sono 600 ultrasonic couplant.

At different time intervals throughout the cure process, the UV light source was blocked so that swept-frequency phase measurements were made with the CFPPLL instrument. The phase of the first reflection from the bond line was measured as a function of frequency. As the adhesive layer is thin with respect to the acoustic tone-burst duration, multiple reflections from inside the adhesive layer are combined within the received tone-burst. The ultrasonic driving frequency was swept in 0.01 MHz increments through the 8.5-11.75 MHz range. Using the CFPPLL instrument to provide the same input phase offset used in the bond line reflection measurement, a reference phase vs. frequency measurement was obtained from the first back wall reflection of an un-bonded section of the lower glass adherent. This measurement is used to account for the phase response caused by the adherent, instrumentation, ultrasonic transducer, and ultrasonic couplant.

6.3.2.3 Post-Cure Ultrasonic and Mechanical Bond Evaluation

To correlate ultrasonic measurements with mechanical bond strength, a set of 10 Borofloat/NOA 60 bonded joints were fabricated with UV-light exposure times varying from 3-60 minutes. The diameter of the circular adhesive cross-section was determined to a tolerance of ±1 mm.

In this study, a load cell and screw clamp were placed in-line with the lap joint/transducer setup, providing a compressive bias of ~178 N to the transducer during each measurement. Ultrasound is coupled into the adherent of the joint under test via Sono 600 ultrasonic couplant. In this setup, the phase of the first reflection from the bond line of each bonded joint was evaluated with the CFPPLL instrument through the 8.5-11.75 MHz range with an Olympus V112 transducer. A reference phase vs. frequency measurement was also obtained from the first back wall reflection of an unbonded section of the structure, using the same load-cell, compressive bias, and ultrasonic phase offset. The purpose of the reference measurement is to subtract out the phase spectra due to the adherent, instrumentation, ultrasonic transducer, and ultrasonic couplant layer.

After ultrasonic testing, metal angle brackets and sheet stock were bonded to the lap joints with room-temperature-curing Hysol 9394 epoxy, as shown in Figure 6.20a. Spring-based clamps applied pressure during cure. The metal sheets on each end of the structure were placed within the grips of an MTS Alliance RT/100 load frame during mechanical tensile testing, as shown in Figure 6.20b. Each SLJ was pull-tested where a constant load rate of 267 N/min was applied until failure.

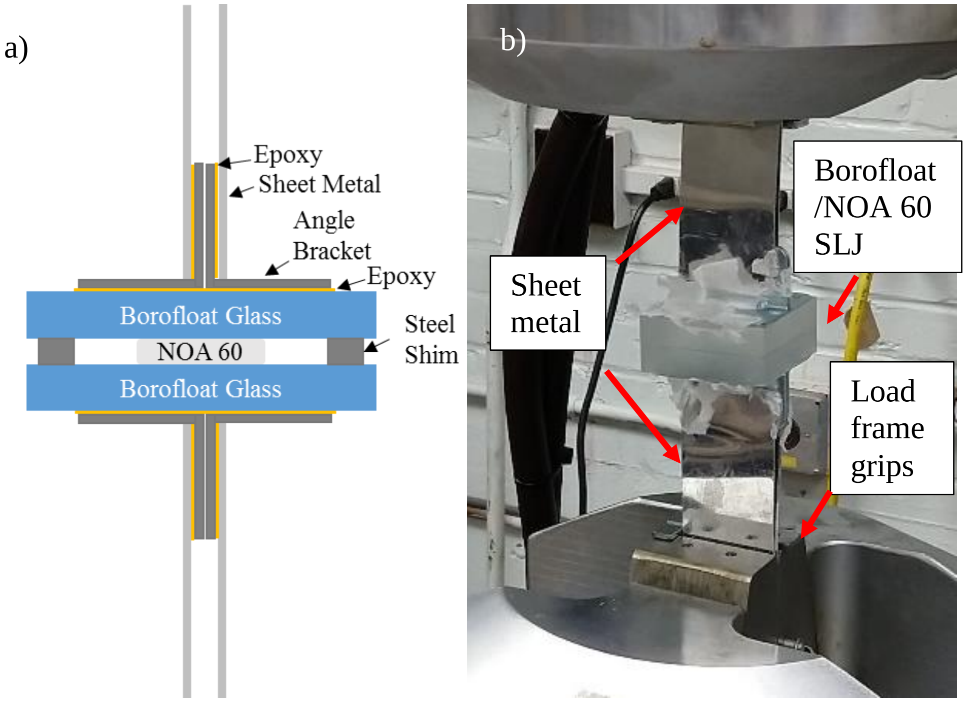

Figure 6.20: a) Tensile testing structural arrangement for Borofloat/NOA 60 lap joints; b) Image of Borofloat/NOA 60 joint within grips of load frame

6.3.3 Results and Discussion

After fabrication, the bonded were optically inspected. Most fabricated joints displayed no visual defects in the adhesive, although several presented small bubbles introduced in the liquid adhesive deposition process. Figure 6.21 shows an optical micrograph showing the few bubbles seen in one of the bonded joints. It was determined that the few bubbles were relatively small in comparison to the ultrasonic transducer diameter and size of the bonded region, and so they were unlikely to cause major inspection or bonding issues.

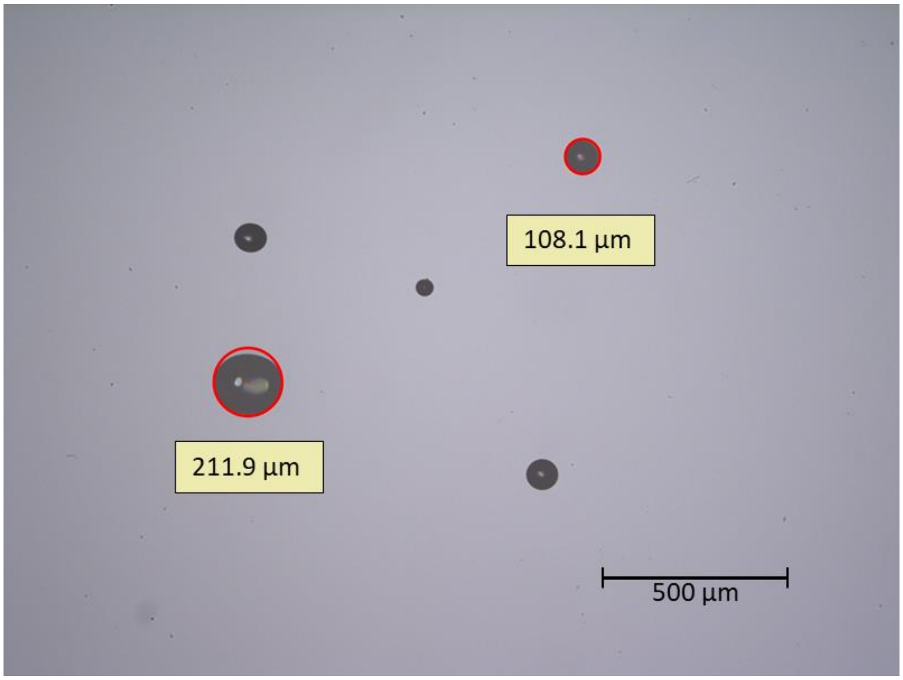

Figure 6.21: Optical micrograph at 5x magnification of bubbles seen in adhesive layer of Borofloat/NOA 60 bonded joint

6.3.3.1 Sound Velocity Measurement via Ultrasonic Time-of-Flight

The amplitude vs. time responses from ultrasonic pulse echoes within the bond line were examined as a function of UV-light exposure. Bond line reflection measurements from several different degrees of cure are plotted in Figure 6.22, which shows three typical measured response curves. The first echo is from the upper adherent/adhesive interface, and the second echo is from the lower adhesive/adherent interface. A trend is observed of the peak amplitude of the second reflection to decreasing in time as a function of cure. A slight increase in amplitude of the second reflection as a function of cure is also visible, due to a decrease in ultrasonic attenuation within the adhesive as it cures.

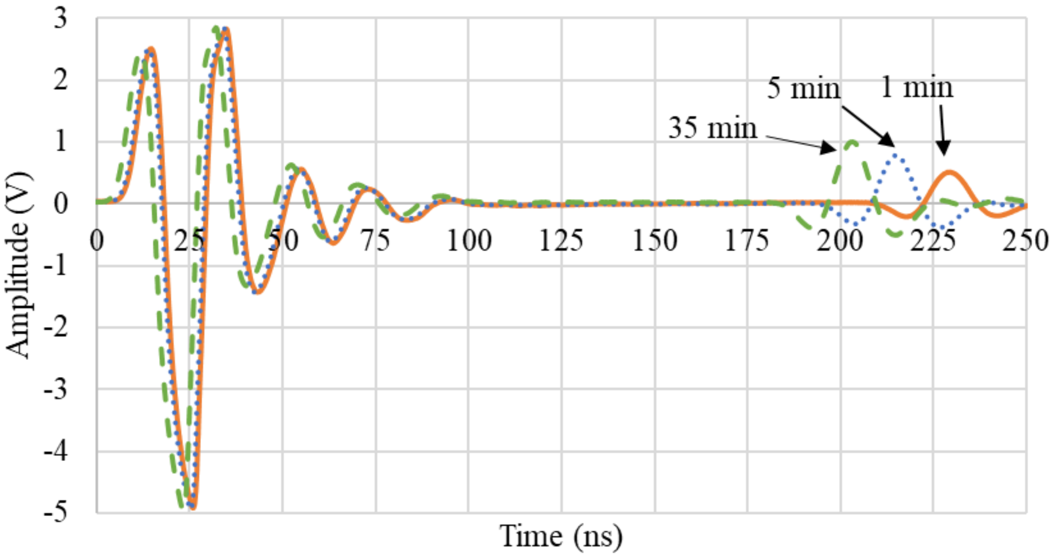

Figure 6.22: Selected ultrasonic pulse reflections from bond line with different UV-light exposure times: 1 minute (solid orange), 5 minutes (dotted blue), and 35 minutes (dashed green)

The ToF of each pulse within the bond line was found by taking the difference in time of maximum amplitude between the first and second bond line reflections. Adhesive longitudinal wave velocity was calculated from Equation 3.3 using the ToF and measured bond line thickness of $206.6 \pm 3.6\ \mu m$. The measured ToF within the bond line and the computed adhesive longitudinal wave velocity are plotted in Figure 6.23. The velocity measurements are used later in modeling the ultrasonic phase and amplitude vs. frequency responses of the bond line as a function of UV light exposure. Additional velocity measurements may not be necessary to measure interfacial stiffness flux in applications where the adhesive properties are well known and the cure-cycle is well controlled.

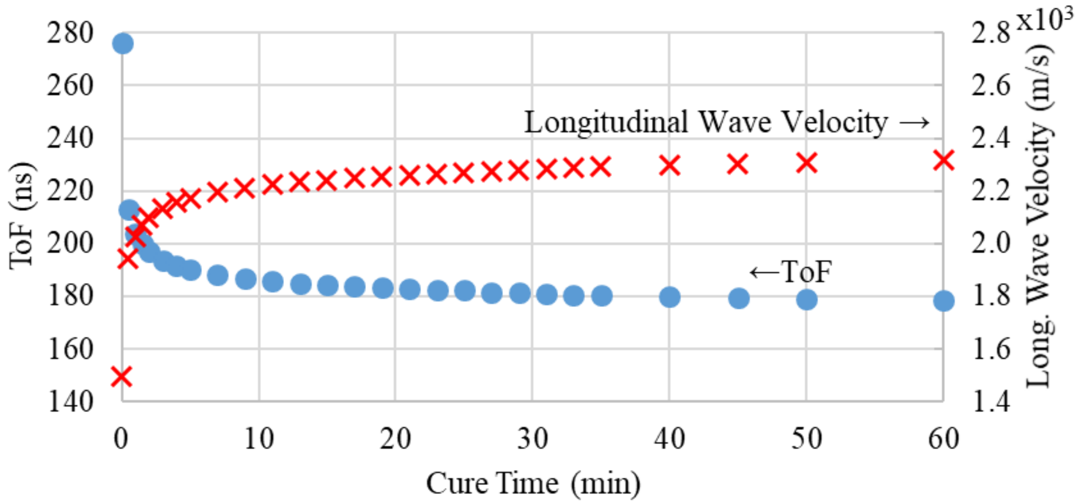

Figure 6.23: Measured time-of-flight of ultrasonic pulses within bond line (blue dots) and calculated longitudinal wave velocity (red crosses) vs. adhesive UV light exposure time

6.3.3.2 In-Situ Ultrasonic Bond Evaluation During Cure

To obtain the phase vs. frequency response of only the adhesive bond line reflection coefficient, the measured reference phase from the back wall of the un-bonded adherent is subtracted from the measured phase from the tri-layer structure at each UV-exposure time. For displacement waves, the acoustic reflection coefficient for a glass/air interface can be simply modeled as $R_{glass/air} = (Z_{glass} - Z_{air})/(Z_{glass} + Z_{air})$, where Z_{glass} and Z_{air} are the acoustic impedances of glass and air, respectively. Near 20°C, air has an acoustic impedance of $Z_{air} = 415\ Rayl$ [145], whereas the glass used in this work has a measured acoustic impedance of $Z_{glass} = 12.3 \times 10^6\ Rayl$. As a result, $R_{glass/air} \approx 1$, and the phase shift at the glass/air interface at the back wall of the unbonded adherent is zero. This makes it straightforward to subtract out the measured reference phase to obtain the phase of the bond line reflection coefficient.

The total measured reference phase from the back wall of the adherent is expressed in Equation 6.4, where $\phi_{adher}(f)$ is the phase shift caused by acoustic waves traveling through the adherent, $\phi_{trans}\ (f)$ is the phase response of the transducer, $\phi_{instr}(f)$ is the phase response of the

CFPPLL instrumentation, and $\phi_{coup}(f)$ is the phase shift caused by acoustic waves traveling through the transducer/couplant/adherent interface when being transmitted and received.

$$\phi_{adher}^{meas}(f) = \phi_{adher}(f) + \phi_{trans}(f) + \phi_{instr}(f) + \phi_{coup}(f) \tag{6.4}$$

Equation 6.5 describes the measured phase vs. frequency response of the first reflection from the adherent/adhesive/adherent interface in the tri-layer structure, where $\phi_{R_{BL}}(f)$ is the phase response of the bond line reflection coefficient and $\phi_{diff}(f)$ accounts for unknown phase shifts caused by differences in the adherent material properties and thickness between measurement points as well as differences in acoustic couplant thickness between tests.

$$\phi_{tri-layer}^{meas}(f) = \phi_{adher}(f) + \phi_{R_{BL}}(f) + \phi_{trans}(f) + \phi_{instr}(f) + \phi_{coup}(f) + \phi_{diff}(f) \tag{6.5}$$

By subtracting $\phi_{adherent}^{meas}(f)$ from $\phi_{tri-layer}^{meas}(f)$, the result is primarily the phase of the bond line reflection coefficient. This new phase, hereafter referred to as the measured phase response of the adhesive bond line, is expressed in Equation 6.6. The unknown phase shifts encompassed by $\phi_{diff}(f)$ should be relatively small, as the smooth glass adherents used in this study are uniform in both composition and thickness. Additionally, care is taken to avoid variations in acoustic couplant thickness by providing a consistent compressive load to the transducer across ultrasonic tests. The resulting bond line phase responses at selected cure times are displayed in Figure 6.24.

$$\phi_{BL}^{meas}(f) = \phi_{tri-layer}^{meas}(f) - \phi_{adherent}^{meas}(f) = \phi_{R_{BL}}(f) + \phi_{diff}(f) \tag{6.6}$$

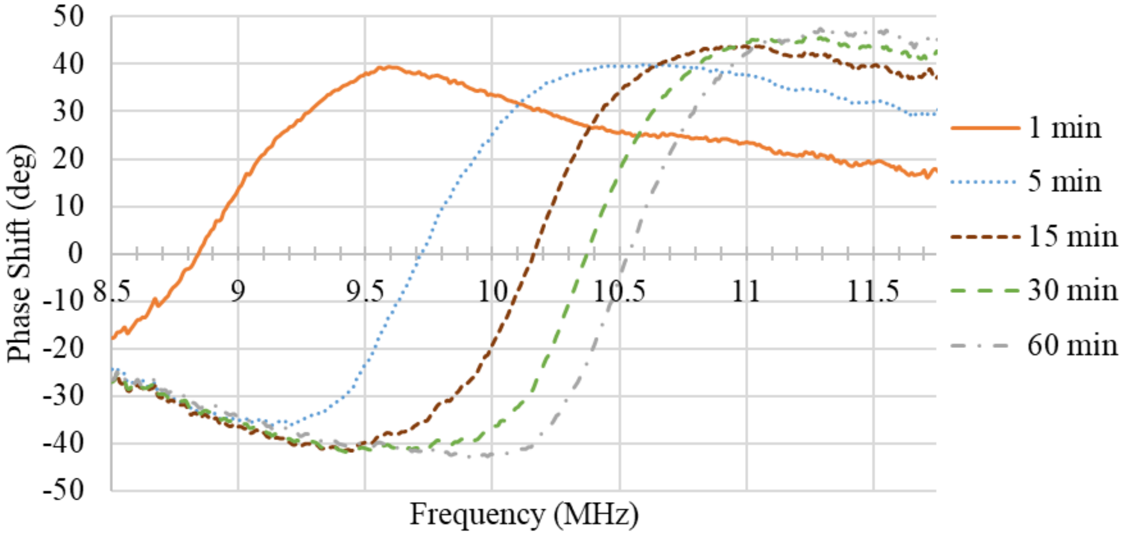

Figure 6.24: Phase vs. frequency responses of bond line reflections, $\phi_{BL}^{meas}(f)$, for selected cure times of in-situ monitored SLJ

Of note from Figure 6.24 is the increase in the anti-resonance frequency (f_{ar}) – where the phase inversion occurs – with increased cure. This frequency increase is caused by the adhesive stiffening due to polymer cross-linking during cure, which is measured as an increase in sound velocity. Additionally, the "sharpness" of the phase inversion or the slope of phase shift ($d\phi/df$) at f_{ar} increases with cure, due to decreasing bulk adhesive attenuation. The decrease in adhesive attenuation as a function of cure was also seen in the ToF measurements taken with 50 MHz pulses in the adhesive. It is thought the decreasing adhesive attenuation coefficient is caused by polymer cross-linking during cure, which decreases ultrasonic scattering within the adhesive.

To solve the inverse problem of obtaining the unknown properties of acoustic attenuation in the adhesive layer and interfacial stiffness, a curve-fitting model was developed using the robust least absolute residual fitting algorithm. In the model described by Equation 6.7, the measured phase response of the bond line, $\phi_{BL}^{meas}(f)$ is fit to the theoretical phase of the bond line reflection coefficient plus a linear term to account for small differences in adherent thickness or material properties as well as couplant thickness variations.

$$\phi_{model}(f; K, \alpha_{adh}, a, b) = \phi_{R_{BL}}^{theor}(f; K, \alpha_{adh}) + af + b \quad (6.7)$$

In Equation 6.7, the input frequency f is the independent variable, $\phi_{R_{BL}}^{theor}$ is the theoretical phase of the bond line reflection coefficient described by Equation 6.3, and a and b are some real numbers. Table 6.2 shows the set constant parameters used in the curve fitting method for the phase response: c_1, ρ_1, ρ_{adh}, and L_{BL}.

Table 6.2: Set parameters in ultrasonic reflection coefficient of bonded joint model

Parameter Name	Value
Adherent Sound Vel.: $c_1 = c_2$	$5640\ m/s$
Adhesive Sound Vel.: c_{BL}	$1500 - 2400\ m/s$
Adherent Density: $\rho_1 = \rho_2$	$2180\ kg/m^3$
Adhesive Density: ρ_{BL}	$1290\ kg/m^3$
Bond line Thickness: L_{BL}	$108.3\ \mu m$

The lap joint's bond line thickness is measured to be 108.3 ± 3.1 µm. The only set parameter which changes is the adhesive sound velocity, c_{adh}, which was measured for each UV-light exposure time and accounts for the stiffening of the adhesive during cure (i.e. increasing E_{adh}). Adherent and adhesive mass densities were obtained from manufacture specifications. Only K, α_{adh}, a, b are free to change in order to the measured phase data to the model. The initial guess, lower bound, and upper bound for each free parameter in the model is shown in Table 6.3.

Table 6.3: Free parameters in model of phase of bond line ultrasonic reflection coefficient, R_{BL}

Parameter (units)	Initial Guess	Lower Bound	Upper Bound
Adhesive Attenuation: α_{adh} (Np/m)	1,000	0	10,000
Interfacial Stiffness Flux: K (N/m^3)	10^{16}	10^{12}	10^{20}
Linear Term: a (deg/Hz)	0	-3×10^{-6}	3×10^{-6}
Constant Term: b (deg)	0	-10	10

After using the curve-fitting algorithm, Figure 6.25 shows an example of the curve-of-best-fit found for the phase response of the bond line after 30 minutes of UV-light exposure.

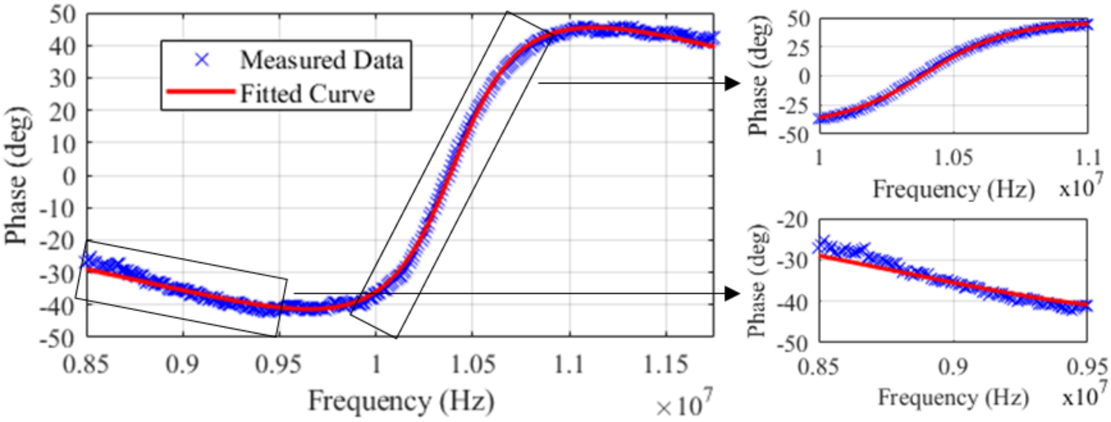

Figure 6.25: Curve fit of $\phi_{BL}^{meas}(f)$ response from 30 minute cured bond line

From the curve fitting of the phase response in the $8.5 - 11.75\ MHz$ range, the interfacial stiffness flux coefficients between the adhesive and adherent as well as the adhesive attenuation coefficient were extracted as a function of UV-light exposure time and are plotted in Figure 6.26.

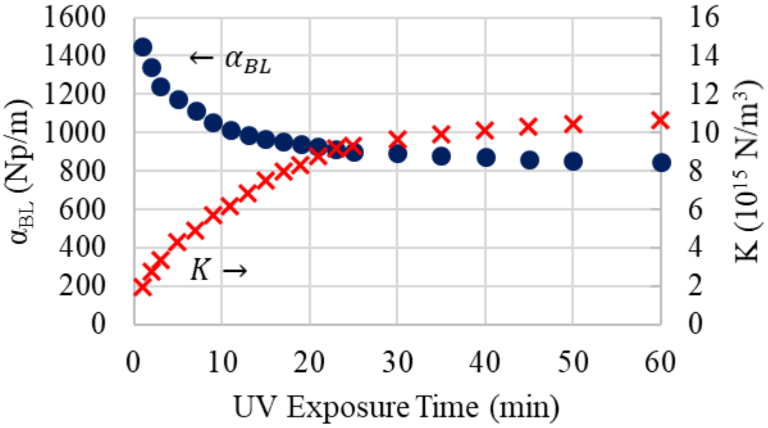

Figure 6.26: Adhesive attenuation coefficient (α_{BL}) and interfacial stiffness (K) vs. UV-light exposure time, extracted from curve-fitting phase of bond line reflections

A 95% confidence interval was also found for each of the parameters, but they are not plotted in Figure 6.26 as they are too small to be visible. The mean confidence interval for the interfacial stiffness flux parameter is $\pm 1.3\%$ of the fitted value, and the mean confidence interval for the attenuation coefficient is $\pm 0.6\%$ of the fitted value. As mentioned previously, the adhesive attenuation coefficient is known to decrease as a function of cure time. In addition to the bulk attenuation property, the phase responses show a monotonically increasing interfacial stiffness per unit area constant during the cure process, leveling off at the same time as bulk attenuation at ~25 minutes of UV light exposure. Showing sensitivity to small interfacial quality changes during this cure-monitoring experiment suggests ultrasonic phase measurements around the bond line's resonance frequency may be able to identify previously undetectable kissing bonds.

6.3.3.3 Post-Cure Ultrasonic and Mechanical Bond Evaluation

In the same manner as the cure-monitored SLJ, the glass adherent phase response was subtracted from each bonded joint's phase response to obtain the phase response of the bond line, $\phi_{BL}^{meas}(f)$. The $\phi_{BL}^{meas}(f)$ curves were fitted to the theoretical model of ultrasonic interactions with SLJs expressed in Equation 6.7.

The same parameters in Table 6.2 were used in the curve-fitting model with the exception of bond line thickness, which was measured for each specimen individually. The adhesive sound velocity was set for each UV-exposure time from the measurement results discussed in Section 6.3.3.1. The same free parameters and initial guesses shown in Table 6.3 were used again by the curve-fitting algorithm in this study. For each bonded joint, the adhesive attenuation coefficient and interfacial stiffness flux constant were extracted. However, only the interfacial stiffness flux is of interest to this work.

From the mechanical testing, the tensile strength of each SLJ is determined by dividing the maximum load by the adhesive cross-sectional area. Ultimate tensile strength of each of the 10 SLJs is plotted as a function of UV-light exposure time in Figure 6.27a. Notably, each SLJ broke adhesively at one of the adhesive/adherent interfaces, regardless of tensile strength.

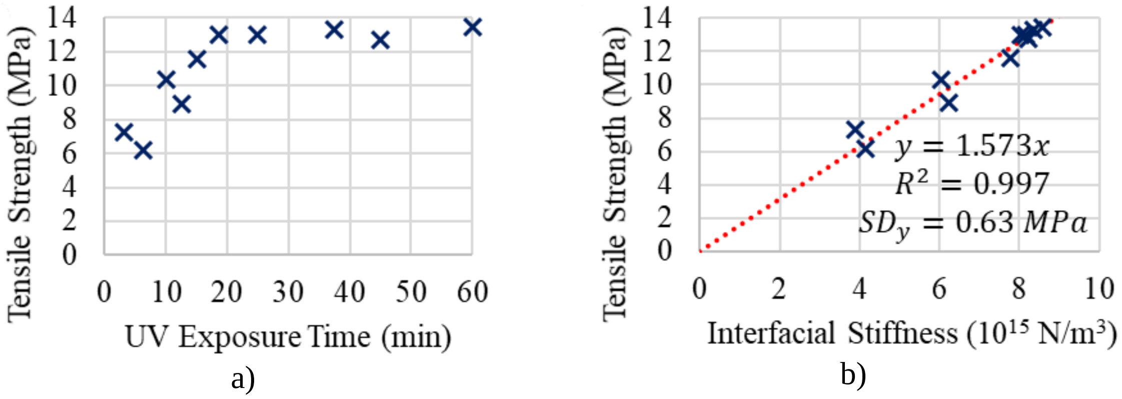

Figure 6.27: a) Measured tensile strength as a function of adhesive UV light exposure; b) Measured tensile strength vs. interfacial stiffness flux for glass/UV-curable adhesive SLJs, including linear fit

Similar to the attenuation and interfacial stiffness curves from the cure-monitored SLJ in Figure 6.26, the tensile strength of the SLJs levels off after about 25 minutes of UV light exposure. Since all SLJs failed at the adhesive/adherent interface, correlation of the ultrasonically measured interfacial stiffness constants with mechanically measured tensile strengths was performed. The measured tensile strength vs. interfacial stiffness flux of each SLJ is plotted in Figure 6.27b.

According to results of Cantrell in epoxy/alumina bonds, the ultrasonic interfacial stiffness flux constant has a linear relationship with tensile bond strength [64]. The linear fit of the experimental tensile strength vs. interfacial stiffness from this study shows this relationship holds true in Borofloat/NOA 60 SLJs, as well. The strong correlation between ultrasonically measured interfacial stiffness and mechanical bond strength suggests swept-frequency phase measurements have sufficient sensitivity to predict interfacial bond quality.

6.3.3.4 Single Phase Parameter Correlation to Tensile Strength

To aid in speed and simplicity of interfacial bond quality evaluation, an additional method of using a single measured parameter from the measured phase spectrum was studied for its correlation to interfacial bond strength. Without using a curve-fitting method to solve the inverse problem of finding K from the measured phase spectrum, the anti-resonance frequency is correlated to tensile strength, directly. This method was initially discussed at the end of the discussion on the theoretical phase vs. frequency response of bonded joints in Section 3.2.

In this study, the anti-resonance frequency of the bond line reflection coefficient is approximated by the zero-crossing frequency of the measured bond line phase response. That is, the zero-crossing frequency measured phase spectrum is the frequency at which $\phi_{BL}^{meas}(f_{ar}) = 0\,deg$. For a perfect bonded joint, $f_{ar} = c_{adh}/2L_{BL}$, but weak interfacial stiffness causes a reduction in anti-resonance frequency. Figure 6.28 displays the tensile strength vs. the anti-resonance frequency from the phase response of each joint after normalization to the nominal thickness of 102 µm and fully cured sound velocity of 2316 m/s. The normalization of anti-resonance frequency factors out sound velocity changes as a function of degree-of-cure as well as bond line thickness variations, leaving only anti-resonance shifts due to interfacial stiffness.

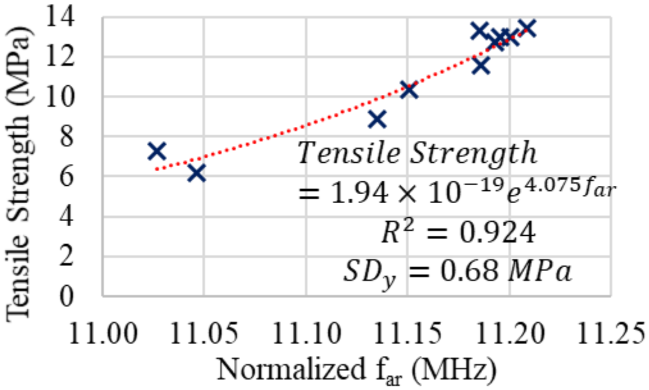

Figure 6.28: Tensile strength vs. normalized anti-resonance frequency approximated from zero-crossing frequency of $\phi_{BL}^{meas}(f)$, including exponential fit

In Figure 6.28, a strong exponential correlation between tensile strength and normalized anti-resonance frequency is observed. Given a normalized anti-resonance frequency measurement, ultimate tensile strength is predicted by the exponential curve fit within a standard deviation of $0.23\ MPa$. Such a curve fit is unique for a given bonded joint configuration. These results indicate interfacial bond strength may be predicted by the zero-crossing frequency of the ultrasonic phase response of a bonded joint.

6.4 Evaluation of Metal/Epoxy Joints with Interfacial Contamination

6.4.1 Theory

The reflection coefficient of a single lap joint with imperfect interfaces, as shown in Equation 3.19, is representative of an aluminum/epoxy SLJ with reduced bond strength due to contamination at one or both interfaces. Several assumptions can be made, however, to simplify the reflection coefficient. First, both adherents are made from the same material, so the elastic constants and wavenumbers are assumed equal in each adherent. Second, for a thin layer of contamination, the mass loading at the interfaces will be negligible, so m is assumed zero. Unlike in Equation 3.20, it cannot be assumed that both interfacial stiffness constants are equal, because in real-world scenarios one adherent may be more contaminated than the other, resulting in different interfacial bond strengths. The resulting bond line ultrasonic reflection coefficient allowing for different interfacial bond strengths is expressed in Equation 6.8.

$$R_{BL} \approx \frac{C_N \cosh(k_{adh}L_{BL}) + S_N \sinh(k_{adh}L_{BL})}{C_D \cosh(k_{adh}L_{BL}) + S_D \sinh(k_{adh}L_{BL})} \tag{6.8}$$

$$C_N = (E_1 k_1 E_{adh} k_{adh}) \left[\frac{E_1 k_1}{(K_1^{-1} + K_2^{-1})^{-1}}\right]$$

$$C_D = (E_1 k_1 E_{adh} k_{adh}) \left[2 + \frac{E_1 k_1}{(K_1^{-1} + K_2^{-1})^{-1}}\right]$$

$$S_N = (E_1^2 k_1^2 - E_{adh}^2 k_{adh}^2) + E_1 k_1 E_{adh}^2 k_{adh}^2 \left(\frac{1}{(K_1^{-1} - K_2^{-1})^{-1}} + \frac{E_1 k_1}{K_1 K_2}\right)$$

$$S_D = (E_1^2 k_1^2 + E_{adh}^2 k_{adh}^2) + E_1 k_1 E_{adh}^2 k_{adh}^2 \left(\frac{1}{(K_1^{-1} + K_2^{-1})^{-1}} + \frac{E_1 k_1}{K_1 K_2} \right)$$

Just as in the glass/UV-curable adhesive study in Section 6.3, the ultrasonic anti-resonance frequency of the bonded joint will shift based the interfacial stiffness constants. When the interfacial stiffness constants are equal, the slope of phase shift at the anti-resonance frequency will only be determined by the adhesive ultrasonic attenuation coefficient. However, the difference between stiffness constants at each interface will also modify the “sharpness” of the phase inversion near the anti-resonance frequency. Consequently, measurement of both the slope of phase inversion and the anti-resonance frequency will be necessary to measure the two unknown interfacial stiffness constants, and thereby determine interfacial bond strengths.

6.4.2 Experimental Setup

6.4.2.1 Bonded Joint Fabrication

Single lap joints of different interfacial bond quality were fabricated to study the ability of the swept-frequency phase measurement method to assess bond quality. Spray coating of polytetrafluoroethylene (PTFE) – commercially known as Teflon – onto an adherent surface prior to bonding is used to modify interfacial bond strength, as PTFE provides a poor bonding surface. In this study, pristine bonded joints are compared to bonded joints with PTFE contamination at one of the adhesive/adherent interfaces.

Originally, PDMS – a silicone based contaminant – was going to be used for interfacial contamination in this study, as it had been successfully used in Section 6.2. However, PDMS was found not to affect the film adhesive used in this study, FM73 from Cytec, as it had the FL901AO adhesive from Master Bond used in the previous study. Even though different concentrations of PDMS dissolved in hexanes were spray-coated to the bonding surface, the ultimate shear strength was not appreciably modified and interfacial failure did not occur. As a final test, pure PDMS was applied to the adherent, but the bond strength still did not drop off as it had with the first adhesive. It is believed that since liquid PDMS was used, instead of remaining at the interface, it diffused into the FM73 adhesive layer during cure. For an unknown reason, the PDMS affected the FL901AO adhesive differently, remaining at the surface and inhibiting bonding. As alternative, PTFE contamination was examined, which dries solid on the surface and was found to inhibit interfacial bonding as required.

To match typical bonded joints found in the aerospace industry, aluminum alloy 6061-T651 (Al 6061-T651) from Midwest Steel Supply Co. were chosen for adherents and were machined into 2.54 cm wide x 1.27 cm tall x 15.24 cm long specimens to be used in a lap-shear joint configuration. The adherents were bonded together with FM73 unsupported epoxy film adhesive from Cytec with a nominal thickness of 127 µm. A diagram showing the SLJ configuration after fabrication is shown in Figure 6.29.

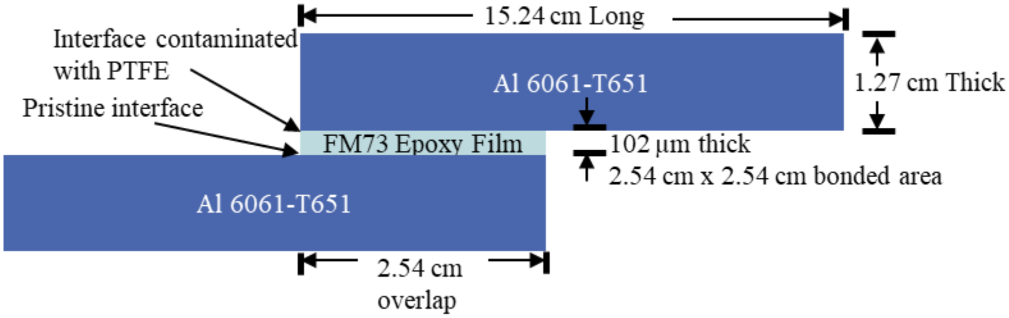

Figure 6.29: Setup of Al 6061/epoxy film adhesive lap joints, showing contaminated interface

The machined Al 6061-T651 coupons were cleaned prior to bonding to provide a clean and consistent bonding surface. The cleaning process consisted of a detergent wipe and water rinse, ethanol wipe and ethanol rinse, 30 minute ultrasonic cleaning bath in ethanol, and vapor degreasing in ethanol. For the contaminated specimens, one Al 6061-T651 coupon from each set of adherents was then spray coated with PTFE for ~2 seconds at a distance of ~20 cm using MS-122AD Dry

Film PTFE release agent in aerosol form from Miller-Stephenson Chemicals. The other adherent on each lap joint specimen was left pristine (i.e. uncontaminated).

A variation in interfacial bond strength was obtained by controlling the area coverage of PTFE on the adherent surface prior to bonding. Masks with distributed circular holes made of perforated sheet metal stock, shown in Figure 6.30, were fixed to the adherent surface during spray coating. This resulted in a distributed array of circular PTFE islands on the surface of the adherent. Ultimately, five bonded joints with different areas of PTFE contamination were fabricated.

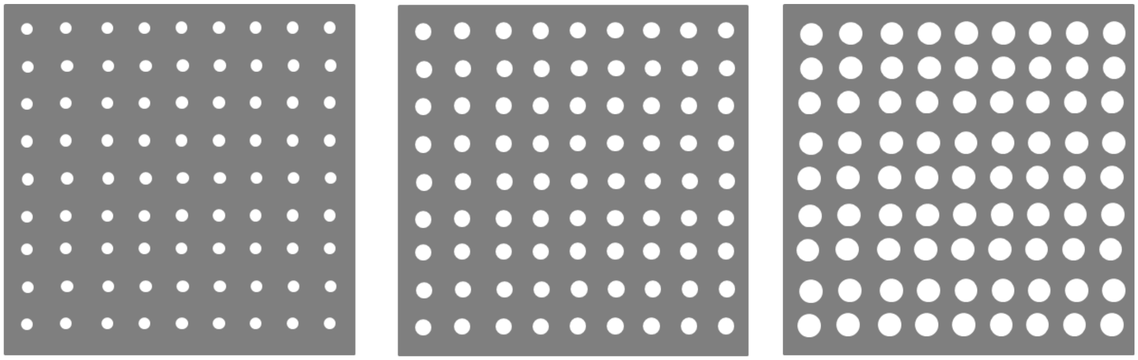

Specimen 2 Mask:
Hole Diam.=1.0mm
12% exposed

Specimen 3 Mask:
Hole Diam.=1.6mm
29% exposed

Specimen 4 Mask:
Hole Diam.=2.4mm
65% exposed

Figure 6.30: Masks used for PTFE contamination of adherents prior to bonding

While the exposed area in the masks provides a good estimate of the ultimate PTFE relative area of coverage on the adherent surface, additional witness specimens were also spray-coated using the same masks to better understand the PTFE islands deposited on the adherents. After spray coating, the spacing between PTFE islands should remain the same as the spacing between the holes in the masks. However, there is some spreading of the PTFE under the edges of the mask holes, so that the circular PTFE islands are slightly larger than the original mask hole diameters. Figure 6.31 shows optical micrographs of the PTFE islands from spray coating through each of the three masks. As the layer is very thin, it is almost transparent and just appears as a hazy white region on the Al surface.

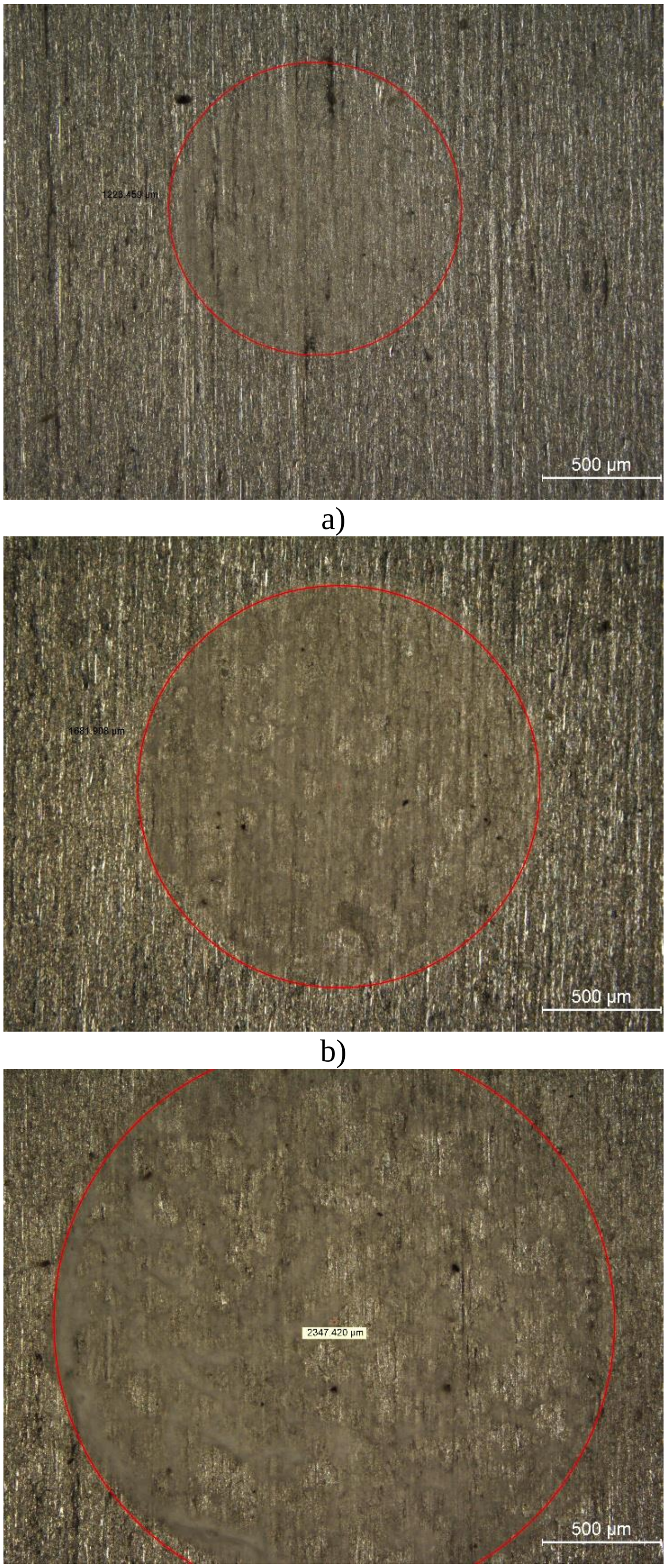

a)

b)

c)

Figure 6.31: Optical micrographs at 5x magnification of circular PTFE islands deposited on Al adherent surfaces through a) Mask 1, b) Mask 2, and c) Mask 3

From the micrographs, the diameter of circular PTFE islands was measured, and the adjusted relative area covered by PTFE is shown in Figure 6.3. As predicted, there is indeed some spreading of the PTFE under the edges of the masks, so that the diameters of the circular PTFE islands on the surface were slightly larger than the diameters of the mask holes. This effectively increased the relative area coverage of PTFE on the adherent surface prior to bonding.

Table 6.4: PTFE contamination mask critical dimensions and measured PTFE island dimensions

Specimen	Mask Hole Diameter	Mask Rel. Exposed Area	PTFE Island Diameter	PTFE Rel. Covered Area
1 (Pristine)	0 mm	0%	0 mm	0%
2 (Mask 1)	1.0 mm	12%	1.2 mm	18%
3 (Mask 2)	1.6 mm	29%	1.7 mm	34%
4 (Mask 3)	2.4 mm	65%	2.5 mm	73%
5 (100% PTFE)	N/A	100%	N/A	100%

After surface preparation, the lower pristine adherent was placed on a surface and a 2.54 cm x 2.54 cm square of FM73 film adhesive was applied to the prepared end of the adherent surface, leaving a small amount of space for metal shims. Next, $101.6\ \mu m$ metal shims cut into thin strips of 2.54 cm length were applied to both sides of the film adhesive. This adhesive bond line thickness was specifically chosen to produce a resonance frequency within the $8.5 - 11.75\ MHz$ range viewable by the PPLL ultrasonic phase measurement instrument. The peel-ply of the film adhesive was then removed and the upper adherent was placed on the adhesive/adherent stack to form the SLJ. Metal clips of 2.54 cm thickness were used to apply pressure on the SLJ during cure. The SLJs were then cured in an oven according to manufacturer specifications.

Several witness specimens were created to verify the effect of the change in surface area of the PTFE. Five 2.54 cm x 2.54 cm square Al 6061 coupons were spray coated with PTFE in the same method as the adherents. Then, OSEE measurements – originally mentioned in Section 1.2.2 – were conducted on the surface of the coupons. With OSEE, the measured peak voltage should drop as the amount of surface contamination increases, as the UV light is prevented from reaching the Al 6061 surface. Figure 6.32 displays the drop in OSEE voltage after contamination for each of the coupons. OSEE is extremely sensitive to surface contamination, and as a result, shows a sharp change in voltage for even the lowest amount of contamination used in this study. A monotonic trend in voltage drop as a function of PTFE area coverage is seen, confirming that changing the area coverage of PTFE indeed modifies the amount of contamination on the surface.

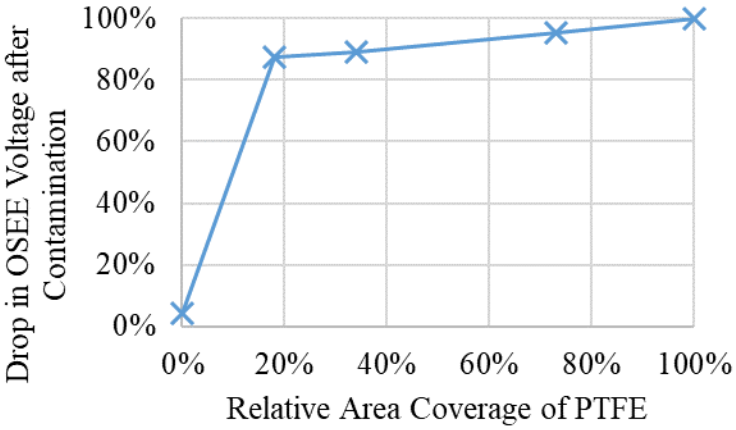

Figure 6.32: Drop in OSEE voltage after contamination vs. PTFE area coverage on surface

6.4.2.2 Ultrasonic and Mechanical Testing Setup

After curing in the oven, the bonded joints were ultrasonically evaluated with a 10 MHz center frequency Olympus V112 ultrasonic transducer via the swept-frequency phase measurement method and broadband pulse-echo ultrasound. The swept-frequency phase measurements, taken with the PPLL instrument described in Chapter 4, were conducted from 8.5-11.75 MHz with a 0.01 MHz step size. Broadband ultrasonic pulses were generated using a GE Panametrics Model 5900PR pulser-receiver using a pulse energy of 1 μJ and a passband of 1 kHz-200 MHz, so that the ultrasonic frequency range was only limited by the transducer bandwidth. The first echo from the bond line was amplified and then received on a LeCroy WaveRunner 6200 oscilloscope. A reference ultrasonic measurement on a bare metal section of the adherent was also obtained so that the amplitude and phase response of the adherent could later be subtracted out of the response of the completed bonded joint, leaving only the response from the adhesive bond line. After ultrasonic analysis, quasi-static mechanical pull testing was conducted to find the shear strength of each SLJ.

6.4.3 Results and Discussion

6.4.3.1 Mechanical Testing Results

Figure 6.33 shows the measured bond strengths from quasi-static shear loading. Also shown is a linear fit of the data with the constraint that the shear strength at 100% PTFE coverage area is $0\ MPa$. These results show there is indeed a strong linear relationship between relative PTFE coverage area and shear strength.

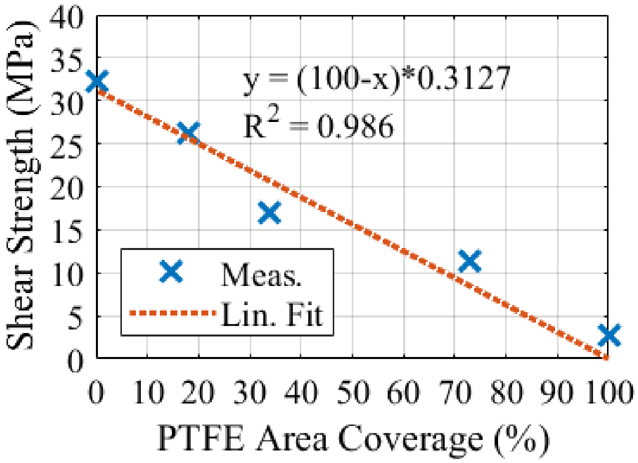

Figure 6.33: Measured shear strength vs. PTFE coverage area at interface for Al/epoxy SLJs, including linear fit of data constrained to $\tau(100\%\ PTFE) = 0\ MPa$

6.4.3.2 Amplitude and Phase Results

Both the PPLL phase measurements and broadband pulse measurements were analyzed for the frequency-domain responses around the resonance frequency of the bond line. The received ultrasonic pulses from the bond line were converted from the time-domain to the frequency domain by use of a Fast Fourier Transform (FFT). By nature of the swept-frequency method, the phase measurements were obtained already in the frequency domain, so no conversion was necessary.

Reference phase measurements on bare Al adherents were subtracted out of the phase response from the whole bonded joint, leaving the phase response of the bond line. Similarly, the amplitude spectra from the bonded joint was divided by the reference amplitude spectra from the bare Al adherent to obtain the amplitude spectra from the bond line.

The resulting phase and amplitude spectra are shown in Figure 6.34. As previously explained theoretically in Section 3.1.2 and demonstrated in glass/UV-curable adhesive joints in Section 6.3, the phase inversion and amplitude minimum are caused by a resonance cavity effect within the bond line, nominally occurring when the bond line thickness is equal to half of the acoustic wavelength within the adhesive layer.

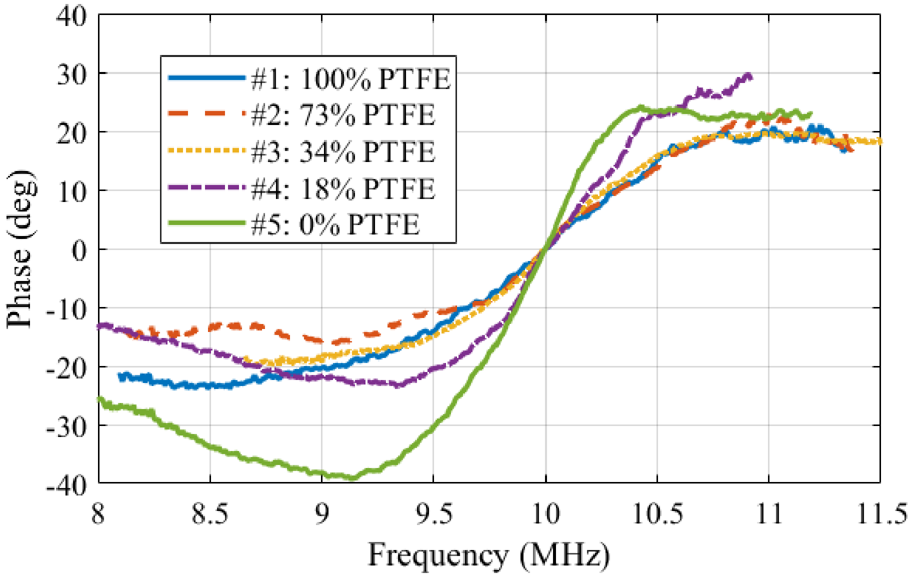

a)

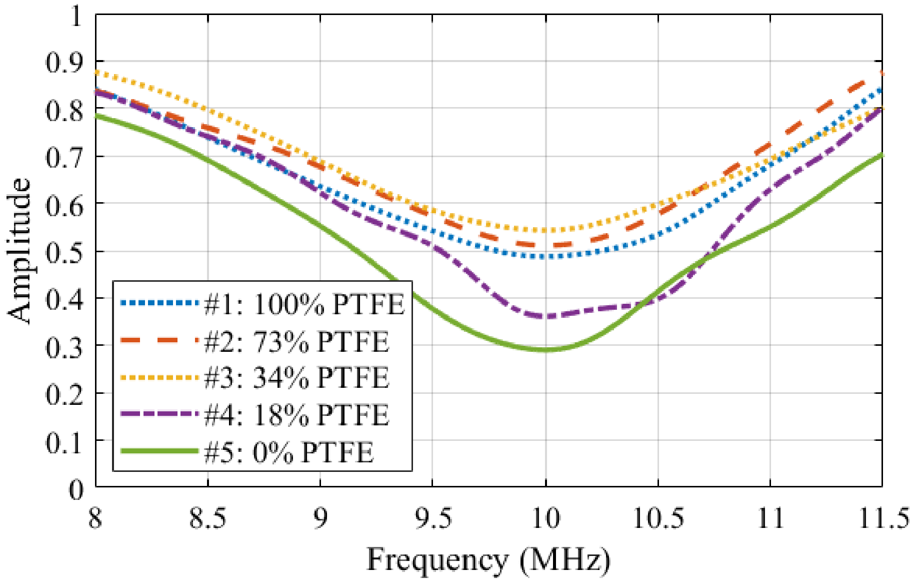

b)

Figure 6.34: a) Phase vs. frequency responses from PPLL, normalized to $f_{res} = 10\ MHz$ and $\phi(f_{res}) = 0\ deg$, and b) amplitude vs. frequency responses from broadband pulse-echo, normalized to $f_{res} = 10\ MHz$

From Figure 6.34a, the phase response measured with the PPLL method clearly shows a difference in sharpness of the phase inversion depending upon the relative area of PTFE coverage at the interface. A dampening of the ultrasonic resonance response due to reduced interface quality at one adhesive/adherent interface was predicted by theory in Section 3.2.2 and shown in Figure 3.7. In addition, notable in the phase response is the pristine, 0% PTFE interfacial contamination SLJ that displays a much sharper phase inversion than the other contaminated bonded joints. Meanwhile, the amplitude spectra show a general trend of increasing minimum amplitude or a dampening of the resonance response with increasing PTFE area coverage, but for higher PTFE coverage areas, there is not a monotonically increasing trend.

6.4.3.2.1 Analysis of Bond line Acoustic Resonance to Find K_1

To further analyze the measured amplitude and phase spectra, two inverse methods for determining interface stiffness were developed and compared. First, the properties of the phase and amplitude responses at the bond line resonance frequency were determined. For the amplitude spectra, the amplitude minimum and the frequency at amplitude minimum were found. For the phase spectra, a partial derivative of the phase shift with respect to frequency was conducted to find the maximum slope of phase shift, shown in Figure 6.35. Immediately noticeable is the change in peak phase slope as a function of PTFE area coverage.

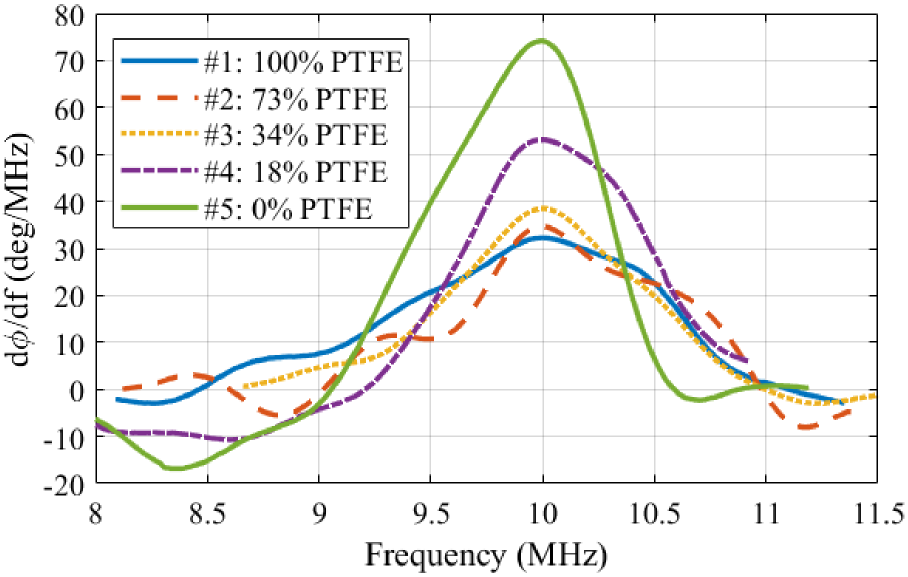

Figure 6.35: Phase slope vs. frequency response of bond line reflections, smoothed and normalized to $f_{res} = 10\ MHz$

The computed amplitude minimums and phase slope maximums are plotted together in Figure 6.36. The $d\phi/df_{max}$ parameter shows a monotonically decreasing trend as a function of relative area of interfacial PTFE coverage. Similarly, the A_{min} parameter displays an increasing trend with increasing PTFE area coverage, but it does display some uncertainty for the higher PTFE coverage areas. In particular, the amplitude minimum for the 34% and 73% PTFE coverage areas appear higher than the 100% PTFE coverage area SLJ.

Equation 6.8 was used to model the Al/epoxy SLJs with different interfacial stiffness constants at the upper adherent/adhesive interface and then used to find the theoretical $d\phi/df_{max}$ and A_{min} as a function of K_1. Then, the interfacial stiffness for each measured $d\phi/df_{max}$ and A_{min} parameter is found by identifying the corresponding K_1 on the theoretical curve.

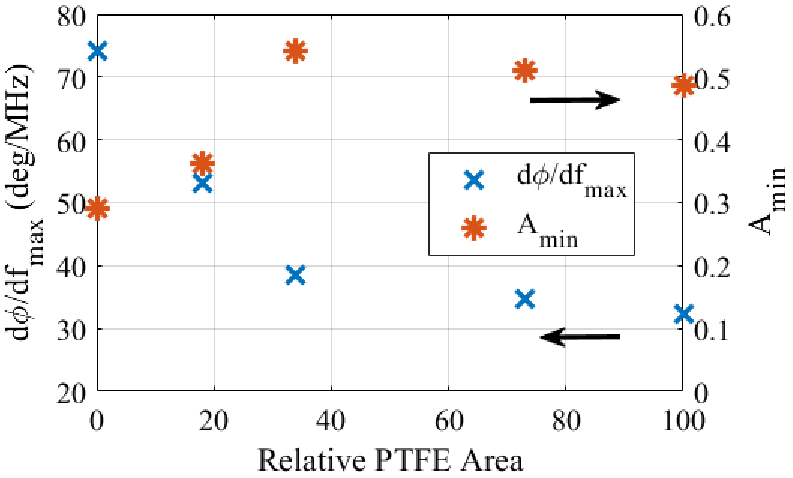

Figure 6.36: Measured maximum phase slope and amplitude minimum for each SLJ as a function of the percent relative PTFE area

6.4.3.2.2 Curve-Fitting Algorithm to Find K_1

The second method developed to determine interfacial stiffness from the measured amplitude and phase spectra uses a curve-fitting algorithm of the measured spectra in the entire 8.5-11.75 MHz range. For the phase response Equation 6.9 is used, which is similar to the model used in the previous study described in Section 6.3.3.2. In both Equations 6.9 and 6.10, R_{BL}^{Theor} is the reflection coefficient expressed in Equation 6.8.

$$\phi_{model}(f; K_1, L_{BL}, a, b) = \phi_{R_{BL}}^{theor}(f; K_1, L_{BL}) + af + b \tag{6.9}$$

$$|R|_{model}(f; K_1, L_{BL}, c) = c * \left|R_{BL}^{Theor}(f; K_1, L_{BL})\right| \tag{6.10}$$

The set, constant parameters used in these curve-fitting models are shown in Table 6.5.

Table 6.5: Set parameters used in curve-fitting models for Al/epoxy SLJs

Parameter Name	Value
Adherent Sound Vel.: $c_1 = c_2$	6428 m/s
Adhesive Sound Vel.: c_{adh}	2328 m/s
Adherent Density: $\rho_1 = \rho_2$	2681 kg/m^3
Adhesive Density: ρ_{BL}	1189 kg/m^3
Adhesive Attenuation: α_{adh}	0.05 f^{-1}

The free parameters used in the curve-fitting models are shown in Table 6.6. The bond line thickness is initially set to be the average bond line thickness across all bonded joints measured with a micrometer, and it is allowed to vary ±5 μm. The upper bound of the interfacial stiffness constant is set to $3.8 \times 10^{17}\ N/m^3$ based on Cantrell's work showing that this value represents perfect bonding between aluminum and epoxy [64].

Table 6.6: Free parameters used in curve-fitting models for Al/epoxy SLJs

Parameter (units)	**Initial Guess**	**Lower Bound**	**Upper Bound**
Bond line Thickness: L_{BL} (μm)	109.3	104.3	114.3
Interfacial Stiffness Flux: K_1 ($\mathrm{N/m^3}$)	10^{16}	10^{12}	3.8×10^{17}
Linear Phase Term: a (deg/Hz)	0	-3×10^{-6}	3×10^{-6}
Constant Phase Term: b (deg)	0	-10	10
Amplitude Factor: c (unitless)	1	0	2

Figure 6.37 shows examples of how well the measured phase and amplitude data is fit via the curve-fitting algorithm. Blue crosses represent measured data points, while red lines represent the fitted curve. Prediction bounds with dotted red lines are not easily seen in the plots, as they are so close to the fitted curve lines.

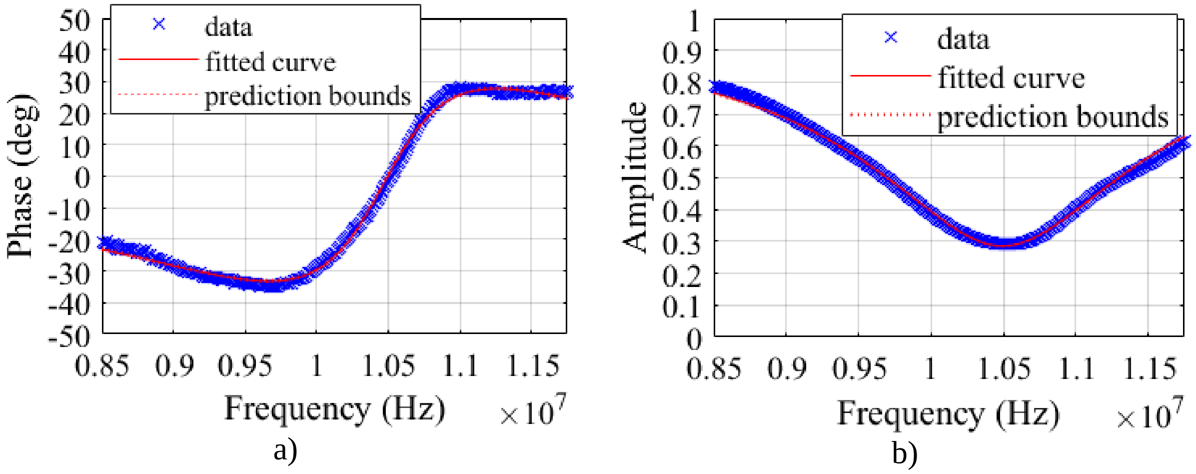

Figure 6.37: Examples of curve fitting results on SLJ sample #5: Pristine for a) phase vs. frequency and b) amplitude vs. frequency responses

The interfacial stiffness constants found for each bonded joint with both the single-parameter method and the curve-fitting method are plotted against measured shear strength in Figure 6.38.

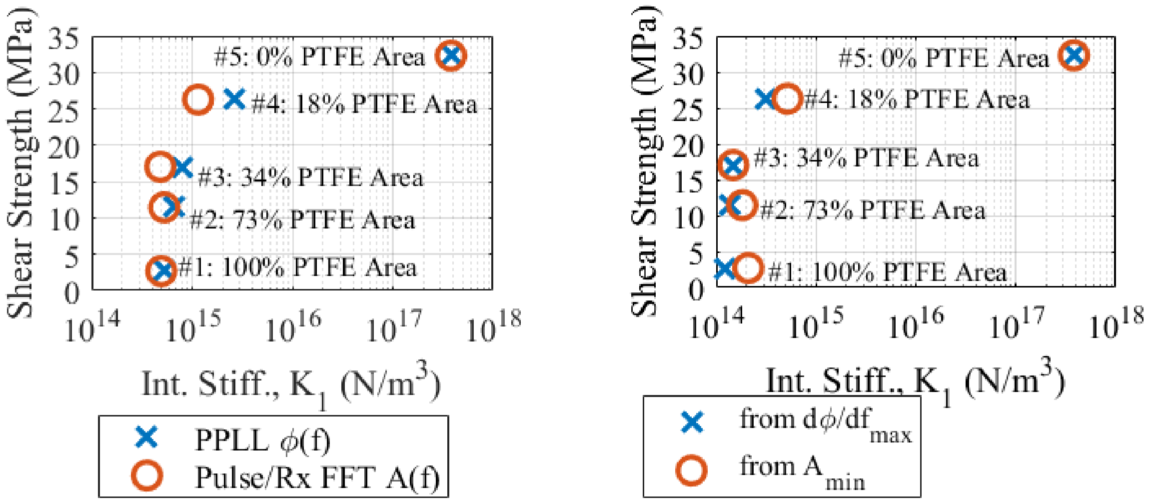

Figure 6.38: Measured shear strength vs. interfacial stiffness from amplitude and phase response of bond line reflections from a) Curve fitting of entire frequency response in $8.5 - 11.75\ MHz$ range and from b) Curve behavior at bond line acoustic resonance frequency

The single-parameter method tends to underestimate K_1 for all PTFE-contaminated joints. For the uncontaminated joints, all methods determined K_1 to be its maximum value of $3.8 \times 10^{17}\ N/m^3$, successfully predicting a well-bonded interface. As noted in the phase slope and amplitude minimum data from Figure 6.36, the phase measurements here all show bond strength as a monotonically increasing function of K_1. The amplitude results, on the other hand, show a slight negative shift in interfacial stiffness as the bond strength increases for the first three data points. Overall though, the amplitude and phase data show good agreement in terms of K_1 assessment as a function of bond strength and PTFE interfacial contamination.

6.4.3.3 Connection between Measured Interfacial Stiffness to Theory

From the work of Cantrell, the relationship between interfacial bond strength and ultrasonically measured interfacial stiffness in alumina-epoxy bonds is found [64]. Both bond strength and interfacial stiffness are a function of the number of bonds per unit area at the interface. In this study, the fraction disbond area at the interface is modified by the relative area of coverage of

PTFE on the adherent prior to bonding. Figure 6.39 shows the measured bond strength and interfacial stiffness values along with the theoretical values based on their relationship with fractional interfacial disbond area.

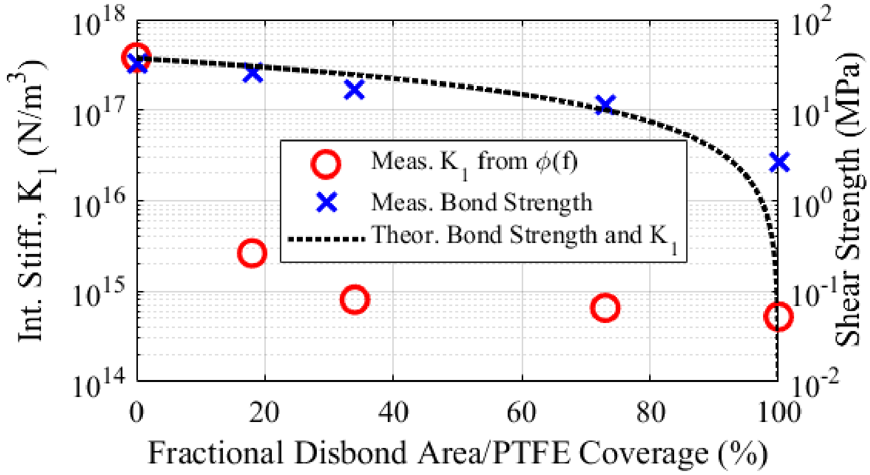

Figure 6.39: Measured interfacial stiffness and bond strength vs. disbond area at the interface, including line showing theoretical interfacial stiffness and bond strength from Cantrell [64]

In Figure 6.39, it is seen that shear strength matches quite well with PTFE interfacial coverage, according to theory. It should be noted that the 100% PTFE coverage area bonded joint broke at some value above 0 MPa, partially due to the adhesive squeezing out of the sides of the joint during cure. Thus, the tacking on of the adhesive on the sides of the joint produce some apparent bond strength when there otherwise should be none.

Next, it is notable that the trend in the measured interfacial stiffness vs. PTFE coverage area does not at all track with theory. The main problem seems to lie in the bonded joints contaminated through masks to vary the shear strength and not the 0% and 100% PTFE coverage area bonded joints, which match quite well with theory. In an attempt to determine the mechanism by which interfacial stiffness does not track with Cantrell’s theory, additional literature review was conducted.

After some search, it was found that the patterning of PTFE on the surface in circular islands might behave like a distributed array of interfacial cracks to ultrasonic waves, rather than a simple fractional disbond area [146], [98], [147]. Figure 6.40 shows the theoretical interfacial stiffness as a function of relative disbond area for a distributed array of interfacial disk and strip cracks, Cantrell's theory, as well as the measured K_1 from $d\phi/df_{max}$.

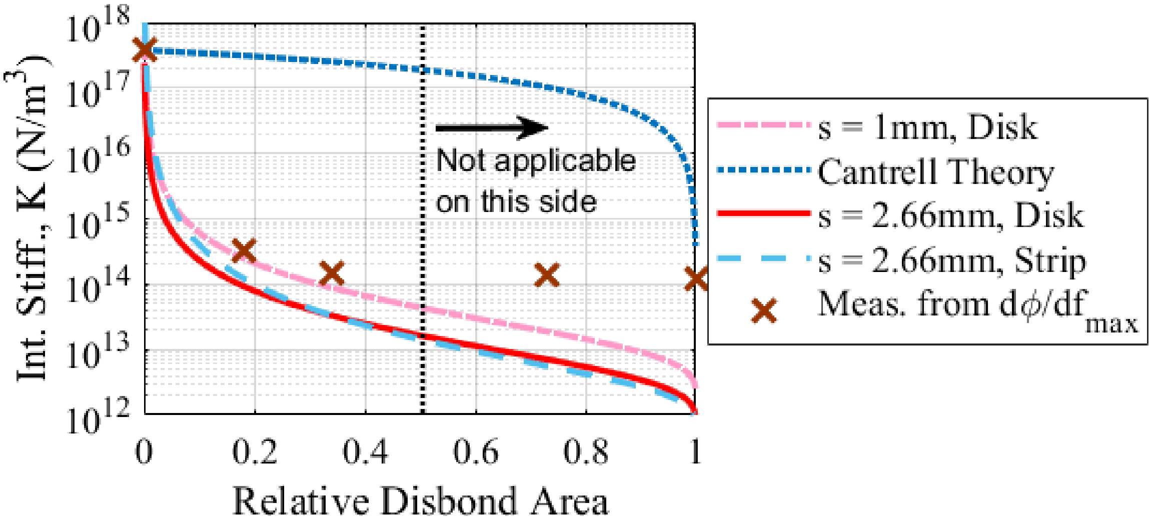

Figure 6.40: Interfacial stiffness vs. relative disbond area from different theoretical treatment and as measured

Throughout Figure 6.40, s is the distance between crack centers. An interfacial array of disk cracks is most similar to the circular islands of PTFE used in this study. The value of $s = 2.66\ mm$ was chosen for its similarity to the distance between the centers of the circular PTFE islands in this study, and the value of $s = 1\ mm$ was chosen as it seemed to fit closely with the measured data. It should be noted that the distributed array of interfacial cracks theory used here is only applicable for non-interacting cracks, which occurs approximately for relative disbond areas less than 50%.

From this new theory, it seems that the circular PTFE islands behave similar to a distributed array of disk cracks with a center spacing near 1 mm. Above a disbond area of 50%, the array of cracks is considered interacting, and the analysis becomes much more difficult. As such, there is not much theory in the literature about this region.

Overall, the 0% and 100% PTFE coverage area bonded joints fit well into Cantrell's theory of interfacial stiffness and relative disbond area. For the bonded joints with PTFE spray-coated through masks with circular holes, the interfacial stiffness behaves similar to a distributed array of circular cracks model due to ultrasonic scattering and diffraction at the interface, rather than a simple disbond density model. In all bonded joints, however, the shear strength follows the disbond density model presented by Cantrell. Accordingly, ultrasound is affected differently by the presence of a distributed array of interfacial cracks than actual bond strength is affected.

6.5 Conclusions

Throughout this chapter, ultrasonic phase measurement methods of evaluating interface quality in adhesively bonded SLJs have been investigated. In particular, these methods use the CFPPLL-based ultrasonic phase measurement instrument to obtain the phase response of the normal-incidence ultrasonic displacement wave reflection coefficient of the bond line in a SLJ.

Initially, a constant-frequency method for measuring phase shifts as a function of small temperature changes in a ceramic/Salol SLJs is demonstrated. The $d\phi/dT$ parameter over a $5°C$ temperature span is able to distinguish well-bonded regions, porous regions, and disbonded regions across the joint. While showing some promise, this method was found in practice to be very time intensive waiting for the sample to reach thermal equilibrium, and it was found difficult to obtain temperature dependent material properties for many aerospace adhesives and adherents to be studied. Consequently, it was determined to explore an improved method of phase analysis of adhesive bonding, which might have a wider range of applicability and be simpler to use.

Next, the CFPPLL instrument was modified to allow for swept-frequency ultrasonic phase measurements, rather than tracking the phase at a single frequency while the joint undergoes some sort of external stimuli. The new swept-frequency method is investigated in Al/epoxy SLJs and compared to conventional broadband amplitude-based ultrasound. Two sets of bonded joints are fabricated: one with pristine adhesive bonding and another with silicone-based contamination at one of the adhesive/adherent interfaces. Ultrasonic results found that the swept-frequency phase method was able to distinguish the pristine joints from the contaminated joints via the slope of the phase vs. frequency response over a 9-10 MHz range. Conversely, both in the time domain and the frequency domain, broadband amplitude-based ultrasound was unable to distinguish strong from weak bonds. Mechanical shear testing confirmed the silicone contamination reduced interfacial bond strength to about 25% of the pristine bond strength. This study proved that swept-frequency phase measurements are sensitive to reduced adhesion strength not easily detectable with conventional ultrasonic methods.

In the next study, analysis of swept-frequency ultrasonic phase measurements of bond line reflections in glass/UV-curable adhesive tri-layer bonded joints has been shown to quantitatively assess adhesive bonding properties without the presence of interfacial contamination or gross bonding defects. By focusing on the phase response near the ultrasonic anti-resonance frequency of the bond line reflection coefficient, the shift in anti-resonance frequency is measured as a function of adhesive cure. The adhesive stiffness and resulting sound velocity change during cure is measured separately via broadband ultrasound ToF. After curve fitting to the theoretical ultrasonic interaction with imperfectly bonded joints, the attenuation coefficient as well as the interfacial stiffness flux are extracted. The correlation to mechanical tensile strength is consistent with the theoretical linear relationship between interfacial stiffness and absolute interfacial bond strength. In this work, interfacial bond strength is predicted by interfacial stiffness flux to a standard deviation of 0.63 MPa.

Finally, the swept-frequency phase method is extended to real-world bonded structures with rough Al adherents and epoxy film adhesive. Interfacial bond strength in this study is modified by Teflon-based contamination spray-coated through masks onto one adherent surface prior to bonding. Masks with distributed holes of different size and spacing are used to modify the relative area of Teflon contamination coverage on the adherent surface. Mechanical testing results found a linear relationship between relative contamination coverage at the interface and shear strength, as was predicted. Ultrasonic phase and amplitude spectra in the 8.5-11.75 MHz range were obtained on each SLJ and were found to both give consistent predictions of interfacial stiffness which varied as a negative monotonic function of Teflon contamination coverage, although the phase results displayed less uncertainty. Interfacial stiffness results from ultrasonic phase measurements could clearly distinguish the Teflon coverage area and bond strength in each specimen. While the trend in measured interfacial stiffness for SLJs with Teflon contamination sprayed through masks did not initially match theory, further research found an adequate explanation of the measured interfacial stiffness values in these cases.

Overall, these results prove the swept-frequency ultrasonic phase measurements can quantify interfacial stiffness in SLJs. Interface stiffness is determined by either a curve-fitting method or assessment of the resonance frequency and maximum phase slope. The method can determine intermediate bond strengths rather than simply identify good or bad bonds. As such, this method has the potential to reliably evaluate bond strength and therefore promote the use of advanced composite structures using adhesive bonding.

Chapter 7: Limitations and Challenges of the Ultrasonic Phase Measurement Method

Throughout this work, the swept-frequency ultrasonic phase measurement has been studied for its ability to assess adhesive bond quality, focusing on the measurement of the stiffness constant at adhesive/adherent interfaces. From this study, ultrasonic phase has proved able to quantify interface stiffness from phase measurements of ultrasonic reflections, and these stiffness measurements are well correlated to both theory and interfacial bond strength. However, the CFPLL-based method has been used in specific laboratory setups thus far, and other practical considerations are necessary to identify when this technique may be ideal and challenges of its use in some applications. Consequently, a discussion of the limitations and challenges of the swept-frequency ultrasonic phase measurement method for adhesive bond strength evaluation is necessary for a more complete understanding of its efficacy and future uses.

This chapter begins by discussing general limitations of CFPPLL-based ultrasonic phase measurements. Next, there is a discussion of limitations of the current CFPPLL instrument, which could be overcome with future modifications and improvements. Finally, the challenges in using swept-frequency ultrasonic phase measurements in single lap joints (SLJs) are investigated. In each section, potential methods for overcoming these limitations and challenges are also proposed.

7.1 General Limitations

7.1.1 Phase Uncertainty with Contact Measurements

To transmit ultrasound into a material testing, the acoustic waves must first travel through some intermediate medium from the transducer to the material under test. This medium is often referred to as the ultrasonic couplant, as under ideal design, it couples the ultrasonic signal into the test material with minimal loss and maximum amplitude. In practice, the couplant medium is often a liquid -- especially water -- because longitudinal ultrasound transmits very well through most liquids. Noncontact ultrasonic methods do exist but require higher power, are very lossy, and are typically limited to about $500\ kHz$ in frequency. Laser ultrasound has also been investigated in recent years, as it can provide non-contact generation and detection of ultrasound in a test article with higher frequencies and wider bandwidth than is typically possible with piezoelectric transducers.

Common methods for using liquid couplant include fully immersing the test article in water, using a trapped water column with rubber membrane touching the test article, and providing full contact between the transducer surface and the test article with a thin liquid couplant layer in between. This last method is usually referred to as contact ultrasonic testing and is the exclusive method used throughout this work for its simplicity of use in a laboratory setting.

As initially discussed in Section 4.4.1.4 and Section 4.5, contact ultrasonic phase measurements introduce some degree of measurement uncertainty based on the thickness of the ultrasonic couplant layer. When applying pressure on an ultrasonic transducer on a test specimen with a liquid couplant medium on top, some of the couplant squeezes out from under the transducer. At a basic level, changing the couplant layer thickness changes the amplitude and phase of any measured ultrasonic echo from a test article, as the ultrasonic waves transmit through and reflect off the couplant layer. In many amplitude-based ultrasonic measurements, small changes in couplant thickness do not cause significant amplitude changes, because the couplant medium typically has a small acoustic attenuation coefficient. As such, amplitude changes due to couplant thickness are usually only considered in certain applications that require high accuracy [127] [128] [129] [130] [131] [132].

Meanwhile, changes in path length have a measureable effect on high-resolution ultrasonic phase measurements, and it was found in practice that these couplant-related phase shifts must be considered. As this liquid layer is very thin (i.e. in the micrometer range), individual reflections from within the layer cannot be time-resolved and the net sum of all internal couplant layer reflections must be considered. In the thickness gaging study described in Section 4.4, even though multiple back wall echoes were probed to subtract out many sources of phase shift, there was still a remaining undesired phase shift due to reflections from the couplant layer. By modeling the phase response of the reflection coefficient from a glass/couplant/transducer boundary, Figure 4.7 shows that even if the couplant layer is only a few microns thick, the phase shift can be very large for higher frequencies.

In contact measurements, the thickness of the couplant layer nominally depends on the couplant material as well as the pressure on the ultrasonic transducer. A study was conducted, explained in Section 4.5, on an 11 mm thick glass specimen where the load on the ultrasonic transducer was increased and swept-frequency ultrasonic phase measurements were obtained. As there was no change in the underlying specimen throughout this experiment, only the couplant layer thickness between the transducer and the test specimen were modified. Measured phase slope data from this study is shown in Figure 4.13, where it was found experimentally and backed up by theory that there is a minimum phase slope for some couplant layer thickness followed by a small increasing slope for lower thicknesses. From this study, it is concluded that for highly accurate and repeatable phase measurements obtained in a contact ultrasonic testing setup, the load on the transducer must be highly controlled. Consequently, most of the ultrasonic phase testing throughout this work was obtained by placing a load cell in the path between the transducer and a screw clamp so that a consistent couplant thickness could be obtained across all tests.

In applications of thickness gaging and single-interface characterization with ultrasonic phase, control of couplant layer thickness is very important when taken with a contact transducer. For evaluation of SLJs around acoustic resonance, however, it is found that the mostly linear phase shifts with respect to frequency from the couplant layer are less bothersome. Around acoustic resonance of a SLJ, the phase spectrum is highly nonlinear as it shifts very quickly from negative to positive values. As such, small linear offsets in the phase spectrum are accounted for in the curve-fitting model used to extract interfacial stiffness, described in Section 6.3.3.2, and do not provide a significant impediment to bond quality evaluation in SLJs.

While the testing throughout this work was obtained with contact ultrasonic measurements, it is thought that moving to a setup with a longer couplant layer path length would decrease the severity of this issue. In an immersion tank, for example, if the ultrasonic transducer is held at a fixed position away from the surface of a test article, the phase shifts caused by the couplant medium can be measured and subtracted out from the phase response of the test article, itself. Consequently, it is believed that many of the problems involving couplant thickness would be negated in an immersion-based ultrasonic scanning system and that highly accurate, repeatable phase measurements could be obtained with less complexity than was needed throughout this work with contact measurements.

7.1.2 Adherent Phase Shifts

Common to most ultrasonic evaluations of adhesive bonding is that ultrasonic waves must pass through an adherent before interacting with a bonded joint. For amplitude measurements in metals and ceramics, the losses due to attenuation through the adherent may be relatively small so that small changes in adherent thickness do not significantly affect the amplitude of bond line reflections. On the other hand, ultrasonic phase measurements for bond quality assessment are dominated by phase shifts coming from the adherent.

The ultrasonic phase shift due to propagation through a material under test is described by Equation 4.1, which shows phase is a strong linear function of frequency and dependent upon specimen thickness and sound velocity. For the metal and glass adherents used in this work, the phase shifts at 10 MHz are in the range of $1000\ deg$ per mm of thickness, and phase slopes are in the range of 100 deg/MHz per mm of thickness. Extending this, an adherent thickness change of 1 μm causes a phase shift of $\sim 1\ deg$, which is easily measureable with the CFPPLL instrument. Due to the sensitivity of the developed ultrasonic phase measurement method and the small phase changes due to interfacial stiffness to be measured, care must be taken to remove the phase shift from the adherent from the phase shift from the bond line to obtain the phase of the reflection coefficient of the bond line.

Throughout this work, two methods are employed to negate the effect of the adherent on phase shifts. In the work on single-interface characterization of dry-contact joints in Section 5.2, the phase of the bond line reflection coefficient is assumed zero with no loading and then tracked throughout the loading process where interfacial stiffness increases. In all other studies, the phase response from the back wall reflection of the adherent is taken as a reference measurement on each bonded joint. In some cases, such as in Section 5.1, the adherent phase response is measured prior to bonding in the same location the adhesive will be applied. In most of the studies of swept-frequency phase evaluation of SLJs in Chapter 6, however, the adherent phase reference measurement is obtained on an un-bonded section of the adherent after bonding. It is then assumed that the adherent thickness and sound velocity is approximately the same in the probed region as it is above the bond line. Even if there are small variations in adherent thickness between the two locations, the resulting linear phase offsets do not significantly affect interface quality assessment, because the curve-fitting method described in Section 6.3.3.2 accounts for linear phase offsets.

In practice, there are several other methods of accounting for phase shifts in the adherent. In cases where adherent thickness and sound velocity are well known, the phase response of the adherent can be simply determined based on theory from Equations 4.1 and 4.2. This method will be very sensitive to any errors in the input adherent thickness and sound velocity.

In cases where the adherent is nondispersive to ultrasound, the phase response from SLJ reflections over wide frequency ranges will be linear except for small perturbations at integer multiples of the bond line resonance frequency. A linear fit can then be conducted on the phase response, and the residuals of the linear fit will mostly contain the phase inversion that occurs near around the resonance frequency. Additionally modeling of this case may be necessary to find the precise phase response of the linear fit residuals, but the basic idea should work without the need for an adherent reference measurement.

Finally, the swept-frequency ultrasonic phase method may be paired with a broadband pulse method to obtain information about the adherent thickness and sound velocity. At each position where the SLJ is to be probed with the CFPPLL instrument, a broadband pulse can also be excited into the adherent and the time-of-flight (ToF) of the echo from the bond line can be recorded to approximate the adherent thickness using Equation 4.3. The received echo will be modified by the presence of the bond line in its frequency response, but the group velocity of the adherent will be primarily affecting the ToF of the pulse. Then, the measured thickness can be used in Equations 4.1 and 4.2 to determine the phase shift from the adherent to subtract out of the phase shift from the bond line.

7.2 Limitations of Current Phase Measurement Instrument Design

7.2.1 Time for Obtaining Phase Measurements

A practical consideration for a bonded joint assessment method to be used in real-world scenarios is the time it takes to obtain each measurement. The time it takes to make each CFPPLL measurement depends on the set repetition rate of the tone-burst as well as the number of samples averaged for each phase measurement. The repetition rate is set by a number of sine wave cycles between transmissions, and the number of samples averaged can be changed by factors of four from $4^0 = 1$ to $4^4 = 256$ samples to reduce phase noise.

The measurement time can be minimized by using the maximum repetition rate, which depends on the ultrasonic attenuation in a given specimen, as echoes should decay to the noise level prior to transmitting the next signal. In an experiment using ~11 mm thick borosilicate glass, back wall echo amplitudes dropped below the noise level after ~25 μs, meaning the repetition rate at driving frequency 10 MHz could be set as low as once every 250 cycles. Thus, averaging over 16 samples results in a phase measurement every 0.4 ms, making real-time high-resolution constant-frequency phase measurements possible in a practical setup, even with averaging to reduce uncertainty.

The current CFPPLL design is much more limited in terms of repetition rate and therefore phase measurement time. Due to the way the CFPPLL instrument communicates to the computer, during the time when the microcontroller is writing measured phase data to the computer, the instrument is unable to receive new phase measurements consistently. It was found in practice to miss phase measurements occasionally when the repetition rate is set too fast. Consequently, the repetition rate of tone-bursts is set slow enough that the microcontroller fully has time to write data to the computer prior to the next phase measurement being received. This results in a new tone-burst every 60,000 sine wave cycles at a driving frequency of 10 MHz, or one phase measurement every 6 ms. With averaging over 16 samples, this means phase measurements are output every 96 ms, making real-time ultrasonic phase tracking still possible.

When conducting swept-frequency ultrasonic phase measurements, the reduced sampling rate currently possible with the CFPPLL instrument becomes more evident. Consider a frequency sweep from 8.5-11.75 MHz in 0.01 MHz increments, as was used for interface quality evaluation in Section 6.3. The current CFPPLL instrument could obtain this phase spectra in $124.8\,s$ assuming it takes four phase measurements at each frequency to drive the output of the phase detector to quadrature. Under the same assumptions, the CFPPLL instrument is theoretically capable of obtaining the phase spectra as fast as $5.2\ s$, a major improvement on the current speed capabilities. For the swept-frequency ultrasonic phase measurement method to be developed into a scanning system that can take data a time-efficient manner, the limitation of phase measurement speed should be addressed.

7.2.2 Bandwidth

For the swept-frequency ultrasonic phase measurement method to be truly useful in a wide-variety of bonding scenarios, it needs to be capable of phase measurement at a wide variety of frequencies. This method showed the most success in interface quality evaluation when sweeping frequency around the acoustic resonance frequency of a SLJ. In this work, the bond line thickness was chosen specifically so the acoustic resonance would fall within a range viewable with the CFPPLL instrument. The current CFPPLL pass-band is at maximum about 8-12 MHz, with best amplitude response in the 9-10 MHz range. A more practical instrument, however, should be capable of assessing bond quality in SLJs with different bond line thicknesses.

The bandwidth of the current CFPPLL design is limited on purpose. Central to the CFPPLL design, after an ultrasonic echo is received by the transducer, it is narrowband filtered to remove contributions from other frequencies. Narrowband filtering is one of the primary advantages over broadband phase measurements, reducing phase noise and uncertainty. To maintain suppression of undesired frequencies while supporting a wide variety of frequencies, a design improvement of the CFPPLL instrument might include a tunable band-pass filter or a superheterodyne receiver.

7.3 Limitations on Bond Quality Evaluation in Single Lap Joints

7.3.1 Thin Adherents

There is a trade-off involved in the use of constant frequency ultrasonic measurements as opposed to broadband measurements concerning the relationship between the time and frequency domains. While constant-frequency measurements allow for higher resolution and lower uncertainty phase measurements than typically possible with broadband ultrasonic analysis, the ability to resolve separate ultrasonic signals in the time-domain is reduced.

Under basic Fourier analysis, a signal that is wide in the frequency domain is narrow in the time domain, and a signal that is narrow in the frequency domain is wide in the time domain. In conventional ultrasonic testing, a high amplitude of reflection is used to indicate a large flaw, and the time-of-flight when the pulse is received is used to identify how deep the flaw is in the specimen. With broadband ultrasound, the time-duration of the pulse is short so that reflections within a test specimen can be time-resolved. Conversely, constant frequency ultrasonic tone-bursts are relatively wide in the time-domain in order to approximate a single frequency. Consequently, a limitation of the swept-frequency phase measurement method is the relatively long time-duration of the transmitted wave needed to obtain a measurement.

With constant-frequency tone-bursts, as the adherent of a bonded joint becomes very thin, multiple echoes from the bond line and back wall of the lower adherent will be received during the time the input tone-burst is still being transmitted. Without being able to distinguish the first bond line reflection from other echoes, the theoretical modeling of the received echoes becomes much more complicated. To overcome this potential limitation, thick adherents are used throughout most of this work.

To characterize the swept-frequency ultrasonic phase measurement method on thin-adherent bonded joints, a small study was conducted on Al/epoxy bonded joints. This study ultimately also found a limitation with the CFPPLL operation, which was remedied. A set of Al 6061 single lap joints were fabricated with different adherent thicknesses, as shown in Table 7.1. In each specimen, a 2.54 cm wide x 2.54 cm long x 127 µm thick piece of epoxy film adhesive (FM73U from Cytec) was used to bond together 2.54 cm wide x 15.24 cm long Al 6061-T651 adherents. Thin metal spacers of 102 µm thickness were used to maintain a consistent bond line thickness during cure. The SLJ dimensions are similar to the diagram in Figure 6.29, with the exceptions that adherent thickness varies in this study and no interfacial contamination is used.

Table 7.1: Adherent thicknesses used in thin-adherent bonded joint study

Specimen	Adherent Thickness (in)
1	0.5
2	0.3125
3	0.25
4	0.19
5	0.125
6	0.063

After fabrication, the bonded joints were ultrasonically evaluated with the swept-frequency phase measurement method. The standard configuration of sweeping the input ultrasonic frequency from 8.5-11.5 MHz with 0.01 MHz increments was initially tested on each specimen. It was quickly determined, however, that thinner adherents make it difficult to choose a sample point on the received ultrasonic signal from the bond line, which must remain on the first echo from the bond line throughout the entire frequency range.

The issue with choosing a single sampling point which works across the entire frequency range is that during the frequency sweep, the same number of sine-wave cycles was being held fixed for the sample and hold (S/H) position as well as the length of the transmitted (TX) tone-burst. Importantly, the period of a transmitted sine wave decreases as frequency increases, meaning the S/H position or transmitted tone-burst of a constant number of cycles shrinks in the time-domain during the frequency sweep. In many relevant media (i.e. lowly dispersive media), however, acoustic echoes will return at approximately the same time regardless of frequency (i.e. the group and phase velocities are equal). As such, sampling the phase of an echo at a certain number of sine-wave cycles at lower frequencies may no longer sample the echo at higher frequencies.

It was therefore determined to improve the inspection method by modifying the CFPPLL system to set the S/H position as well as the TX tone-burst length to be constant in the time-domain rather than a constant number of sine wave cycles. Figure 7.1 displays how the changes to the CFPPLL system improve the ability to assess bonded joints with thinner adherents, where *Ampl.* is the output of the received ultrasonic echoes after narrowband filtering and amplification, *Phase* is the output of the phase detector with 0 V corresponding to the transceived and reference waves being in quadrature, and *S/H* is used to choose sample and hold point on the phase signal.

Figure 7.1a displays the amplitude, phase, and chosen S/H position at 8.5 MHz of echoes from the Al 6061/epoxy bonded joint with 0.3125” adherents. Figure 7.1b and Figure 7.1c then display the resulting S/H position and TX tone-burst length after a frequency sweep to 10 MHz when using a constant number of sine-wave cycles and constant time-duration, respectively. As shown in Figure 7.1b, when the S/H and TX length are held to a constant number of sine wave cycles, the S/H is driven off the ideal flat portion of the phase signal after frequency has been swept from 8.5 MHz to 10 MHz. At the same 10 MHz frequency, when the S/H and TX length have been held fixed in the time-domain, these issues do not occur, and the phase signal is properly sampled, as shown in Figure 7.1c.

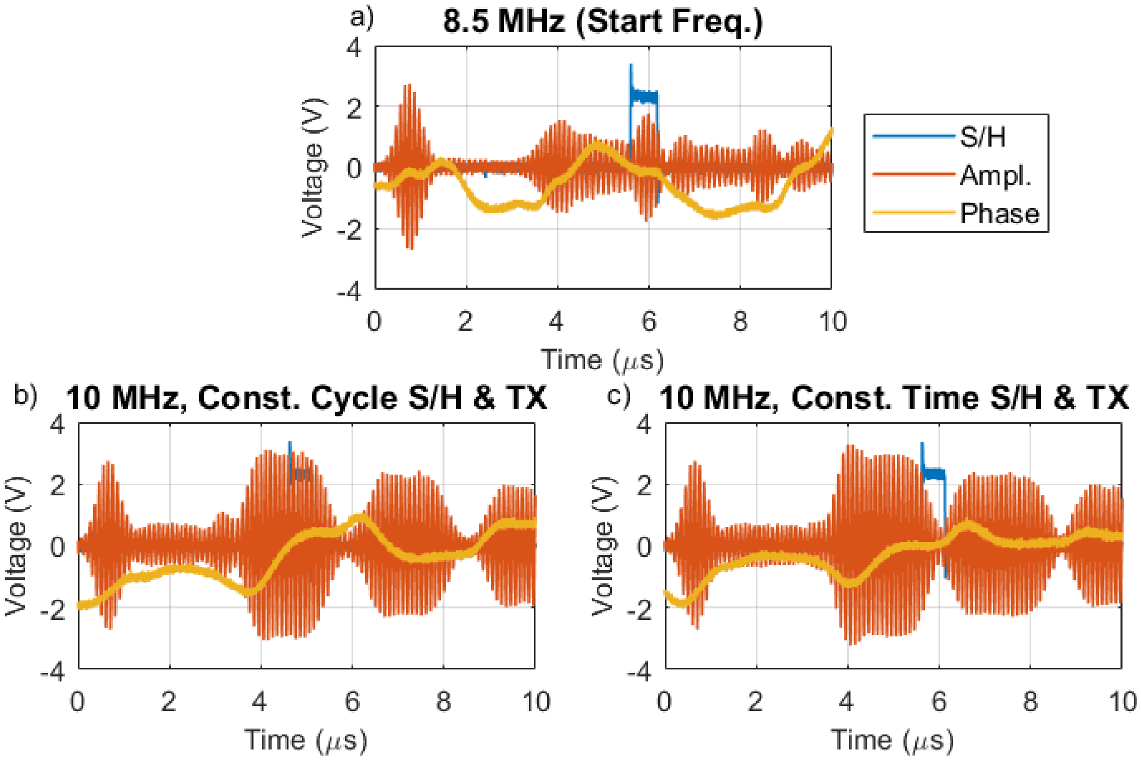

Figure 7.1: S/H position, amplitude, and phase from bond line reflections on single lap joint with 0.3125” adherents at a) 8.5 MHz starting frequency, b) 10 MHz after frequency sweep with S/H and TX held at constant cycle number, and c) 10 MHz after frequency sweep with S/H and TX held constant in time

The effect of the CFPPLL system improvements on the measured phase spectra can be seen in Figure 7.2. The variations in the phase signal caused by non-ideal sampling – i.e. sampling off the bond line – are removed by the system modifications to fix S/H and TX lengths constant in the time-domain.

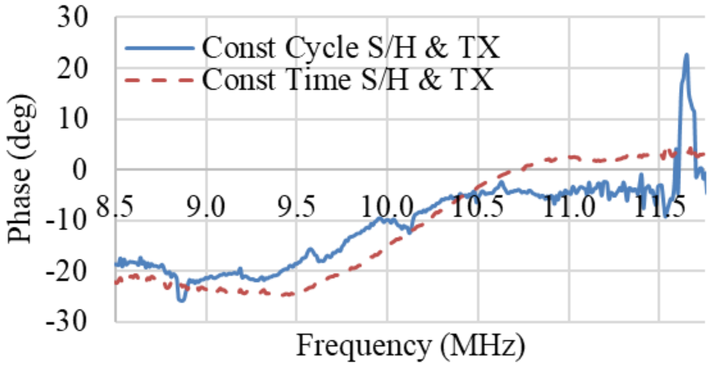

Figure 7.2: Phase vs. frequency response of bond line with 0.3125” adherents for different CFPPLL configurations

After improvements were made to the CFPPLL measurement system, thin-adherent bonded joints were re-inspected with the swept-frequency ultrasonic phase measurement method. It was found that down to 0.19” adherent thickness, it is simple to obtain a clean phase vs. frequency response from the bond line, as shown in Figure 7.3. Even at 0.19” adherent thickness, though, there is some extra uncertainty causing a few sharp spikes in the measured phase signal, which could likely be removed through a smoothing algorithm. At 0.125” adherent thickness, it begins to be difficult to choose a S/H time-delay that works over the entire frequency range of 8.5-11.75 MHz, and as a result, the measured phase response becomes obscured using the current measurement setup.

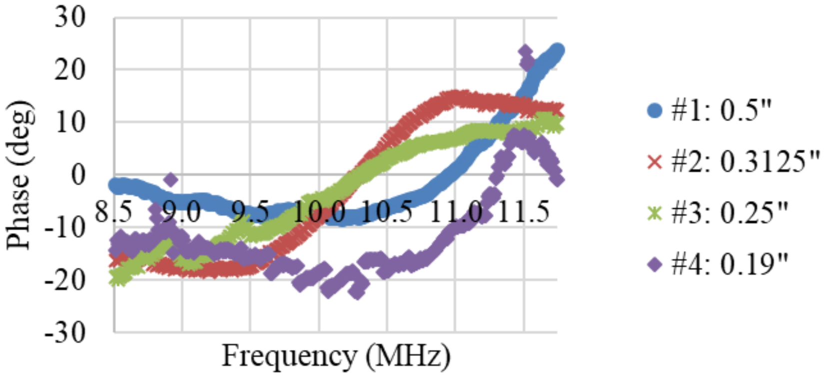

Figure 7.3: Phase vs. frequency response of bond line reflections for different adherent thickness

The minimum thickness at which individual echoes can be time-resolved should extend to other adherent materials by the ToF through the adherent. In Al 6061, a thickness of 0.125” corresponds to a ToF of $\sim 1\ \mu s$, which is determined to be the minimum ToF in the adherent needed to use the swept-frequency phase method over the entire 8.5-11.75 MHz range. To give additional context, at a driving frequency of 10 MHz, 0.125” adherent is about five wavelengths thick.

If Al adherents below 0.125” thick or any adherents with an acoustic ToF less than $\sim 1\ \mu s$ need to be assessed, there are several methods which could be investigated. First, if compatible with the bonded joint thickness, higher frequency ultrasound could be used to transmit more tone-burst cycles into the specimen. The use of an even more broadband ultrasonic transducer would reduce the ringing time of the transducer when initially receiving the first echo and could allow for good measurements using a shorter tone-burst. Another option is to allow the user to set a particular S/H position at the starting frequency and during the sweep, stop to allow the user to reset the S/H position. This adjustment would allow for better choice of S/H position in different frequency ranges, which could provide better measurements over the entire range. A final method to resolve thinner adherent joints is to sweep over a smaller frequency range. For this method to work most effectively for SLJs, the phase needs to be measured around the resonance frequency of the bond line. In practice, the frequency range may not need to be the full bandwidth of the filtering circuit used here and a smaller range may be sufficient.

7.3.2 Uncertainty in Material Properties

Another challenge for bond quality assessment in SLJs with the ultrasonic phase measurement method is the uncertainty in material properties of the adhesive layer. When analyzing the phase response of the bond line reflection coefficient around the resonance frequency, the curve-fitting algorithm used to determine interface stiffness relies on knowledge of bond line thickness and adhesive sound velocity. If those estimates are a bit off, it could affect the ideal resonance frequency, changing the extracted interfacial stiffness as well as the predicted bond strength.

A modeling study was conducted to characterize the impact of uncertainty of the material properties of the adhesive layer. An Al/epoxy SLJ was modeled with a bond line thickness of $110\ \mu m$ and variable interface stiffness, similar to the model used to predict resonance frequency at the end of Section 3.2.2. In this scenario, bond line thicknesses $\pm 5\ \mu m$ of the nominal thickness are also modeled to show the effect of the input bond line thickness being incorrect by up to $\sim 5\%$. While only bond line thickness uncertainty is modeled here, adhesive sound velocity uncertainty should have a very similar effect, as both bond line thickness and adhesive sound velocity affect the sine and cosine terms of the reflection coefficient in Equation 3.20.

Figure 7.4 shows the modeled resonance frequency changes as a function of interfacial stiffness with error bars showing the resonance frequency with $\pm 5\ \mu m$ bond line thickness errors. Two scenarios are plotted: one with only the upper interface quality changing and another with both interfaces of equal quality changing. Additionally, the approximate interfacial bond strength at a given interface stiffness based on Cantrell's theory is shown on the x-axis for reference [64].

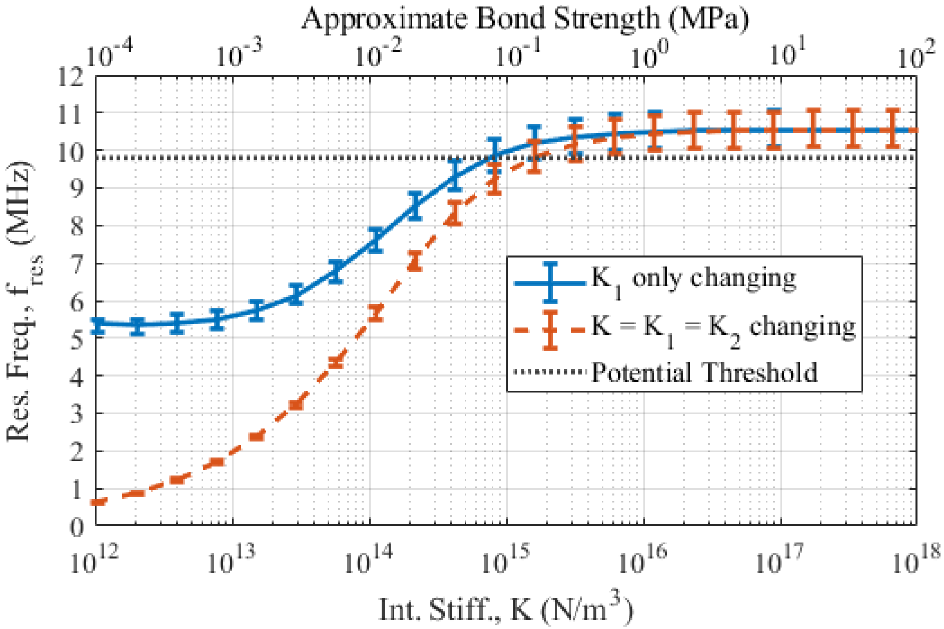

Figure 7.4: Modeled resonance frequency vs. interfacial stiffness in Al/epoxy SLJs with error bars showing bond line thickness errors of $\sim 5\%$

It is notable in Figure 7.4 that bond line thickness uncertainty is most impactful for high interfacial stiffness, well-bonded joints. The effect of 5% bond line thickness uncertainty drops off as the interface degrades so that there is very little effect on resonance frequency for very low interfacial stiffness values. This makes sense, as for kissing bonds and for complete disbonds, more of the ultrasonic amplitude will be reflected at the poor interface rather than transmitted into the joint.

Errors in predicted bond line thickness of 5% are likely reasonable in a number of industrial applications, and they may provide difficulty in using the swept-frequency ultrasonic phase measurement method to assess intermediate bond strengths. Instead of having sensitivity to reduced interface stiffness near $10^{16}\ N/m^3$ found in the ideal case at the end of Section 3.2.2, the bond line thickness error causes the method to only have sensitivity to reduced interfacial stiffness at about $10^{15}\ N/m^3$. At this point, the interfacial bond strength is about two orders of magnitude below its pristine value and can therefore be considered a poor bond.

It is therefore proposed that in situations where material properties such as bond line thickness may have a 5% variance that a reasonable threshold decrease in resonance frequency be used to determine when the interfacial bond strength is degraded. A proposed threshold in the modeled setup of 9.8 MHz is shown in Figure 7.4. If the resonance frequency is measured above the threshold, the joint is concluded to retain some strength and not be a kissing bond. However, if the resonance frequency drops below the threshold, it is concluded that there is essentially no remaining interfacial bond strength at that location.

An alternative method to obtain high-accuracy material properties in the adhesive layer is to pair the swept-frequency phase method with a higher-frequency broadband pulse method for obtaining ToF information from within the adhesive layer. At each measurement location, short time-duration pulses may be used to probe the adhesive layer and determine bond line thickness.

7.4 Conclusions

Fundamental limitations of the ultrasonic phase measurement method as applied to adhesion strength evaluation are discussed in this chapter. Some of the limitations are general contact ultrasonic phase assessment, as the phase shifts due to the couplant layer and the adherent must be accounted for or otherwise minimized. Other limitations in this method are caused by the current design of the CFPPLL instrument, including the bandwidth of operation and the time it takes to obtain phase measurements. These design limitations are solvable with a redesign of the CFPPLL instrument receiving circuit and modifications to the microcontroller.

Finally, there are several limitations of constant-frequency phase measurements for bond quality evaluation in SLJs. The problem of time-resolving echoes from thin adherents is a difficult one to solve. While several measurement considerations are discussed to improve the minimum resolvable adherent thickness, there will always be some minimum adherent thickness with this CFPPLL method. As such, for inspection on SLJs with very thin adherents, higher ultrasonic frequencies or more complicated modeling of the phase response will be necessary. In addition, the knowledge of material properties and bond line thickness in SLJs will always affect the ability to assess interfacial bond strength, as ultrasonic phase measurements are compared to a physical model for extracting interface stiffness. It is proposed that the swept-frequency method be combined with a broadband ultrasonic method to obtain relevant material properties and bond-line thickness for applications where the properties or thickness are not well-known. Ultimately, applications with highly variable material properties may limit the ultrasonic phase measurement method to only detect kissing bonds or complete disbonds, rather than quantify a range of interfacial bond strengths.

Chapter 8: Other Applications of the Ultrasonic Phase Detection Method

This chapter highlights additional potential applications of the ultrasonic phase measurement method demonstrated in this work, which do not involve adhesive bond quality assessment. The two applications presented here contain a background literature review on the problem being addressed as well as experimental results using the ultrasonic phase method.

First, a study on early detection of bonded joint failure is described. Metal/epoxy single lap joints (SLJs) are fabricated and quasi-static shear loaded until failure. During loading, an ultrasonic transducer is mounted to the face of the adherent and the phase of the ultrasonic reflection coefficient from the bond line is monitored. Next, the application of interface quality assessment in additively manufactured parts is examined. Preliminary results of the ultrasonic phase and amplitude of additively manufactured plastic parts with varying degrees of under-extrusion are presented, and challenges in the assessment of additively manufactured parts with ultrasonic phase are discussed.

8.1 Early Detection of Bonded Joint Failure with Ultrasonic Phase

8.1.1 Background

Despite several NDE methods showing sensitivity to interfacial adhesion quality, few methods exist to characterize adhesive bonds in-situ. While not in-situ monitoring during failure loading, modulated ABUS observes how the resonance frequency of a bonded joint changes when a low-frequency sinusoidal shaker table is used to stress the interface [68]. It was found that the measured interfacial stiffness of a good bond is independent of low-frequency stress, while in poor bonds, the interfacial stiffness decreases under tension. Consequently, the modulation of the ultrasonic resonance frequency is used to discriminate good and bad bonds via mechanically stressing the joint.

In most laboratory tensile load tests, the crack growth in an adhesive joint can be observed from the side of the bonded joint. In quasi-static shear loading tests, however, ultimate failure occurs quickly, and crack growth cannot be observed in the same way. Most NDE methods for characterizing bonded joints under shear load rely on information from the surface of the adherent to infer information about what is happening within the joint. By depositing a speckled pattern on the surface of a bonded part, Digital Image Correlation (DIC) is used to obtain high-resolution strain maps of the adherent surface [88], [148], [149]. Infrared thermography has also shown success in detecting poor bonding in joints under load and detecting bond failure [150], [151]. While these methods have shown some success in detecting bonding defects, they only provide information from the adherent surface and often rely on finite-element modeling (FEM) for validation and understanding of results, increasing processing time and complexity.

Other methods of investigating bonded joints under shear loading have been developed for structural health monitoring (SHM) purposes and largely rely on sensors or particles embedded in the adhesive [152], [153], [154]. A recent study uses embedded particles and ultrasonic testing to conduct a form of ultrasonic DIC to measure strain within the adhesive bond line [155]. There are several concerns with embedded sensors in bonded joints, limiting their acceptance. First is the possibility of the sensors causing a reduction in bond strength. Second, it can be difficult and costly to add embedded sensors into an adhesive bonding process.

Recent experimental and finite-element analysis work by Jeenjitkaew and Guild show evidence that the lateral and out-of-plane stress-strain relationship within the adhesive bond line will have different characteristic “signatures” depending on the adhesive/adherent interface quality [156], [157]. The local strain within the bond line was measured using a strain gauge across the bond line during shear loading. Additional research using strain gauges around the bonded and disbonded regions in a lap joint undergoing an asymmetric wedge test also shows the importance of understanding the local strain within the bond line during loading [158]. Nominally, ultrasonic methods should be able to interrogate local strain within an adhesive bond line by measuring the acoustic time-of-flight within the adhesive layer. While not measured in-situ, Scanning Acoustic Microscopy (SAM) has even shown that changes in local sound velocity can be used to identify damage initiation sites in fatigue-loaded bonded composites [159].

In this study, a method is demonstrated for interrogating an adhesively bonded joint undergoing lap shear testing with high-resolution, normal-incidence longitudinal ultrasonic phase measurements. An ultrasonic transducer is mounted to the face of a SLJ adherent with a set of 3D-printed parts. While the joint is undergoing quasi-static shear loading, the ultrasonic phase shift of the reflection coefficient from the bond line is tracked using the constant-frequency pulsed phase-locked-loop method developed in this work and explained in detail in Chapter 4. Phase shifts from the bond line for normal-incidence longitudinal ultrasonic waves should be highly sensitive to strain within the bond line, which could allow for identification of good and bad bonding as suggested by [156]. Additionally, this high-resolution ultrasonic phase method has proved sensitive to small changes in interfacial adhesion strength in SLJs. Through the tracking of ultrasonic phase shifts during loading, this technique seeks to measure strain within the bond line as well as detect changes in interface quality as the bonded interface fails. To test this method, two sets of metal/epoxy bonded joints are fabricated with different interfacial bond qualities. The bonded joints are then mechanically shear loaded until failure along with in-situ ultrasonic phase monitoring.

8.1.2 Theory

To understand how ultrasonic phase of reflections from an adhesive bond line changes during mechanical loading, the ultrasonic interactions within the bond line are modeled. The imperfect interfaces within a SLJ are physically approximated as a distributed spring system, according to the quasi-static model for ultrasonic interactions with imperfect interfaces proposed by Baik and Thompson [62]. With this interfacial spring system model, the normal-incidence particle-displacement-wave reflection coefficient from the bond line of a SLJ is derived.

Assume an ultrasonic particle-displacement plane wave is excited into the bond line of a SLJ at normal incidence. The incidence wave is represented by Equation 8.1, where T_i is the incident wave amplitude, $i = \sqrt{-1}$, ω is the input angular frequency, t is time, k_1 is complex acoustic wavenumber in the incident adherent medium, and x is the distance traveled by the wave.

$$u_i(x,t) = T_i e^{i(\omega t - k_1 x)} \tag{8.1}$$

Assuming the adhesive layer is very thin with respect to the adherents, it is assumed that reflections from the bond line are time-resolved from back wall reflections from the lower adherent. Adherents 1 and 2 are assumed semi-infinite half-spaces so that only ultrasonic interactions within the bond line are considered. The material setup from Figure 3.1 is once again used, where T_i is the incident wave amplitude, assumed unity for simplicity; L_{BL} is the bond line thickness; R_{adh} and T_{adh} are the reflection and transmission coefficients for the adhesive layer, respectively; T_o is the transmission coefficient through the bond line, and R_{BL} is the adhesive bond line reflection coefficient. Described in more detail by [98], the quality of the two adhesive/adherent interfaces are described by $K_1$and K_2, the spring constant flux of each interface, and m_1 and m_2, the mass per unit area at each interface.

Within the adhesive layer, individual reflections coming from the lower adhesive/adherent interface are separated in time by a time-of-flight (ToF) of $2L_{BL}/c_{adh}$, where c_{adh} is the adhesive sound velocity. In many practically encountered SLJs, the adhesive ToF is small in comparison to the incident tone-burst duration, so the cumulative effect of all reflections within the bond line is considered. Derived in detail in general form in Section 3.2.1 and expressed in Equation 3.19, the bond line reflection coefficient R_{BL} is found by solving for $R_{BL}, R_{adh}, T_{adh},$ and T_o under the boundary conditions at each interface.

In the case of interest in this work, the general R_{BL} solution can be greatly simplified. First, both adherents are assumed to be made from the same material, so the elastic moduli and wavenumbers in the adherents are equal (i.e. $E_1 = E_2$ and $k_1 = k_2$). Second, for thin interfacial contamination and for thin interface layers, the interfacial mass contribution is negligible, so $m_1 = m_2 = 0\ kg/m^2$. Third and finally, the upper interface may be contaminated so that K_1 should be left variable. However, the lower interface is left pristine throughout the entire experiment, so $K_2 \to \infty$. Under these assumptions, an approximation of the bond line reflection coefficient R_{BL} can be seen in Equation 8.2.

$$R_{BL} \approx \frac{\left[G_1 G_{adh}\left(\frac{G_1}{K_1}\right)\right]\cos(k_{adh}L_{BL}) + i\left[G_1^2 + G_{adh}^2\left(\frac{G_1}{K_1} - 1\right)\right]\sin(k_{adh}L_{BL})}{\left[G_1 G_{adh}\left(2 + \frac{G_1}{K_1}\right)\right]\cos(k_{adh}L_{BL}) + i\left[G_1^2 + G_{adh}^2\left(\frac{G_1}{K_1} + 1\right)\right]\sin(k_{adh}L_{BL})} \tag{8.2}$$

$$G_1 = iE_1k_1, \qquad G_{adh} = iE_{adh}k_{adh}$$

In Equation 8.2, $k_n = \omega/c_n + i\alpha_n$ is the complex acoustic wavenumber, c_n is sound velocity, α_n is the acoustic attenuation coefficient, ρ_n is the mass density, and $E_n (= \rho_n c_n^2)$ is the elastic modulus in the n^{th} medium. The amplitude and phase response of R_{BL}, as defined by Equation

8.2, are computed for a given set of material properties and input frequency by expressing R_{BL} in complex form: $R_{BL}(f) = |R_{BL}(f)|e^{i\phi_{R_{BL}}(f)}$. Of interest to this work is the phase of the reflection coefficient, given by $\phi_{R_{BL}}(f)$.

8.1.3 Experimental Approach

8.1.3.1 Single Lap Joint Fabrication

Sets of SLJs made with metal adherents and epoxy film adhesive were fabricated to approximate bonded joint configurations commonly seen in the aerospace industry. The adherent coupons were cut to size from aluminum 6061-T651 (Al 6061-T651) plate stock to dimension of 15.24 cm long x 2.54 cm wide x 0.79 cm thick. The adherents are thicker than typical aerospace applications to allow for sufficient ultrasonic time-of-flight in the adherent so that sequential echoes from the adhesive bond line are easily time-resolved in this initial study. In practice, such thick adherents may not be necessary for this method to work. The Al 6061-T651 adherents were bonded together with FM73U, an unsupported epoxy film adhesive from Cytec. The final bonded joint configuration and dimensions can be seen in Figure 8.1.

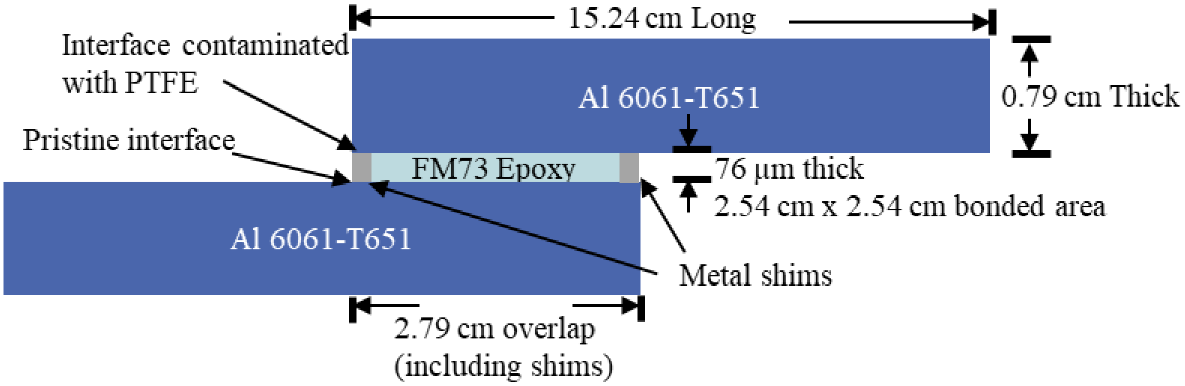

Figure 8.1: Diagram of SLJ configuration

Prior to bonding, the adherent surfaces are prepared via detergent wipe and rinse, solvent wipe with ethanol, ultrasonic cleaning bath in ethanol, and vapor degreasing with ethanol. To inhibit bonding, several adherent coupons are spray coated from a distance of 4 inches through a mask with a polytetrafluoroethylene (PTFE) mold release agent. The mold release agent leaves a thin film of PTFE on the surface that inhibits bonding between the epoxy adhesive and the metal surface, which mimics a kissing bond region of a joint. The mask allows for a small region of in the center of the specimen to be coated, while leaving pristine regions surrounding it. The rest of the joint is bonded in accordance with manufacturer's recommendation.

Two sets of bonded joints of three specimens each are fabricated, with different adherent surface treatments: pristine with no PTFE contamination, and spray-coated with PTFE through a mask with a 1.27 cm diameter circular hole in the center. This mask resulted in 29% PTFE coverage over the 2.54 cm x 2.54 cm region to be bonded. Only one adherent of the SLJ is modified, providing only one imperfect interface in the contaminated joints.

After spray coating, the Al 6061-T651 adherents are bonded together with FM73U film adhesive. The film adhesive is warmed to room temperature prior to opening to prevent atmospheric moisture condensation. A 2.54 cm x 2.54 cm square of the film adhesive is placed near the end of one adherent, to leave a small gap on the end. Metal shims are used to maintain bondline thickness during cure. A thin 2.54 cm long strip of 76 μm thick Al shim stock is placed on both sides of the film adhesive on the adherent surface. The second adherent is placed on top of the film adhesive to complete the SLJ. The completed bonded joints are oven cured according to the manufacture's specification.

8.1.3.2 Mechanical Testing Configuration

Mechanical testing procedure of the bonded joints is performed with an MTS Alliance RT/100 electromechanical load frame. The bonded joints are loaded into grips with 0.79 cm thick spacers to align the bondline to the center of the load frame axis. The SLJs are loaded with a quasi-static shear load with a constant displacement rate of 1 µm/s until failure. During testing, the displacement, load, and time were logged at a rate of 10 measurements per second.

8.1.3.3 Ultrasonic Phase Measurement Setup

8.1.3.3.1 Ultrasonic Transducer Mounting

During mechanical testing, a 0.64 cm diameter, 10 MHz center frequency ultrasonic transducer (Olympus model V112-RM) is mounted over the bondline with a specially designed transducer mounting apparatus (TMA) consisting of two parts. One TMA part slides over the bondline edge of one adherent and keeps the transducer from moving laterally across the bondline. The second TMA part slides onto the same adherent and places pressure on the ultrasonic transducer to keep adequate transducer-adherent coupling and to assure geometrical integrity over the bondline during mechanical testing. Images of the ultrasonic transducer mounted onto a SLJ are shown in Figure 8.2. Sono 600 ultrasonic couplant from Magnaflux transfers ultrasonic waves from the transducer into the upper adherent.

This 3D-printed apparatus was initially developed to hold an ultrasonic transducer on a bonded joint during cyclic fatigue loading. However, initial fatigue tests showed the rate of movement of the bonded joint tended to cause a loss of received ultrasonic amplitude over time, even over a few hundred cycles. It is thought that as the transducer and couplant are moved up and down quickly, the transducer starts to de-couple from the adherent surface. To obtain reliable ultrasonic phase measurements on bonded joints during fatigue loading, the transducer mounting apparatus should include a more rigid beam holding at higher pressure on the ultrasonic transducer during testing. Additionally, a high-viscosity ultrasonic couplant should be used so that it does not move from the adherent surface due to vibrations during testing. By holding higher pressure on the transducer and using high-viscosity couplant, the de-coupling effect due to cyclic loading should be minimized so that ultrasonic phase can be monitored during fatigue loading.

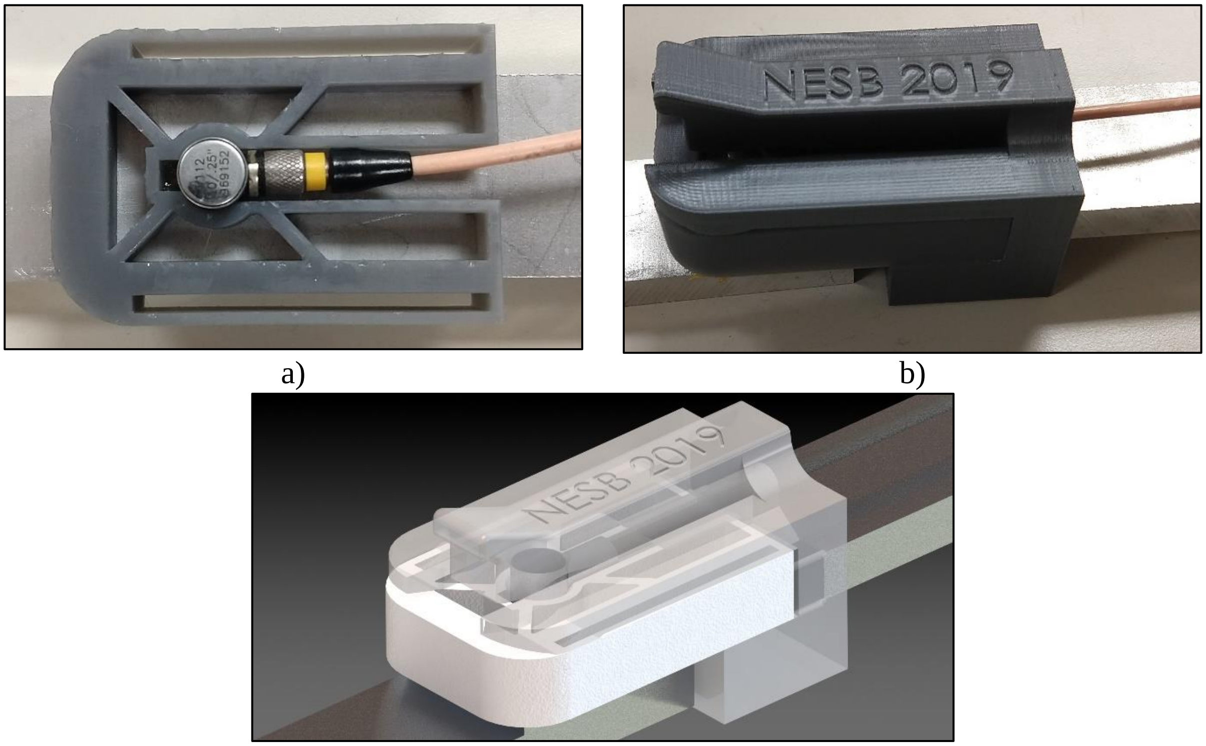

a) b)

c)

Figure 8.2: Images of 3D-printed transducer mounting apparatus with a) lower part holding transducer in place laterally on adherent face, b) entire apparatus showing beam holding pressure on transducer, and c) 3D-model with transparent upper part showing transducer mounted on joint

8.1.3.3.2 Constant-Frequency Ultrasonic Phase Tracking

Prior to quasi-static loading the bonded joints, the stability of ultrasonic phase measurements at a constant load while using the TMA is tested. The load frame is held fixed for 1 hour with a constant load of ~240 N throughout the duration of the test. After an initial settling period where the phase changed $\sim 2.8\, deg$ over the course of the first 15 minutes, the phase then remained roughly constant with a value of $2.807 \pm 0.050\, deg$ throughout the final 45 minutes of the test. The standard deviation of $0.050\, deg$ is a little over twice the phase measurement resolution of the CFPPLL instrument itself, which is $0.022\, deg$. The initial phase change period is thought to be due to settling of the ultrasonic transducer and couplant onto the part due to relaxation of the TMA.

It was thus determined to allow some time for the ultrasonic phase to settle after mounting the SLJ to the load frame before beginning each quasi-static load test.

The ultrasonic phase of the first echo from the adhesive bond line of the SLJ is tracked at a constant frequency of 10 MHz during quasi-static shear loading. High-resolution ultrasonic phase measurements are obtained with the constant-frequency pulsed phase-locked loop (CFPPLL) instrument described in Chapter 4.

A 10 MHz ultrasonic tone-burst is transmitted by the transducer. Reflections from the adhesive bondline are later received by the same transducer. The phase of the first echo from the bondline is measured by the CFPPLL system at a repetition rate of 10 samples per second to match sampling rate of the mechanical testing system. The start of the ultrasonic phase tracking is synchronized with the start of the quasi-static shear loading so that ultrasonic phase measurements and shear loads are directly comparable. It is noted that for the PTFE-contaminated bonded joints that the ultrasonic transducer is mounted directly over the contaminated region of the adherent/adhesive interface.

8.1.4 Results and Discussion

8.1.4.1 Shear Load and Displacement Measurements

The measured data for load vs. time during quasi-static shear loading for each SLJ are shown in Figure 8.3. As the displacement rate is held constant at $1\,\mu m/s$ throughout the test, the displacement of the load cell grips at a given time is also shown on the x-axis. As the displacements in Figure 8.3 are directly from the load frame, they include contributions from tensile strain in the adherents and shear strain in the adhesive. In each plot, an initial high load rate is seen for a few minutes, which is thought to be due to specimen- grip dynamics. After the initial high load rate, there is a long, mostly linear, region where the bonded joint is thought to undergo elastic deformation.

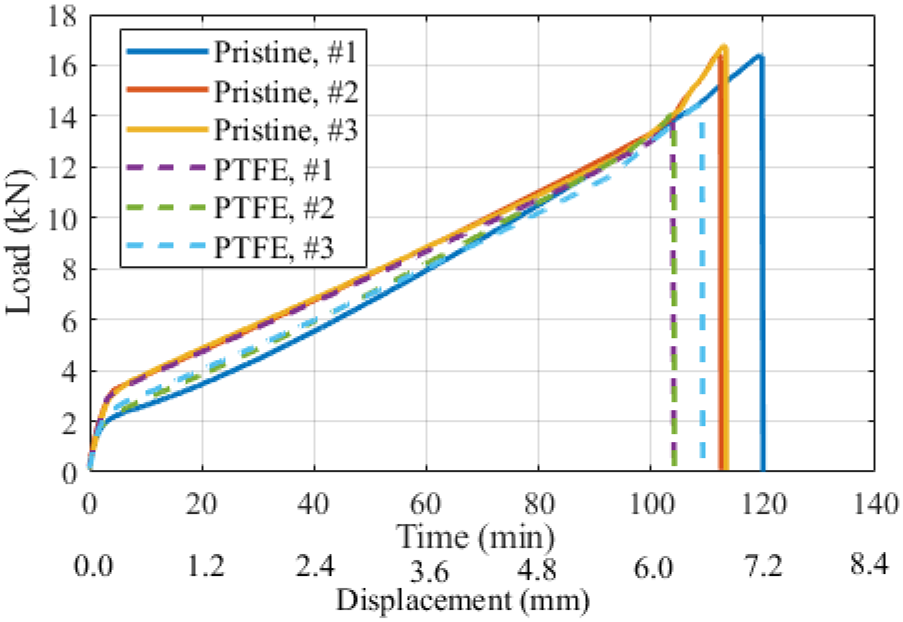

Figure 8.3: Load vs. time and displacement curves for shear loaded SLJs

The ultimate failure load, as well as the time and displacement at which failure occurred is shown in Table 8.1. The contaminated joints failed at about 85% of the load of the pristine joints.

Table 8.1: Failure load, time, and displacement from Al/epoxy bonded joints

Specimen	**Failure Load (kN)**	**Failure Displ. (mm)**
Pristine, #1	16.4	7.17
Pristine, #2	16.5	6.72
Pristine, #3	16.8	6.78
Pristine Avg. ± SD	*16.6 ± 0.2*	*6.89 ± 0.24*
29% PTFE, #1	13.9	6.22
29% PTFE, #2	14.1	6.22
29% PTFE, #3	14.4	6.53
29% PTFE Avg. ± SD	*14.1 ± 0.3*	*6.32 ± 0.18*

After failure, the bonded joints were examined visually for their failure modes. Figure 8.4 shows images of the top (contaminated) and bottom (uncontaminated) adherents after bond failure. The pristine, uncontaminated bonded joints each displayed cohesive failure in places and showed no strong preference for failing at a particular interface. Meanwhile, the white PTFE coated regions in the contaminated bonded joints are clearly visible on the broken adherents in Figure 8.4. There is a clear tendency for the joints to fail at the contaminated interface around the PTFE islands, as seen in the broken joint surfaces, where the adhesive layer remains on the lower adherent at those locations and cohesive failure occurs in the surrounding region.

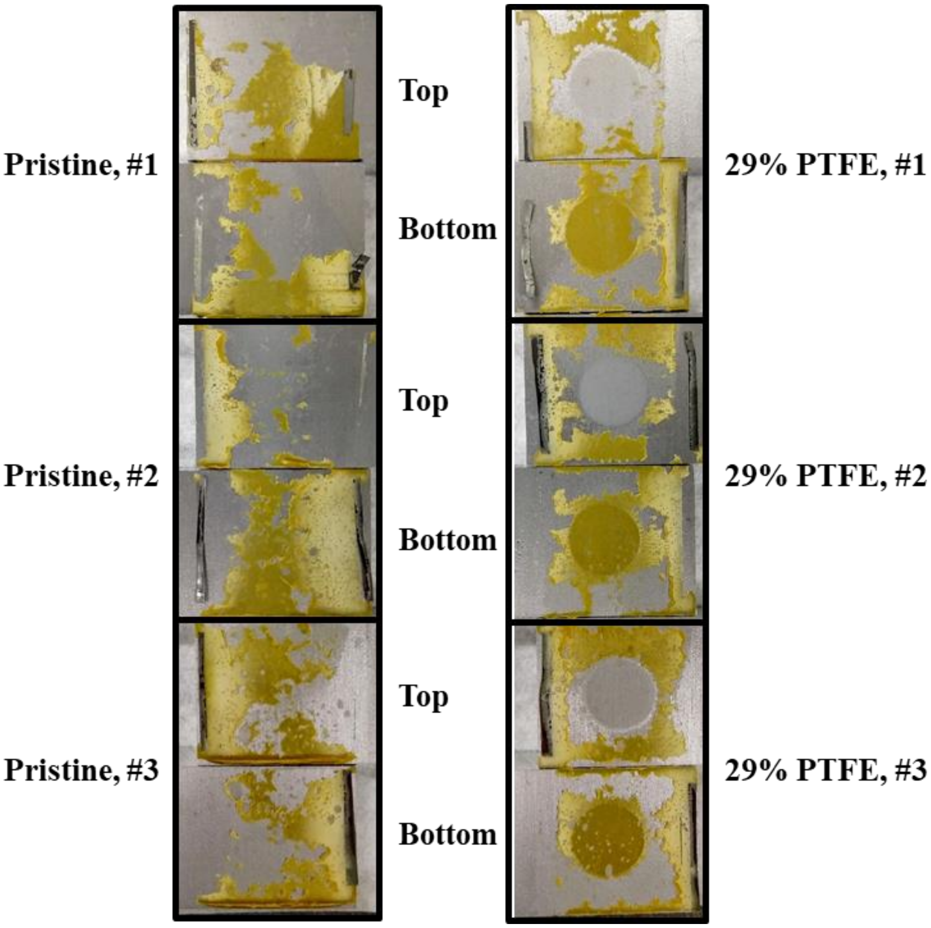

Figure 8.4: Images of adherents after bond failure

8.1.4.2 Ultrasonic Phase Measurements

The measured phase at 10 MHz of the ultrasonic reflection coefficient from the first bond line echo is plotted as a function of time and displacement during quasi-static loading in Figure 8.5. The phase is plotted from the beginning of quasi-static loading until the failure time, as the phase undergoes a large shift after the bond breaks. In each bonded joint, there is an initial linear region of phase shift as the load increases followed by sharper phase changes preceding bond failure. As displacement rate is held constant, the phase drop is not just a measure of strain in the bondline. It is noted that the PTFE-contaminated joints display an increase followed by a decrease in phase shift as failure is occurring, whereas the pristine joints only display a negative phase shift during failure.

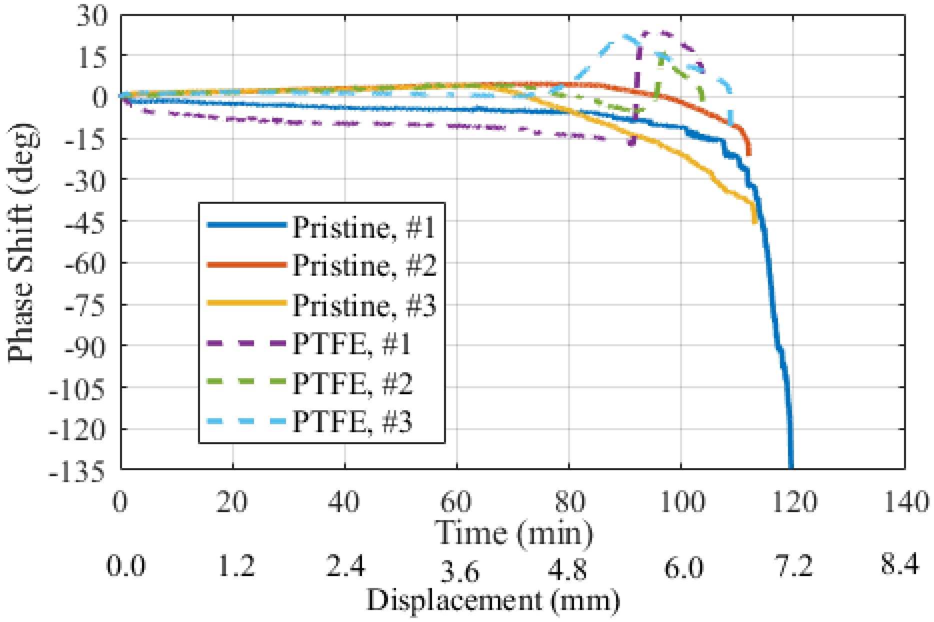

Figure 8.5: Phase vs. time and displacement for shear loaded SLJs

During the linear region of phase shift, there is not a clear preference for positive or negative phase for the pristine or contaminated SLJs. It is thought that a positive or negative phase slope in this initial linear region depends on the alignment in the load frame during the shear test. With perfect alignment, the bondline should only be subject to shear loading. Due to Poisson's ratio, out-of-plain strain in the bondline should cause the bondline thickness to decrease as load increases. This would result in a small positive phase slope effect. However, if there is any misalignment in the grips, there would be some tensile or peeling bondline force, which would cause an increase in the bondline thickness and result in a small negative phase slope.

To understand the sharp phase changes prior to failure, the slope of phase shift vs. time is computed. To minimize large variations in phase slope due to phase noise and to see the general trend in the phase data, $d\phi/dt$ is smoothed via a Gaussian moving average over a time interval of 10 minutes (i.e. ~6000 measured data points). The smoothed phase slope for each curve is plotted in Figure 8.6.

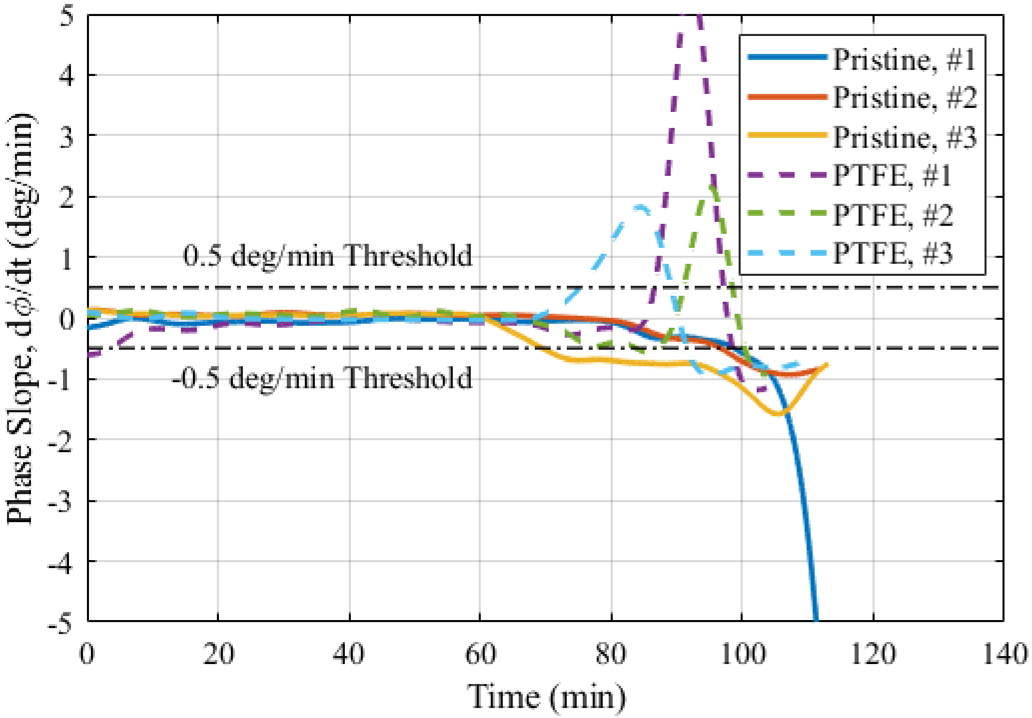

Figure 8.6: Slope of phase shift vs. time for shear loaded SLJs

As noted from Figure 8.5 and again noticeable in Figure 8.6, the pristine joints each show only a negative phase slope prior to failure, while the PTFE-contaminated SLJs display a strong positive phase slope before a negative slope prior to failure. A threshold of $\pm 0.5\ deg/min$ is chosen to indicate the beginning of ultimate joint failure based on the $d\phi/dt$ plots. This phase slope does not appear during the linear region of phase shift but does appear once the phase begins significantly changing prior to failure. The load at which $d\phi/dt$ crosses the threshold is shown in Table 8.2. The threshold load relative to the ultimate failure load is displayed. Regardless of pristine or contaminated, the phase threshold indicates joint failure at about 80% of the ultimate failure load for most specimens, while detecting indications of bondline changes as early as 58% of ultimate failure for one of the pristine joints. Between the pristine and contaminated joints, there is substantial variability in phase threshold results. Hence, there is not a statistically significant difference in the relative load at which the phase threshold is reached.

Table 8.2: Load when phase slope reaches $\pm 0.5\ deg/min$ threshold

Specimen	Load at Threshold (kN)	Rel. Load at Threshold
Pristine, #1	13.1	0.80
Pristine, #2	12.9	0.78
Pristine, #3	9.8	0.58
Pristine Avg. ± SD	11.9 ± 1.9	0.72 ± 0.12
29% PTFE, #1	11.4	0.82
29% PTFE, #2	11.9	0.85
29% PTFE, #3	9.7	0.67
29% PTFE Avg. ± SD	11.0 ± 1.2	0.78 ± 0.10

It is postulated that the length of the phase dropping region is dependent on the amount of plastic deformation in the adhesive prior to failure. Some bonds fracture quickly once crossing some critical point while others continue to stretch for longer prior to failure. Further testing would be necessary to draw stronger conclusions about this phenomenon.

To better compare the phase shift from the bond line to the shear load on the SLJ, Figure 8.7 plots the measured phase shift vs. load for each SLJ throughout the duration of the mechanical test. This plot further shows that the phase shifts measured from the bondline reflection coefficient do not linearly track the shear strain or load on the bondline. As the load rate is nominally linear with respect to displacement for most of the test, the phase curves here look very similar to the phase vs. time and displacement curves in Figure 8.5.

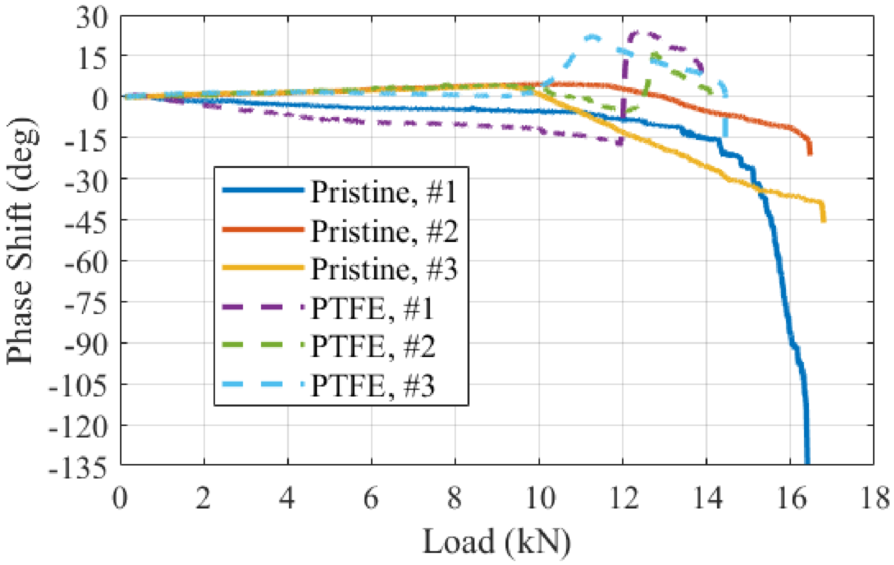

Figure 8.7: Phase shift vs. load for shear loaded SLJs

8.1.4.3 Comparison to Interfacial Spring Model of Bonded Joints

A theoretical model of the ultrasonic reflection coefficient from an Al/epoxy bonded joint is developed using Equation 8.2 to compare with the measured phase results. The model assumes the elastic modulus and density as provided by the manufacturer for the Al 6061-T651 adherents and FM73 adhesive. The bond line thickness is assumed nominally $76.2\ \mu m$ at the start of the test. In this model, the complex attenuation coefficient in the adhesive layer is assumed a linear function of ω/c_n such that $k_{adh} = \omega/c_{adh}\,(1 + \alpha_{adh} i)$. This was found to be a good approximation for acoustic attenuation in epoxy adhesives over small frequency ranges by [160]. Figure 8.8 shows the modeled phase shift of R_{BL} in Equation 8.2 vs. different adhesive layer material properties that could change during quasi-static loading. In each plot, all other parameters are held fixed at their nominal value at the start of the test. K_1 is assumed perfect in all plots except for Figure 8.8a where it is the independent variable.

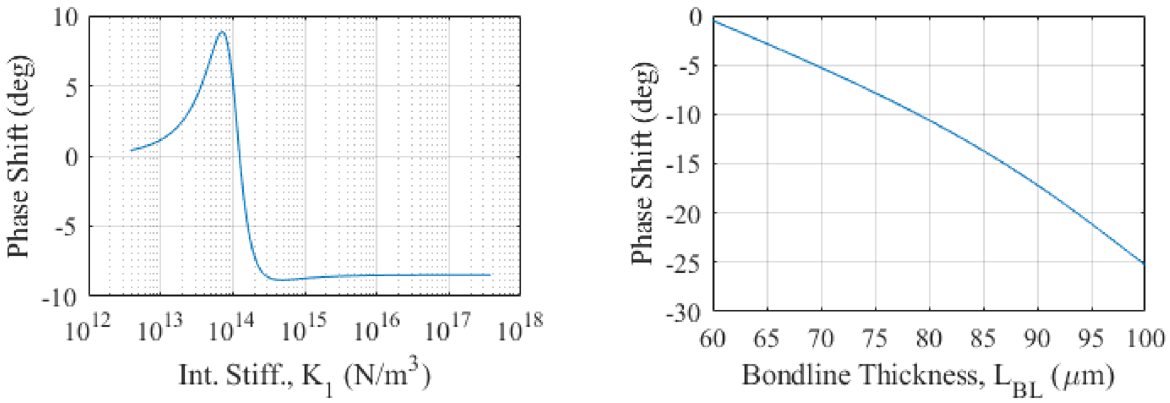

a) b)

Figure 8.8: Modeled phase shift at 10 MHz of bond line reflection coefficient as a function of different changing bond line parameters with all other parameters fixed at their nominal value: a) Phase vs. interfacial stiffness K_1, and b) Phase vs. bond line thickness

The two plots in Figure 8.8 provide indications of what may be happening in the bonded joints just prior to ultimate failure. For the pristine joints, which only exhibit a negative phase slope as failure occurs, it is likely the bond line thickness increasing due to out-of-plane strain, producing a negative phase shift as shown in Figure 8.8b. As the bond fails mostly cohesively in the pristine joints, the elastic out-of-plane strain becomes plastic deformation in the adhesive layer. Plastic deformation may produce small cracks or voids in the adhesive, effectively slowing down the ultrasonic waves and sharply reducing the phase shift.

In the PTFE-contaminated joints, however, there exists a sharp increase in ultrasonic phase followed by a decrease just prior to failure. This phenomenon is consistent with the interfacial stiffness at the contaminated interface decreasing prior to ultimate failure, as shown in Figure 8.8a. As K_1 decreases, the phase first increases sharply to some peak value followed by a decrease. As the bonded joint is placed under high loads, the kissing bond between the PTFE-layer and the adhesive layer may separate, causing the observed decrease in interfacial stiffness.

8.1.5 Conclusions

A nondestructive method for monitoring SLJs undergoing quasi-static shear loading is demonstrated. A specially designed mounting apparatus secures an ultrasonic transducer to a geometrically stable location on the SLJ during the mechanical test. The transducer monitors ultrasonic phase shifts from the first echo of the adhesive bondline with a specially designed CFPPLL-based high-resolution ultrasonic phase measurement system. SLJs fabricated using Al 6061-T651 adherents bonded together with FM73 epoxy film adhesive and with varying interfacial bond qualities are studied. This method is shown to provide early indications of joint failure at as low as 58% of the ultimate joint strength. The ultrasonic phase exhibits a different characteristic response depending on whether the probed region is well-bonded or poorly-bonded. This method has the potential for use as an inspection technique to better understand the nature of adhesive bond failure by its ability to receive material property information from within the bondline. Constant-frequency ultrasonic phase monitoring of bonded joints in-service may be useful as a structural health monitoring technique. This method to monitor bonded joints under mechanical load and investigate ultrasonic phase changes for early signs of bond failure is shown to hold promise. Future work should develop this method to monitor bonded joints under cyclic fatigue loading and investigate ultrasonic phase changes for early signs of bond failure.

8.2 Ultrasonic Phase Evaluation of Additively-Manufactured Parts

8.2.1 Background

Another potential application of the ultrasonic phase measurement method is the inspection of additively manufactured parts. Additive manufacturing (AM) has become quite popular in recent years in a variety of industries for its ability to fabricate complex shapes not easily possible with subtractive manufacturing. Originally used primarily for rapid prototyping, AM is being developed to fabricate complex, customized metal parts for use in critical structures.

At this point, however, there is a clear lack of robust NDE methods for evaluating AM parts, which have their own inspection considerations not commonly seen in bulk parts. In particular, for critical aerospace components, NASA has identified a lack of mature NDE for both finished AM parts as well as in-situ AM processing monitoring [161]. Of particular concern in additively manufactured parts are the interfaces between layers, where porosity and cracking reduce the strength and modify the material properties of manufactured parts.

Several acoustic NDE methods have been investigated for quality assessment of additively manufacture parts. In general, NDE methods are developed for a specific AM process type, such as selective laser melting (SLM), metal powder bed fusion, or ultrasonic additive manufacturing (UAM), but most methods focus on porosity assessment. Ultrasonic methods for AM process monitoring and control have been demonstrated, using an ultrasonic transducer mounted underneath the build plate during AM [162] [163] [164]. Another method listens for acoustic changes throughout a direct energy deposition (DED) AM process and correlates the acoustic signatures to AM process parameters [165]. While not obtaining much information from the underlying bulk structure, surface acoustic waves have shown sensitivity to AM defects and material properties when measured on a layer-by-layer basis [166]. Laser ultrasonic methods have also been investigated [167].

A few studies have looked into modeling the interfaces between layers as spring-boundaries like was done in this work. Both post-manufacturing inspection [168] and in-situ process monitoring during ultrasonic AM [169] using ultrasonic methods have been developed.

Similar ultrasonic spectroscopy methods have been employed to assess bonding in multi-layered composite laminates [170]. Each of these techniques use broadband ultrasonic pulses and analyze the frequency response of back wall echoes from AM parts. The ultrasonic spring-model theory of multilayered structures developed in these works would likely serve as the foundation of the ultrasonic phase model for evaluating interface quality in AM parts.

The basic idea of this approach is that ultrasonic phase of back wall reflections from a witness block in an AM process is monitored in-situ or inspected post-fabrication. The witness block is meant to represent an easily inspectable part with matching AM process parameters as used for the part being fabricated. The ultrasonic phase method would then determine whether the AM process parameters in use are producing the desired material property results. Ideally, the phase method would inspect for interfacial bonding issues between deposited layers and identify defects within the manufactured part, such as porosity.

To obtain preliminary results on whether the ultrasonic phase measurement method may have sensitivity to such defects, additively manufactured parts are fabricated with different process parameters to induce porosity and voids between printed layers. Plastic AM, rather than metal, is used here as plastic 3D-printing resources were easily and quickly available for this project. Basic principles and results on plastic AM parts may be adjusted for use in metal AM parts. The AM parts are ultrasonically evaluated with broadband ultrasonic pulses as well as swept-frequency ultrasonic phase measurements.

8.2.2 Method Description

In this preliminary study, 11 additively manufactured blocks are fabricated with different degrees of under-extrusion. Specifically, blocks with dimensions 12.7 cm wide x 12.7 cm long x 2.54 cm tall are fabricated using an Original Prusa i3 MK3 3D printer from Prusa Research. In total, 11 blocks were fabricated with different values of the process parameter called the extrusion coefficient (EC). The EC is set as a percentage from 0 to 100, and it affects the rate at which plastic is extruded during the printing process. A lower EC results in under-extruded plastic filament, which causes porosity and voids between layers in the printing process.

In practice with the plastic filament used in this study, it was been found that an EC of 97% produces properly extruded filament in AM parts. Using EC values above 97% sometimes results in visible signs of over-extrusion. As such, 97% is taken as the maximum EC value in this study, and the 11 AM blocks vary in EC values from 97% to 87% in 1% decrements.

The 11 AM blocks are ultrasonically evaluated with broadband ultrasonic pulses and the swept-frequency ultrasonic phase method in pulse-echo mode, where the reflection coefficient from the back wall of the part is interrogated. Figure 8.9 shows a diagram depicting the ultrasonic measurement setup, as well as the interfacial stiffness between the layers, which would be assumed constant as part of a model of ultrasonic interactions within the part. The layer thickness, L_0, would be assumed constant and found from the total thickness, L, of the part divided by the number of layers, n. In an in-situ process, the interfacial stiffness would be assessed as the number of layers increases with the layer thickness assumed constant.

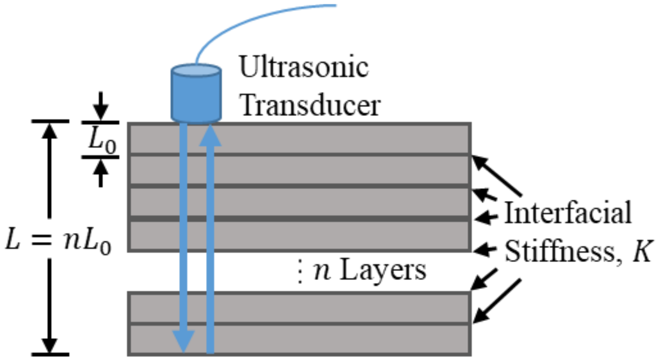

Figure 8.9: Diagram showing measurement of ultrasonic reflections from additively manufactured block specimen

It is theorized that an approach similar to the one taken in Section 6.2 is applicable here, where the linear fit of the phase vs. frequency response over a small frequency range is obtained. By fitting the measured phase response of back wall reflections to the equation $\phi(f) = d\phi/df * f + \phi_0$, the linear portion of the phase shift should primarily be a function of bulk layer material properties and the constant portion should be a measure of interfacial properties. In addition to the study in this work, other researchers have used a similar approach with broadband ultrasonic pulses to probe a structure with a single interface stiffness [77], [78]. This approach would essentially extend the single-interface method to assess multiple interfaces assumed to be of equal quality.

8.2.3 Results and Discussion

8.2.3.1 X-Ray CT Results

Figure 8.10 shows X-ray CT images of selected 3D printed parts from the side with 13.345 µm resolution. Notable in this image are the interfaces between layers, where voids are evident, and as EC decreases, porosity increases. For the EC = 97% part, the volume appears to have almost no porosity, which is consistent with the original assumption that EC = 97% provides no under-extrusion. This data confirms that lowering EC introduces porosity in each layer, as predicted.

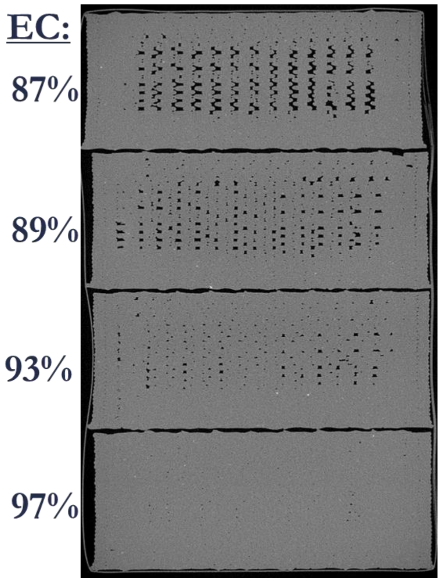

Figure 8.10: X-ray CT images of 3D-printed parts with different extrusion coefficients

8.2.3.2 Amplitude Results

The amplitude vs. time response of the first four back wall echoes from selected additively manufactured blocks is plotted in Figure 8.11. Each plot is normalized so that the peak of the first pulse occurs at a value of -1. The normalized amplitude response more easily shows how the secondary echoes decay over time. For EC values of 97% and 94%, the amplitude responses appear very similar. As the EC reaches 89%, however, there begins to be noticeable ultrasonic backscatter appearing as noise between back wall echoes and making the third and fourth echoes essentially invisible. Ultrasonic backscatter occurs when air pockets, porosity, or inclusions cause scattering events in which some amplitude is reflected back toward the transducer. Using an EC value of 87%, the backscatter has such amplitude that it has overtaken the second echo as well. If not for previous knowledge on where the second echo should be, it would be difficult to determine the time of the second echo's peak amplitude. The high level of backscatter is likely due to small air pockets or porosity developing at the interface between layers.

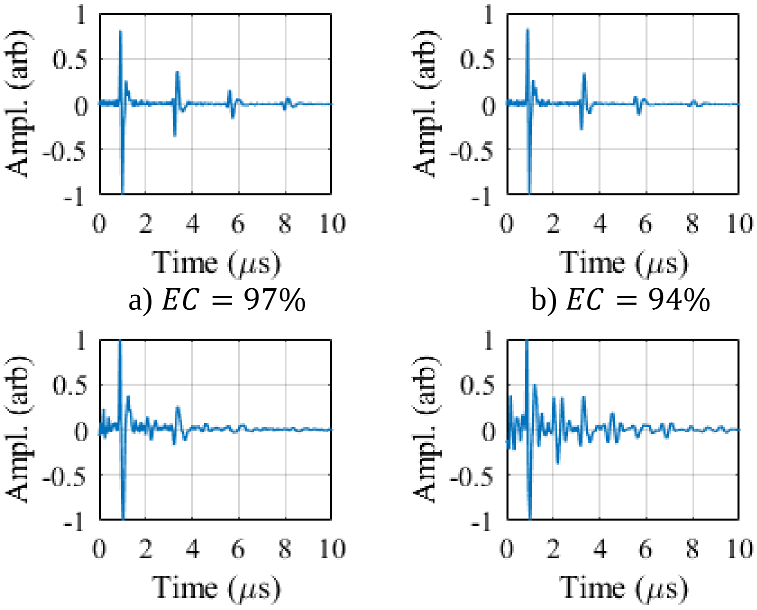

a) $EC = 97\%$ b) $EC = 94\%$

c) $EC = 89\%$ d) $EC = 87\%$

Figure 8.11: Normalized amplitude vs. time response of back wall echoes from additively manufactured blocks with different extrusion coefficients

From the amplitude vs. time response for each specimen, the peak amplitude for the first four back wall echoes are determined and plotted in Figure 8.12.

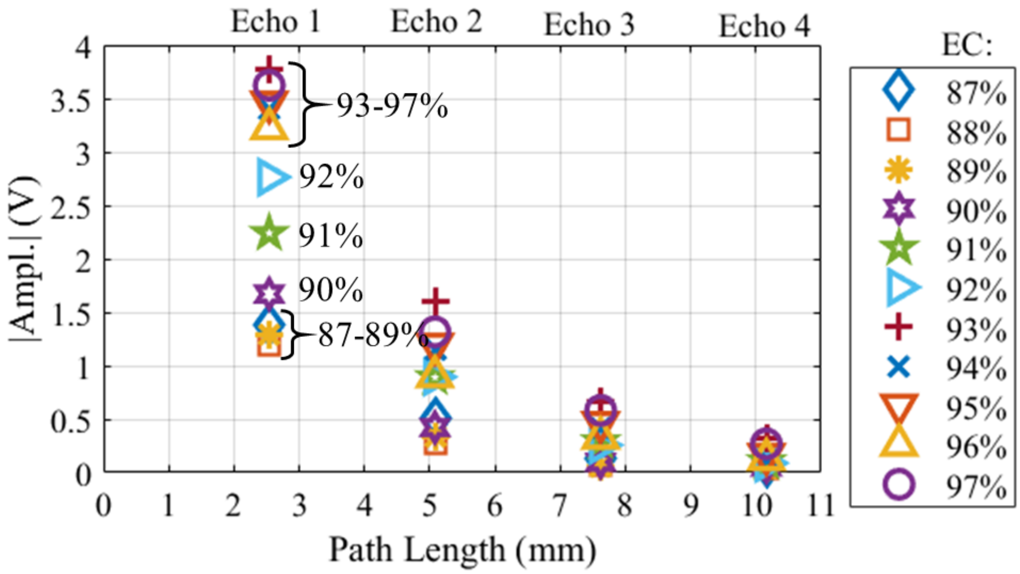

Figure 8.12: Peak amplitude of back wall echoes in additively manufactured blocks

From the first echoes in Figure 8.12, the amplitudes can clearly be placed into different categories that depend on EC. EC values from 93-97% all display amplitudes around 3.5 V. Then, there is a transition region from EC values from 92% to 90% where the amplitude is dropping. Finally, EC values in the 87% to 89% range display measured amplitudes around 1.3 V. These three categories are more easily seen in Figure 8.13, where the peak amplitude of the first echo is plotted.

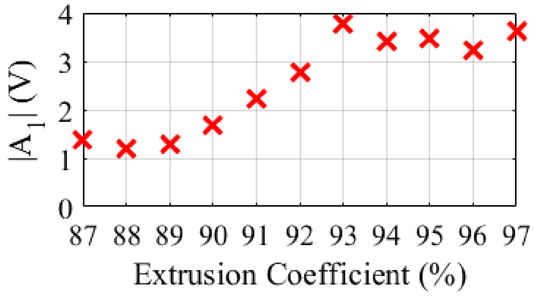

Figure 8.13: Peak amplitude of first back wall echo as a function of extrusion coefficient in additively manufactured blocks

As acoustic attenuation generally scales exponentially as a function of path length, depending upon the attenuation coefficient, an exponential fit of the data in Figure 8.12. The fit uses the equation, $y = ae^{-2\alpha L}$, where a is a scaling coefficient that should be influenced by the reflection coefficient from the transducer/couplant boundary, α is the acoustic attenuation coefficient, and L is the thickness of the layer at a given echo. This exponential function was found to show a good fit to the data, and the fit parameters are plotted as a function of EC in Figure 8.14.

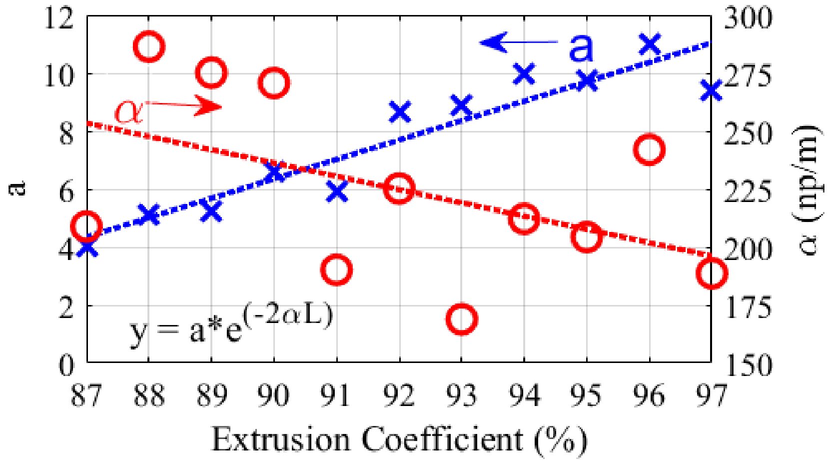

Figure 8.14: Parameters from exponential fit of amplitude vs. path length data as a function of extrusion coefficient

Interestingly, the attenuation coefficient, α, is not a strong function of EC as might be expected. Instead, the scaling coefficient, a, is much better correlated with EC with $R^2 = 0.88$ from the linear fit, whereas the linear fit of α only has $R^2 = 0.24$. Furthermore, a provides a good predictor of EC, as for a measured a value, EC is predicted from the linear fit to a standard deviation of only 1.24 percentage points.

Several different phenomenon could be causing the results seen here. For one, the porosity/under-extrusion may not affect ultrasound in a standard attenuation manner, as an ultrasound absorbing material. The scattering here is likely better modeled by an interfacial spring model at the interface between in layer, which will not affect ultrasonic amplitude in a typical exponential manner. The interfacial stiffness model may explain why the scaling term changes instead of the attenuation coefficient. Another alternative for why the scaling coefficient changes as a strong linear function of EC is that the surface roughness on the probed surface may be affected by the EC. Changing surface roughness on the probed surface will change the reflection coefficient from the AM block/couplant/transducer interface, which would be seen in the a parameter here. Further modeling work is necessary to draw stronger conclusions about the mechanisms causing the observed amplitude responses.

8.2.3.3 Phase Results

From measurements with the swept-frequency phase method, it is first noticeable how quickly the amplitude of echoes deteriorates with thickness. Figure 8.15 shows the amplitude, phase, and sample/hold signals from echoes on AM blocks with an EC of 97% in two different thicknesses. Note how the amplitude of these signals look compared to Al 6061-T651 specimens from Figure 4.2. The attenuation in these plastic parts, even when properly extruded, is very high at 10 MHz as seen by single-frequency ultrasonic tone-bursts. Initially, it was thought to compare phase measurements at two different specimen thicknesses or multiple back wall echoes, but with such high attenuation, it was only possible to probe the first echo from the 2.54 cm thick specimens for different EC values. For lower EC values, the amplitude of received echoes is even lower.

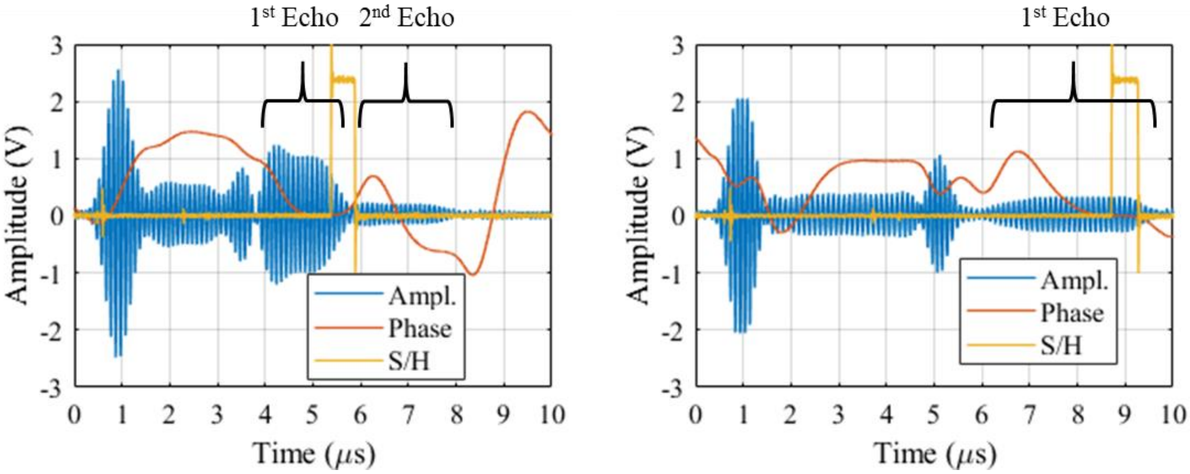

a)　b)

Figure 8.15: Amplitude, phase, and sample/hold position signals from back wall echoes of additively manufactured parts with extrusion coefficient of 97% and specimen thickness of a) 2.54 cm and b) 5.08 cm

When testing on the 2.54 cm thick blocks, it was found that reliable data could only be obtained down to an EC of 91%. Below this threshold, the amplitude of received echoes was too low and phase noise too high to obtain phase measurements over the entire 9-10 MHz range. The phase response of the first echo from the AM blocks with EC from 91-97% is plotted in Figure 8.16.

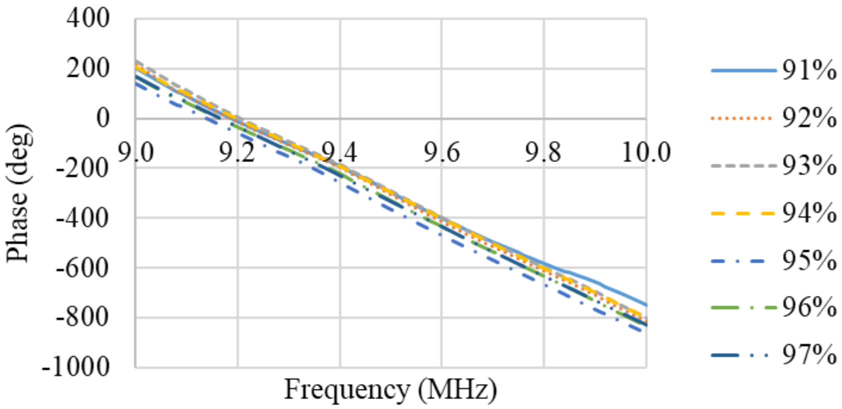

Figure 8.16: Measured phase vs. frequency data from first back wall echo of additively manufactured blocks

The raw phase results in Figure 8.16 are difficult to inspect visually and draw conclusions from, because of the large phase shift range and how closely packed the data are. Thus, further analysis of the phase at 9.5 MHz as well as a linear fit of the phase data are conducted and shown in Figure 8.17. It should be noted that for the last 0.2 MHz or so of the phase measurement on the EC = 91% specimen, there was very low received amplitude and phase noise was very high. This effect is seen in the phase data, where the phase slope changes over the 9.8-10 MHz range for EC = 91%.

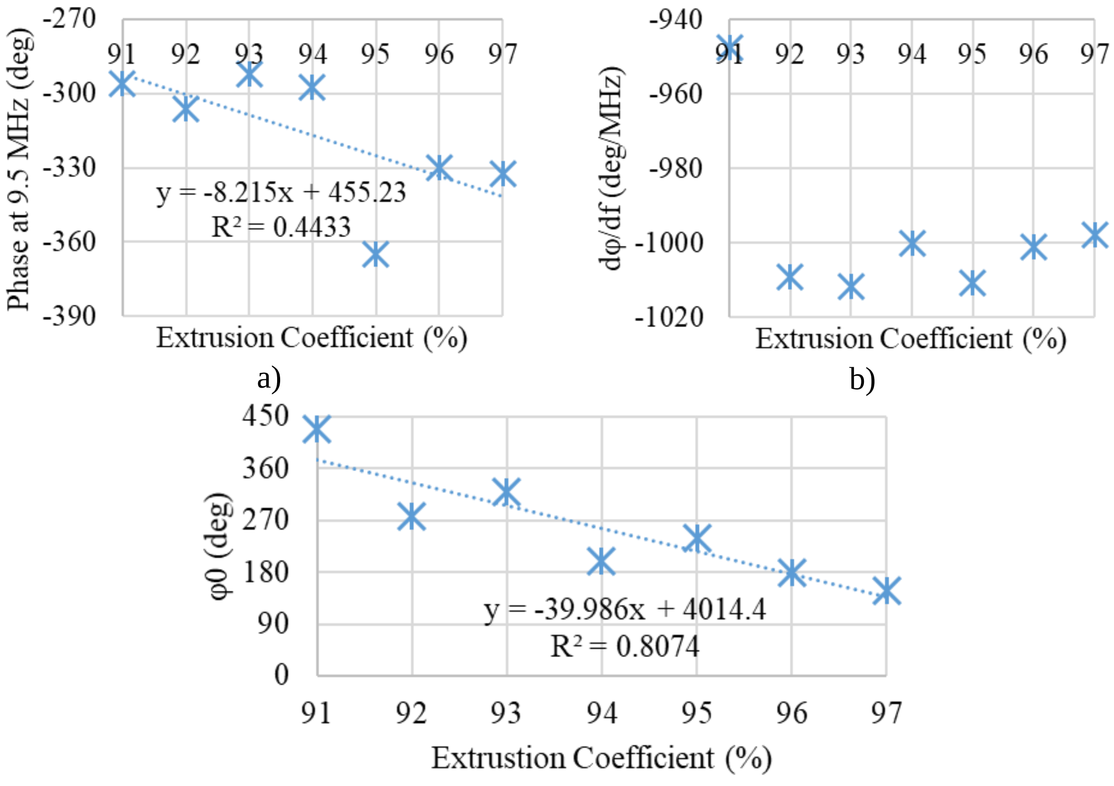

a)

b)

c)

Figure 8.17: Parameters extracted from measured phase spectra from back wall echoes in additively manufactured blocks: a) Phase at 9.5 MHz vs. extrusion coefficient, b) Linear term from linear fit in 9-10 MHz range vs. extrusion coefficient, and c) Constant term from linear fit in 9-10 MHz range vs. extrusion coefficient

An analysis of phase parameters leads to several interesting results. First, with the exception of the EC = 95% block, the phase at 9.5 MHz shown in Figure 8.17a seems to show a negative linear trend with increasing EC. Next, as shown in Figure 8.15b, it is notable that the phase slope in the 9-10 MHz range does not appear to change significantly with EC. The outlier data point at EC =

91% occurs due to the previously mentioned low amplitude response and high phase noise over the last 0.2 MHz of the measured phase response. This result is expected, as only the interfaces between layers should be changing in this study; no AM process parameters are modified which would change the material properties of the filament itself. Finally, it is shown that the constant term from the linear fit, ϕ_0, is a very good predictor of EC. For a given ϕ_0 measurement, EC is predicted by the linear fit to a standard deviation of 0.95 percentage points. These phase measurement results are consistent with the original hypothesis that ϕ_0 should be sensitive to interface properties and $d\phi/df$ should be sensitive to interlayer properties.

8.3 Conclusions

These initial results show that swept-frequency ultrasonic phase measurements show sensitivity to porosity at interfaces between layers deposited through an AM process due to under-extrusion of filament. X-ray CT images as well as broadband ultrasonic measurements confirm the under-extrusion in visible porosity between deposited layers and that attenuation of received echoes are directly related to the EC used in the fabrication process. In addition, the constant term from the linear phase vs. frequency response of the 3D-printed blocks is found well correlated with EC, as was originally predicted. Further theoretical development is necessary to make predictions about material properties, such as interfacial stiffness between layers, from frequency-dependent ultrasonic phase measurements.

Ultrasonic assessment in plastic AM parts is challenging, as shown in this work, due to the high sound attenuation in such materials. A reduction in driving ultrasonic frequency should reduce the attenuation issues in testing on plastic parts. The movement to testing on metal parts should prove less troublesome, as metals are typically much less attenuating to ultrasound.

Another challenge in assessing AM parts is the variation in interface properties across the specimen. Ultrasonic measurements in this work were found to vary from slight movements across the surface of the specimen, as toward the edges of the block, the layered structure changes. While care was taken in this study to make sure the transducer was in the very center of the block for each test, using a larger block area in the witness specimen would help the method's repeatability.

With sensitivity to both layer properties through the slope of phase shift and interlayer properties through the constant phase shift from the phase vs. frequency response, this method has the potential to identify bulk filament issues as well as interfacial flaws in an AM process. The modification to the ultrasonic phase method developed here to add a simple amplitude measurement each time the phase is sampled would provide additional information useful to the inspection of AM parts. While phase is sensitive to interface quality, the addition of amplitude measurements would allow for better assessment of attenuation caused by porosity and other defects in the part. Additionally, this method is compatible with an ultrasonic transducer mounted under the AM bed so that ultrasonic phase may be monitored in real-time for an AM process control and feedback methodology. Future work with this technology should explore post-manufacturing defect detection and interfacial stiffness assessment in more detail, as well as investigate in-situ AM process monitoring of interface properties.

Chapter 9: Conclusions and Future Work

9.1 Conclusions

A novel ultrasonic phase measurement method has been developed and demonstrated for adhesive bond quality assessment. The phase measurement method uses a CFPPLL-based instrument to measure ultrasonic phase with unprecedented accuracy and precision. With a frequency-independent phase resolution of $0.022°$, the instrument can detect thickness changes as small as 6.1×10^{-5} of an ultrasonic wavelength, which is equal to a thickness change of $\sim 20\, nm$ via reflection measurements in Al. Experimental results show the CFPPLL method has lower phase measurement uncertainty than other high-resolution ultrasonic time-delay measurement methods, such as cross-correlation and conventional broadband pulse ToF.

At a single interface, single-frequency ultrasonic phase measurements have proved able to assess interface quality. A study on the interface between glass adherents and UV-curable adhesives demonstrated interface stiffness threshold assessment as well as interface stiffness measurement throughout the entire cure process. In simulated kissing bonds, where metal surfaces are held in dry-contact under compressive loads, the ultrasonic phase method is demonstrated to assess interfacial stiffness regardless of the acoustic impedance values around the boundary.

Using the swept-frequency capabilities of the CFPPLL instrument, the phase response of a SLJ is interrogated. Near the ultrasonic resonance frequency, the amplitude of ultrasonic reflection is minimized, and the phase undergoes a sharp inversion from negative to positive values. By using a distributed spring model of the ultrasonic interactions with the bonded joint, it has been shown that interfacial bond strength (represented by a stiffness constant) causes changes to the ideal phase response around the resonance frequency. A study on ideal bonded joints fabricated with polished glass adherents and UV-curable adhesive proved ultrasonic phase is sensitive to cohesive and interfacial bonding changes during cure. In agreement with theoretical work, a strong linear correlation is found between interfacial stiffness and measured tensile bond strength. Additionally, the shift in anti-resonance frequency of the bond line is found to be a sufficient parameter to measure reduced bond strength when both interfaces can be assumed equally strong.

Additional results on Al/epoxy SLJs demonstrated interface quality assessment with ultrasonic phase when one interface is contaminated with a thin layer of silicone or Teflon. Bond strength was modified by different concentrations of interfacial contamination. Ultrasonic evaluation results show a strong difference in the characteristic phase vs. frequency curves from pristine lap joints and highly contaminated lap joints, especially in the slope of phase inversion. Interfacial stiffness constants are extracted from either curve fitting the entire phase spectra or by measurement of the resonance frequency and maximum slope of phase shift from the phase spectra. Overall, the phase method is able to distinguish varying degrees of interfacial contamination, and it able to identify kissing bonds when the entire interface is contaminated.

The ultrasonic phase measurement method also has applications beyond adhesive bond strength evaluation, including additive manufacturing process monitoring, thin film quality assessment, material porosity assessment, and adhesive bond monitoring for early signs of bond failure when under load. Several such applications have been briefly studied in this work.

First, an additional investigation showed constant-frequency ultrasonic phase monitoring is capable of identifying precursors to bonded joint failure at around 80% of the failure load during quasi-static shear loading. Furthermore, the slope of phase shift is found to show a different characteristic response for interfacially contaminated joints in comparison to pristine joints. Early detection of bond failure would provide a significant impact to the SHM community, as in-service bonds could be monitored and weak joints could be identified prior to failure. Additionally, this method could be used as a tool for fracture mechanics experts to obtain better information about mechanisms in the bond line affecting bonded joint failure.

Second, ultrasonic phase was investigated for the assessment of additively manufactured (AM) parts. Initial results show that swept-frequency ultrasonic phase measurements have sensitivity to porosity at interfaces between layers deposited through an AM process due to under-extrusion of filament. With sensitivity to both interlayer and interfacial properties, this method has the potential to identify bulk filament issues as well as interfacial flaws in an AM process. This technique has the potential to be developed into an in-situ AM process control methodology.

This method uses commercial ultrasonic transducers with CFPPLL technology to obtain high-resolution ultrasonic phase measurements of ultrasonic tone-burst reflections over a selectable range of frequencies. Narrowband filtering of the measured tone-burst promotes noise suppression and higher signal-to-noise ratio, resulting in lower phase measurement uncertainty. Furthermore, the CFPPLL method is compatible with existing ultrasonic inspection methods, including commercially available transducers and scanning systems. By providing a high-resolution, practical system for adhesive bond evaluation, this method will be a valuable contribution to the NDE and SHM communities and will promote the use of composite structures in aerospace, automotive, and other designs.

9.2 Future Work

While this work proved that ultrasonic phase measurements may be used to assess adhesive bond quality, there are many opportunities for future work to further this technology. For this method to find use in industry, it must be developed into a larger-scale scanning method using focused ultrasonic transducers. Throughout this work, unfocused transducers were used to obtain single spot measurements of ultrasonic phase. In order to make this system practical in this setup, the time it takes to obtain ultrasonic measurements should be addressed using some of the suggestions found in Section 7.2.1. Additionally, the bandwidth of the current CFPPLL instrument limits the bond line thicknesses assessable using phase resonance analysis. As discussed in Section 7.2.2, this issue could be addressed by a redesign of the receiver circuit. Automated inverse algorithms for the real-time determination of interfacial stiffness from phase measurements should also be investigated.

Another modification to the CFPPLL instrument that would improve its capabilities is the addition of a simple ultrasonic amplitude assessment each time the phase is adjusted. This should be a relatively minor change to the instrument, not requiring a major redesign, as the amplitude signal to be probed is already being viewed on an oscilloscope during setup. By adding an amplitude measurement, even if it were low resolution, additional information could be gathered from a bonded joint. It would be especially useful in the study discussed in Section 5.1, where the phase of both good and bad bonding appears the same when $Z_1 > Z_2$. An amplitude assessment in this scenario should distinguish whether good or bad bonding is causing the measured phase.

In terms of increasing the sensitivity to bond quality, this method could be modified for use with ultrasonic shear waves rather than longitudinal waves. Several amplitude-based ultrasonic methods have demonstrated greater sensitivity to small changes in interface quality by using shear waves [67] [68] [69], especially in the case of so-called “slip boundaries”, where the interface may transfer normal stress but not shear stress. Slip boundaries typically occur due to hot, wet aging of a joint, which causes moisture absorption at the interface. While longitudinal waves easily propagate through water, shear waves will not, making weak bonds in this scenario difficult to detect with longitudinal methods.

The problem with introducing shear waves into a test specimen is that shear waves do not transmit well through conventional liquid ultrasonic couplants, such as water. Normal-incidence shear wave couplants must have a very high viscosity to support adequate transmission. Most commonly, bee’s honey is used as shear wave couplant, which is difficult to work with, expensive in comparison to water, and difficult to clean off from test specimens. Instead, most approaches use angled longitudinal ultrasonic waves, which cause shear waves to transmit into a part when reflection off a boundary at the appropriate angle. With the ultrasonic phase method, normal-incidence shear waves may be first investigated in a laboratory setting using a shear wave transducer and couplant, but some sort of angle-beam longitudinal approach may be necessary for more practical use.

Finally, the ultrasonic phase method should be thoroughly investigated for use in composite structures. As discussed throughout, adhesive bonding is the preferred method of joining composite materials to promote their weight and strength advantages over metals. While the general principles of ultrasonic phase assessment of adhesive bonding still apply to composites, the practical challenges of assessment on composites should be explored.

A key issue expected to be encountered in composite bonded joints is the acoustic impedance matching between adherents and adhesive. In ultrasonic reflections, the difference in acoustic impedance between two media controls the reflection coefficient. In most metal lap joints, the acoustic impedance difference between the metal adherent and epoxy adhesive is large enough to provide a significant amplitude of reflection from the adhesive/adherent interface. In contrast, commonly-used CFRP adherents use carbon fibers embedded in an epoxy matrix, which means the adhesive and adherent have a very similar acoustic impedance and the amplitude of the ultrasonic reflection coefficient from the bond line may be too small for reliable detection.

Additionally, the presence of carbon fibers in a matrix will affect ultrasound propagation. Even though carbon fiber diameters are much smaller than the acoustic wavelengths typically used, ultrasonic phase is quite sensitive to changes in sound velocity and path length, so the effect of carbon fibers on ultrasonic phase should be characterized.

Methods for overcoming this challenge in composites include through-transmission assessment with two transducers, as well as measuring the phase of the reflection coefficient from the back wall of the lower adherent can be measured. As the lower adherent will have a significantly different acoustic impedance than air on the other side, there will be a sufficiently high amplitude of reflection for phase measurements. In this setup, the ultrasonic wave will be transmitted through the adhesive twice: once while traveling down to the back wall of the lower adherent and once on the return path.

In composites, phase noise due to scattering in the adherents may be much higher than in metals, so this effect should be characterized. At the same time, however, the ultrasonic phase method may be able to assess interlaminar bond strength between composite plies by modeling the interfaces as a distributed spring boundary system. Overall, the efficacy and limitations of ultrasonic phase measurements on composite-adherent bonded joints should be identified.

References

[1] R. D. Adams and B. W. Drinkwater, "Nondestructive Testing of Adhesively-Bonded Joints," *NDT&E International,* vol. 30, no. 2, pp. 93-98, 1997.

[2] P. Cawley, T. Pialucha and M. Lowe, "A Comparison of Different Methods for the Detection of a Weak Adhesive/Adherend Interface in Bonded Joints," *Review of Progress in QNDE,* vol. 12, pp. 1531-1538, 1993.

[3] G. M. Light and H. Kwun, "Nondestructive Evaluation of Adhesive Bond Quality: State-of-the-Art Review," Nondestructive Testing Information Analysis Center, 1989.

[4] B. Ehrhart, B. Valeske, C.-E. Muller and C. Bockenheimer, "Methods for the Quality Assessment of Adhesive Bonded CFRP Structures - A Resume," in *2nd International Symposium on NDT in Aerospace,* 2010.

[5] L. Tong, J. K. Spelt and G. Fernlund, "Strength Determination of Adhesive Bonded Joints," in *Recent Advances in Structural Joints and Repairs for Composite Materials,* L. Tong and C. Soutis, Eds., Dordrecht, The Netherlands, Kluwer Academic Publishers, 2003, pp. 27-66.

[6] Y. Y. Hung, Y. S. Chen, S. P. Ng, L. Liu, Y. H. Huang, B. L. Luk, R. W. Ip, C. M. Wu and P. S. Chung, "Review and Comparison of Shearography and Active Thermography for Nondestructive Evaluation," *Materials Science and Engineering: R: Reports,* vol. 64, no. 5-6, pp. 73-112, 2009.

[7] D. M. McCann and M. C. Forde, "Review of NDT Methods in the Assessment of Concrete and Masonry Structures," *NDT&E International,* vol. 34, no. 2, pp. 71-84, 2001.

[8] V. P. Vavilov and D. D. Burleigh, "Review of Pulsed Thermal NDT: Physical Principles, Theory and Data Processing," *NDT&E International,* vol. 73, pp. 28-52, 2015.

[9] M. A. Drewry and G. A. Georgiou, "A Review of NDT Techniques for Wind Turbines," *Insight,* vol. 49, no. 3, pp. 137-141, 2007.

[10] O. S. Salawu, "Detection of Structural Damage Through Changes in Frequency: A Review," *Engineering Structures,* vol. 19, no. 9, pp. 718-723, 1997.

[11] Y.-K. Zhu, G.-Y. Tian, R.-S. Lu and H. Zhang, "A Review of Optical NDT Technologies," *Sensors,* vol. 11, no. 8, pp. 7773-7798, 2011.

[12] D. N. Markatos, K. I. Tserpes, E. Rau, S. Markus, B. Ehrhart and S. Pantelakis, "The Effects of Manufacturing-Induced and In-Service Related Bonding Quality Reduction on the Mode-I Fracture Toughness of Composite Bonded Joints for Aeronautical Use," *Composites: Part B,* vol. 45, pp. 556-564, 2013.

[13] S. Dixon, D. Jaques, S. B. Palmer and G. Rowlands, "The Measurement of Shear and Compression Waves in Curing Epoxy Adhesives using Ultrasonic Reflection and Transmission Techniques Simultaneously," *Measurement Sciences and Technology,* vol. 15, pp. 939-947, 2004.

[14] T. B. Hudson and F.-G. Yuan, "Automated In-Process Cure Monitoring of Composite Laminates using a Guided Wave-Based System with High-Temperature Piezoelectric Transducers," *ASME Journal of Nondestructive Evaluation,* vol. 1, no. 2, p. 021008, 2018.

[15] M. K. Budzik, B. Mascaro, J. Jumel, M. Castaings and M. E. Shanahan, "Monitoring of Crosslinking of a DGEBA-PAMAM Adhesive in Composite/Aluminum Bonded Joint using Mechanical and Ultra-sound Techniques," *International Journal of Adhesion and Adhesives,* vol. 35, pp. 120-128, 2012.

[16] E. Y. Maeva, I. Severina and G. B. Chapman II, "Ultrasonic Analysis of the Degree of Cure and Cohesive Properties of the Adhesive in a Bond Joint," *Research in Nondestructive Evaluation,* vol. 18, no. 2, pp. 121-138, 2007.

[17] G. W. Critchlow and D. M. Brewis, "Review of Surface Pretreatments for Aluminum Alloys," *International Journal of Adhesion and Adhesives,* vol. 16, pp. 255-275, 1996.

[18] A. Higgins, "Adhesive Bonding of Aircraft Structures," *International Journal of Adhesion and Adhesives,* vol. 20, no. 5, pp. 367-376, 2000.

[19] K. Uehara and M. Sakurai, "Bonding Strength of Adhesives and Surface Roughness of Joined Parts," *Journal of Materials Processing Technology,* vol. 127, pp. 178-181, 2002.

[20] Y. Boutar, S. Naimi, S. Mezlini and M. Ali, "Effect of Surface Treatment on the Shear Strength of Aluminum Adhesive Single-Lap Joints for Automotive Applications," *International Journal of Adhesion and Adhesives,* vol. 67, pp. 38-43, 2016.

[21] T. Sekercioglu, H. Rende, A. Gulsoz and C. Meran, "The Effects of Surface Roughness on the Strength of Adhesively Bonded Cylindrical Components," *Journal of Materials Processing Technology,* vol. 142, pp. 82-86, 2003.

[22] E. Sancaktar and R. Gomatam, "A Study on the Effects of Surface Roughness on the Strength of Single Lap Joints," *Journal of Adhesion Science and Technology,* vol. 15, no. 1, pp. 97-117, 2001.

[23] A. Rudawska, "Selected Aspects of the Effect of Mechanical Treatment on Surface Roughness and Adhesive Joint Strength of Steel Sheets," *International Journal of Adhesion and Adhesives,* vol. 50, pp. 235-243, 2014.

[24] E. G. Baburaj, D. Starikov, J. Evans, G. A. Shafeev and A. Bensaoula, "Enhancement of Adhesive Joint Strength by Laser Surface Modification," *International Journal of Adhesion and Adhesives,* vol. 27, no. 4, pp. 268-276, 2007.

[25] R. C. Wong, A. P. Hoult, J. K. Kim and T. X. Yu, "Improvement of Adhesive Bonding in Aluminum Alloys using a Laser Surface Texturing Process," *Journal of Materials Processing Technology,* vol. 63, no. 1-3, pp. 579-584, 1997.

[26] F. L. Palmieri, K. A. Watson, G. Morales, T. Williams, R. Hicks, C. J. Wohl, J. W. Hopkins and J. W. Connell, "Laser Ablative Surface Treatment for Enhanced Bonding of Ti-6Al-4V Alloy," *ACS Applied Material Interfaces,* vol. 5, no. 4, pp. 1254-1261, 2013.

[27] I. De Iorio, C. Leone, L. Nele and V. Tagliaferri, "Plasma Treatments of Polymeric Materials and Al Alloy for Adhesive Bonding," *Journal of Materials Processing Technology,* vol. 68, pp. 179-183, 1997.

[28] C. Mandolfino, E. Lertora, S. Genna, C. Leone and C. Gambaro, "Effect of Laser and Plasma Surface Cleaning on Mechanical Properties of Adhesive Bonded Joints," *Procedia CIRP,* vol. 33, pp. 458-463, 2015.

[29] C. Sperandio, J. Bardon, A. Laachachi, H. Aubriet and D. Ruch, "Influence of Plasma Surface Treatment on Bond Strength Behaviour of an Adhesively Bonded Aluminum-

Epoxy System," *International Journal of Adhesion and Adhesives,* vol. 30, pp. 720-728, 2010.

[30] M. Noeske, J. Degenhardt, S. Strudthoff and U. Lommatzsch, "Plasma jet treatment of five polymers at atmospheric pressure: Surface modifications and the relevance for adhesion," *International Journal of Adheison and Adhesives,* vol. 24, pp. 171-177, 2004.

[31] W. Leahy, V. Barron, M. Buggy, T. Young, A. Mas, F. Schue, T. McCabe and M. Bridge, "Plasma surface treatment of aerospace materials for enhanced adhesive bonding," *The Journal of Adhesion* , vol. 77, pp. 215-249, 2001.

[32] J. Comyn, "Contact Angles and Adhesive Bonding," *International Journal of Adhesion and Adhesives,* vol. 12, no. 3, pp. 145-149, 1992.

[33] R. J. Good, "Contact Angle, Wetting, and Adhesion: A Critical Review," *Journal of Adhesion Science and Technology,* vol. 6, no. 12, pp. 1269-1302, 2012.

[34] R. Ledesma, F. Palmieri, J. Connell, W. T. Yost and J. Fitz-Gerald, "Surface Characterization of Carbon Fiber Reinforced Polymers by Picosecond Laser Incuded Breakdown Spectroscopy," *Spectrochimica Acta Part B: Atomic Spectroscopy,* vol. 140, pp. 5-12, 2018.

[35] K. Brune, L. Lima, M. Noeske, K. Thiel, C. Tornow, S. Dieckhoff, M. Hoffmann and D. Stubing, "Pre-bond Quality Assurance of CFRP Surfaces Using Optically Stimulated Electron Emission," in *3rd International Conference of Engineering Against Failure,* Kos, Greece, 2013.

[36] D. K. Hsu, B. A. Fischer and M. Koskamp, "Shear wave ultrasonic technique as an NDE tool for composite laminates before and after curing," in *Review of Progress in Quantitative Nondestructive Evaluation,* La Jolla, CA, 1997.

[37] Y. V. Gulyaev, "Review of shear surface acoustic waves in solids," *IEEE Transactions on Ultrasonics, Ferroelectrics, and Frequency Control,* vol. 45, no. 4, pp. 935-938, 1998.

[38] Z. Su, L. Ye and Y. Lu, "Guided lamb waves for identification of damage in composite structures: A review," *Journal of Sound and Vibration,* vol. 295, no. 3-5, pp. 753-780, 2006.

[39] S. N. Ramadas, R. L. O'Leary and A. Gachagan, "Ultrasonic sensor design for NDE application: Design challenges and considerations," in *National Seminar and Exhibition on Non-Destructive Evaluation,* Tiruchirapalli, India, 2009.

[40] M. Castaings, P. Cawley, R. Farlow and G. Hayward, "Single sided inspection of composite materials using air coupled ultrasound," *Journal of Nondestructive Evaluation,* vol. 17, no. 1, pp. 37-45, 1998.

[41] I. Solodov, K. Pfleiderer, H. Gerhard, S. Predak and G. Busse, "New opportunities for NDE with air-coupled ultrasound," *NDT&E International,* vol. 39, no. 3, pp. 176-183, 2006.

[42] E. R. Dobbs and J. D. Llewellyn, "Generation of ultrasonic waves without using a transducer," *Non-Destructive Testing,* vol. 4, no. 1, pp. 49-56, 1971.

[43] S. Boonsang and R. J. Dewhurst, "A sensitive electromagnetic acoustic transducer for picometer-scale ultrasonic displacement measurements," *Sensors and Actuators A,* vol. 127, pp. 345-354, 2006.

[44] S. J. Davies, C. Edwards, G. S. Taylor and S. B. Palmer, "Laser-generated ultrasound: Its properties, mechanisms and multifarious applications," *Journal of Physics D: Applied Physics,* vol. 26, pp. 329-348, 1993.

[45] T. Sanderson, C. Ume and J. Jarzynski, "Longitudinal wave generation in laser ultrasonics," *Ultrasonics,* vol. 35, pp. 553-561, 1998.

[46] C. B. Scruby, "Some applications of laser ultrasound," *Ultrasonics,* vol. 27, pp. 195-209, 1989.

[47] A. Blouin, C. Padioleau, C. Neron, D. Levesque and J. P. Monchalin, "Differential confocal fabry-perot for the optical detection of ultrasound," in *Review of Progress in Quantitative Nondestructive Evaluation*, Golden, CO, 2007.

[48] A. M. Aindow, R. J. Dewhurst, S. B. Palmer and C. B. Scruby, "Laser-based non-destructive testing techniques for the ultrasonic characterization of subsurface flaws," *NDT International,* vol. 17, no. 6, pp. 329-335, 1984.

[49] I. Pelivanov, A. Shtokolov, C.-w. Wei and M. O'donnell, "A 1 kHz a-scan rate pump-probe laser ultrasound system for robust inspection of composites," *IEEE Transactions on Ultrasonics, Ferroelectrics, and Frequency Control,* vol. 62, no. 9, pp. 1696-1703, 2015.

[50] ASTM, "ASTM Standard D1002: Standard test method for apparent shear strength of single-lap-joint adhesively bonded metal specimens by tension loading (metal-to-metal)," in *Annual Book of ASTM Standards,* vol. 15.06, 2019.

[51] H.-Y. Yeh and D. Tandjung, "Mixed mode fracture analysis of the lap shear specimen test per ASTM D1002," *Journal of Reinforced Plastics and Composites,* vol. 24, no. 8, pp. 839-853, 2005.

[52] H. S. da Costa Mattos, E. M. Sampaio and A. H. Monteiro, "Static failure analysis of adhesive single lap joints," *International Journal of Adhesion and Adhesives,* vol. 31, pp. 446-454, 2011.

[53] J. Galy, J. Moysan, A. El Mahi, N. Ylla and N. Massacret, "Controlled reduced-strength epoxy-aluminum joints validated by ultrasonic and mechanical measurements," *International Journal of Adhesion and Adhesives,* vol. 72, pp. 139-146, 2017.

[54] M. Lucic, A. Stoic and J. Kopac, "Investigation of aluminum single lap adhesively bonded joints," in *11th International Scientific Conference on Contemporary Achievements in Mechanics, Manufacturing, and Materials Science,* Gliwice - Zakopane, Poland, 2005.

[55] ASTM, "ASTM Standard D3433: Standard test method for fracture strength in cleavage of adhesives in bonded metal joints," in *ASTM Book of Standards*, 2019.

[56] B. Blackman, J. P. Dear and A. J. Kinloch, "The calculation of adhesive fracture energies from double-cantilever beam test specimens," *Journal of Materials Science Letters,* vol. 10, pp. 253-256, 1991.

[57] F. A. Mehrabadi, "Experimental and numerical failure analysis of adhesive composite joints," *International Journal of Aerospace Engineering,* vol. 2012, p. 925340, 2012.

[58] R. D. Adams, J. W. Cowap, G. Farquharson, G. M. Margary and D. Vaughn, "The relative merits of the Boeing wedge test and the double cantilever beam test for assessing the durability of adhesively bonded joints, with particular reference to the use of fracture mechanics," *International Journal of Adhesion and Adhesives,* vol. 29, no. 6, pp. 609-620, 2009.

[59] J. D. Bardis and K. T. Kedward, "Surface preparation effects on Mode I testing of adhesively bonded composite joints," *Journal of Composites Technology and Research,* vol. 24, no. 1, pp. 30-37, 2002.

[60] M. Wetzel, J. Holtmannspotter, H. J. Gudladt and J. V. Czarnecki, "Sensitivity of double cantilever beam test to surface contamination and surface pretreatment," *International Journal of Adhesion and Adhesives,* vol. 46, pp. 114-121, 2013.

[61] H. G. Tattersall, "The Ultrasonic Pulse-Echo Technique as Applied to Adhesion Testing," *Journal of Physics D: Applied Physics,* vol. 6, pp. 819-832, 1973.

[62] J.-M. Baik and R. B. Thompson, "Ultrasonic Scattering from Imperfect Interfaces: A Quasi-Static Model," *Journal of Nondestructive Evaluation,* vol. 4, no. 3/4, pp. 177-196, 1984.

[63] N. Mori, N. Matsuda and T. Kusaka, "Effect of interfacial adhesion on the ultrasonic interaction with adhesive joints: A theoretical study using spring-type interfaces," *Journal of the Acoustical Society of America,* vol. 145, no. 6, pp. 3541-3550, 2019.

[64] J. H. Cantrell, "Determination of Absolute Bond Strength from Hydroxyl Groups at Oxidized Aluminum-Epoxy Interfaces by Angle Beam Ultrasonic Spectroscopy," *Journal of Applied Physics,* vol. 96, no. 7, pp. 3775-3781, 2004.

[65] J. H. Cantrell, "Hydrogen Bonds, Interfacial Stiffness Moduli, and the Interlaminar Shear Strength of Carbon Fiber-Epoxy Matrix Composites," *AIP Advances,* vol. 5, p. 037125, 2015.

[66] J. Cantrell, "Assessment of Adhesive Bond Strength from Ultrasonic Tone-Bursts," *Journal of Nondestructive Evaluation,* vol. 37, p. 81, 2018.

[67] A. I. Lavrentyev and S. I. Rokhlin, "Determination of Elastic Moduli, Density, Attenuation, and Thickness of a Layer using Ultrasonic Spectroscopy at Two Angles," *Journal of the Acoustical Society of America,* vol. 102, no. 6, pp. 3467-6477, 1997.

[68] S. I. Rokhlin, L. Wang, B. Xie, V. A. Yakovlev and L. Adler, "Modulated Angle Beam Ultrasonic Spectroscopy for Evaluation of Imperfect Interfaces and Adhesive Bonds," *Ultrasonics,* vol. 42, pp. 1037-1047, 2004.

[69] P. B. Nagy, "Ultrasonic Detection of Kissing Bonds at Adhesive Interfaces," *Journal of Adhesion Science and Technology,* vol. 5, no. 8, pp. 619-630, 1991.

[70] C. Gauthier, M. E.-C. El-Kettani, J. Galy, M. Predoi, D. Leduc and J.-L. Izbicki, "Lamb wave characterization of adhesion levels in aluminum/epoxy bi-layers with different cohesive and adhesive properties," *International Journal of Adhesion and Adhesives,* vol. 74, pp. 15-20, 2017.

[71] M. Castaings, "SH ultrasonic guided waves for the evaluation of interfacial adhesion," *Ultrasonics,* vol. 54, no. 7, pp. 1760-1775, 2014.

[72] D. Yan, B. W. Drinkwater and S. A. Neild, "Measurement of the ultrasonic nonlinearity of kissing bonds in adhesive joints," *NDT&E International,* vol. 42, pp. 459-466, 2009.

[73] R. J. Freemantle and R. E. Challis, "Combined compression and shear wave ultrasonic measurements on curing adhesive," *Measurement Science and Technology,* vol. 9, no. 8, pp. 1291-1302, 1998.

[74] E. Siryabe, M. Renier, A. Mezaine, J. Galy and M. Castaings, "Apparent anistropy of adhesive bonds with weak adhesion and non-destructive evaluation of interfacial properties," *Ultrasonics,* vol. 79, pp. 34-51, 2017.

[75] A. I. Lavrentyev and J. T. Beals, "Ultrasonic measurement of the diffusion bond strength," *Ultrasonics,* vol. 38, pp. 513-516, 2000.

[76] D. D. Palmer, D. K. Rehbein, J. F. Smith and O. Buck, "Nondestructive characterization of the mechancial strength of diffusion bonds. II. Application of a quasi-static spring model," *Journal of Nondestructive Evaluation,* vol. 7, no. 3/4, pp. 167-174, 1988.

[77] K. Milne, P. Cawley, P. B. Nagy, D. C. Wright and A. Dunhill, "Ultrasonic Non-Destructive Evaluation of Titanium Diffusion Bonds," *Journal of Nondestructive Evaluation,* vol. 30, pp. 225-236, 2011.

[78] E. Escobar-Ruiz, D. C. Wright, I. J. Collison, P. Cawley and P. B. Nagy, "Reflection Phase Measurements for Ultrasonic NDE of Titanium Diffusion Bonds," *Journal of Nondestructive Evaluation,* vol. 33, pp. 535-546, 2014.

[79] G. Rosa, R. Oltra and M.-H. Nadal, "Evaluation of the coating-substrate adhesion by laser-ultrasonics: Modeling and experiments," *Journal of Applied Physics,* vol. 91, no. 10, pp. 6744-6753, 2002.

[80] H. Wang, M. L. Qian and W. Liu, "Laser ultrasonic characterization of adhesive bonds between epoxy coating and aluminum substrate," *Ultrasonics,* vol. 44, pp. e1349-e1353, 2006.

[81] R. S. Dwyer-Joyce, "The application of ultrasonic NDT techniques in tribology," *Proceedings of the Institution of Mechanical Engineers, Part J: Journal of Engineering Tribology,* vol. 219, no. 5, pp. 347-366, 2005.

[82] S. Mezil, F. Bruno, S. Raetz, J. Laurent, D. Royer and C. Prada, "Investigation of interfacial stiffness of a tri-layer using zero-group velocity lamb modes," *Journal of the Acoustical Society of America,* vol. 138, no. 5, pp. 3202-3209, 2015.

[83] A. Baltazar, L. Wang, B. Xie and S. I. Rokhlin, "Inverse ultrasonic determination of imperfect interfaces and bulk properties of a layer between two solids," *Journal of the Acoustical Society of America,* vol. 114, no. 3, pp. 1424-1434, 2003.

[84] S. Biwa, S. Hiraiwa and E. Matsumoto, "Stiffness evaluation of contacting surfaces by bulk and interface waves," *Ultrasonics,* vol. 47, no. 1-4, pp. 123-129, 2007.

[85] J. Krolikowski and J. Szczepek, "Phase Shift of the Reflection Coefficient of Ultrasonic Waves in the Study of the Contact Interface," *Wear,* vol. 157, pp. 51-64, 1992.

[86] M. Y. Hung, Y. S. Chen, S. P. Ng, S. M. Shepard, Y. Hou and J. R. Lhota, "Review and Comparison of Shearography and Pulsed Thermography for Adhesive Bond Evaluation," *Optical Engineering,* vol. 46, no. 5, p. 051007, 2007.

[87] J. A. Schroeder, T. Ahmed, B. Chaudhry and S. Shepard, "Non-Destructive Testing of Structural Composites and Adhesively Bonded Composite Joints: Pulsed Thermography," *Composites: Part A,* vol. 33, pp. 1511-1517, 2002.

[88] R. L. Vijaya Kumar, M. R. Bhat and C. R. Murthy, "Evaluation of Kissing Bond in Composite Adhesive Lap Joints using Digital Image Correlation: Preliminary Studies," *International Journal of Adhesion and Adhesives,* vol. 42, pp. 60-68, 2013.

[89] A. Nieminen and J. L. Koenig, "NMR Imaging - A Promising New Adhesive Evaluation Technique," *Journal of Adhesion Science and Technology,* vol. 2, no. 1, pp. 407-414, 1988.

[90] B. Ehrhart, R. Ecault, F. Touchard, M. Boustie, L. Berthe, C. Bockenheimer and B. Valeske, "Development of a Laser Shock Adhesion Test for the Assessment of Weak Adhesive Bonded CFRP Structures," *International Journal of Adhesion and Adhesives,* vol. 52, pp. 57-65, 2014.

[91] M. Perton, A. Blouin and J. P. Monchalin, "Adhesive Bond Testing of Carbon-Epoxy Composites by Laser Shockwave," *Journal of Physics D: Applied Physics,* vol. 44, p. 034012, 2011.

[92] S. Barradas, R. Molins, M. Jeandin, M. Arrigoni, M. Boustie, C. Bolis, C. Berthe and M. Ducos, "Application of laser shock adhesion testing to the study of interlamellar strength and coating-substrate adhesion in cold-sprayed copper coating of aluminum," *Surface and Coatings Technlogy,* vol. 197, no. 1, pp. 18-27, 2005.

[93] V. Guipont, M. Jeandin, S. Bansard, K. A. Khor, M. Nivard, L. Berthe, J.-P. Cuq-Lelandais and M. Boustie, "Bond strength determination of hydroxyapatite coatings on Ti-6Al-4V substrates using the LAser Shock Adhesion Test (LASAT)," *Journal of Biomedical Materials Research Part A,* vol. 95, no. 4, pp. 1096-1104, 2010.

[94] T. Yilmaz, B. Ercikdi, K. Karaman and G. Kulekci, "Assessment of strength properties of cemented paste backfill by ultrasonic pulse velocity test," *Ultrasonics,* vol. 54, no. 5, pp. 1386-1394, 2014.

[95] R. L. V. Kumar, M. R. Bhat and C. R. L. Murthy, "Some studies on evaluation of degradation in composite adhesive joints using ultrasonic techniques," *Ultrasonics,* vol. 53, pp. 1150-1162, 2013.

[96] A. Baudot, J. Moysan, C. Payan, N. Ylla, J. Galy, B. Verneret and A. Baillard, "Improving adhesion strength analysis by the combination of ultrasonic and mechanical tests on single lap joints," *Journal of Adhesion,* vol. 90, no. 5-6, pp. 555-568, 2014.

[97] L. Adler, S. Rokhlin, C. Mattei, G. Blaho and Q. Xie, "Angle beam ultrasonic spectroscopy system for quantitative inspection of adhesive bonds," *Review of Progress in Quantitative Nondestructive Evaluation,* vol. 18, pp. 1553-1559, 1999.

[98] J.-M. Baik and R. B. Thompson, "Ultrasonic scattering from imperfect interfaces: A quasi-static model," *Journal of Nondestructive Evaluation,* vol. 4, no. 3/4, pp. 177-196, 1984.

[99] H. J. McSkimin, "Pulse Superposition Method for Measuring Ultrasonic Wave Velocities in Solids," *Journal of the Acoustical Society of America,* vol. 33, no. 1, pp. 12-16, 1961.

[100] E. P. Papadakis, "Ultrasonic Phase Velocity by the Pulse-Echo-Overlap Method Incorporating Diffraction Phase Corrections," *Journal of the Acoustical Society of America,* pp. 1045-1051, 1967.

[101] R. Odru, C. Riou, J. Vacher, P. Deterre, P. Peguin and F. Vanoni, "New instrument for continuous and simultaneous recording of changes in ultrasonic attenuation and velocity," *Review of Scientific Instruments,* vol. 49, no. 2, pp. 238-241, 1978.

[102] S. Taki, Y. Furuta and T. Takemura, "New Instrument for Rapid Measurement of Changes in Ultrasonic Velocity," *Review of Scientific Instruments,* vol. 52, no. 9, pp. 1388-1391, 1981.

[103] G. Horvath-Szabo, M. Hoiland and E. Hogseth, "An Automated Apparatus for Ultrasound Velocity Measurements Improving the Pulse-Echo-Overlap Method to a Precision Better than 0.5 ppm in Liquids," *Review of Scientific Instruments,* vol. 65, pp. 1644-1648, 1994.

[104] D. J. McClements and P. Fairley, "Ultrasonic Pulse Echo Reflectometer," *Ultrasonics,* vol. 29, no. 1, pp. 58-62, 1991.

[105] T. Pialucha and P. Cawley, "The Detection of Thin Embedded Layers using Normal Incidence Ultrasound," *Ultrasonics,* vol. 32, no. 6, pp. 431-440, 1994.

[106] C. Jin, "A Continuous Wave Method for Simultaneous Sound Velocity and Attenuation Measurements," *Review of Scientific Instruments,* vol. 67, no. 1, pp. 271-273, 1996.

[107] U. Kaatze, F. Eggers and K. Lautscham, "Ultrasonic Velocity Measurements in Liquids with High Resolution -- Techniques, Selected Applications and Perspectives," *Measurement Science and Technology,* vol. 19, no. 6, pp. 1-21, 2008.

[108] D. Marioli, C. Narduzzi, C. Offelli, D. Petri, E. Sardini and A. Taroni, "Digital Time-of-Flight Measurement for Ultrasonic Sensors," *IEEE Transactions on Instrumentation and Measurement,* vol. 41, no. 1, pp. 93-97, 1992.

[109] D. R. Hull, H. E. Kautz and A. Vary, "Ultrasonic Velocity Measurement Using Phase-Slope and Cross-Correlation Methods," in *Spring Conference of the American Society for Nondestructive Testing*, Denver, CO, USA, 1984.

[110] J. D. Aussel and J. P. Monchalin, "Precision Laser-Ultrasonic Velocity Measurement and Elastic Constant Determination," *Ultrasonics,* vol. 27, no. 3, pp. 165-177, 1989.

[111] I. Fujii and K. Kawashima, "Digital Measurement of Ultrasonic Velocity," *Review of Progress in Quantitative Nondestructive Evaluation,* vol. 14, pp. 203-209, 1995.

[112] R. E. Guerjouma, A. Mouchtachi, Y. Jayet and J. C. Baboux, "Non-Destructive Evaluation of Graphite by Ultrasonic Velocity Measurement using Cross-Correlation and Hilbert Transform Methods," in *IEEE Ultrasonics Symposium*, Tucson, AZ, USA, 1992.

[113] P. Brassier, B. Hosten and F. Vulovic, "High-Frequency Transducers and Correlation Method to Enhance Ultrasonic Gas Flow Metering," *Flow Measurement and Instrumentation,* vol. 12, no. 3, pp. 201-211, 2001.

[114] S. Hirata, M. K. Kurosawa and T. Katagiri, "Accuracy and Resolution of Ultrasonic Distance Measurement with High-Time-Resolution Cross-Correlation Function Obtained by Single-Bit Signal Processing," *Acoustical Science and Technology,* vol. 30, no. 6, pp. 429-438, 2009.

[115] T. Chen, P. Que, O. Zhang and Q. Liu, "Ultrasonic Nondestructive Testing Accurate Sizing and Locating Technique Based on Time-of-Flight-Diffraction Method," *Russian Journal of Nondestructive Testing,* vol. 41, no. 9, pp. 594-601, 2005.

[116] Y.-R. Liang, H.-Z. Duan, H.-C. Yeh and J. Luo, "Fundamental Limits on the Digital Phase Measurement Method Based on Cross-Correlation Analysis," *Review of Scientific Instruments,* vol. 83, no. 9, p. 095110, 2012.

[117] R. J. Blume, "Instrument for the Dontinuous and High Resolution Measurement of Changes in the Velocity of Ultrasound," *Review of Scientific Instruments,* vol. 34, no. 12, pp. 1400-1407, 1963.

[118] J. S. Heyman and E. J. Chern, "Ultrasonic Measurement of Axial Stress," *ASTM Journal of Testing and Evaluation,* vol. 10, no. 5, pp. 202-211, 1982.

[119] W. T. Yost, J. H. Cantrell and P. W. Kushnick, "Fundamental aspects of pulse phase-locked loop technology-based methods for measurement of ultrasonic velocity," *Journal of the Acoustical Society of America,* vol. 91, no. 3, pp. 1456-1468, 1992.

[120] W. T. Yost, J. H. Cantrell and P. W. Kushnick, "Constant Frequency Pulsed Phase-Locked-Loop Instrument for Measurement of Ultrasonic Velocity," *Review of Scientific Instruments,* vol. 62, no. 10, pp. 2451-2456, 1991.

[121] K.-Y. Jhang, H.-H. Quan, J. Ha and N.-Y. Kim, "Estimation of Clamping Force in High-Tension Bolts through Ultrasonic Velocity Measurement," *Ultrasonics,* vol. 44, pp. 1339-1342, 2006.

[122] S. Adenwalla, S. W. Lin, Q. Z. Ran, Z. Zhao, J. B. Ketterson, J. A. Sauls, L. Taillefer, D. G. Hinks, M. Levy and B. K. Sarma, "Phase Diagram of UPt3 from Ultrasonic Velocity Measurements," *Physical Review Letters,* vol. 65, no. 18, pp. 2298-2301, 1990.

[123] P. Palanichamy, A. Joseph, T. Jayakumar and B. Raj, "Ultrasonic Velocity Measurements for Estimation of Grain Size in Austenitic Stainless Steel," *NDT&E International,* vol. 28, no. 3, pp. 179-185, 1995.

[124] P. H. Nicholson, G. Lowet, C. M. Langton, J. Dequeker and G. Van der Perre, "A Comparison of Time-Domain and Frequency-Domain Approaches to Ultrasonic Velocity Measurements in Trabecular Bone," *Physics in Medicine and Biology,* vol. 41, no. 11, pp. 2421-2435, 1996.

[125] M. Cutroni and A. Mandanici, "The alpha-relaxation process in simple glass forming liquid m-toluidine. II. the temperature dependence of the mechanical response," *The Journal of Chemical Physics,* vol. 114, no. 16, pp. 7124-7129, 2001.

[126] T. Ueno, B. R. Macias, W. T. Yost and A. R. Hargens, "Noninvasive Assessment of Intercranial Pressure Waveforms by using Pulsed Phase Lock Loop Technology," *Journal of Neurosurgery,* vol. 103, no. 2, pp. 361-367, 2005.

[127] V. N. Bindal, "Water-Based Couplants for General Purpose Use for Ultrasonic NDT Applications," *Journal of Scientific and Industrial Research,* vol. 59, pp. 935-939, 2000.

[128] M. Redwood and J. Lamb, "On the Measurement of Attenuation in Ultrasonic Delay Lines," *Proceedings of the IEEE: Radio and Electronic Engineering,* vol. 103, no. 12, pp. 773-780, 1956.

[129] T. Inamura, "The Effect of Bonding Materials on the Characteristics of Ultrasonic Delay Lines with Piezoelectric Transducers," *Japanese Journal of Applied Physics,* vol. 9, no. 3, pp. 255-259, 1970.

[130] Y. H. Kim, S.-J. Song, S.-S. Lee, J.-K. Lee, S.-S. Hong and H. S. Eom, "A Study on the Couplant Effects on Contact Ultrasonic Testing," *Journal of the Korean Society for Nondestructive Testing,* vol. 22, no. 6, pp. 621-626, 2002.

[131] A. Vincent, "Influence of Wearplate and Coupling Layer Thickness on Ultrasonic Velocity Measurement," *Ultrasonics,* vol. 25, pp. 237-243, 1987.

[132] J. Williams and J. Lamb, "On the Measurement of Ultrasonic Velocity in Solids," *The Journal of the Acoustical Society of America,* vol. 30, no. 4, pp. 308-313, 1958.

[133] T. Reddyhoff, S. Kasolang, R. S. Dwyer-Joyce and B. W. Drinkwater, "The Phase Shift of an Ultrasonic Pulse at an Oil Layer and Determination of Film Thickness," *Proceedings of the Institution of Mechanical Engineers, Part J: Journal of Engineering Tribology,* vol. 219, no. 6, pp. 387-400, 2005.

[134] H. B. Huntington, A. G. Emslie and V. W. Hughes, "Ultrasonic Delay Lines," *Journal of the Franklin Institute,* vol. 245, no. 1, pp. 1-23, 1948.

[135] H. Seki, A. Granato and R. Truell, "Diffraction Effects in the Ultrasonic Field of a Piston Source and Their Importance in the Accurate Measurement of Attenuation," *Journal of the Acoustical Society of America,* vol. 28, no. 2, pp. 230-238, 1956.

[136] A. O. Williams, "The Piston Source at High Frequencies," *Journal of the Acoustical Society of America,* vol. 23, no. 1, pp. 1-6, 1951.

[137] E. Papadakis, "Ultrasonic Diffraction Loss and Phase Change in Anisotropic Materials," *Journal of the Acoustical Society of America,* vol. 40, no. 4, pp. 863-876, 1966.

[138] A. S. Khimunin, "Ultrasonic Propagation Parameter Measurements Incorporating Exact Diffraction Corrections," *Acoustica,* vol. 39, pp. 87-95, 1978.

[139] J. Kushibiki and M. Arakawa, "Diffraction Effects on Bulk-Wave Ultrasonic Velocity and Attenuation Measurements," *Journal of the Acoustical Society of America,* vol. 108, no. 2, pp. 564-573, 2000.

[140] K. Negishi, K. Takagi and H. Ozawa, "Observation of Phase Advance due to Diffraction of Ultrasonic Phase," *Journal of the Acoustical Society of Japan,* vol. 1, no. 1, pp. 11-15, 1980.

[141] P. H. Rogers and A. L. Van Buren, "An Exact Expression for the Lommel Diffraction Correction Integral," *Journal of the Acoustical Society of America,* vol. 55, no. 4, pp. 724-729, 1974.

[142] Norland Products, "Norland Optical Adhesive 60," Norland Products, Inc., [Online]. Available: https://www.norlandprod.com/adhesives/noa%2060.html. [Accessed 22 March 2018].

[143] Macken Instruments, Inc., "Ultraviolet Lamps for Thermal Image Plates," [Online]. Available: https://cdn.shopify.com/s/files/1/0708/4817/files/22UV_User_Information.pdf.

[144] Schott, "Borofloat 33 -- Optical Properties," [Online]. Available: http://www.us.schott.com/d/borofloat/1ca1519d-b5b3-469d-b3eb-9b80235b1783/1.2/borofloat33_opt_usa_web.pdf. [Accessed 22 March 2018].

[145] L. E. Kinsler, A. R. Frey, A. B. Coppens and J. V. Sanders, "Tables of Physical Properties of Matter," in *Fundamentals of Acoustics,* New York, Wiley, 2000, pp. 526-528.

[146] H. Lekesiz, N. Katsube, S. Rokhlin and R. Seghi, "Effective Spring Stiffness for a Planar Periodic Array of Collinear Cracks at an Interface between Two Dissimilar Isotropic Materials," *Mechanical Materials,* vol. 43, no. 2, pp. 87-98, 2011.

[147] Y. C. Angel and J. D. Achenbach, "Reflection and Transmission of Elastic Waves by a Periodic Array of Cracks: Oblique Incidence," *Wave Motion,* vol. 7, pp. 375-397, 1985.

[148] D. Corr, M. Accardi, L. Graham-Brady and S. Shah, "Digital image correlation analysis of interfacial debonding properties and fracture behavior in concrete," *Engineering Fracture Mechanics,* vol. 74, pp. 109-121, 2007.

[149] A. J. Comer, K. B. Katnam, W. F. Stanley and T. M. Young, "Characterising the behaviour of composite single lap bonded joints using digital image correlation," *International Journal of Adhesion and Adhesives,* vol. 40, pp. 215-223, 2013.

[150] R. C. Tighe, J. M. Dulieu-Barton and S. Quinn, "Identificaiton of kissing defects in adhesive bonds using infrared thermography," *International Journal of Adhesion and Adhesives,* vol. 64, pp. 168-178, 2016.

[151] M. Genest, M. Martinez, N. Mrad, G. Renaud and A. Fahr, "Pulsed thermography for non-destructive evaluation and damage growth monitoring of bonded repairs," *Composite Structures,* vol. 88, no. 1, pp. 112-120, 2009.

[152] P. J. Steinbild, R. Hohne, R. Fubel and N. Modler, "A sensor detecting kissing bonds in adhesively bonded joints using electric time domain reflectometry," *NDT&E International,* vol. 102, pp. 114-119, 2019.

[153] R. Mactabi, I. D. Rosca and S. V. Hoa, "Monitoring the integrity of adhesive joints during fatigue loading using carbon nanotubes," *Composites Science and Technology,* vol. 78, pp. 1-9, 2013.

[154] R. Dugnani, Y. Zhuang, F. Kopsaftopoulos and F.-K. Chang, "Adhesive bond-line degradation detection via a cross-correlation electromechanical impedance-based approach," *Structural Health Monitoring,* vol. 15, no. 6, pp. 1-18, 2016.

[155] S. F. Karimian, M. Mosayebi and T. P. Chu, "Evaluation of Adhesive Joints with Ultrasonic Digital Image Correlation," in *ASNT Research Symposium,* Jacksonville, FL, 2017.

[156] C. Jeenjitkaew and F. J. Guild, "The Analysis of Kissing Bonds in Adhesive Joints," *International Journal of Adhesion and Adhesives,* vol. 75, pp. 101-107, 2017.

[157] C. Jeenjitkaew, Kissing bonds in adhesive joints: a holistic approach for surface chemistry and joint mechanics, Ph.D. Thesis, University of London, 2011.

[158] M. K. Budzik, J. Jumel and M. E. R. Shanahan, "An in-situ technique for the assessment of adhesive properties of a joint under load," *International Journal of Fracture,* vol. 171, no. 2, pp. 111-124, 2011.

[159] S. Patra, S. Banerjee, E. Habtour and R. Haynes, "A Novel Ultrasonic Technique for the Detection of Distributed Precursor Damages in Composites," in *International Mechanical Engineering Congress and Exposition*, Phoenix, AZ, USA, 2016.

[160] S. I. Rokhlin, D. K. Lewis, K. F. Graff and L. Adler, "Real-time study of frequency dependence of attenuation and velocity of ultrasonic waves during the curing reaction of epoxy resin," *Journal of the Acoustical Society of America,* vol. 79, no. 6, pp. 1786-1793, 1986.

[161] J. M. Waller, B. H. Parker, K. L. Hodges, E. R. Burke and J. L. Walker, "Nondestructive evaluation of additive manufacturing: State-of-the-discipline report," NASA, Hampton, VA, 2014.

[162] J. A. Slotwinski, E. J. Garboczi and K. M. Hebenstreit, "Porosity measurements and analysis for metal additive manufacturing process control," *Journal of Research of the National Institute of Standards and Technology,* vol. 119, pp. 494-528, 2014.

[163] H. Rieder, A. Dillhofer, M. Spies, J. Bamberg and T. Hess, "Online monitoring of additive manufacturing processes using ultrasound," in *11th European Conference on Non-Destructive Testing (ECNDT),* Prague, Czech Republic, 2014.

[164] H. Rieder, M. Spies, J. Bamberg and B. Henkel, "On- and offline ultrasonic characterization of components built by SLJ additive manufacturing," in *42nd Annual Review of Progress in Quantitative Nondestructive Evaluation (QNDE),* Minneapolis, MN, 2016.

[165] L. J. Bond, L. W. Koester and H. Taheri, "NDE in-process for metal parts fabricated using powder based additive manufacturing," in *SPIE Smart Structures and Nondestructive Evaluation,* Denver, CO, 2019.

[166] R. J. Smith, M. Hirsch, R. Patel, W. Li, A. T. Clare and S. D. Sharples, "Spatially resolved acoustic spectroscopy for selective laser melting," *Journal of Materials Processing Technology,* vol. 236, pp. 93-102, 2016.

[167] A. J. Manzo, S. Kenderian and H. Helvajian, "Application of laser ultrasonic non-destructive evaluation technique to additive manufacturing," in *SPIE LASE*, San Francisco, CA, 2016.

[168] Y. Ishii and S. Biwa, "Ultrasonic evaluation of interlayer interfacial stiffness of multilayered structures," *Journal of Applied Physics*, vol. 111, p. 084907, 2012.

[169] V. K. Nadimpalli, L. Yang and P. B. Nagy, "In-situ interfacial quality assessment of ultrasonic additive manufacturing components using ultrasonic NDE," *NDT&E International*, vol. 93, pp. 117-130, 2018.

[170] Y. Ishii and S. Biwa, "Evaluation of interlayer interfacial stiffness and layer wave velocity of multilayered structures by ultrasonic spectroscopy," *Journal of the Acoustical Society of America*, vol. 136, no. 1, pp. 183-191, 2014.

Appendices

Appendix A. List of Publications and Awards

Publications Related to this Work

1. **H. A. Haldren**, D. F. Perey, W. T. Yost, K. E. Cramer, and M. C. Gupta. "A Constant-Frequency Ultrasonic Phase Method for Monitoring Imperfect Adherent/Adhesive Interfaces," (under preparation).
2. **H. A. Haldren**, D. F. Perey, W. T. Yost, K. E. Cramer, and M. C. Gupta. "A Method for Ultrasonic Phase Monitoring of Single Lap Joints under Quasi-Static Shear Load," (under preparation).
3. **H. A. Haldren**, D. F. Perey, W. T. Yost, K. E. Cramer, and M. C. Gupta. "Swept-Frequency Ultrasonic Phase Evaluation of Adhesive Bonding in Tri-Layer Structures," *Journal of the Acoustical Society of America,* vol 145, no. 3, pp. 1609-1618, 2019.
4. **H. A. Haldren**, D. F. Perey, W. T. Yost, K. E. Cramer, and M. C. Gupta. "A Digital, Constant-Frequency Pulsed Phase-Locked-Loop Instrument for Real-Time, Absolute Ultrasonic Phase Measurements," *Review of Scientific Instruments,* vol. 89, no. 5, pp. 54902, 2018.
5. **H. A. Haldren**, D. F. Perey, W. T. Yost, K. E. Cramer, and M. C. Gupta. "Nondestructive Evaluation of Interfacial Bond Strength in Single Lap Joints via Swept-Frequency Ultrasonic Phase Measurements," *AIP Conference Proceedings,* vol 2102, no. 1, pp. 40016, 2019.

6. **H. A. Haldren**, D. F. Perey, W. T. Yost, K. E. Cramer, and M. C. Gupta. “Ultrasonic Phase Measurement of Adhesion Quality in Aluminum/Epoxy Lap Joints,” in *Proceedings of 40th Annual Meeting of the Adhesion Society*, St. Petersburg, FL, USA, 2017.
7. **H. A. Haldren**, D. F. Perey, W. T. Yost, K. E. Cramer, and M. C. Gupta. “Nondestructive Evaluation of Adhesive Bonds via Ultrasonic Phase Measurements,” in *Proceedings of 31st American Society for Composites Technical Conference*, Williamsburg, VA, USA, 2016.

Conference Presentations Related to this Work

1. **H. A. Haldren**, D. F. Perey, W. T. Yost, K. E. Cramer, and M. C. Gupta. “Bond Strength Evaluation of Interfacially-Contaminated Adhesively Bonded Single Lap Joints using Ultrasonic Phase Measurements ” at *The American Society for Nondestructive Testing Annual Conference*, Houston, TX, USA, 2018.
2. **H. A. Haldren**, D. F. Perey, W. T. Yost, K. E. Cramer, and M. C. Gupta. “Nondestructive Evaluation of Interfacial Bond Strength in Single Lap Joints via Swept-Frequency Ultrasonic Phase Measurements,” at *The 45th Annual Review of Progress in Nondestructive Evaluation*, Burlington, VT, USA, 2018.
3. **H. A. Haldren**, D. F. Perey, W. T. Yost, K. E. Cramer, and M. C. Gupta. “Ultrasonic Phase Measurement of Adhesion Quality in Aluminum/Epoxy Lap Joints,” at *40th Annual Meeting of the Adhesion Society*, St. Petersburg, FL, USA, 2017.
4. **H. A. Haldren**, D. F. Perey, W. T. Yost, K. E. Cramer, and M. C. Gupta. “Nondestructive Evaluation of Adhesive Bonds via Ultrasonic Phase Measurements,” at *31st American Society for Composites Technical Conference*, Williamsburg, VA, USA, 2016.

Invention Disclosures

1. **H. Haldren**, D. Perey, W. Yost, K. Cramer, and M. Gupta. "Method for the Evaluation of Adhesive Bond Strength via Swept-Frequency Ultrasonic Phase Measurements"

Awards

1. National Institute of Aerospace Best Student Paper Award 2018, for **H. A. Haldren,** D. F. Perey, W. T. Yost, K. E. Cramer, and M. C. Gupta. "A Digital, Constant-Frequency Pulsed Phase-Locked-Loop Instrument for Real-Time, Absolute Ultrasonic Phase Measurements," *Review of Scientific Instruments,* vol. 89, no. 5, pp. 54902, 2018.
2. Awarded NASA Space Technology Research Fellowship (2016-2019).
3. Presented fellowship research to US Congressmen, NASA officials, and staff at the NASA Space Technology Mission Directorate Technology Day on the Hill event (2018).
4. National Institute of Aerospace Martin L. Drews Scholarship Award 2016.

Additional Publications

1. **H. A. Haldren**. "Studies in Software Defined Radio System Implementation," *Undergraduate Senior Honors Thesis for Liberty University*, 2014.
2. P. Dulal, A. Block, **H. A. Haldren**, D. C. Hutchings, and B. J. H. Stadler. "Effects of Different Seedlayers on the Magneto-optic Properties of Rare Earth Iron Garnets Grown on Semiconductor Substrates," in *Joint MMM-Intermag Conference*, San Diego, CA, USA, 2016.
3. P. Dulal, A. D. Block, T. E. Gage, **H. A. Haldren**, S.-Y. Sung. D. C. Hutchings, and B. J. H. Stadler. "Optimized Magneto-Optical Isolator Designs Inspired by Seedlayer-Free Terbium Iron Garnets with Opposite Chirality," *ACS Photonics*, vol. 3, no. 10, pp. 1818-1825, 2016.

Appendix B. Curve Fitting of Amplitude and Phase vs. Frequency Responses of Bond line Reflection MATLAB Code

The MATLAB code used to find interfacial stiffness from measured phase and amplitude curves, as is conducted in Chapter 6, is shown below. The model for ultrasonic interactions with imperfect interfaces is described in detail in Chapter 3.

The code shown in this appendix was written for MATLAB version R2017b and uses MATLAB's Curve Fitting Toolbox. For fitting a phase spectrum, the following MATLAB functions are required: `PhaseSLJReflKM12Fit`, `PhaseSLJReflKm12Model`, `PhaseBondReflKm12`, and `BondReflKm12`. For curve-fitting a measured amplitude spectrum, the following MATLAB functions are required: `AmpSLJReflKM12Fit`, `AmpSLJReflKm12Model`, `AmpBondReflKm12`, and `BondReflKm12`. The curve-fitting models shown here can be run in a short amount of time on a typical desktop computer and parallel processing is not necessary.

For a phase or amplitude curve-fit, the `XXXXSLJReflKM12Fit` function is used to take in input data as well as set parameters to conduct the curve-fitting process. This function is named as such, because it fits the input data to the reflection coefficient from a SLJ and with a mass-spring model of the adhesive/adherent interfaces, denoted by subscripts 1 and 2. It uses a custom fitting process using MATLAB's Curve Fitting Toolbox and ultimately outputs the fit object along with all material parameters used in the fit, including both set and found values from the fit. It also outputs a plot showing the measured data as well as the theoretical curve with the fit parameters. In practice, the fit parameters as well as their upper and lower bounds are modified within this function code before running the curve fitting method.

The custom fit model used for the amplitude and phase curve-fitting processes are defined by the `XXXXSLJReflKm12Model` function. This function takes all of the input parameters from the `XXXXSLJReflKM12Fit` function and models the phase or amplitude response combined with linear coefficients which account for measurement uncertainty.

The phase and amplitude response of the reflection coefficient from a SLJ is computed using the `XXXXBondReflKm12` function. This function takes input data from the `XXXXSLJReflKm12Model` function and computes the phase or amplitude of the reflection coefficient of a SLJ with imperfect interfaces.

Finally, the reflection coefficient from a SLJ with imperfect interfaces is computed by the `BondReflKm12` function. Both amplitude and phase curve-fitting methods use this function to find the complex reflection coefficient. This function may be used independently from curve fitting to simply theoretically model how the amplitude or phase spectra changes as different material properties of the SLJ change, such as bond line thickness or interfacial stiffness.

B.1 Function `PhaseSLJReflKm12Fit`

```
function [PhaseFitObj,rhofit,cfit,L2fit,alphafit,Kfit,mfit,afit,bfit]  =
PhaseSLJReflKm12Fit(frange,rhoStart,cStart,L2Start,alphaStart,KExpStart,mStar
t,aStart,bStart,PhaseMeas)
% [PhaseFitObj,rhofit,cfit,L2fit,alphafit,Kfit,mfit,afit,bfit] =
PhaseSLJReflKm12Fit(frange,rho,c,L2,alpha,K,m,a,b,PhaseMeas)
% This function takes an input phase vs. frequency response and fits the
% theoeretical parameters to cause that response.
% INPUTS:
%   frange, frequency range swept over (Hz)
%   rhoStart = [rho1, rho2, rho3], prediction densities of each medium
(kg/m^3)
%   cStart = [c1, c2, c3], prediction of longitudinal sound velocity in each
medium (m/s)
%   L2Start, adhesive bond line thickness (m)
%   alphaStart = [alpha1, alpha2, alpha3], prediction of attenuation
coefficient in each
%             medium (nepers/m)
%   KExpStart = [K1ExpStart, K2ExpStart], KStart = 10^KExpStart prediction of
interfacial stiffnesses (N/m^3)
%   mStart = [m1, m2], prediction of interfacial mass-loading (kg)
%   aStart, prediction of linear frequency dependent phase correction term
(deg/Hz)
```

```
%   bStart, prediction of constant phase correction term (deg)
%   PhaseMeas, Measured phase response from frequency sweep
% OUTPUTS:
%   PhaseFitObj, phase from model fit
%   rhofit = [rho1, rho2, rho3], densities of each medium (kg/m^3)
%   cfit = [c1, c2, c3], longitudinal sound velocity in each medium (m/s)
%   L2fit, adhesive bond line thickness (m)
%   alphafit = [alpha1, alpha2, alpha3], attenuation coefficient in each
%            medium (nepers/m)
%   Kfit = [K1, K2], interfacial stiffnesses (N/m^3)
%   mfit = [m1, m2], interfacial mass-loading (kg)
%   afit, linear frequency dependent phase correction term (deg/Hz)
%   bfit, constant phase correction term (deg)

%% Fit measured data to model
SLJFitType =
fittype('PhaseSLJReflKm12Model(frange,rho1,rho2,rho3,c1,c2,c3,L2,alpha1,alpha
2,alpha3,K1Exp,K2Exp,m1,m2,a,b)','independent',{'frange'},'problem',{'rho1','
rho3','alpha1','alpha3','c1','c3','m1','m2','rho2','c2','alpha2','K2Exp'});
%coeffnames(SLJFitType)
SLJFitOptions = fitoptions(SLJFitType);
SLJFitOptions.StartPoint = [KExpStart(1), L2Start       , aStart , bStart ];
SLJFitOptions.Lower =      [12          , L2Start - 5e-6, -10e-6 ,-10   ];
SLJFitOptions.Upper =      [18          , L2Start + 5e-6, 10e-6  ,10    ];
SLJFitOptions.MaxFunEvals = 1e5;
SLJFitOptions.MaxIter = 1e5;
SLJFitOptions.Robust = 'LAR';
PhaseFitObj =
fit(frange,PhaseMeas,SLJFitType,SLJFitOptions,'problem',{rhoStart(1),rhoStart
(3),alphaStart(1),alphaStart(3),cStart(1),cStart(3),mStart(1),mStart(2),rhoSt
art(2),cStart(2),alphaStart(2),KExpStart(2)})

%% Plot Data w/ Fit
figure
plot(PhaseFitObj,frange,PhaseMeas,'predfunc')
xlabel('Frequency (Hz)','FontSize',18)
ylabel('Phase (deg)','FontSize',18)
set(gca,'FontSize',18)
grid on
title('Measured and Fitted Phase vs. Freq. from Bond line','FontSize',24)
axis([8.5e6 11.75e6 -50 50])
set(gca,'XTick',8.5e6:0.25e6:11.75e6,'YTick',-90:10:90)
%% Output fitted values
%coeffs = coeffnames(SLJFitType)
coeffFit= coeffvalues(PhaseFitObj);
Kfit = [10^coeffFit(1), 10^KExpStart(2)];
L2fit = coeffFit(2);
afit = coeffFit(3);
alphafit = [alphaStart(1),alphaStart(2),alphaStart(3)];
bfit = coeffFit(4);
cfit = [cStart(1),cStart(2),cStart(3)];
mfit = mStart;
rhofit = [rhoStart(1),rhoStart(2),rhoStart(3)];
```

B.2: Function `PhaseSLJReflKm12Model`

```
function Phase =
PhaseSLJReflKm12Model(frange,rho1,rho2,rho3,c1,c2,c3,L2,alpha1,alpha2,alpha3,
K1Exp,K2Exp,m1,m2,a,b)
% Phase =
PhaseSLJReflKm12Model(frange,rho1,rho2,rho3,c1,c2,c3,L2,alpha1,alpha2,alpha3,
K1Exp,K2Exp,m1,m2,a,b)
% Used for curve-fitting measured SLJ phase vs. frequency data to
% theoretical model. Allows for theoretical ultrasonic SLJ reflection
% response vs. frequency as well as linear correction term to aid in fit,
% in case there are adherent or couplant thickness differences.
% INPUTS:
%   frange = driving frequency (Hz)
%   [rho1, rho2, rho3], mass density (kg/m^3) in each medium
%   [c1,c2,c3], longitudinal sound velocity (m/s) in each medium
%   L2, adhesive bond line thickness (m)
%   [alpha1, alpha2, alpha3], attenuation coefficient (nepers/m) in
%      each medium
%   [K1Exp, K2Exp], K = 10^KExp stiffness(N/m^3) at each interface
%   [m1, m2], mass-loading (kg) at each interface
%   a, linear frequency dependent phase correction term (deg/Hz)
%   b, constant phase correction term (deg)
% OUTPUTS:
%   Phase = phase of reflection coefficient summed with
%           linear term

%% Group Parameters
rho = [rho1, rho2, rho3];
c = [c1, c2, c3];
alpha = [alpha1, alpha2, alpha3];
K = [10^K1Exp, 10^K2Exp];
m = [m1, m2];

%% Evaluate Phase Response
Phase = PhaseBondReflKm12(rho,c,frange,L2,alpha,K,m);
Phase = Phase + a.*frange + b;
```

B.3 Function `PhaseBondReflKm12`

```
function Phase = PhaseBondReflKm12(rho,c,f,L2,alpha,K,m)
% Outputs phase of bond line reflections with different
% stiffnesses and mass loading at each interface.

Phase = radtodeg(unwrap(angle(BondReflKm12(rho,c,f,L2,alpha,K,m))));
for n = 1:length(Phase)
    if isnan(Phase(n)) == 1
        Phase(n) = 0;
    end
end
```

B.4 Function `AmpSLJReflKm12Fit`

```
function [AmpFitObj,rhofit,cfit,L2fit,alphafit,Kfit,mfit,afit,bfit]  =
AmpSLJReflKm12Fit(frange,rhoStart,cStart,L2Start,alphaStart,KExpStart,mStart,
aStart,bStart,AmpMeas)
% [AmpFitObj,rhofit,cfit,L2fit,alphafit,Kfit,mfit,afit]  =
AmpSLJReflKm12Fit(frange,rhoStart,cStart,L2Start,alphaStart,KExpStart,mStart,
aStart,bStart,AmpMeas)
% This function takes an input amplitude vs. frequency response and fits the
% theoeretical parameters to cause that response.
% INPUTS:
%   frange, frequency range swept over (Hz)
%   rhoStart = [rho1, rho2, rho3], prediction densities of each medium
(kg/m^3)
%   cStart = [c1, c2, c3], prediction of longitudinal sound velocity in each
medium (m/s)
%   L2Start, adhesive bond line thickness (m)
%   alphaStart = [alpha1, alpha2, alpha3], prediction of attenuation
coefficient in each
%             medium (nepers/m)
%   KExpStart = [K1ExpStart, K2ExpStart], KStart = 10^KExpStart, prediction
of interfacial stiffnesses (N/m^3)
%   mStart = [m1Start, m2Start], prediction of interfacial mass-loading (kg)
%   aStart, prediction of linear coefficient to the amplitude
%   bStart, prediction of constant coefficient to the amplitude
%   AmpMeas, Measured amplitude response from frequency sweep
% OUTPUTS:
%   AmpFitObj, amplitude from model fit
%   rhofit = [rho1, rho2, rho3], densities of each medium (kg/m^3)
%   cfit = [c1, c2, c3], longitudinal sound velocity in each medium (m/s)
%   L2fit, adhesive bond line thickness (m)
%   alphafit = [alpha1, alpha2, alpha3], attenuation coefficient in each
%             medium (nepers/m)
%   Kfit = [K1fit, K2fit], interfacial stiffnesses (N/m^3)
%   mfit = [m1fit, m2fit], interfacial mass-loading (kg)
%   afit, linear amplitude correction coefficient
%   bfit, constant amplitude correction coefficient

%% Fit measured data to model
SLJFitType =
fittype('AmpSLJReflKm12Model(frange,rho1,rho2,rho3,c1,c2,c3,L2,alpha1,alpha2,
alpha3,K1Exp,K2Exp,m1,m2,a,b)','independent',{'frange'},'problem',{'rho1','rh
o2','rho3','c1','c2','c3','alpha1','alpha3','m1','m2','a','L2','alpha2'});
%coeffnames(SLJFitType)
SLJFitOptions = fitoptions(SLJFitType);
SLJFitOptions.StartPoint = [KExpStart(1), KExpStart(2), bStart];
SLJFitOptions.Lower =      [12          , 12          , 0     ];
SLJFitOptions.Upper =      [18          , 18          , 10    ];
SLJFitOptions.MaxFunEvals = 1e6;
SLJFitOptions.MaxIter = 1e6;
SLJFitOptions.Robust = 'LAR';
SLJFitOptions.TolFun = 1e-8;
SLJFitOptions.TolX = 1e-8;
AmpFitObj =
fit(frange,AmpMeas,SLJFitType,SLJFitOptions,'problem',{rhoStart(1),rhoStart(2
```

```
),rhoStart(3),cStart(1),cStart(2),cStart(3),alphaStart(1),alphaStart(3),mStar
t(1),mStart(2),aStart,L2Start,alphaStart(2)});

%% Plot Data w/ Fit
% figure
% plot(AmpFitObj,frange,AmpMeas,'predfunc')
% xlabel('Frequency (Hz)','FontSize',18)
% ylabel('Amplitude','FontSize',18)
% set(gca,'FontSize',18)
% grid on
% str = sprintf('Amp. vs. Freq. Curve Fit\nBorofloat/NOA 60 SLJ: 1 min.
Cure');
% title(str,'FontSize',24)
% axis([8.5e6 11.75e6 0 1])
% set(gca,'XTick',8.5e6:0.25e6:11.75e6,'YTick',0:0.1:1)
%% Output fitted values
%coeffs = coeffnames(SLJFitType)
coeffFit= coeffvalues(AmpFitObj);
Kfit = [10^coeffFit(1), 10^coeffFit(2)];
L2fit = L2Start;
afit = aStart;
alphafit = [alphaStart(1),alphaStart(2),alphaStart(3)];
bfit = coeffFit(3);
cfit = [cStart(1),cStart(2),cStart(3)];
mfit = mStart;
rhofit = [rhoStart(1),rhoStart(2),rhoStart(3)];
```

B.5 Function `AmpSLJReflKm12Model`

```
function Amp =
AmpSLJReflKm12Model(frange,rho1,rho2,rho3,c1,c2,c3,L2,alpha1,alpha2,alpha3,K1
Exp,K2Exp,m1,m2,a,b)
% Amp =
AmpSLJReflKm12Model(frange,rho1,rho2,rho3,c1,c2,c3,L2,alpha1,alpha2,alpha3,K,
m,a,b)
% Used for curve-fitting measured SLJ amplitude vs. frequency data to
% theoretical model. Allows for theoretical ultrasonic SLJ reflection
% response vs. frequency as well as linear correction term to aid in fit,
% in case there are adherent or couplant thickness differences.
% INPUTS:
%   frange = driving frequency (Hz)
%   [rho1, rho2, rho3], mass density (kg/m^3) in each medium
%   [c1,c2,c3], longitudinal sound velocity (m/s) in each medium
%   L2, adhesive bond line thickness (m)
%   [alpha1, alpha2, alpha3], attenuation coefficient (nepers/m) in
%      each medium
%   [K1Exp, K2Exp], K = 10^KExp, stiffness(N/m^3) at each interface
%   [m1, m2], mass-loading (kg) at each interface
%   a, linear offset factor
%   b, constant offset factor
% OUTPUTS:
%   Amp = Amp of reflection coefficient summed with
%           linear term

%% Group Parameters
```

```
rho = [rho1, rho2, rho3];
c = [c1, c2, c3];
alpha = [alpha1, alpha2, alpha3];
K = [10.^K1Exp, 10.^K2Exp];
m = [m1, m2];

%% Evaluate Phase Response
Amp = AmpBondReflKm12(rho,c,frange,L2,alpha,K,m);
Amp = (a.*frange + b).*Amp;
```

B.6 Function `AmpBondReflKm12`

```
function Amp = AmpBondReflKm12(rho,c,f,L2,alpha,K,m)
% Outputs amplitude of bond line reflections with different
% stiffnesses and mass loading at each interface.

Amp = abs(BondReflKm12(rho,c,f,L2,alpha,K,m));
```

B.7 Function `BondReflKm12`

```
function R = BondReflKm12(rho,c,f,L2,alpha,K,m)
% R = BondReflKm12(rho,c,f,L2,alpha,K,m)
% This function gives the complex, normal-incidence ultrasonic displacement
% wave reflection coefficient for a tri-layer, SLJ. It can take into
% account different stiffness and mass-loading at each interface.
%          K1,m1  K2,m2
%  ----------|------|----------
%         -->|----->|-->
%          1 |  T2  | T3
%      Z1    |  Z2  |    Z3
%         R1 |  R2  |
%         <--|<-----|
%  ----------|------|----------
% INPUTS:
%   rho = [rho1, rho2, rho3], mass density (kg./m.^3) in each medium
%   c = [c1,c2,c3], longitudinal sound velocity (m./s) in each medium
%   L2, adhesive bond line thickness (m)
%   f = driving frequency of ultrasonic plane wave (Hz)
%   alpha = [alpha1, alpha2, alpha3], attenuation coefficient (nepers./m) in
%           each medium
%   K = [K1, K2], stiffness (N./m.^3) at each interface
%   m = [m1, m2], mass-loading (kg) at each interface
% OUTPUTS:
%   R =  complex reflection coefficient from imperfect SLJ

%% Define Parameters
w = 2.*pi.*f; % angular frequency
beta1 = w./c(1); % real wavenumber
beta2 = w./c(2);
beta3 = w./c(3);
k1 = beta1.*(alpha(1) + 1i);
k2 = beta2.*(alpha(2) + 1i);
k3 = beta3.*(alpha(3) + 1i);
% k1 = alpha(1) + 1i.*beta1;
```

```
% k2 = alpha(2) + 1i.*beta2;
% k3 = alpha(3) + 1i.*beta3; % complex wavenumber
E = rho.*c.^2; % elastic modulus (Longitudinal)

%% Define Numerator and Denominator terms for multiplication
CoshNTerm = (E(2).*k2).*((E(1).*k1 - E(3).*k3).*(16.*K(1).*K(2) +
m(1).*m(2).*w.^4 - 4.*w.^2.*(K(1).*m(2) + K(2).*m(1))) + 4.*(K(1) +
K(2)).*(4.*E(1).*k1.*E(3).*k3 - m(1).*m(2).*w.^4) - 4.*w.^2.*(m(1) +
m(2)).*(E(1).*k1.*E(3).*k3 - 4.*K(1).*K(2)) - 16.*w.^2.*(E(1).*k1.*K(2).*m(2)
- E(3).*k3.*K(1).*m(1)));
CoshDTerm = (E(2).*k2).*((E(1).*k1 + E(3).*k3).*(16.*K(1).*K(2) +
m(1).*m(2).*w.^4 - 4.*w.^2.*(K(1).*m(2) + K(2).*m(1))) + 4.*(K(1) +
K(2)).*(4.*E(1).*k1.*E(3).*k3 + m(1).*m(2).*w.^4) - 4.*w.^2.*(m(1) +
m(2)).*(E(1).*k1.*E(3).*k3 + 4.*K(1).*K(2)) - 16.*w.^2.*(E(1).*k1.*K(2).*m(2)
+ E(3).*k3.*K(1).*m(1)));
SinhNTerm = (E(1).*k1.*E(3).*k3 - E(2).^2.*k2.^2).*(16.*K(1).*K(2) +
m(1).*m(2).*w.^4 - 4.*w.^2.*(K(1).*m(2) + K(2).*m(1))) + 4.*(E(1).*k1.*K(2) -
E(3).*k3.*K(1)).*(4.*E(2).^2.*k2.^2 + m(1).*m(2).*w.^4) -
4.*w.^2.*(E(1).*k1.*m(2) - E(3).*k3.*m(1)).*(E(2).^2.*k2.^2 + 4.*K(1).*K(2))
+ 16.*(E(1).*k1.*E(2).^2.*k2.^2.*E(3).*k3 - K(1).*K(2).*m(1).*m(2).*w.^4);
SinhDTerm = (E(1).*k1.*E(3).*k3 + E(2).^2.*k2.^2).*(16.*K(1).*K(2) +
m(1).*m(2).*w.^4 - 4.*w.^2.*(K(1).*m(2) + K(2).*m(1))) + 4.*(E(1).*k1.*K(2) +
E(3).*k3.*K(1)).*(4.*E(2).^2.*k2.^2 + m(1).*m(2).*w.^4) -
4.*w.^2.*(E(1).*k1.*m(2) + E(3).*k3.*m(1)).*(E(2).^2.*k2.^2 + 4.*K(1).*K(2))
+ 16.*(E(1).*k1.*E(2).^2.*k2.^2.*E(3).*k3 + K(1).*K(2).*m(1).*m(2).*w.^4);

%% Reflection Coefficient
R = (cosh(k2.*L2).*CoshNTerm +
sinh(k2.*L2).*SinhNTerm)./(cosh(k2.*L2).*CoshDTerm +
sinh(k2.*L2).*SinhDTerm);
```